Trinity College Dublin
Coláiste na Tríonóide, Baile Átha Cliath
The University of Dublin

3D Modelling Tool to Optimise Advanced Plasmonic Luminescent Solar Devices for Building Integrated Photovoltaic Applications

By: Mehran Rafiee

Trinity College Dublin, The University of Dublin

Department of Civil, Structural and Environment Engineering

Supervisor: Professor Sarah McCormack

Co-Supervisors: Dr. Subhash Chandra and Dr. Hind Ahmed

Advisor: Professor Keith Barnham

Date: 30/08/2019

Declaration:

I declare that this thesis has not been submitted as an exercise for PhD Thesis at this or any other university and it is entirely my own work.

I agree to deposit this thesis in the University's open access institutional repository or allow the Library to do so on my behalf, subject to Irish Copyright Legislation and Trinity College Library conditions of use and acknowledgement.

Signature:…… Date:…….

Abstract:

This research concentrates on modelling and optimisation of a static building integrated PV (BIPV) component in which both direct and diffuse solar radiation are harvested through luminescent solar (LS) devices. Plasmonic coupling between luminescent species such as quantum dots (QD), organic dyes, and metal nanoparticles (MNPs) have been investigated and modelled for their application in plasmonically enhanced luminescent solar (pLS) devices to concentrate and convert both direct and diffuse solar radiation to the wavelength region spectrally matched with the PV cell.

A 3D Monte Carlo ray tracing (MCRT) algorithm has been developed to analyse the optical properties of LS device. Moreover, plasmonic modelling of MNPs were undertaken using a 3D finite difference time domain (FDTD) method. The combination of MCRT and FDTD achievements were used in a novel mathematical model and algorithm to develop the first comprehensive 3D tool (referred as PEDAL program) which can optimise and investigate both LS and pLS devices.

A new optimised FDTD (OFDTD) model has been developed which reduces the total memory requirement of the modelling by ~52%. As regards PEDAL, several proposed methods improved the modelling performance e.g. in a modelling with ~125k incident ray, the simulation time was decreased from ~6400 minutes to only ~3 minutes without mitigating the modelling accuracy.

In addition to pLS device modelling, PEDAL was also used to model the optical properties of a variety of LS device configurations where the modelling results were found in close agreement with experimental outcomes. Overall, ~96% average modelling accuracy was achieved. Finally, a new structure has been proposed using pLS device in a large scale BIPV component which not only gives the designer the ability to control the building's interior and exterior visual comfort but also guaranties the optimisation of the BIPV component with any required size and shape of the interest.

Acknowledgment:

"*I'd Put My Money on the Sun and Solar Energy. What a Source of Power! I Hope We Don't Have to Wait until Oil and Coal Run out before we Tackle that. I Wish I Had More Years Left.*" – **Thomas Edison-1931**

"*I'd Put My Money on the Sun and Wind Energy. Hybrid Systems are more Efficient! I Hope We Don't Have to Wait until the Wars on Oil Terminates the Whole Humanity. I Wish I Had the Money.*" – **Mehran Rafiee-2019**

It was a great pleasure for me to work in Solar Energy Application Group (SEAG). I would like to specially thank my supervisor Professor Sarah McCormack for her kindness, compassionate and active supervision. I thank my co-supervisors Dr. Hind Ahmed and Dr. Subhash Chandra for their active guidance and time throughout my PhD work. I would also like to thank Professor Keith Barnham for his advisory supports and encouragements. Thanks goes to all my colleagues and friends in SEAG especially Arunima Sethi and Sarah Gilligan for their help and advice.

Above all, I heartily thank my God, parents, brother and my lovely fiancée who have been always kind supporter, advisor and encouraging to me in my private and professional life.

I would like to acknowledge the funding from the European Research Council grant entitled PEDAL: Plasmonic Enhancement and Directionality of Emission for Advanced Luminescent Solar Devices (639760) and funding from Science Foundation Ireland (SFI)

"*Mehran Rafiee*"

List of Contents

List of Figures

List of Tables

Nomenclature

		Units
A	Absorbance	
A_{Edge}	PV cell area in luminescent solar concentrator (LSC)	m^2
A_{PV}	Total PV cell area in the luminescent solar device	m^2
A_{APR}	Surface of the aperture	m^2
a_j	Coefficient of complexity weight	
B	Magnetic flux density	Wb/m^2
$C^E\|_t$	Curl terms of *E* field	
$C^H\|_{t+\frac{\Delta t}{2}}$	Curl terms of *H* field	
C	Total Solar Concentration Ratio	
C_i	$cos\ (\theta_i)$	
c	Light speed	m/s
c_0	Light speed in vacuum	m/s
$c_{ICP-OES}$	Concentration obtained from ICP method	ppm
c_{MNP}	Concentration of MNP	N/L
C_P	Photon Concentration ratio	
D	Electric flux density	C/m^2
Dim	Dimension	
d	Thickness	cm
d_i	Distance	m
DP	Distance of plane from the coordinate system origin	m
E	Electric field intensity	V/m
E_g	Gap energy	eV or J
E_i	Intensity of incident	J
$E_P(\lambda)$	Energy of photon in each wavelength	eV or J
$E_{P_{OUT}}(\lambda)$	Output energy spectrum of the photons obtained in the detector plane	J
$E_{P_{IN}}(\lambda)$	Input energy spectrum of the system	J
$EM_L(\lambda)$	Emission spectrum absorption spectrum of the luminescent material	
$EQE(\lambda)$	External quantum efficiency spectrum	
e_p	Dipole moment	
f	Frequency	Hz
f_0	Natural frequency	Hz
f_d	damping rate	Hz
f_c	Maximum frequency	Hz
f_{d_K}	Dominant factor for the Kth event	
f_i^{OPT}	Optimization factor of matrix group *i*	
f_{op}	Optimization factor	
FF	Fill factor	
G	Airgap	mm
G_g	Geometric gain	
H	Magnetic field intensity	A/m
h	Planck's constant	J.s
I	Incident ray	
$I_0 : [X_0\ Y_0\ Z_0]$	Origin point	
I_{CE}	Integration terms for curl of *E* field	
I_{CH}	Integration terms for curl of *H* field	
$I_d : [X_d\ Y_d\ Z_d]$	Normalized vector	
I_D	Integration terms of *D*	
I_H	Integration terms of *H*	
I_L	Ray vector with length L	
I_M	Current of the PV terminal at maximum power	A
I_o	Intensity of the detected electric field	V/m
$I_{sc}(\lambda)$	Short circuit current	A
I_t	Intensity of the illuminated electric field	V/m

$IQE(\lambda)$	External quantum efficiency spectrum	
J	Electric current density	A/m^2
J_0	Dark current density	$A.m^{-2}.nm^{-1}$
J_{sc}	Short-circuit current density	$A.m^{-2}.nm^{-1}$
K	Internal Event index	
k	Random number between 0 - 1	
k_0	Radiation free space wavelength	1/nm
k_b	Boltzmann constant	$A.m^2.kg.s^{-2}.K^{-1}$
L	Length	m
L_d	Length of the component	m
L_{PML}	Length of the PML	m
M_{Au}	Molar mass of gold	g/mol
M_m	Mass	Kg
MC	Multiplication constant	
MEM_i	Memory size of matrix group i	
MEM_{total}	Total FDTD memory size	
m	Constitutive relation terms	
$me(\lambda)$	Number of electrons which are generated by the PV at each wavelength	
$mp(\lambda)$	Number of photons striking the PV cell at each wavelength	
N	Surface normal	
N_A	Avogadro number	1/Mol
N_{Au}	Number of gold ions	
$N_{Au/MNP}$	Number of gold atom in one MNP	
N_{BUF}	Number of cells required for the buffers	
N_d	Total number of grid cells	
$N_{Iteration}$	Total number of iteration	
N_{int}	Total number of internal cycles	
N_i^G	Total number of matrices in matrix group i	
N_K	Total number of events in the internal cycles	
N_L	Number of layers with different material in the luminescent solar device	
N_m	Total number of used 3D spatial tracing matrixes	
$N_{P_{IN}}(\lambda)$	Number of input photons at wavelength λ	
$N_{P_{OUT}}(\lambda)$	Number of output photons at wavelength λ	
N_{PML}	Number of cells required for the PMLs	
N_{R_S}	Estimated number of the refracted rays with similar calculations	
$N_{R_{tot}}$	Total number of refracted rays	
N_{Ray}	Total number of rays	
$N_{Records}$	Number the record points	
N_{res}	Grid resolution constant	
N_{SRC}	Number of the source injection point	
n	Ideality factor	
OE	Optical efficiency	
$\vec{P}$	Polarisation vector	
$P(\lambda)$	Incident power	W
$P_{T.abs}^L$	Total power absorbed by the luminescent material	W
$P_{abs}^L(\lambda)$	power absorbed by the luminescent material in each wavelength	W
P_{atte}	Attenuation power	W
P_{cone}	Escape cone loss power	W
P_{direct}	Power reaching PV directly	W
$P_{emit}(\lambda)$	Power emitted by luminescent material in each wavelength	W
$P_{T.emit}$	Total power emitted by luminescent material	W
$P_{in}(\lambda)$	Flux (power) density of the incident light	$W.m^{-2}.nm^{-1}$
$P_{lost}(\lambda)$	Power lost due to loss mechanisms including the reabsorption, escape cone, attenuation and scattering losses	W
$P_{out}(\lambda)$	Power reached to the PV cell	W
$P_{reflect}(\lambda)$	Reflected power	W
$P_{refract}(\lambda)$	Refracted power	W

$P_{re-abs}(\lambda)$	Reabsorbing loss	W
$P_{SPR}(\lambda)$	SPR power	W
P_{scat}	Scattering loss	W
P_{trans}	Transmitted power	W
P_{trap}	Trapped power	W
$\vec{P}_x$	x-component of polarization vector	
$\vec{P}_y$	y-component of polarization vector	
PCE	Power Conversion Efficiency	
PDEF	Photon density enhancement factor	
$PL : [a_P \ b_P \ c_P \ D_P]$	Plane in Space	
PR	Probability or weighted probability of event	
PR_{abs}^{L}	Probability of absorbance by luminescent material	
PR_{abs}^{MNP}	Probability of absorbance by MNP	
PR_{atte}	Probability of attenuation	
PR_{emit}	Weighted probability from emission spectrum	
PR_{PDEF}	Probability of enhancement due to PDEF	
PR_{QF}	Probability of quenching	
PR_{QY}	Probability of emission (from QY)	
PR_r	Probability of reflection	
PR_{re-abs}	Probability of reabsorption	
PR_{scat}	Probability of scattering	
$PR_{T.abs}^{L}$	Luminescent material total absorbance probability	
QF	Quenching factor	
q	Electric charge	Coulombs
R	Reflected ray	
r	Vector of position	
$r_i : [x_i \ \ y_i \ \ z_i]$	Intersection points	
S_u	strength of the resonator	
Sz_i	Total size of the *i*th 3D spatial tracing matric	
SC	Stem component	
SR	Spectral response	A/W
T	Transmitted ray	
T_{Fill}	Total amount of time consumed to survey the conditions to fill the arrays of the 3D spatial tracing matrices	S
$T_{Intersection}$	Total consumed time for calculating the intersection point in the whole ray tracing algorithm	S
T_{PV}	PV temperature	Kelvin
T_{Staus}	Total time consumed for surveying the ray tracing events in internal cycles	S
$T_{Staus_{OPT}}$	Optimised total time consumed for surveying the ray tracing events in internal cycles	S
T_t	Total simulation time	S
t	time	S
t_C	The consumed time of conditional statement	S
t_{C_k}	The consumed time of conditional statement which is used for the Kth ray tracing event	S
t_{ex}	Exposing time	S
t_{ITR}	The consumed time of iterative statement	S
t_S	Time consumed by the mathematical method to calculate the intersection point	S
$Tran$	Transmittance	a.u.
U	number of resonators	
V_M	Voltage of the PV terminal at maximum power	V
V_{MNP}	Volume of MNP	m^3
V_{oc}	Open-circuit voltage	V
V_{Sample}	Volume of sample	L
V_{Tot}	Total volume of primary sample	L
V_{UC}	Volume of unit cell	m^3
W_i	Complexity weight	
X_d	Place of particle	
Z_{m0}	Material impedance in vacuum	Ω

Z_m	Material impedance	Ω
α_{Abs}	Absorption coefficient	1/cm
α_{Atte}	Attenuation coefficient	1/cm
α_{Scat}	Scattering coefficient	1/cm
Γ_{nr}	Non-radiative decay	
Γ_r	Radiative decay	
Γ_{rM}	Radiative decay due to the MNP presence	
Γ_u	Damping rate of the resonator	eV
Δd	Grid cell's size	m
ΔMEM_{total}	Total deducted memory size	
Δt	Time step	S
Δx	Grid cell's size in x direction	m
Δy	Grid cell's size in y direction	m
Δz	Grid cell's size in z direction	m
$\Delta\eta_{opt}$	discrepancy error	
$\Delta\theta$	The ray angle step	Degree
ε	Permittivity (dielectric constant)	F/m
ε_0	Vacuum permittivity	F/m
ε_r	Relative permittivity	F/m
$\varepsilon(\omega)$	Complex frequency-dependent absolute permittivity of the material,	F/m
η	Refraction index of the medium	
θ_c	Critical solid angle	Degree
θ_i	Angle of direction	Degree
θ_r	Angle of reflection	Degree
θ_t	Angle of transmission	Degree
λ	Wavelength	m
μ	Permeability	H/m
μ_0	Vacuum permeability	H/m
μ_r	Relative permeability	H/m
σ	Conductivity	$1/\Omega$
τ	Optical depth	
τ_0	Life Time	s
ρ_v	Volume charge density	C/m^3
$\varphi_p(\lambda)$	Flux density spectrum of the input solar radiation	$s^{-1}.m^{-2}.nm^{-1}$
$\Psi(e_p, x_d, \lambda_{ex})$	Excitation rate	
ω	frequency	eV
$\omega_{0,u}$	Natural frequency of metal nano particle	eV
ω_P	Plasma frequency	eV

List of Acronyms

a.u.	Arbitrary Unit
ABC	Absorbing Boundary Condition
Ag NP	Silver nanoparticle
AM1.5G	Air Mass 1.5 Global standard solar spectrum
AR	Aspect ratio
ARC	Anti-Reflection Coating
Au NP	Gold nanoparticle
BIPV	Building Integration Photovoltaic
c-Si	Crystalline silicon
CdS/CdTe	Cadmium Sulfide/Cadmium Telluride
CdSe/CdS	Cadmium Selenide/ Cadmium Sulfide
CIGS	Copper Indium-Gallium-diSelenid
DTB	di-benzo-thiadiazole
DPA	di-phenyl-anthracene
DSSC	Dye Sensitized Solar Cell
EF	Enhancement factor
EQE	External Quantum Efficiency
E_{SPR}	SPR energy
$Eu(tta)_3$	Europium Triethylammonium
EuD_4Tta	Tetraki Dibenzoylmethide Triethylammonium
EVA	Ethylene-vinyl acetate
FDTD	Finite Difference Time Domain
FFT	Fast Fourier Transform
GaAs	Gallium Arsenide
GaInP	Gallium Indium Phosphide
ICP-OES	Inductively coupled plasma optical emission spectroscopy
GUI	Graphical User Interface
IQE	Internal Quantum Efficiency
ITO	Indium Tin Oxide
LDS	Luminescent Down Shifting
LSC	Luminescent Solar Concentrator
LS	Luminescent Solar
MCRT	Monte Carlo Ray Tracing
mc-Si	Multi Crystalline silicon
MLD	Multi-Layer Device
MNP	Metal Nanoparticle
NIR	Near infrared
NP	Nanoparticles
NR	Nano rod
NS	Nano sphere
PAE	Poly Arylene Ethynylene
PBC	Periodic Boundary Condition
PDEF	Photon density enhancement factor
PbS	Lead Sulphide
PCE	Power Conversion Efficiency
PLMA	Poly lauryl methacrylate
PML	Perfectly Matched Layer
PMMA	Poly methyl methacrylate
PV	Photovoltaic
PVA	Polyvinyl Acetate
PVB	PolyVinyl Butyral
PVSK	Perovskite
pBIPV	Plasmonic Building Integrated Photovoltaic
pLDS	Plasmonically enhanced Luminescent Down Shifting
pLSC	Plasmonically enhanced Luminescent Solar Concentrator
pLS	Plasmonically enhanced Luminescent Solar
QD	Quantum Dot
QE	Quantum Efficiency

QY	Quantum Yield
SEM	Scanning electron microscope
Si	Silicon
SLD	Single Layer Device
SPR	Surface Plasmon Resonance
TIR	Total Internal Reflection
UV	Ultra Violet

Chapter 1: Introduction

The efficiency of photovoltaic (PV) panels is increasing progressively while their manufacturing and installation costs is reducing continuously. However, developing conventional PV systems has been found to be highly challenging in populated cities due to lack of available space and land. Thus, facade and building integrated PV (BIPV) systems are more preferred in metropolitan areas. This Chapter briefly introduces luminescent solar (LS) devices as a solution for the aforementioned PV challenges. LS devices can be developed as a low-cost (semi-) transparent component in BIPV systems and used to improve the performance of PV systems under diffuse light. The limitations and loss mechanisms of LS devices, which contribute to reducing their optical performance, are explained. Plasmonically enhanced luminescent solar (pLS) device is introduced as an alternative technology to enhance the LS device performance and optical properties. The aims, objectives and contribution to knowledge of the research are outlined followed by the road map and structure of the thesis.

1.1. Photovoltaic (PV) Solar Cells

1.1.1. PV Solar Panel for Buildings

Buildings play a significant role in the global energy balance. Typically they account for 20-30% of the total primary energy requirement of industrialized countries and ~40% in the EU (Eu-Parliament, 2018). Applying PV panels to buildings is an important application which can help to achieve the goal of the European Parliament and the Council of the European Union enacted in 2009 on using renewable energy to reduce pollution and fossil energy consumption (Eu-Parliament, 2010) and achieving 20% of final consumed energy in EU from renewable energy sources by 2020 (Eu-Union, 2010) or at least 27% by 2030 (Eurostat, 2018). This was only 8.5% in 2004 and increased to 17% in 2016 (Eurostat, 2018).

1.1.2. Limitations and Losses of PV Solar Cells

When a photon strikes a semiconducting material such as gallium arsenide (GaAs) or silicon (Si), the photon is absorbed, and the energy is received by bound valence band electrons. If the energy of the photon (E_p) is more than the band gap energy (E_g) of the semiconducting material, the valence band electron is exited and promoted to the conduction band while leaving a positive hole in the valence band. In a p-n junction, if no recombination of the exited electron and hole happens, the exited electron reaches the junction where it can be flown and be collected through solar cell electrodes. Solar cells made of such materials can generate current (electrical energy) from solar radiation (electromagnetic energy) in a process called the PV effect (Chapin *et al.*, 1954).

The PV current generation process is limited by the efficiency of solar cell. PV solar cells only operate efficiently for the incident photons with E_p close or a little higher than E_g. For example, the market commonly-used PV solar cells such as Si-based cells are efficient in ~600 nm to ~900 nm (close to visible band of incident solar radiation). Moreover, optical losses reduce the efficiency of PV modules. These losses are produced from the absorption and reflection of the module top glass, encapsulation layer and the anti-reflective coating (ARC) layer (Klampaftis *et al.*, 2009, Rothemund, 2014).

LS devices were introduced (Goetzberger and Greube, 1977, Goetzberger, 1978, Batchelder *et al.*, 1979, Hovel *et al.*, 1979) as low cost technologies to overcome the aforementioned PV challenges and limitations by reducing losses and improve the efficiency of PV modules.

1.2. Luminescent Solar (LS) and Plasmonically Enhanced Solar (pLS) Devices

1.2.1. LS Device Configuration and Losses

LS devices, such as luminescent solar concentrators (LSC) and luminescent down shifting (LDS) devices illustrated in Fig. 1.2, can enhance the performance of PV modules by converting and concentrating the incident solar radiation spectrum (in LSC) or red-shifting it (in LDS) to the energy band where PV cells have relatively high efficiency.

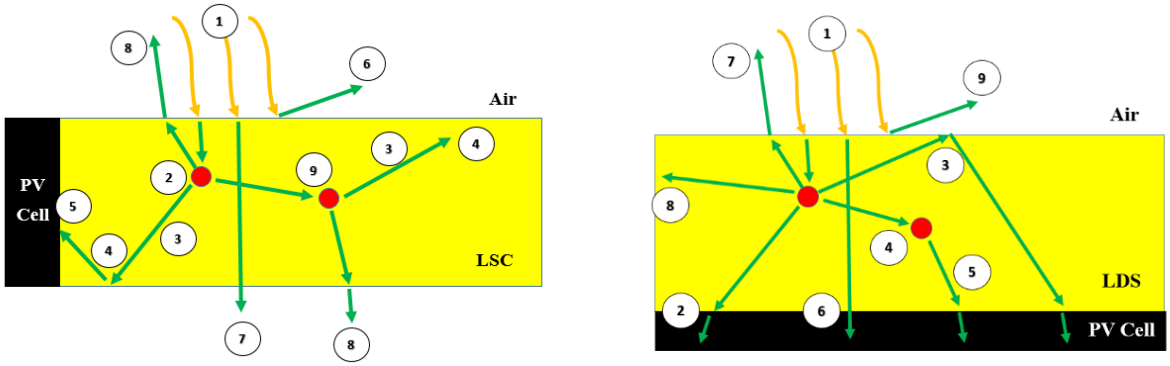

(a) (b)

Fig. 1.1: Configuration of LS devices including: (a) LSC: 1- photon enters the device, 2- absorbed by the luminescent material, then 3- re-emitted at longer wavelength and 4- wave-guided by total internal reflection (TIR) and 5- reaches the PV cell. Losses include: 6- front surface reflection 7- the fraction of light which is lost through the bottom and 8- other surfaces (escape cone loss) and 9- the emitted light which is reabsorbed by another luminescent molecules and its energy is decreased. (b) LDS: 1- photon enters the LDS absorbed by the luminescent material. Then, 2- re-emitted at longer wavelength and reaches the PV cell 3- or it is wave-guided to the PV cell by TIR 4- or re-absorbed by another luminescent molecule and 5- re-emitted with less energy and then reaches the PV cell. 6- Some photons directly reach the PV cell without red-shifting. The other losses include: 7- escape cone loss 8- edge losses and 9- front surface reflection. Note that, the light may also be scattered or attenuated by the host material in LS devices which is not shown here (Ross *et al.*, 2012, Kerrouche *et al.*, 2014).

LS devices can collect both diffuse and direct solar radiation (Kerrouche *et al.*, 2014), which also makes it a suitable technology to be used in countries where diffuse solar radiation is dominant (van Sark *et al.*, 2008). With static nature and structure, it is a suitable device for façades and BIPV systems enabling buildings to be positive energy generators or achieve zero-carbon-energy consumption (Pagliaro *et al.*, 2010, Aste *et al.*, 2011, Debije and Verbunt, 2012, Meinardi *et al.*, 2017b), which helps in reducing environmental pollution caused by fossil fuels (Eu-Parliament, 2010). LSCs can be developed as large-scale windows and solar noise barriers with different colours and shapes to enhance visual comfort and daylighting (Earp *et al.*, 2004, Sholin *et al.*, 2007, Yoon *et al.*, 2011, Zhao and Lunt, 2013, Vossen *et al.*, 2016, Cambié *et al.*, 2017, Debije *et al.*, 2017, Gajic *et al.*, 2017, Kanellis *et al.*, 2017, Meinardi *et al.*, 2017c, Merkx *et al.*, 2017, van Sark *et al.*, 2017, Wilson *et al.*, 2017, Reinders *et al.*, 2018, Renny *et al.*, 2018). They can be also fabricated as colourless transparent windows where natural light is required

inside the building (Sanguineti *et al.*, 2012, Zhao *et al.*, 2014, Chen *et al.*, 2017, Yang and Lunt, 2017, Bergren *et al.*, 2018, Brennan *et al.*, 2018, Brovelli *et al.*, 2018, Lunt *et al.*, 2018, Vasiliev *et al.*, 2018).

LS devices inherently suffer from different sources of losses (van Sark *et al.*, 2008, van Sark, 2013). Some part of solar radiation is lost through the device reflection due to the non-matched refraction indices of air and device host material (Glassner, 1989). A portion of radiation is lost in the wave guiding process during total internal reflection (TIR) inside the device through non-unity quantum yield (QY) of the luminescent material, attenuation, scattering and escape cone losses (Gutierrez *et al.*, 2016a). The attenuation and scattering losses are governed by the host material characterisation including the material absorption spectrum. When the photon strikes device boundaries, if its incident angle is less than the critical solid angle (θ_c) of the host material, it is lost as escape cone loss (Glassner, 1989). Emitted photons can be re-absorbed by another luminescent species and lost energy for luminescent materials with small Stokes-shift (spectral overlap of emission and absorption profiles) (Bronstein *et al.*, 2015, Tummeltshammer *et al.*, 2016). All aforementioned loss mechanisms are magnified by increasing the size and geometric gain of LS devices (Currie *et al.*, 2008, van Sark *et al.*, 2008, van Sark, 2013, Erickson *et al.*, 2014).

1.2.2. Advantages and Limitations pLS Devices

To overcome the aforementioned limitations, pLS devices, including plasmonically enhanced LSC (pLSC) and LDS (pLDS) devices, are alternative advanced technologies which offer higher optical performance than LS devices due to coupling luminescent species and metal nano particles (MNPs) (Chandra *et al.*, 2012, Chandra, 2013, El-Bashir *et al.*, 2013b, El-Bashir *et al.*, 2014, Ahmed *et al.*, 2016, Ahmed *et al.*, 2017b).

The optical properties of MNPs is due to the collective response of conductive electrons which form an electron cloud (plasma) around the metal nuclei. When an electric field is applied, the electrons are pushed away from the nuclei which forces the electron cloud to be displaced and asymmetrical with respect to nuclei forming a dipole. This is known as the material polarization which creates restoring force. It results in oscillating the conduction electron cloud which is characterized by the resonance frequency of the MNP (Ritchie, 1957). When the incident photon frequency is resonant with collective oscillation of the conduction electron cloud (referred as

surface plasmon resonance (SPR)), the local electric field around the MNP is enhanced. If luminescent species are placed in the optimised proximity of MNP where they are able to spectrally interact with MNP SPR energy (i.e. they are plasmonically coupled), the optical performance of the whole coupling is enhanced due to increasing the coupling QY and excitation rate. In pLS devices, this can improve the performance and optical efficiency (OE) of the whole component.

On the downside, the optimisation process of pLS devices is more complex than LS devices. This includes optimising the doping concentration of luminescent material and MNP (i.e. the distance between them), device size and optical properties of the utilised material which have nonlinear impact on the performance of pLS devices.

As a solution, developing a novel modelling tool for pLS device can be helpful to ease the process of device optimisation and analysis before manufacturing stage.

1.3. Research Aim, Objective and Contribution to Knowledge:

The main aim and objective of this project is to develop the first novel tool with a comprehensive algorithm to model, optimise and analyse the performance and optical properties of small and large scale pLS devices.

The contribution to the current knowledge is categorised in 3 main fields:

- ❖ To develop the first novel pLS device modelling and optimisation tool:
  - Propose a configuration and mathematical model for pLS devices
  - Design and development of a new comprehensive algorithm to 3D-model small and large-scale pLS devices using Monte Carlo ray tracing (MCRT) and finite difference time domain (FDTD) methods
  - Validate the developed model by comparing experimental and modelling results.
- ❖ To study the impact of gold nano rod (Au NR) alignment directionality on its optical properties and also pLS device performance.
- ❖ To propose a new large-scale structure for pLS-based BIPV components

As additional contributions in the project, the final modelling tool has been developed as a novel comprehensive software which can model both LS and pLS devices with various configurations

and structures. Meanwhile, the tool has been used in modelling and studying of various complex configurations such as optical cavities, waveguides with selective mirrors and multi-layer structures. Although optimisation and investigation of LSC and pLSC are more focused here (at the time of finishing this thesis), the software is also capable of modelling LDS and pLDS devices.

1.4. Thesis Layout

The thesis layout can be found in Fig. 1.2. Chapter 2 reviews the features of LS devices and the ray tracing modelling of them. Based on the reviewed studies, the performance of LS devices depend on two main parameters: (1)-Materials including the host and luminescent materials and (2)- Device configuration including its shape, dimensions, structure and doping concentration. Therefore, before LS device fabrication, it is very useful to design and optimise them which can be undertaken by ray tracing modelling. Ray tracing has a loop-based algorithm and its main challenges are simulation time and the modelling accuracy. Chapter 2 continues with reviewing the characteristics and modelling of MNPs and plasmonic effect required in pLS devices modelling. FDTD method is reviewed as a grid-based, robust, accurate, and straightforward method to model and study the optical response of MNPs.

Chapter 3 presents the design and development of a 3D MCRT model (referred as "Ray Tracer" program). The Ray Tracer was developed as a software and used to model single and multi-layer LS devices. MCRT was inherently found time-consuming process implemented based on probability-calculation of optical phenomena such as absorption, emission, transmission, scattering and attenuation for each incident ray in an iterative loop. Therefore, the computational cost and accuracy were the main challenges in the MCRT algorithm and needed to be improved for modelling pLS devices.

In Chapter 4, FDTD numerical method was used to design and develop a program for MNP modelling (referred as "Plasmon"). Plasmon was used to model the optical properties of real periodic homogenous devices doped with MNP (including the MNP extinction spectra). The model was validated by comparing the simulation and experimental results. Simulation time, time steps, accuracy and memory requirements of modelling were found dependent to FDTD grid resolution. Although the model could estimate the experimental results in acceptable

agreement, FDTD still required some optimizations to enhance the memory and computational requirements. Therefore, a 3D optimized FDTD (OFDTD) was designed and developed which introduced new FDTD approximation terms based on the physical events happening during the plasmonic oscillations of MNP.

Chapter 5 presents the proposed configuration and mathematical model for pLS devices. The mathematical model was used in development of a 3D software (referred as "PEDAL") which is a novel comprehensive modelling tool to simulate both LS and pLS devices. The achievement of both Ray Tracer and Plasmon programs (in Chapter 3 and 4) have been combined and used in PEDAL development. In PEDAL, the defects of Ray Tracer mentioned in Chapter 3 (challenges about accuracy and high simulation time) have been also improved by applying optimisation techniques to the program which significantly decreased simulation time and improved modelling accuracy. Then, PEDAL was validated for LS and pLS device modelling where a computational method was also used for converting the unit of MNP doping concentration from ppm (mg/L) (used in experiments) to number of particle per litre (N/L) (used in modelling). Finally, the modelling and experimental results were compared and found to be in close agreement. Doping concentration of MNP was found to be an important parameter in pLS device performance. Enhancement was only observed in a narrow optimised band of MNP doping concentration in pLS device. Below the optimised concentration band, the relative interaction between the MNP and luminescent molecule decreased which reduced the total plasmonic enhancement. Above the optimised concentration, the probability of energy quenching and thermal losses increased due to relatively short distance between the MNP and luminescent molecule.

Chapter 6 studies modelling and optimisation of various configurations including multi-layer thin film LSC, LSC devices with near-unity QY and LSC with polydimethylsiloxane (PDMS) host material. Meanwhile, it analyses the impact of NR alignment directionality on its optical properties. It also discusses additional studies undertaken by PEDAL including studying the impact of optical coupling quality on performance of LSC and LDS devices, investigating the optical properties of multi-layer LDS devices and also the impact of loss mechanisms on performance of luminescent solar devices.

In Chapter 7, a large scale pLS device was modelled and optimised in which aligned NRs (from Chapter 6) were coupled to luminescent material. The optimisation was undertaken step by step

in terms of luminescent material and MNP doping concentration and size of the device. The impact of diffuse, direct and global solar incident was also investigated on device optical performance. Moreover, the impact of NR alignment was studied on the device optical properties. A new large-scale structure for BIPV component was also proposed.

Then, the conclusion and future works are presented in Chapter 8.

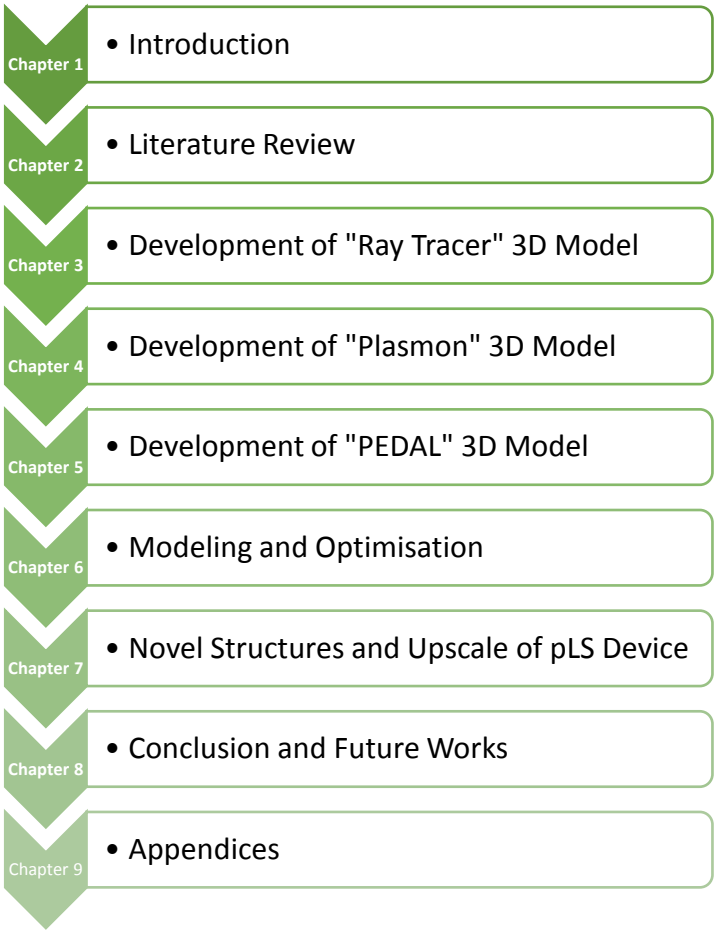

Fig. 1.2: Thesis layout and roadmap

Chapter 2: Literature Review

This Chapter reviews the subjects which are necessary to understand and put the research into context. It starts with introducing the photovoltaic (PV) solar cell, its limitations and parameters used to evaluate its performance. Luminescent solar (LS) devices including luminescent solar concentrators (LSC) and downshifting (LDS) are introduced and discussed as techniques to overcome PV solar cell losses. As the thesis is mainly focused on results of conventional and plasmonic LSCs, large and small scale LSCs as well as host and luminescent material are comprehensively and critically reviewed. LSC generations are categorised based on their configurations; moreover, their material, limitations and losses are discussed.

Plasmonically enhanced luminescent solar (pLS) devices doped with coupled metal nanoparticles (MNP)-luminescent material are introduced as a solution to overcome the limitation of LS devices.

Optimisation of pLS device is found to be complex; therefore, developing an accurate model is crucial to ease device development. Modelling methods for LS and pLS devices are reviewed and critically assessed.

2.1. Improving the Performance of PV Systems Using LS Devices

The PV cell which has attracted the most attention and has been used more is multi-crystalline silicon (mc-Si) PV solar cell (Altermatt *et al.*, 2018). Its advantages include low cost, reasonable stability and power conversion efficiency (PCE) under global standard solar radiation spectrum (AM1.5G) (Wilson and Richards, 2009, NREL, 2019). However, when solar radiation is incident on the mc-Si PV solar cell, the absorption probability is rapidly reduced due to two main loss sources including optical and recombination losses, (Proise, 2014, Rothemund, 2014). This significantly decreases quantum efficiency (QE) which shows the ratio of the collected carriers to the input photons energy of the PV cell. (Wilson and Richards, 2009). Most PV materials are not efficient in ultra violet (UV) and blue region of the solar spectrum. This can be evaluated and quantified by internal QE (IQE) and external QE (EQE). IQE is defined as the ratio of the collected electrons by the PV to the absorbed photons and EQE is known as the ratio

of the number of collected electrons to the number of incident photons (Radziemska, 2006, Wen *et al.*, 2012, Wenham, 2012, Abderrezek *et al.*, 2013, Şahin and Ilan, 2013, Solanki, 2015) calculated by $Eqn\ (2.1)$:

$$EQE(\lambda) = \frac{me(\lambda)}{mp(\lambda)} \qquad Eqn\ (2.1)$$

Where $me(\lambda)$ is the number of electrons which are generated by the PV, $mp(\lambda)$ is the number of photons striking the PV cell at each wavelength λ (Yang *et al.*, 2008).

Another parameter to evaluate PV cells performance is spectral response which measures the sensitivity of the solar cell to different wavelengths of solar radiation. It can be calculated by $Eqn\ (2.2)$ (Chander *et al.*, 2015b):

$$SR = \frac{I_{sc}(\lambda)}{P(\lambda)} \qquad Eqn\ (2.2)$$

Where $I_{sc}(\lambda)$ is the generated short circuit current of the solar cell in Ampere and $P(\lambda)$ is the incident power in Watts.

To evaluate the electrical efficiency of the PV cell, PCE is calculated by $Eqn\ (2.3)$ (Proise, 2014):

$$PCE = \frac{V_{oc}.J_{sc}.FF}{P_{in}} \quad , \quad V_{oc} = \frac{n.k_b.T_{PV}}{q} ln(\frac{J_{sc}.C}{J_0}) \qquad Eqn\ (2.3)$$

Where J_{sc} is the short-circuit current density in A.m^{-2}, V_{oc} is the open-circuit voltage, P_{in} is the total power density of the incident light (for instance, it is 1000 W.m^{-2} for AM1.5G solar radiation), n is ideality factor, T_{PV} is temperature in Kelvin, k_b is Boltzmann constant = 1.38064852 × 10^{-3} A.m^2.kg.s^{-2}.K^{-1}, C is solar concentration ratio, q is electric charge ($\approx 1.602 \times 10^{-19}$ Coulombs), J_0 is dark current density in A.m^{-2} and FF is fill factor which can be calculated by $Eqn\ (2.4)$:

$$FF = \frac{V_M.I_M}{V_{oc}.I_{sc}} \qquad Eqn\ (2.4)$$

Where V_M and I_M are respectively the voltage and current of the PV terminal at maximum power. I_{sc} is the short-circuit current in Ampere. Note that the J_{sc} can be calculated by $Eqn\ (2.5)$:

$$J_{sc} = q \int_{\lambda_{min}}^{\lambda_{min}} \varphi_p(\lambda) \,.\, EQE(\lambda).\, d\lambda \qquad Eqn\ (2.5)$$

Where λ_{min} and λ_{max} determine the wavelength range of interest in nm, $\varphi_p(\lambda)$ is the flux density spectrum of the input solar radiation in $s^{-1}.m^{-2}.nm^{-1}$ which shows the spectrum of number of input photons per unit time and per unit area over their wavelength and can be calculated by $Eqn\ (2.6)$:

$$\varphi_p(\lambda) = \frac{P_{in}(\lambda)}{E_P(\lambda)} \qquad Eqn\ (2.6)$$

Where $E_P(\lambda)$ is the energy of photon in each wavelength in Joules and is obtained by $Eqn\ (2.7)$:

$$E_P(\lambda) = \frac{h.c}{\lambda} \qquad Eqn\ (2.7)$$

Where *h* is Planck's constant ($h \approx 6.63 \times 10^{-34}$ J.s) and *c* is the light speed ($\approx 3 \times 10^8$ m/s).

PCE of PV solar cell is limited by its EQE and spectral losses. Different methods can be used to decrease spectral losses of PV solar cells such as using PVs with enhanced QE (Hovel *et al.*, 1979, Maruyama and Kitamura, 2001, van Sark *et al.*, 2005, Ahmed, 2014).

An alternative method to enhance the output efficiency of PV systems and improve the spectral response is down-conversion or downshifting of the incident solar radiation spectrum to the wavelength band where EQE is maximum. This approach boosts the rate of photon-electron conversion in PV solar cell increasing the final PCE. A low-cost strategy to apply this method is using luminescent solar (LS) devices which was first introduced in 1970s and first generations were based on dyes. (Weber and Lambe, 1976a, Goetzberger and Greube, 1977, Goetzberger, 1978). In LS devices, a polymeric host material is doped with luminescent species.

As is shown in Fig. 2.1 (Geddes, 2017), when a luminescent molecule is excited by an incident photon energy, it reaches a higher electron level. When it falls down from the excited state to the ground state, it undergoes decay which may be radiative (Γ_r) or non-radiative (Γ_{nr}). The radiative decay results in luminescent emission while the non-radiative decay causes thermal losses. During the emission process, a photon is emitted with energy equal to the gap between the two states. Since the energy of emitted photon determines the wavelength, the whole process

of photon absorption and emission can be called as a wavelength or energy conversion process. For example, a luminescent molecule can absorb a photon in UV and emit it in visible band.

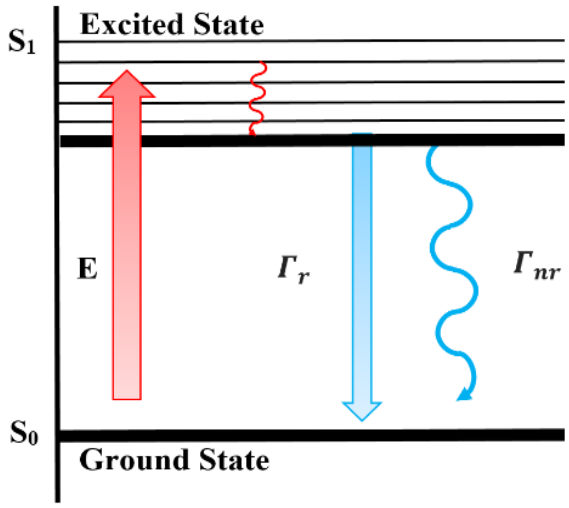

Fig. 2.1: The emission process of a single luminescent molecule (E is the excitation energy for luminescent molecule)

The same process happens for luminescent species inside LS devices. The incident solar radiation strikes the top surface of the devices. Some portion of light is refracted into the device characterised by the refraction indices of polymer and air. Some part of the refracted light is absorbed by luminescent molecule based on its absorption band and emitted at longer wavelength determined by optical properties of luminescent material including its QY and emission spectrum. Therefore, a portion of absorbed light is lost due to non-unity QY. Moreover, due to the spectral overlap between absorption and emission spectra (stokes-shift) of luminescent species, some part of the emitted light is re-absorbed leading to increase in reabsorption and thermal losses. During the optical process, a small part of the light is also attenuated and scattered by non-ideal transparent host material. Giving the aforementioned optical losses, the down-converted or downshifted light reaches the mounted PV cell through two LS device techniques:

- One technique is based on doping luminescent material in a thin film of polymer deposited on top PV cells which is known as LDS thin layer. This method is used to red-shift the incident solar spectrum to longer wavelengths where the solar cell is more efficient exhibiting

higher EQE (Hovel *et al.*, 1979, Ahmed, 2014, Gheno *et al.*, 2018, Ho *et al.*, 2018, Wang *et al.*, 2018a, Alexandre *et al.*, 2019). LDS works efficiently under diffuse solar radiation due to increasing the pathlength of the refracted light improving both the absorption and trapping efficiency of the device which increase the probability of light red-shifting e.g. 28.6% increase in LDS efficiency was reported under diffuse solar radiation spectra (van Sark, 2005). The performance of LDS is characterised by the spectral response of the selected PV, the thickness of film and concentration of the used luminescent material (Ross *et al.*, 2014, Alonso-Álvarez *et al.*, 2015, Chander *et al.*, 2015a, Griffini *et al.*, 2015, Kennedy *et al.*, 2015). The attenuation spectrum of the used host material is also an important parameter. Different host materials start to be transparent after around 300nm wavelength; however, their optical response in the region between 300 to 400nm can characterise the amount of red-shifting and efficiency of LDS devices. LDS can be also applied using the encapsulation layer of the PV cell as host material doped with luminescent material (Klampaftis and Richards, 2011).This is an excellent method in LDS-PV systems which can reduce the complexity and cost of the device in the fabrication process. In addition, the number of layers is decreased in this method which is able to decrease the losses due to the optical couplings. Coupling MNPs such as silver nanoparticles (Ag NP) and gold nanoparticles (Au NPs) to luminescent materials with optimum concentration is a recent method to enhance the efficiency of LDS devices by which between ~20% to 40% enhancement in performance was reported in several studies (Ahmed, 2014, Ahmed *et al.*, 2016, H. Ahmed, 2017, Ho *et al.*, 2018). The improvement is due to the plasmonic effect of MNPs which enhances the optical efficiency.

- The second technique which is more focused in this thesis is based on using luminescent material in a transparent waveguide and fabricate a planar LSC (Yamada *et al.*, 2010). LSCs convert solar radiation spectra to a single wavelength (ideally) where Si PV solar cell has relatively high EQE e.g. in 600 nm to 900 nm wavelength range. Then, the photons are wave-guided and concentrated by total internal reflection (TIR) to the edges where the PV cell is attached. This not only enhances the performance of PV solar cell, but also reduces the required PV area; accordingly, decreasing the cost of the solar panel. Performance is evaluated by important parameters (de Cardona *et al.*, 1985, Salem *et al.*, 2000, Kennedy,

2010, Wang *et al.*, 2011a, Desmet *et al.*, 2012, El-Bashir *et al.*, 2013a, Correia *et al.*, 2014, Aste *et al.*, 2015, Vishwanathan *et al.*, 2015, Zhang *et al.*, 2015) outlined below:

Geometric gain is the ratio of the top surface aperture area (A_{APR}) to the total edge area of LSC covered by PV solar cell (A_{Edge}) and given by Eqn (2.8):

$$G_g = \frac{A_{APR}}{A_{Edge}} \qquad Eqn\ (2.8)$$

Optical efficiency (OE) is the ratio of the output energy to input energy in the wavelength range of interest (λ_{min} to λ_{max}) and can be obtained by Eqn (2.9):

$$OE = \frac{\int_{\lambda_{min}}^{\lambda_{max}} E_{P_{OUT}}(\lambda).d(\lambda)}{\int_{\lambda_{min}}^{\lambda_{max}} E_{P_{IN}}(\lambda).d(\lambda)} \qquad Eqn\ (2.9)$$

Where $E_{P_{OUT}}(\lambda)$ is the output energy spectrum of the photons obtained in the detector plane and $E_{P_{IN}}(\lambda)$ is input energy spectrum of the system in Joules (e.g. AM1.5G solar spectrum).

Photon concentration ratio (C_P) is obtained by Eqn (2.10):

$$C_P = G_g \times OE \qquad Eqn\ (2.10)$$

And the total solar concentration ratio (*C*) of the device attached to PV cell is defined by Eqn (2.11):

$$C = G_g \times \frac{\int_{\lambda_{min}}^{\lambda_{max}} N_{P_{OUT}}(\lambda).EQE(\lambda).d(\lambda)}{\int_{\lambda_{min}}^{\lambda_{max}} N_{P_{IN}}(\lambda).EQE(\lambda).d(\lambda)} \qquad Eqn\ (2.11)$$

Where $N_{P_{OUT}}(\lambda)$ and $N_{P_{IN}}(\lambda)$ are respectively the number of output and input photons at wavelength λ.

C of LSC is an important parameter because increasing C results in logarithmic-increase in V_{oc} and PCE as can be seen in *Eqn* (2.3) (Proise, 2014). Note that, higher solar concentration linearly increases both power (received by PV solar cell at the edge) and short-circuit current density (J_{sc}); therefore, their gains are cancelled out in boosting PCE (Proise, 2014). Increasing C (and geometric gain) in LSCs to achieve higher PCE is limited by their losses (including thermal and optical losses) which are increased by enlarging LSC (Currie *et al.*, 2008, Bomm *et al.*, 2011,

Zhang *et al.*, 2015, Gutierrez *et al.*, 2016b). To study the impact of LSC configuration on its performance, the recent studies on LSC need to be critically reviewed.

2.1.1. Recent Luminescent Solar Concentrator Research

Proposing a method to minimize loss mechanisms in LSCs and increase their PCE has always been a goal for LSC developers (Goldschmidt *et al.*, 2009, Tsoi *et al.*, 2010, Hernandez-Noyola *et al.*, 2012, Albers *et al.*, 2013). This section reviews various LSC devices for PV applications from 2007 to 2019. The configurations and achieved performance of each device are summarised in Table 2-1 (Rafiee *et al.*, 2019). Each work and the lessons learnt from them are then expanded and studied. The section is then closed with a comprehensive discussion on the parameters impacting on the performance of LS and pLS devices. The correlation of the parameters and their impact are required in developing an algorithm for the pLS device modelling.

Table 2-1: Summarised results of various LSC configurations

Ref	Luminescent Material	PV	LSC size	Results (%)
(Gallagher *et al.*, 2007)	CdSe/CdS QDs	Si	5×5×0.3 cm	PCE=2.1
	Red-305			PCE=3.3
(Currie *et al.*, 2008)	DCJTB	GaInP	2.5×2.5×0.2 cm	PCE=5.9 ($G_g = 3$)
				PCE=4.0 ($G_g = 45$)
	DCJTB (rubrene-based)			PCE=5.5 ($G_g = 3$)
				PCE=4.7 ($G_g = 45$)
	Pt(TPBP)	GaAs		PCE=4.1 ($G_g = 3$)
				PCE=4.1 ($G_g = 45$)
	Tandem with DCJTB/Pt(TPBP) (rubrene-based)			PCE=6.8 ($G_g = 3$)
				PCE=6.1 ($G_g = 45$)
	Tandem with DCJTB (rubrene-based)	CdTe		PCE=11.9 ($G_g = 3$)
				PCE=11.1 ($G_g = 45$)
		CIGS		PCE=14.5 ($G_g = 3$)
				PCE=13.8 ($G_g = 45$)
(Slooff *et al.*, 2008)	Red-305/Yellow-CRS040 (With Diffuse Backside Reflector)	mc-Si	5×5×0.5 cm	PCE=2.7
		GaAs		PCE=4.6
		GaAs × 4		PCE=7.1
(van Sark *et al.*, 2008)	Red-305	Si		PCE=2.4
	Red-305/Yellow-CRS040			PCE=2.7
(Goldschmidt *et al.*, 2009)	BA241	GaInP × 4	2×2×0.3 cm	PCE=5.1
	BA241,BA856		(2×2×0.3 cm) × 2	PCE=6.7
	BA241	GaInP	5×10×0.5 cm	PCE=2.6
(Inman *et al.*, 2011)	PbS QD	c-Si	Cylinder LSC (0.6 cm radius and 2.5cm long)	OE=3
			Cylinder LSC (with a 0.38 cm radius hollow)	OE=6.5

(Sanguineti *et al.*, 2012)	ytterbium chelate OPyr–Yb–Phen	-	-	OE=1
(El-Bashir *et al.*, 2013b, El-Bashir *et al.*, 2014)	Coumarin dyes coupled with MNP (25 ppm)	mc-Si	20 × 8 × 0.3 cm	+33.4 Increase in PCE
	Coumarin dyes coupled with MNP (10 ppm)	c-Si		+25.8 Increase in PCE
	Coumarin dyes coupled with MNP (20 ppm)	a-Si		+53.2% Increase in PCE
(Coropceanu and Bawendi, 2014)	CdSe/CdS core/shell QD	c-Si	2×2×0.2 cm	OE=48
(Flores Daorta *et al.*, 2014)	DTB Lumogen F-Red 305	Si	11 × 11 × 0.6 cm 10.8 × 0.6 × 0.6 cm	+56% Increase in PCE
(Meinardi *et al.*, 2015)	ZnS-coated CISeS QD	c-Si	12×12×0.3 cm	OE=3.27
(Li *et al.*, 2015a)	$CuInS_2/ZnS$ QD		2.2×2.2×0.3 cm	PCE=8.71
(Bronstein *et al.*, 2015)	CdSe/CdS QDs (with trench reflector)	mc-Si	(3.9×3.9 cm)×30 μm	PCE=54.37
	CdSe/CdS QDs (with trench reflector and photonic mirror)			PCE=77.38
(Zhang *et al.*, 2015)	Red-305/Yellow-083	mc-Si × 4	7.8×7.8×0.3 cm	PCE=2.8
			15.6×15.6×0.3 cm	PCE=1.81
		mc-Si × 8	31.2×31.2×0.3 cm	PCE=0.98
		mc-Si × 20	61×122×0.3 cm	PCE=0.33
	Red-305/Yellow-083 (Bottom-Mounted without Reflector)	(mc-Si with size: 15.6) × 2		PCE=2
	Red-305/Yellow-083 (Bottom-Mounted with Reflector)			PCE=2.28
	Red-305/Yellow-083 (Bottom-Mounted without Reflector	(mc-Si with size: 15.6) × 1		PCE=1.14
	Red-305/Yellow-083 (Bottom-Mounted with Reflector			PCE=1.36
	Red-305/Yellow-083 (Bottom-Mounted without Reflector	(mc-Si with size: 12.5) × 2		PCE=1.75
	Red-305/Yellow-083 (Bottom-Mounted with Reflector			PCE=2.02
	Red-305/Yellow-083 (Bottom-Mounted without Reflector	(mc-Si with size: 12.5) × 1		PCE=0.93
	Red-305/Yellow-083 (Bottom-Mounted with Reflector			PCE=1.1
(Aste *et al.*, 2015)	DTB and DPA	c-Si	100×150×0.6 cm	PCE=1.26
(Vishwanathan *et al.*, 2015)	Red-305 (Flat Bottom-Mounted LSC)		10×10×0.3 cm	PCE=2.9
	Red-305 (Bent Bottom-Mounted LSC)		10×15.7×0.3 cm	PCE=3.4
(Nikolaidou *et al.*, 2016)	Organic-inorganic hybrid perovskite		1.5×1.5×0.1 cm	OE=29
(Gutierrez *et al.*, 2016b)	Lumogen F Red-305	(Not Mentioned) × 4	1.75×1.75×0.15 cm	OE=40
(Zhou *et al.*, 2016)	PbS/CdS	Si	10 × 2 × 0.2 cm	OE=6.1
	Giant core/alloyed-shell QD ($CdSe/Cd_xPb_{1-x}S$ core/shell)		7 × 1.5 × 0.3 cm	PCE=1.15
(Li *et al.*, 2016)	Giant CdSe/CdS QDs (doctor-blade deposition)	-	413 cm^2	OE=17 (single λ)
(Tummeltshammer *et al.*, 2017)	Conjugated QD 545 and AFdye	p-Si	2 × 2 × 0.3 cm	PCE=2.87
(Wilson *et al.*, 2017)	Lumogen red 305 dye	Multi-size c-Si solar cells	60 × 60 × 0.3 cm	PCE=1.55
(Meinardi *et al.*, 2017c)	Silicon QD	-	12 × 12 × 0.26 cm	PCE=2.85
(Chen *et al.*, 2017)	N-CQDs	mc-Si	2.5 × 1.6 × 0.1 cm glass spin-coated by 6.67 μm N-CQD/PMMA	PCE=3.98
(Bergren *et al.*, 2018)	$CuInS_2/ZnS$ QD (with black background)	c-Si	10 × 10 cm^2	PCE=2.18
	$CuInS_2/ZnS$ QD (with reflective substrate)			PCE=2.94
(Schrecengost *et al.*, 2018)	Lumogen F Red-300 (with white background of the same size)	-	12.5 × 12.5 × 0.68 cm	+26% Increase in PCE
	Lumogen F Red-300 (with 16X-area of white background)	-		+54% Increase in PCE
(Ha *et al.*, 2018)	Dual Band PdTPBP/BPEA	DSSC	5 × 1 × 0.1 cm	PCE=6.1
(Wu *et al.*, 2018)	$CuInSe_2$ (CISe) / Mn^{2+}doped $Cd_xZn_{1-x}S$-based QDs	GaAs	15.24 × 15.24 cm^2	PCE=3.1 OE=6.4
(Sol *et al.*, 2018)	LSC smart window: K160 dye embedded in STN LC cell	-	5 × 5 cm^2	PCE=3.8 (coloured) PCE=3 (scattering) PCE=2.6 (transparent)
(Mateen *et al.*, 2019)	LSC smart window: coupling of N-CQD-based LSC and PDLC	p-Si	50 × 25 × 4.2 mm	PCE=2.49(OFF) PCE=1.52 (ON)

Gallagher et al. fabricated several tandem LSCs with mirrors attached to three edges and a silicon PV cell coupled to the fourth edge (Gallagher *et al.*, 2007). The host material was poly(methyl methacrylate) (PMMA) doped with cadmium selenide/cadmium sulfide (CdSe/CdS) quantum dots (QDs) and Lumogen F Red-30 (BASF) organic dye. The PCE obtained for QD-based LSCs devices was ~2.1% while it was 3.3% for the dye-based devices. The observed increase in PCE could be explained by high QY of the dye. However, both QD and organic dye suffered from a small Stokes-shift which increased re-absorption losses.

Currie et al. presented single and tandem LSCs with different configurations in 2008 (Currie *et al.*, 2008) in which they used two different dyes: 4-(dicyanomethylene)-2-t-butyl-6-(1,1,7,7-tetramethyljulolidyl-9-enyl)-4H-pyran (DCJTB) and platinum tetra phenyl tetra benzo porphyrin (Pt(TPBP)). The host material used was tris(8-hydroxyquinoline) aluminium (ALQ_3). Single and tandem structures were fabricated with geometric gains of 3 and 45, respectively to study the impact of size variations on LSC performance. PCE was estimated using the optical quantum efficiency, EQE of the PV solar cell, emission spectra of films and AM1.5G solar radiation spectrum. It was found that increasing geometric gain (G_g), had no benefit, rather it decreased PCE due to re-absorption, attenuation and scattering losses.

In the same year, Slooff et al. investigated tandem LSCs coupled to a diffuse backside mirror (Slooff *et al.*, 2008). They incorporated PMMA with a mixture of Lumogen Red-305 and Yellow-CRS040 organic dyes. LSCs were developed with the same size and configuration but various PV solar cells including multicrystalline silicon (mc-Si) and gallium arsenide (GaAs). PCE was calculated to evaluate the power performance of the devices. 2.7% and 4.6% PCE was achieved for single mc-Si and GaAs devices respectively because the emission spectrum of luminescent material was spectrally matched with GaAs PV solar cell. Under this circumstance, PV cell was able to harvest the edge-emitted photons with its maximum EQE (~90%). By increasing the number of PV cells at LSC edges, the total PCE increased. When four GaAs solar cells were attached, total PCE reached 7.1%.

Van Sark et al. designed two 5 × 5 × 0.3 cm planar LSCs (van Sark *et al.*, 2008). One was doped with Lumogen Red-305 and the other was developed by a mixture of Lumogen Red-305 and Yellow-CRS040 dyes. Mc-Si solar cells were attached to one edge and the other three sides were coupled to high-reflectivity (98% average reflectivity) mirrors. The mixed dye-LSC was found to be more efficient with a PCE of 2.7% (compared to 2.4% PCE of Red dye-LSC). Due

to the enhancement in the emission spectra after mixing Lumogen Red-305 and Yellow-CRS040 dyes, concentrated photon density was increased which boosted PCE.

In 2009, a 2 × 2 × 0.3 cm LSC was studied in which a photonic structure acted as a reflective optical filter to reduce the escape cone losses (Fig. 2.2a) (Goldschmidt *et al.*, 2009). It was reported that ~26% of solar radiation was lost due to escape cone loss in the conventional LSC. In the proposed photonic structure, the refracted photons were prevented from exiting the LSC during TIR. This increased trapping efficiency and boosted the rate of the photons concentrated to the edge-mounted PV solar cell. As a result, ~20% increase in optical performance was achieved (PCE = 6.7%). In addition, they developed several LSC devices with various geometric gains. It was observed that by increasing the size (optical path-length) of LSC, PCE decreased, which was due to the increase in thermal losses including re-absorption, attenuation and scattering losses.

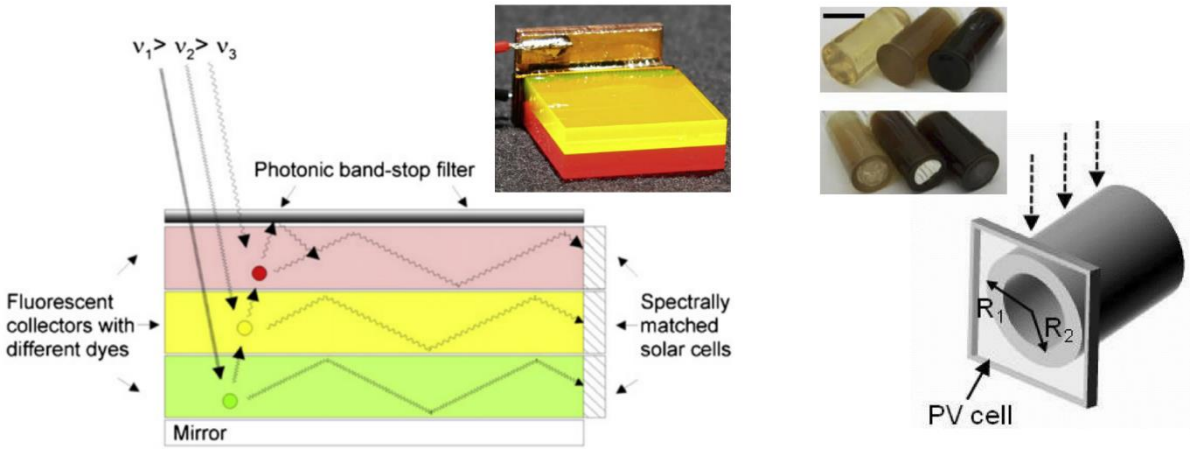

(a) (b)

Fig. 2.2: Schematic and real structure of the (a) Tandem LSC where solar radiation spectrum is absorbed by several collectors doped with different dyes. The LSC is covered by photonic band-stop filter to reduce the escape cone losses. The filter refracts the light in absorption band and reflects the light in the emission band of the dyes (Reproduced from (Goldschmidt *et al.*, 2009)), (b) Cylindrical Solid/Hollow LSCs (The scale bar represents 1.0 cm). The waveguide thickness of the hollow LSC is less than the solid device reducing the attenuation and scattering thermal losses (Reproduced from (Inman *et al.*, 2011))

Later in 2011, Inman et al. introduced cylindrical LSCs (Fig. 2.2b) in which lead sulphide (PbS) QDs were used as luminescent species with different doping concentrations (Inman *et al.*, 2011). The LSC was a solid cylinder with 2.5 cm (height) and 0.6 cm (radius). Performance of

the solid cylindrical LSC was compared to an LSC with 0.38 cm hollow in the centre, having the same dimensions. PV solar cells were attached to the lateral edge of the cylinders. OE of 3% was obtained for the solid LSC, while the hollow structure achieved 6.5% OE. This is believed to be due to the thickness being decreased in the hollow structure which decreases the attenuation and scattering losses, hence increasing the LSC OE (Correia *et al.*, 2016).

Several LSCs were fabricated based on CdSe core/multi shell QDs (QY ~ 45%) (Bomm *et al.*, 2011) in various sizes. The maximum current density and PCE was 77.2 mA/cm^2 and 2.81%, respectively (achieved for 5 × 3.1 cm LSC). The study was a further proof regarding the impact of geometric gain on LSC optical performance. Enlarging top surface aperture of LSC increases thermal losses during the waveguiding process which decrease PCE. Later, Coropceanu et al., also used CdSe/CdS QDs (but with high-QY of 86%) in a 2 × 2 × 0.2 cm LSC development coupled to a crystalline silicon (c-Si) PV solar cell (Coropceanu and Bawendi, 2014). High QY increased the density of solar radiation concentrated to the edge of LSC and as a result, 48% OE enhancement was calculated.

Chandra et al. investigated the optical properties of CdSe/ZnS core-shell QD coupled with noble metal nano particles (MNPs) (Chandra *et al.*, 2012, Chandra, 2013). They reported ~20% to 50% enhancement in OE (depending on the doping concentration of QD and MNP) when QD was coupled with 10 nm gold-NP in a 2 × 1 × 1 cm cuvette (Chandra, 2013). The enhancement was due to the plasmonic coupling between luminescent species and MNPs which can improve the performance of the whole device (Geddes, 2017). Later, the measurements conducted by El-Bashir et al. exhibited a significant fluorescence enhancement when luminescent material was coupled with 60 nm silver-NP (2.4 fold enhancement) and 100 nm gold-NP (4.75 fold enhancement) (El-Bashir *et al.*, 2013b). In 2014, they fabricated several double-layer 20 × 8 × 0.3 cm plasmonically enhanced LSCs (pLSC) (Fig. 2.3a) (El-Bashir *et al.*, 2014). The pLSC comprising of a polycarbonate substrate spin coated by 50 μm PMMA which was doped with coumarin dyes coupled to gold and silver-NPs. The top surface was coated by 20 μm PMMA doped with SiO_2 (to increase the trapping efficiency). The device was tested using amorphous silicon (a-Si), mc-Si and c-Si PV solar cells. Maximum 53.2% enhancement in PCE was achieved when doping concentration of MNP was 20 ppm and the device was attached to a-Si PV solar cell. PLSC optical performance was found to be highly sensitive to the MNP doping concentration. For example, for the device attached to c-Si PV cell, PCE enhancement increased

from 15.14% to 25.80% when MNP concentration only increased from 5 ppm to 10 ppm. However, further increase in MNP concentration significantly reduced the PCE due to the increase in non-radiative decay and fluorescence quenching reducing the total QY (Geddes, 2017).

Daorta et al. fabricated a cascade LSC with PMMA host material in 2014 doped with organic fluorophores attached to Si solar cell (Fig. 2.3b) (Flores Daorta *et al.*, 2014). It comprised of a primary 11 × 11 × 0.6 cm LSC doped with DTB and four secondary 10.8 × 0.6 × 0.6 cm LSCs doped with Lumogen F-Red 305. The absorption spectrum of the secondary LSC was matched to the emission spectrum of the primary LSC. This increased the PCE of the cascade LSC by ~56% in comparison with traditional LSC.

After proposing the near infrared (NIR) colourless single layer LSC (NIR emitting ytterbium chelates) for BIPV in 2012 (Sanguineti *et al.*, 2012), a study was conducted by Meinardi et al. in 2015 where they fabricated a large-scale (12 × 12 × 0.3 cm) colourless transparent LSC (Fig. 2.3c) (Meinardi *et al.*, 2015). Heavy-metal-free colloidal ZnS-coated CISeS QDs were used as the luminescent material and 3.27% OE was calculated (without using any back reflector). Absorption and emission spectra of the colourless LSC were in the UV-band; while most of the common PV technologies are more efficient in the visible and NIR-bands. Thus, PCE of UV-band colourless LSCs is less than the coloured devices. However, they are suitable candidates for transparent applications (such as glazing in buildings).

Li et al. also fabricated a colourless LSC (2.2 × 2.2 × 0.3 cm) using heavy-metal-free $CuInS_2/ZnS$ QDs encapsulated in a PMMA plate (Fig. 2.3d) (Li *et al.*, 2015a). The luminescent material suggested high QY (~81%) and large Stokes-shift (more than 150 nm). Their results showed that the maximum OE of ~26% could be achieved for the QD-based LSC. Current density could significantly increase from 0.72 mA/cm^2 (blank PMMA) to 14.8 mA/cm^2 (LSC) resulting in 8.71% PCE. The results implied the impact of the luminescent material's characteristics on LSC performance. Large Stokes-shift between absorption and emission spectra decreased re-absorption losses; moreover, high QY increased the intensity of detected light at edge of the LSC. Later, a high-performance large-scale $CuInS_2/ZnS$-based LSC (10 × 10 cm) attached to c-Si PV solar cell was introduced (Bergren *et al.*, 2018) which could achieve 8.1% OE and 2.18% PCE when it was coupled to black background. PCE was improved to 2.94% by coupling a reflective substrate below the LSC.

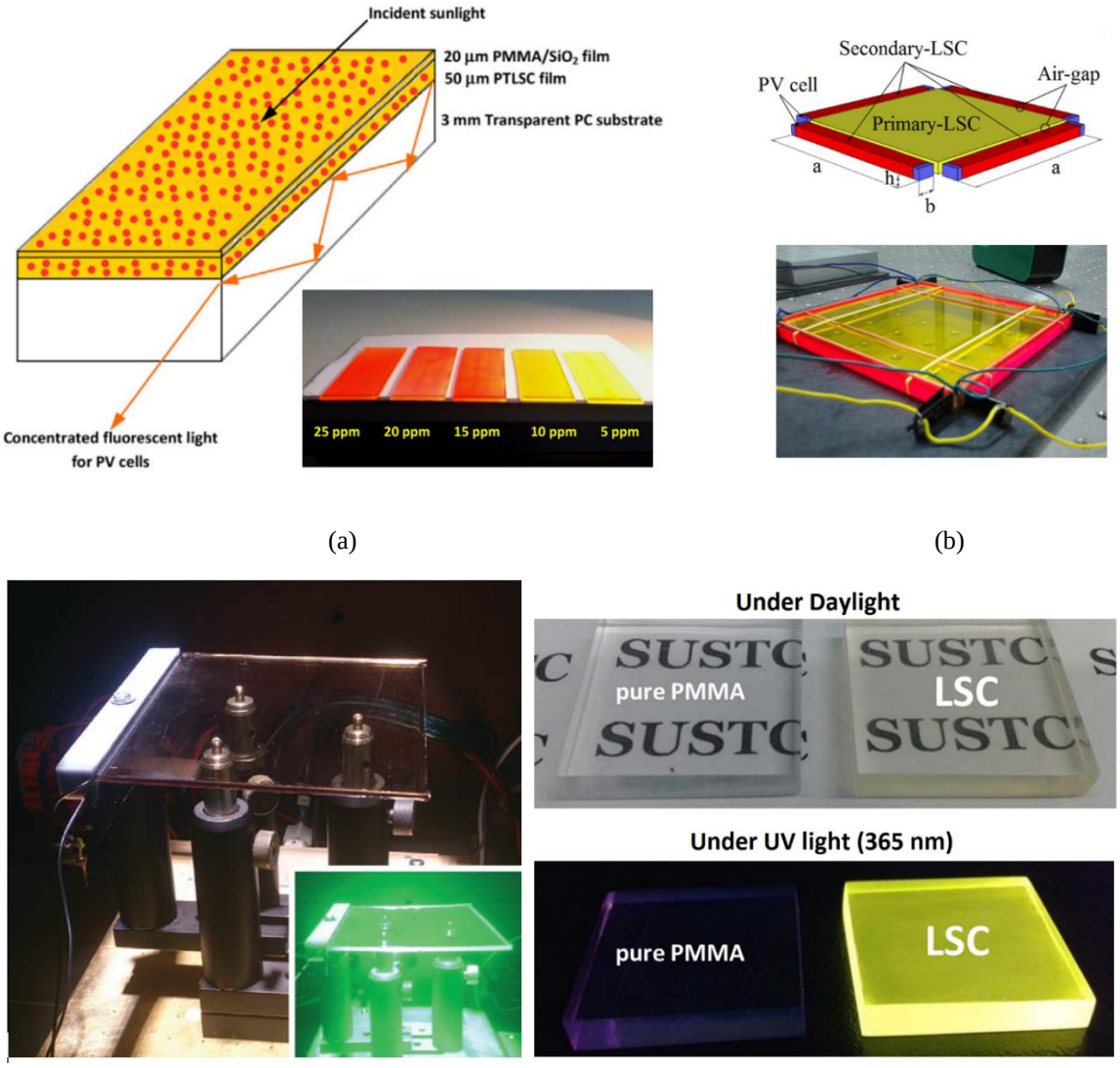

Fig. 2.3: Schematic and real structure of the (a) Thin-film double-layer pLSCs where coumarin dye was plasmonically coupled with gold-NPs significantly enhancing the optical properties of the device (Reproduced from (El-Bashir *et al.*, 2014)), (b) Cascaded LSC where four small LSCs (doped with F-Red 305 dyes) are attached to the lateral edges of a primary LSC (doped with DTB). The LSCs are spectrally matched which increases the OE of the whole device (Reproduced from (Flores Daorta *et al.*, 2014)). Colourless transparent LSCs doped with heavy-metal-free QDs with different emission bands in: (c) NIR: A large-scale 12 × 12 × 0.3 cm device under AM1.5G radiation. The inset photograph has been taken with an infrared camera from the same LSC (Reproduced from (Meinardi *et al.*, 2015)) and (d) UV: A 2.2 × 2.2 × 0.3 cm small-scale device under daylight (Top) and UV lamp (Bottom) (Reproduced from (Li *et al.*, 2015a))

Bronstein et al. used thick-shelled (known as giant) CdSe/CdS QDs in an LSC cavity (Fig. 2.4) (Bronstein, 2015, Bronstein *et al.*, 2015). PLMA/QD composite (30 μm) was placed between two thin glass films. A mc-Si solar cell (0.15 mm^2) was placed inside the structure acting as light detector. The LSC cavity could achieve 30 solar concentration (C) and ~82% waveguide efficiency due to increase in trapping efficiency and reducing escape cone losses. Therefore, the calculated PCE increased from 10.35% to 54.37%. A similar test was performed for an LSC with a trench reflector covered by the photonic mirror where PCE increased to 77.38%.

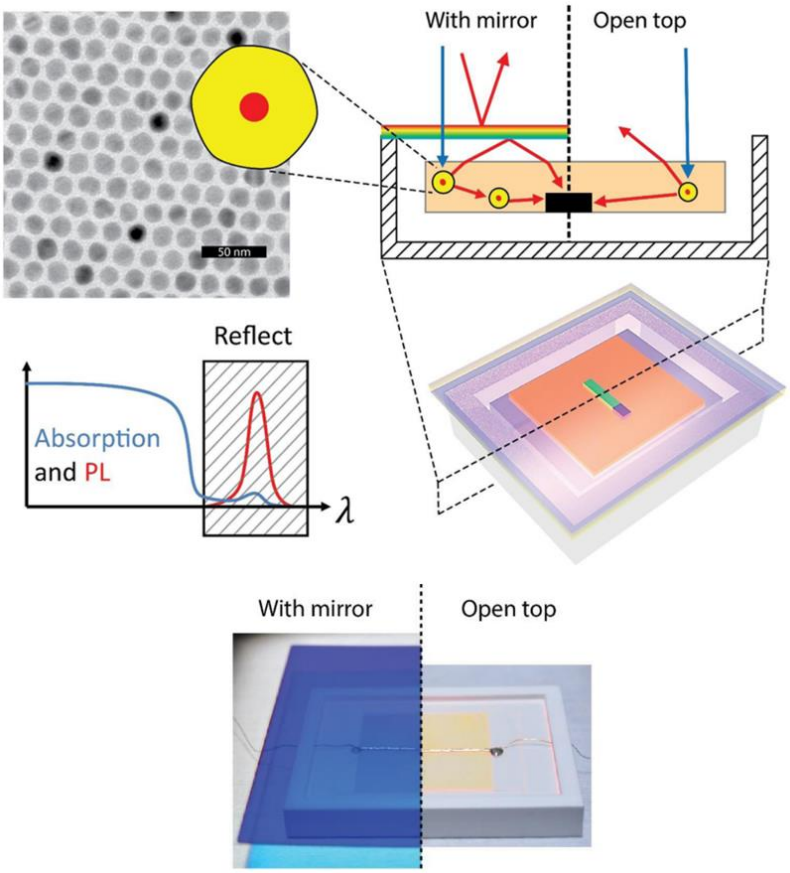

Fig. 2.4: Schematic and real structure of the open-top and with-mirror (wavelength selective photonic mirror) LSCs doped with giant CdSe/CdS QDs. In the cavity structure, the trapping efficiency is higher due to using the selective mirror increasing the OE (Reproduced from (Bronstein, 2015, Bronstein *et al.*, 2015))

Several glass-laminated LSCs with different dimensions (7.8 × 7.8 cm, 15.6 × 15.6 cm, 31.2 × 31.2 cm and 61 × 122 cm) and mc-Si solar cells were fabricated by Zhang et al. (Fig. 2.5) (Zhang *et al.*, 2015). Mixture of Lumogen Red-305 and Yellow-083 was used as doping

luminescent material. The number of photons detected at the edge increased by enlarging the LSC. However, PCE was significantly decreased (from 2.8% to 0.33%). This was due to the geometric gain increase which boosted the possibility of thermal losses. In order to improve PCE, bottom-mounted-PV LSCs were fabricated where four PV solar cells with different sizes were used. Due to the decrease in optical pathlength, the PCE of bottom-mounted LSC was higher than the edge-mounted structure. Maximum PCE of 2.28% was obtained for 61 × 122 × 0.3 cm LSC coupled to edge-reflectors and two 15.6 cm PV solar cells at bottom.

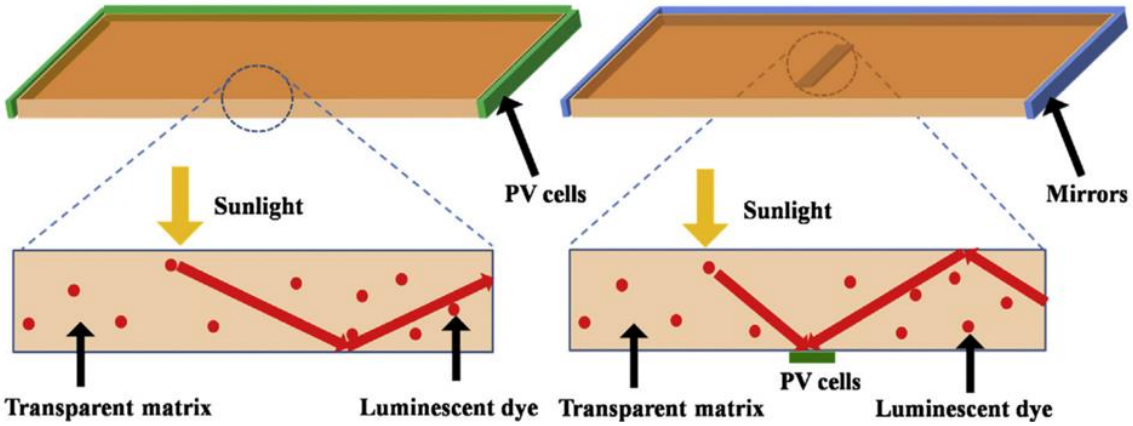

(a) (b)

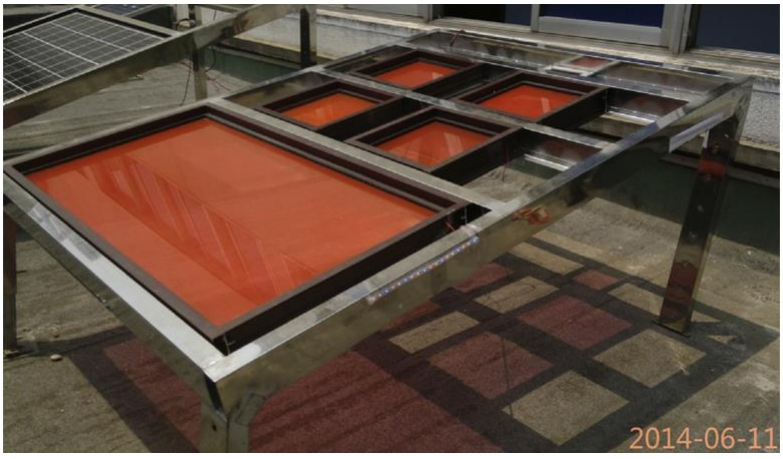

(c)

Fig. 2.5: (a) Edge-mounted LSC where PV solar cells (at the lateral edges of the device) harvest the waveguided solar radiation. (b) Bottom-mounted LSC where the PV cells can harvest both incident and waveguided solar radiation. (c) Fabricated LSCs with different sizes under daylight characterization (Reproduced from (Zhang *et al.*, 2015))

Aste et al. introduced a planar large-scale LSC with a mixture of two dyes: DTB (di-benzo-thiadiazole) and DPA (diphenylanthracene) (Aste *et al.*, 2015). The idea extended the absorbance band of the LSC (300-500 nm). Moreover, the emission peaks were at visible region where c-Si solar cell exhibited the maximum EQE of ~90-95% which enhanced the optical performance the LSC. 1.26% PCE was achieved which was found to be ~10% higher than the reference modules in all conditions, particularly on a clear sunny day.

The impact of LSC shape on optical performance was studied using a ray-trace model simulation validated by experimental results (Vishwanathan *et al.*, 2015). Bent (10 × 15.7 × 0.3 cm) and flat (10 × 10 × 0.3 cm) LSCs doped with Red-305 dye coupled to c-Si solar cell were investigated (Fig. 2.6a and b). Flat device could achieve 2.9% PCE. The bent LSC was found to be less sensitive to the angle of incident solar radiation and could obtain PCE of 3.4%.

Nikolaidou et al. introduced a thin film organic-inorganic hybrid perovskite planar LSC in 2016 (1.5 × 1.5 × 0.1 cm) (Nikolaidou *et al.*, 2016). The host material was glass and a 1.5 × 0.1 cm c-Si solar cell was attached to the edge of the device. The perovskite had high QY of 80% with large Stokes-shift and was spectrally matched with c-Si solar cells which resulted in achieving a significant OE of 29% and PCE of ~ 13%.

Gutierrez et al. fabricated and modelled LSC using two π-conjugated polymers of poly(arylene ethynylene) (PAE) with different gap energies referred to as P_1 and P_2 (Gutierrez *et al.*, 2016b). A high OE was obtained by P_1 polymer (~ 40%) in which low attenuation and scattering coefficients were reported. This may have decreased thermal losses, increasing optical performance. OE was also calculated for different geometric gains using simulation. Results showed that by increasing geometric gain, OE reduced. For example, at a geometric gain of 200 and 400, OE was found to be reduced to 27% and 20% respectively.

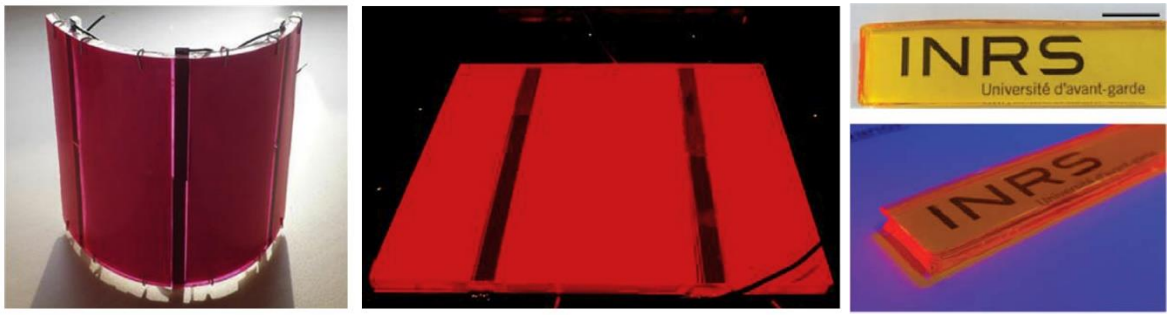

(a) (b) (c)

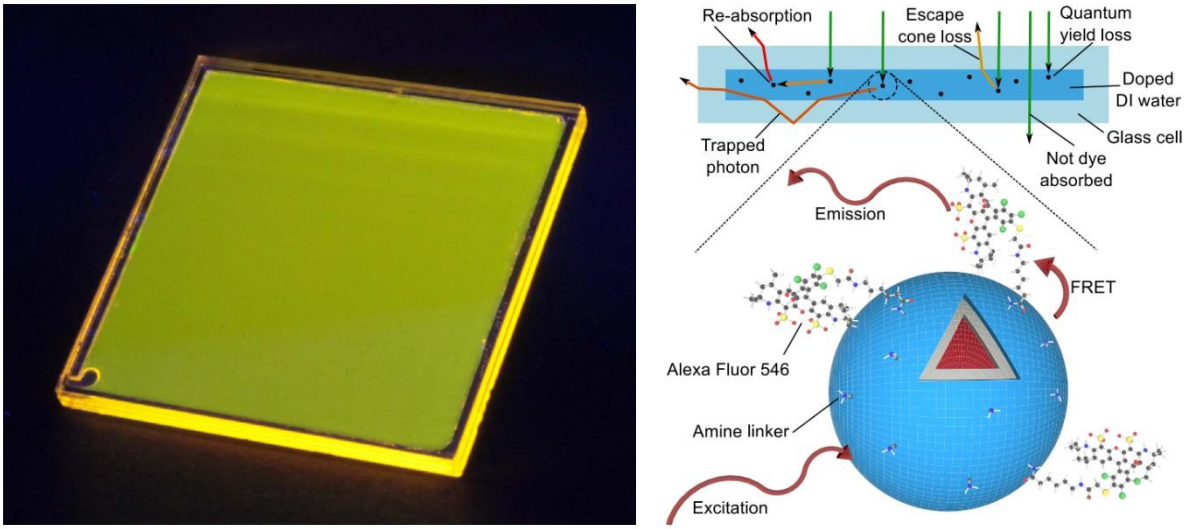

(d) (e)

Fig. 2.6: (a) Transparent bent LSC coupled to six PV solar cell and (b) Flat structure attached to four PV solar cells (Reproduced from (Vishwanathan *et al.*, 2015)). (c) A 7 × 1.5 × 0.3 cm LSC doped with giant core/alloyed-shell QDs with the enhanced absorption spectrum. The device was illuminated under ambient radiation (top) and the UV lamp emitting at 365 nm (bottom). Scale bar represents 1 cm (Reproduced from (Zhao *et al.*, 2016)). (d) A 2 × 2 × 0.3 cm LSC based on conjugated QD/dye (under UV illumination) comprising of (e) A glass cell filled by DI water which is doped with conjugated QD 545 and AF dye. (Reproduced from (Tummeltshammer *et al.*, 2017))

To improve the optical performance of NIR LSC, Zhou et al. introduced a LSC doped with PbS/CdS QDs (Zhou *et al.*, 2016). Si diode was attached to one edge of the LSC working as a photon detector and the other three edges were coupled to mirrors. The side length (geometric gain) of the LSC was optimised to achieve the best OE. Maximum OE of 6.1% was obtained for geometric gain of 10 (10 × 2 × 0.2 cm LSC). The PbS/CdS QDs QY (~40-50%) and photo

stability found to be higher than bare QDs. Moreover, their NIR emission band allowed them to be a suitable choice for semi-transparent facades and windows (Vasiliev *et al.*, 2018).

Giant QDs were first introduced in 2014 by Meinardi et al. to engineer the QD Stokes-shift by optimising the shell thickness (Meinardi *et al.*, 2014). In 2016, the absorption of QD was also enhanced using giant core/alloyed-shell QD ($CdSe/Cd_xPb_{1-x}S$ core/shell) in (Zhao *et al.*, 2016) where a 7 × 1.5 × 0.3 cm PMMA layer was doped with the giant QD (QY of 40%) (Fig. 2.6c). Silicon solar cell was attached to the small edge of the LSC (the other edges were covered by mirrors). PCE of ~1.15% was obtained for the highly transparent device. The device suggested ~15% higher efficiency in comparison with the pure CdS shell-based LSC, which was due to Pb dopants contribution.

In the feasibility study undertaken by Li et al. using giant CdSe/CdS QDs was found to be a low cost technology for large-scale LSCs (Li *et al.*, 2016). The polymer was doped with the giant QDs (with QY of ~70%) and encapsulated into silica shells to increase their stability under real climate conditions. The composite was then employed onto commercial window glass using the doctor-blade deposition method, resulting in fabrication of a semi-transparent LSC. OE of ~17% was achieved when a 413 cm^2 LSC was tested under a single wavelength measurement.

In 2017, the first QD/dye-conjugated LSC was introduced and developed by Clemens et al. where QD 545 and Alexa Fluor 546 (AF) dye were linked (Fig. 2.6d and e) (Tummeltshammer *et al.*, 2017). The developed 2 × 2 × 0.3 cm LSC which was attached to poly-crystalline silicon (p-Si) solar cell, was optically and electrically compared with unlinked LSCs. PCE of the conjugated LSC (2.87%) was found to be higher than both QD LSC (2.24%) and AF dye LSC (2.11%). The conjugated LSC benefited from the wide absorption spectrum of QD 545 and higher QY of AF dye, which overcame the loss mechanisms correlated to re-absorption and non-unity QY.

Wilson et al. characterised a large-scale 60 × 60 × 0.3 cm LSC where different sizes of c-Si solar cells were coupled to lateral edges in order to achieve current matching (Wilson *et al.*, 2017). The LSC was a PMMA sheet doped with Lumogen red 305 dye. Due to using multi-size solar cells, the device performance was enhanced (in comparison with the previously reported large-scale LSCs in 2015 (Aste *et al.*, 2015, Zhang *et al.*, 2015)) and 1.55% overall PCE was achieved.

Meinardi et al. also modelled and developed another large-scale semi-transparent LSC (Fig. 2.7a) (Meinardi *et al.*, 2017c). The host material was PLMA with dimension of 12 × 12 × 0.26 cm doped with indirect bandgap silicon QD (Si QD). The LSC could achieve 2.85% PCE. It can be an ideal option for BIPV systems as silicon is an ultra-abundant material on earth. In addition, authors studied the optical properties of the curved LSC (Fig. 2.7b) in different central angles (from 0 to 180 degrees). Constant performance was observed for all bent angles suggesting the LSC as a suitable candidate for flexible and complex BIPV components.

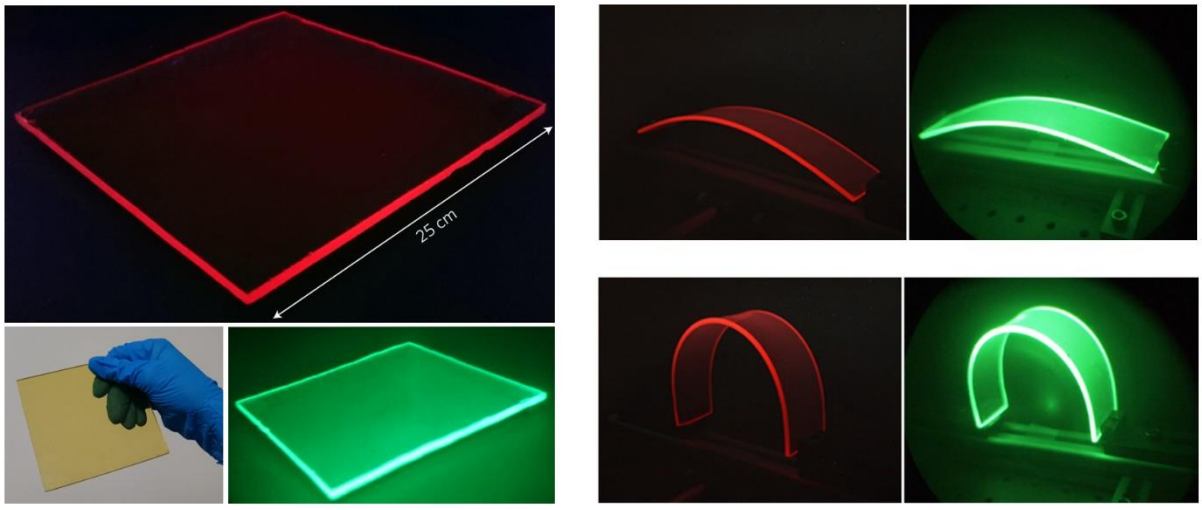

(a) (b)

Fig. 2.7: Semi-transparent LSCs doped with indirect bandgap silicon QD (Si QD): (a) A largescale flat LSC under ambient (bottom left) and UV lamp illumination (365 nm) which have been taken with an UV-filtered visible camera (top) and an UV-filtered infrared camera (bottom right) (b) A 4.5 cm× 20 cm × 0.26 cm curved LSC with different centre angle under UV illumination taken with an UV-filtered visible camera (left photos) and an UV-filtered infrared camera (right photos) (Reproduced from (Meinardi *et al.*, 2017c))

Nitrogen-doped carbon QDs (N-CQDs) were used in LSC for the first time by Li et al. (Chen *et al.*, 2017). N-CQDs offer high stability and QY along with low cost and toxicity. For the LSC fabrication, 2.5 × 1.6 × 0.1 cm glass was covered with different thicknesses of N-CQDs/PMMA by spin coating. Mc-Si was attached to one of the edges. N-CQDs had absorption band of 300-600 nm (peak at ~350 nm) and emission peak at 500-562 nm (based on the excitation wavelength). The highest PCE of 3.98% was obtained when N-CQD/PMMA thickness was 6.67 μm.

In 2018, Schrecengost et al. fabricated a 12.5 × 12.5 × 0.68 cm LSC with PMMA host material doped with Lumogen F Red 300 dye (Schrecengost *et al.*, 2018). They tested and modelled the LSC with various sizes of white background used as a diffusive scattering surface. They also studied the impact of air gap variations (between the white background and LSC) on the device performance. The best performance was obtained when the white background area was 16 times larger than LSC and airgap was 10.7 cm. The optimised device achieved ~54% more power than the LSC with no background surface. Moreover, it produced ~28% more output power than the LSC with a white background of the same area.

Ha et al. introduced a dual-band 5 × 1 × 0.1 cm LSC combined with dye-sensitized solar cell (DSSC) (Fig. 2.8a) (Ha *et al.*, 2018). It consisted of a downshift LSC (where polyurethane doped with an organic fluorophore) and an up-conversion LSC (where PdTPBP/BPEA pair was used). This resulted in an absorption band in UV (300−450 nm) and also in red (~650 nm). The emission peak was at the green band (~530 nm). The rate of the absorbed and waveguided light was increased due to dual absorption band resulting in ~6.1% PCE.

Wu et al. presented a 15.24 × 15.24 cm^2 tandem LSC based on QDs with large Stokes-shift (Fig. 2.8b) (Wu *et al.*, 2018). In the bottom layer, they used $CuInSe_2$ (CISe) QD with QY of 65-75%. For the top layer, they used Mn^{2+}doped $Cd_xZn_{1-x}S$-based QDs with QY of 78%. The LSC exhibited 6.4% OE and 3.1% PCE for AM1.5G solar spectrum. They have also discussed that in the case of using a spectral-matched PV solar cell for each layer (GaAs for bottom layer and GaInP for top layer), 3.8% PCE could be obtained which was ~50% more than a single-layer CISe device.

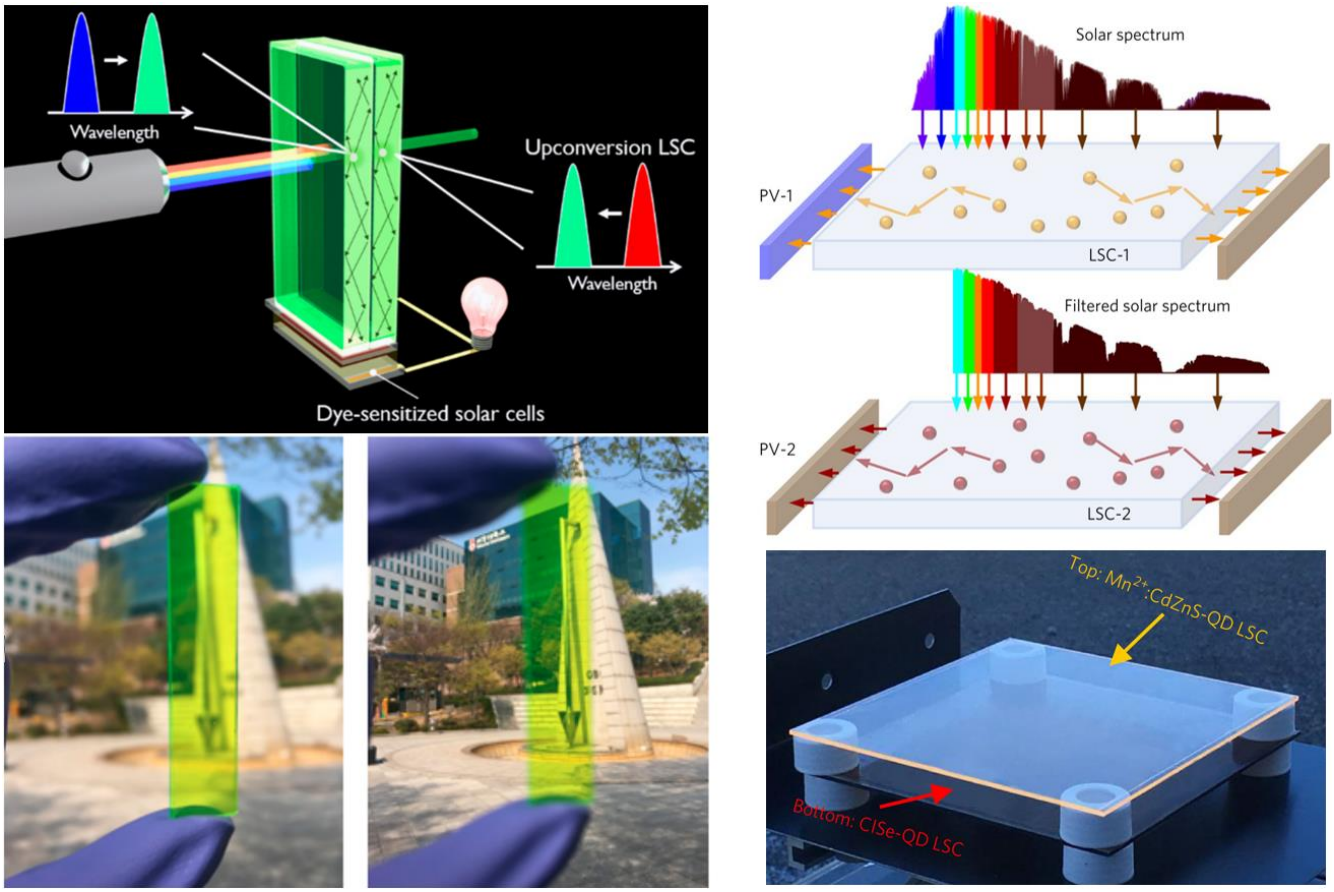

(a) (b)

Fig. 2.8: Schematic and real structure of (a) A dual-band 5 × 1 × 0.1 cm LSC attached to DSSCs. The downshift LSC has a visible emission band and absorbs UV solar radiation. The emission and absorption bands of the upconversion LSC are at green and red respectively (Reproduced from (Ha *et al.*, 2018)). (b) A 15.24 × 15.24 cm tandem LSC with two layers. UV band of solar radiation spectrum is absorbed and waveguided through the top layer while the longer-wavelength band is collected and waveguided by the bottom layer (Reproduced from (Wu *et al.*, 2018))

The idea of multistate LSC smart windows was presented by Jeroen et al. where K160 dye was embedded in a 5 × 5 cm supertwisted nematic (STN) liquid crystal (LC) cell (Fig. 2.9a) (Sol *et al.*, 2018). The device had the absorption band of 400-490 nm and emission peak of ~520 nm. Appling external voltage to LC cells determined the alignment direction of LCs by which the absorption, scattering and edge-emission efficiency of the device could be electrically characterised and switched. This resulted in various LSC states such as coloured, scattering and transparent (based on the amplitude of the applied voltage). The smart window could obtain

PCE of ~3.8%, 3% and 2.6% in coloured (0 v), scattering (10 v) and transparent (28 v) states respectively.

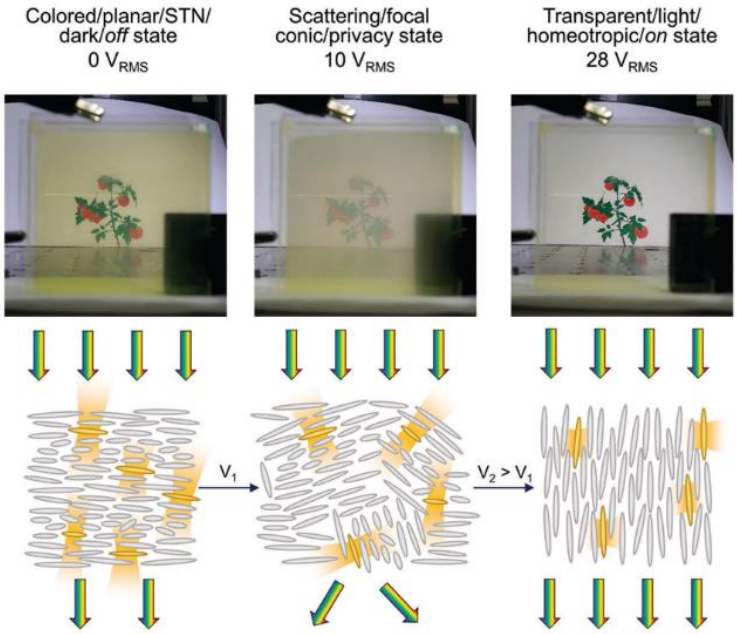

(a)

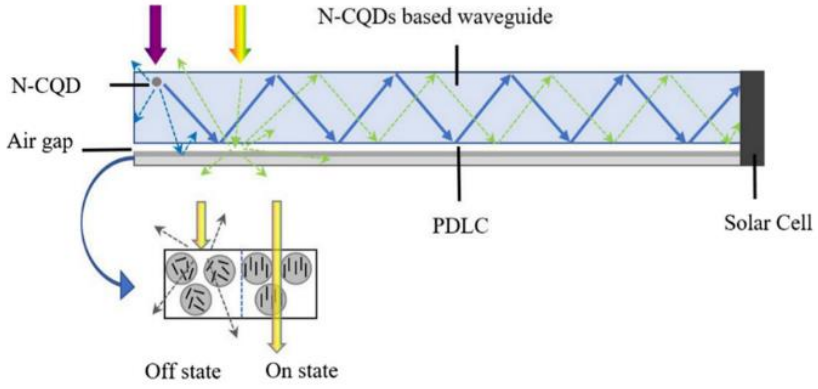

(b)

Fig. 2.9: LSC smart windows: (a) A multistate 5 × 5 cm STN LC cell doped with K160 dye where the alignment of the LCs is characterized by the applied external voltage determining the state (Coloured, Scattering or Transparent) of the LSC (Reproduced from (Sol *et al.*, 2018)) and (b) A large-scale 50 × 25 × 4.2 mm device developed by coupling of N-CQD-based LSC and PDLC. Near-UV band of solar spectrum is absorbed and emitted by N-CQDs. The visible and NIR bands of solar radiation are governed by the voltage amplitude applied to PDLC and can be either scattered/waveguided in the window (in OFF state) or transmitted/exited the device (in ON state) (Reproduced from (Mateen *et al.*, 2019))

Recently in 2019, a large-scale 50 × 25 × 4.2 mm LSC smart window was also developed by coupling of N-CQD-based LSC and polymer dispersed liquid crystals (PDLC) (Fig. 2.9b) (Mateen *et al.*, 2019). The smart window is a suitable choice for BIPV systems and able to selectively harvest UV and near UV solar spectrum. Without applying voltage (OFF state); when droplets in PDLC had un-aligned optical axes, the incident solar radiation was scattered by droplets and waveguided to p-Si PV cell at the edges of window through TIR. Applying voltage (ON state) to PDLC resulted in droplets alignment increasing the transparency of the device by reducing TIR. The achieved PCE was ~2.49% in OFF state and ~1.52% in the high-transparent condition (ON state: 50 v) which was higher than PCE of LSC without PDLC (~1.35%).

2.1.2. Discussion on LSC Parameters, Material and Performance

Optical performance of LSC depends on their configuration parameters such as the device shape, geometric gain, host material, luminescent species, and PV solar cell spectral response (Bose *et al.*, 2009, Kastelijn *et al.*, 2009, Wang *et al.*, 2011b, Vishwanathan *et al.*, 2015, Tummeltshammer *et al.*, 2016). In an ideal LSC, the host material must provide long term photo-stability, compatibility with dispersing luminescent materials, be low cost, highly transparent, and also exhibit low attenuation and scattering coefficients (Rowan *et al.*, 2008, Klampaftis *et al.*, 2009, El-Bashir, 2018). Most host materials used in LSCs were inorganic such as Al_2O_3 (Hovel *et al.*, 1979, Kawano *et al.*, 1997), polymers such as PMMA (Richards and McIntosh, 2007, Slooff *et al.*, 2007, De Nisi *et al.*, 2017) and polyvinyl acetate (PVA) (LeDonne *et al.*, 2008), glass (Yamada *et al.*, 2000, Švrček *et al.*, 2004), organic paint thinner (Maruyama *et al.*, 1998, Maruyama and Bandai, 1999), organic molecule silicate (Inoue *et al.*, 1997). PMMA has been broadly used for LSCs due to its low cost and attenuation coefficient (~10^{-2} 1/cm in visible and NIR regions) as well as high stability and compatibility (Richards and McIntosh, 2007, Slooff *et al.*, 2007). Due to environmentally unfriendly impact of PMMA (Council, 2018), organic-inorganic hybrid materials such as ureasil hybrids (Nolasco *et al.*, 2013, Kaniyoor *et al.*, 2016, Rondão *et al.*, 2017) organic-inorganic glass (Reisfeld *et al.*, 2011), Silsesquioxanes (Freitas *et al.*, 2015) and polysiloxanes (Buffa *et al.*, 2012) can be considered as the alternatives.

The emission spectra of the luminescent material should match the PV cell's spectral response and EQE (Slooff *et al.*, 2008, Erickson *et al.*, 2014, Aste *et al.*, 2015, Nikolaidou *et al.*, 2016, Giebink *et al.*, 2018, Wu *et al.*, 2018). This would result in increasing the number of photons harvested by PV solar cell and total PCE (Ha *et al.*, 2018). PCE can be also characterised by the quality of the LSC optical coupling where a compatible index matching fluid is required (Weber and Lambe, 1976b). Based on the modelling results, ~37% performance reduction was reported when the air gap between the LSC and PV solar cell increased from 0 to 2 mm (Rafiee *et al.*, 2018b). Bottom-mounted and top-mounted-PV LSCs were found to be more efficient compared to edge-mounted-PV devices (Zhang *et al.*, 2015, Needell *et al.*, 2018). This is due to the decrease in path length (which is needed for photons to reach PV solar cell) reducing the possibility of escape cone and re-absorption losses (van Sark *et al.*, 2008). However, edge-mounted-PV LSCs are often preferred in BIPV applications (Meinardi *et al.*, 2017c, Reinders *et al.*, 2018, Renny *et al.*, 2018).

LSCs(introduced during the last decade) are categorised based on their development year in Fig. 2.10a showing their best results achieved to date. Note that, these results cannot be compared to one another as the impact of size (geometric gain) on LSC performance should be studied in Table 2-1 and cannot be seen in Fig. 2.10a. Fig. 2.10a also implies a promising and ongoing trend toward development of large-scale LSCs and smart BIPV devices. Luminescent species in LSCs can be classified in organic dyes, various types of nanostructures, plasmonic (coupled MNP-Luminescent materials) and rare-earth ions (Fig. 2.10b).

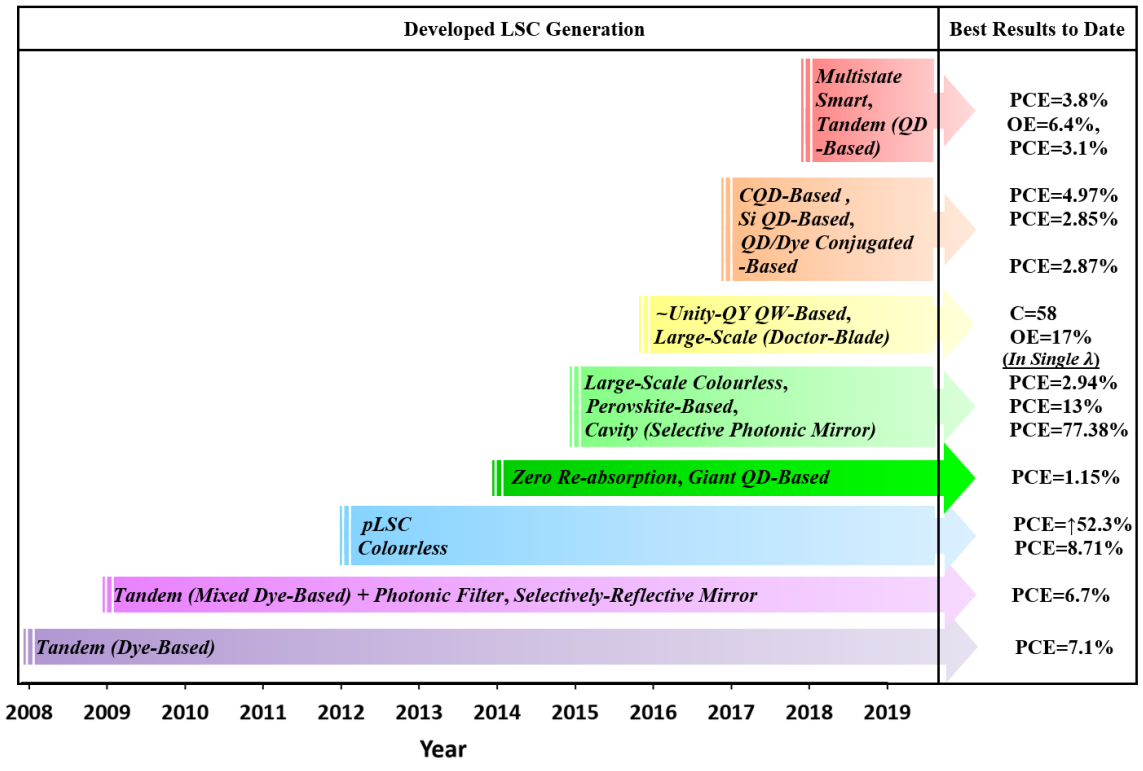

(a)

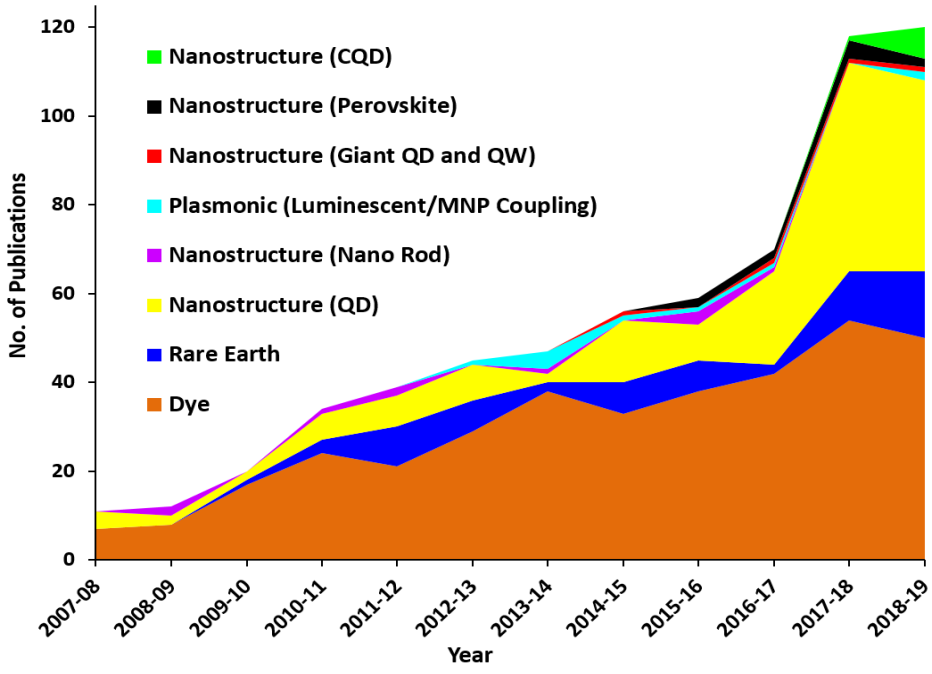

(b)

Fig. 2.10: (a) Various LSC generations developed in the last decade and also their best results achieved to date (b) Number of publications on LSC per year classified based on the doping luminescent material

Rare-earth ions offer high stability, zero self-absorption and high QY (Man *et al.*, 2007, Moudam *et al.*, 2009, Khan *et al.*, 2010, Wang *et al.*, 2011c, Wang *et al.*, 2011d); however, they have narrow absorption band and their cost were found to be more than dyes (Rowan *et al.*, 2008, Desmet *et al.*, 2012). Organic dyes have been broadly used in LSC design and fabrication (Chandra *et al.*, 2012, Debije and Verbunt, 2012, Eisfeld and Briggs, 2018). The most common organic dyes used are from BASF (Lumogen - perylene perinone derivatives) and their absorption ranges cover a large proportion of solar spectrum; however, their small Stokes-shift limits their efficiency (Debije *et al.*, 2011, Desmet *et al.*, 2012, Chandra *et al.*, 2018). Most organic dyes are colourful which may limit their application (Rowan *et al.*, 2008). Tandem and cascaded LSCs (Goldschmidt *et al.*, 2009, Flores Daorta *et al.*, 2014, Chandra *et al.*, 2018) or LSCs doped with mixture of different organic dyes (Slooff *et al.*, 2008, van Sark *et al.*, 2008, Zhang *et al.*, 2015) exhibited a broader absorption spectrum which increased their optical performance. Based on the reviewed literature, the highest reported PCE of planer dye-based LSC is 7.1% (with diffuse backside reflector) (Slooff *et al.*, 2008).

The first nanostructure QDs (Cd-based) were investigated ~19 years ago (Barnham *et al.*, 2000) followed by introducing Pb-based QDs (Shcherbatyuk *et al.*, 2010) to overcome some of the aforementioned disadvantages of organic dyes (Chatten *et al.*, 2004, Gallagher *et al.*, 2007, Bradshaw *et al.*, 2015, Bronstein *et al.*, 2015, Li *et al.*, 2015b, Klimov *et al.*, 2016, Meinardi *et al.*, 2017c, Hill *et al.*, 2018, Needell *et al.*, 2018, Zhou *et al.*, 2018b). Semiconductors-based (such as $CuInSe_2$, $CuInS_2$ (Li *et al.*, 2015a, Meinardi *et al.*, 2015)) and Zn-based (Erickson *et al.*, 2014, Bergren *et al.*, 2018) QDs were also introduced as the alternatives for toxic Cd and Pb-based QDs to mitigate their environmental impact. They exhibited reasonable optical performance as mentioned in the last section. The best results of large-scale colourless LSCs (eligible for BIPV applications), have been recorded for ZnS-coated CISeS-based (3.27% OE with no back reflector (Meinardi *et al.*, 2015)) and $CuInS_2$/ZnS-based (8.1% OE with background reflector (Bergren *et al.*, 2018)) LSCs.

QDs have a wide absorption band which can be tuned by their size and material (Shcherbatyuk *et al.*, 2010, Wang *et al.*, 2018b, Zhou *et al.*, 2018a, Zhu *et al.*, 2019). They can obtain near-unity QY (Coropceanu and Bawendi, 2014) and even, the QD-LSC breakthrough shows unity-QY capability (Chen *et al.*, 2013, Bronstein, 2015, Bronstein *et al.*, 2015, Berends *et al.*, 2016). Their stability, life time and high QY are their advantages over dyes; however, further

improvement is still required regarding their long-term photo-stability (Colvin *et al.*, 1994, Jang *et al.*, 2010, Krumer *et al.*, 2013, Waldron *et al.*, 2017, Wu *et al.*, 2018, Mateen *et al.*, 2019). Carbon QDs (CQDs) discovered in 2004 (Xu *et al.*, 2004), have been recently introduced as highly-stable, abundant and non-toxic emitters with applications in large-scale LSC smart windows (Mateen *et al.*, 2019) as well as enhancing the photo-stability and OE of LSCs (Zhao *et al.*, 2018, Zhou *et al.*, 2018a). Thin film of CQD has been used to cover a large-scale conventional CdSe/CdS QD-based LSCs to improve their photo-stability (by 1.8 times) and OE (by 16%) (Liu *et al.*, 2018). An LSC with N-CQDs embedded in polyvinylpyrrolidone (PVP) thin films achieve PCE of ~4.97% which is the highest PCE for CQD-based LSCs to date (Wang *et al.*, 2018b). Although the improvements in CQDs are still in progress, the aforementioned results make CQDs a promising luminescent material for future large-scale and commercial LSC development.

By increasing the doping concentration of luminescent material in LSC, the OE increases (Krumer *et al.*, 2017). However, past the doping concentration saturation point (which varies for different LSC configurations), OE decreases due to the increase in re-absorption losses (Tummeltshammer *et al.*, 2016, Sumner *et al.*, 2017). Moreover, increasing geometric gain in large-scale LSCs boosts the rate of re-absorption and thermal losses negatively affecting the total PCE (Currie *et al.*, 2008, Bomm *et al.*, 2011, Coropceanu and Bawendi, 2014, Erickson *et al.*, 2014, Knowles *et al.*, 2015, Zhang *et al.*, 2015, Gutierrez *et al.*, 2016b). QDs can be engineered to reduce re-absorption losses similar to the study (Bradshaw *et al.*, 2015) on CdSe/CdS core/shell nanocrystal heterostructures, dot-in-rod, $\mathrm{Zn}_{1-x-y}\mathrm{Cd}_x\mathrm{Mn}_y Se/ZnS$ and $\mathrm{Cd}_{1-x}\mathrm{Cu}_x Se$ doped nanocrystals. Doped nanocrystal have shown better spectral performance than heterostructures which resulted in exhibiting no spectral overlap of emission and absorption profiles (large Stokes-shift) and achieving zero re-absorption LSC (Erickson *et al.*, 2014, Bradshaw *et al.*, 2015). Re-absorption losses of giant QDs (such as CdSe/CdS) can be engineered by their shell thickness where increasing the thickness enlarges the QD Stokes shift and improves stability (Coropceanu and Bawendi, 2014, Meinardi *et al.*, 2014, Bronstein, 2015). This has made giant CdSe/CdS QD a promising emitter for large LSCs development through depositing the polymer/giant QD on commercial large-scale windows (Doctor blade deposition) (Li *et al.*, 2016). The Quantum wells (QW) re-absorption losses, emission spectrum (from visible to NIR) and QY can be also tuned and characterised by their thickness (Sharma

et al., 2017). Recent optimised seed/QW/thick-shell QD suggested a near unity-QY (>95%) (Jeong *et al.*, 2016, Song *et al.*, 2017). However, non-unity QY has been reported after doping the matrix material with QW which needs to be addressed in future optimisations (Sharma *et al.*, 2017).

Furthermore, based on the modelling results, core-shell nano rods (such as CdSe/CdS) exhibited smaller Stokes-shift and re-absorption rate with respect to conventional QDs (Bose *et al.*, 2008, Bomm *et al.*, 2010, Krumer *et al.*, 2013, Fisher *et al.*, 2015, Coropceanu *et al.*, 2016). Indirect band gap Si QD (Meinardi *et al.*, 2017c) is also a low-cost and ultra earth-abundant QD based on semiconductor which is a non-toxic ideal option for large-scale semi-transparent (NIR) LSC due to its near-zero re-absorption rate.

Re-absorption free $Mn/CsPbCl_3$ perovskite emitters (Meinardi *et al.*, 2017a) have been also used offering relatively large Stokes-shift. Perovskite emitters can be developed in inorganic or organic–inorganic metal halides structures (Protesescu *et al.*, 2015, Nikolaidou *et al.*, 2016, Ito *et al.*, 2018). The first perovskite-based LSC was investigated in 2015 (Mirershadi and Ahmadi-Kandjani, 2015) and as it was mentioned in last section, thin film perovskite could very soon achieve the incredible PCE of ~13% in 2016 due to their near-zero spectral overlap and re-absorption losses (Nikolaidou *et al.*, 2016). They still suffer from disadvantages such as environmental risks and impacts (due to toxic Pb and Cd), low photo-stability, near-UV absorption band and wide energy gap. Further optimization are still in progress to use perovskite emitters in large-scale LSC and BIPV systems (Meinardi *et al.*, 2017a, Zhao *et al.*, 2017).

QD/dye-conjugated (Tummeltshammer *et al.*, 2017) and QD-based tandem LSC (Hughes *et al.*, 2017, Liu *et al.*, 2018, Needell *et al.*, 2018, Wu *et al.*, 2018) can be also used to harvest and waveguide broader band of solar radiation spectrum improving their OE and PCE. Based on the results of this review, QD-based LSC with tandem structure (such as (Wu *et al.*, 2018)) and with reflective mirror (such as (Zhou *et al.*, 2016)) could achieve around double OE (~6%) in comparison with other similar single-layer conventional configurations. Both techniques can be optimised using well-spectral-matched PV solar cell, host, and luminescent materials.

Coupling photonic filters (Goldschmidt *et al.*, 2009, Connell *et al.*, 2018, Needell *et al.*, 2018), polarization-independent filters (de Boer *et al.*, 2011) and wavelength selective mirrors (Debije *et al.*, 2009, Goldschmidt *et al.*, 2009, Debije *et al.*, 2010, Bronstein *et al.*, 2015, Song *et al.*, 2017, Connell *et al.*, 2018) to LSC have been found to be one of the most effective technologies

in decreasing escape cone losses and increasing the trapping efficiency. Combination of selective and normal (spectral or diffuse) mirrors in an LSC-cavity, along with using high-QY QD, enhanced the solar concentration ratio (C) to ~30 (Bronstein *et al.*, 2015) with capability of reaching to ~58 (Song *et al.*, 2017). Reflectivity, airgap, size and type of the normal mirrors are also vital parameters affecting the performance of LSC (Pravettoni *et al.*, 2009a, Pravettoni *et al.*, 2009b, Klimov *et al.*, 2016, Xu *et al.*, 2016, Rafiee *et al.*, 2018b). Coupling a 16-times larger white background to an LSC (with 10.7 cm air gap) enhanced the PCE by 54% compared to the bare LSC (Schrecengost *et al.*, 2018). Although using backside mirror and LSC-cavity technology increase the PCE (Slooff *et al.*, 2008, van Sark *et al.*, 2008, Bronstein *et al.*, 2015, Song *et al.*, 2017), they may limit the LSC application in BIPV systems where transparent and semi-transparent waveguides are considered as suitable candidates.

PLSC is also an alternative advanced technology to overcome LSC losses and improve the optical performance of existing LSC (Saraidarov *et al.*, 2010, Chandra *et al.*, 2012, Chandra, 2013, El-Bashir *et al.*, 2013b, Tummeltshammer *et al.*, 2013, El-Bashir *et al.*, 2014, Chen *et al.*, 2015, Levchenko, 2018). 53.2% enhancement in PCE was obtained by coupling luminescent material and MNP in a double-layer pLSC (El-Bashir *et al.*, 2014) which is the highest recorded experimental enhancement in PCE for a transparent LSC to date. Despite the remarkable optical performance, optimising the concentration of MNP in pLSC (spacing between luminescent materials and MNP) was found to be a crucial challenging and complex task. (Chandra *et al.*, 2012, Chandra, 2013, El-Bashir *et al.*, 2013b, El-Bashir *et al.*, 2014). Therefore, they have got less interest compared to other luminescent materials in LS device development. Close spacing increases the non-radiative decay and photo luminescence quenching, which reduces the total QY of MNP-luminescent material coupling (Geddes, 2017).

2.2. Quantum Yield Enhancement in Plasmonically Enhanced Luminescent Solar (pLS) Devices

As discussed in last Section, in pLS devices, the luminescent molecule is coupled with MNP where the plasmonic effect can improve the performance of the whole device (Chandra, 2013, El-Bashir *et al.*, 2013b, El-Bashir *et al.*, 2014, Ahmed *et al.*, 2016).

QY and lifetime (τ_0) of emission processes for a luminescent molecule in the absence of MNP, are correlated to its radiative (Γ_r) and non-radiative (Γ_{nr}) decay rates and calculated by $Eqn\ (2.12)$ (Geddes, 2017):

$$QY = \frac{\Gamma_r}{\Gamma_{nr} + \Gamma_r} \qquad \tau_0 = \frac{1}{\Gamma_{nr} + \Gamma_r} \qquad Eqn\ (2.12)$$

When MNPs (such as gold and silver) are coupled and interact with luminescent species, the intensity of incident energy is amplified due to the excitation photon density enhancement factor (PDEF). PDEF is product of excitation and emission efficiencies (Soller *et al.*, 2007, Darvill *et al.*, 2013, Osinkina, 2014) given by $Eqn\ (2.13)$:

$$PDEF = \Psi(e_p, x_d, \lambda_{ex}).QY(e_p, x_d, \lambda_{em}) \qquad Eqn\ (2.13)$$

λ_{ex} and λ_{em} are the excitation and emission wavelengths respectively, x_d is the location of the particle with a unit dipole moment of e_p and $\Psi(e_p, x_d, \lambda_{ex})$ is the excitation efficiency defined as $Eqn\ (2.14)$ (Geddes, 2017):

$$\Psi(e_p, x_d, \lambda_{ex}) = \frac{|E(x_d, \lambda_{ex}).e_p|^2}{|E_i|^2} \qquad Eqn\ (2.14)$$

E is total electric field and E_i is intensity of the incident solar radiation. Under these conditions, the luminescent emission is either enhanced or quenched. This interaction can be seen in Fig. 2.11 where the total QY and τ_0 is calculated by $Eqn\ (2.15)$ (Geddes, 2017):

$$QY_{total} = \frac{\Gamma_{rM} + \Gamma_r}{\Gamma_{nr} + \Gamma_{rM} + \Gamma_r} \qquad \tau_0 = \frac{1}{\Gamma_{nr} + \Gamma_{rM} + \Gamma_r} \qquad Eqn\ (2.15)$$

Where Γ_{rM} is radiative decay due to the MNP presence.

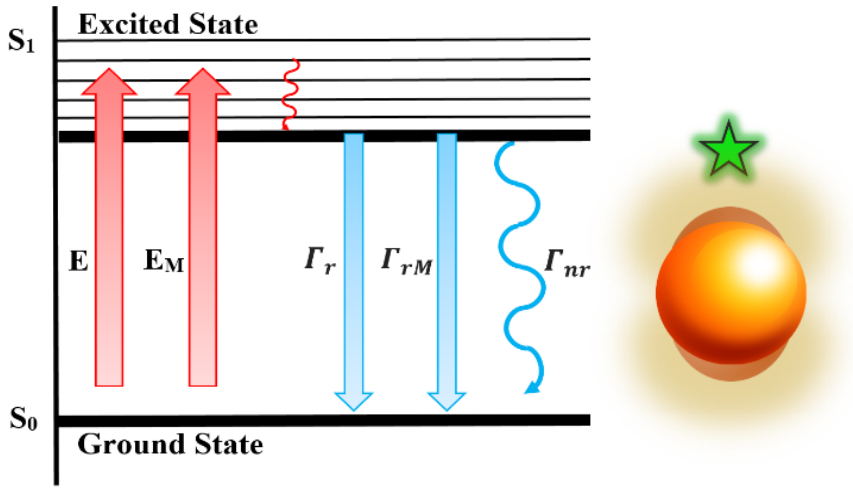

Fig. 2.11: The emission process of a single luminescent molecule coupled with polarized MNP

While many studies reported plasmonic enhancement in the emission spectrum of luminescent material due to the MNP coupling (Nakamura and Hayashi, 2005, Anger *et al.*, 2006, Kühn *et al.*, 2006, Tovmachenko *et al.*, 2006, Aslan *et al.*, 2007, Bharadwaj and Novotny, 2007, Cheng and Xu, 2007, Stranik *et al.*, 2007, Tam *et al.*, 2007, Bardhan *et al.*, 2008, Bardhan *et al.*, 2009, Ming *et al.*, 2009, Fu *et al.*, 2010), few studies have shown quenching of the output emission (Dulkeith *et al.*, 2002, Sönnichsen *et al.*, 2002, Aslan and Pérez-Luna, 2004, Dulkeith *et al.*, 2005, Li *et al.*, 2009).

The reason is PDEF strongly depends on the spacing between the MNP and luminescent molecule (governed by their doping concentration) (Geddes, 2017). In far-field region where MNP and luminescent molecule have relatively long distance between them (>50 nm), the luminescent molecule is hardly affected by MNP surface plasmon resonance (SPR) energy due to weak interaction between particles. At near-field optimised distances between MNP and luminescent molecule (between 20 nm to 50 nm), Γ_{rM} and Γ_{nr} are increased; however, Γ_{rM} is dominant ($\Gamma_{rM} > \Gamma_{nr}$) which boosts QY_{total}. At very close distances between MNP and luminescent molecule (<20 nm), Γ_{nr} is dominant ($\Gamma_{nr} > \Gamma_{rM}$) which reduces PDEF and QY_{total} due to the increase in quenching factor (QF) and non-radiative dissipation (Hövel *et al.*, 1993, Dulkeith *et al.*, 2005, Hsieh *et al.*, 2007, Karthikeyan, 2010, Reineck *et al.*, 2013, Kochuveedu and Kim, 2014, Geddes, 2017).

Distance in luminescent-MNP coupling is the main parameter affecting emission rate; however, quenching is also governed by chemical interface damping (Hövel *et al.*, 1993, Karthikeyan, 2010). Other reasons including multi-scattering of light with multi-NPs and self-quenching can also decrease the QY_{total} enhancement which are neglected in the diluted devices (Geddes, 2017).

Overlap between the emission spectrum of luminescent material and absorption of the MNPs (in close proximity) boosts the quenching rate (Reineck *et al.*, 2013). Note that, the extinction spectrum of MNP (with SPR peak at $\lambda_{\square PR}$) is the summation of both absorption and scattering spectra (Amendola *et al.*, 2017). For MNPs which are smaller than the wavelength of the incident photons i.e. MNP with less than 50 nm size, the absorption spectrum (with peak at $\lambda_{MNP.abs}$) is dominated in the extinction spectrum; thus, $\lambda_{SPR} \approx \lambda_{MNP.abs}$ (Maier, 2007). If the coupled luminescent material's absorption peak (at $\lambda_{L.abs}$) overlaps with SPR, the excitation rate of luminescent material is increased due to larger absorption cross section of MNP and energy transferring from MNP to luminescent material (Dorcéna, 2007). This can increase PDEF and total emission rate (Anger *et al.*, 2006, Geddes, 2017). If the emission peak of luminescent material (at $\lambda_{L.em}$) is matched with SPR, MNP receives energy from excited luminescent material (Dorcéna, 2007). Reducing radiative decay while the excited luminescent molecules quickly come back to ground energy level (due to less life time) increases the number of luminescent molecules in ground level where they have the potential to absorb photons which enhances the absorption of luminescent material (Dorcéna, 2007). Therefore, in summary, $\lambda_{L.abs} = \lambda_{SPR}$ results in maximum excitation efficiency and when $\lambda_{L.em} = \lambda_{SPR}$, maximum emission efficiency is achieved (Liu *et al.*, 2013b). PDEF is product of both excitation and emission efficiencies; however, maximum of these two parameters are not achievable simultaneously (due to $\lambda_{L.em} \neq \lambda_{L.abs}$). Therefore, the optimised case can be considered when $\lambda_{L.abs} < \lambda_{SPR} < \lambda_{L.em}$ (Liu *et al.*, 2013b).

Overall, due to the complex optical and plasmonic energy transfer procedures, experimental optimisation of pLS device in terms of their size, doping concentration and spacing between MNP and luminescent material and their spectral overlap is quite challenging in comparison with conventional LS devices. These challenges implies the need to develop an accurate model to investigate and optimise the optical properties of pLS devices before fabrication. Although various studies have been undertaken for modelling conventional LS based on ray tracing

algorithm (reviewed in Section 2.3), there is no algorithm established for modelling small and large scale pLS devices. The reason is ray tracing model is not able to model the plasmonic effect of MNP in pLS. To overcome this, FDTD method (reviewed in Section 2.4) can be used prior to ray tracing algorithm to achieve MNP optical properties.

2.3. Ray Tracing Modelling for LS Devices

From a ray trace modelling perspective, the algorithm of tracing light in both LS devices (LSC and LDS) is the same. A ray tracing model is used to simulate the optical processes in LS devices such as reflection, refraction, absorbtion, emission, scattering, attenuation, wave-guiding and transmission (Kennedy, 2010). In ray tracing, each incident ray (with specific wavelength and vector) is traced until its fate is detected during the simulation (Glassner, 1989).

Based on the optical and physical processes happening in LS devices, Fig. 2.12 exhibits a ray tracing algorithm for a single incident photon in a LS device with no mirror or PV where the final fates of the ray are shown in yellow boxes.

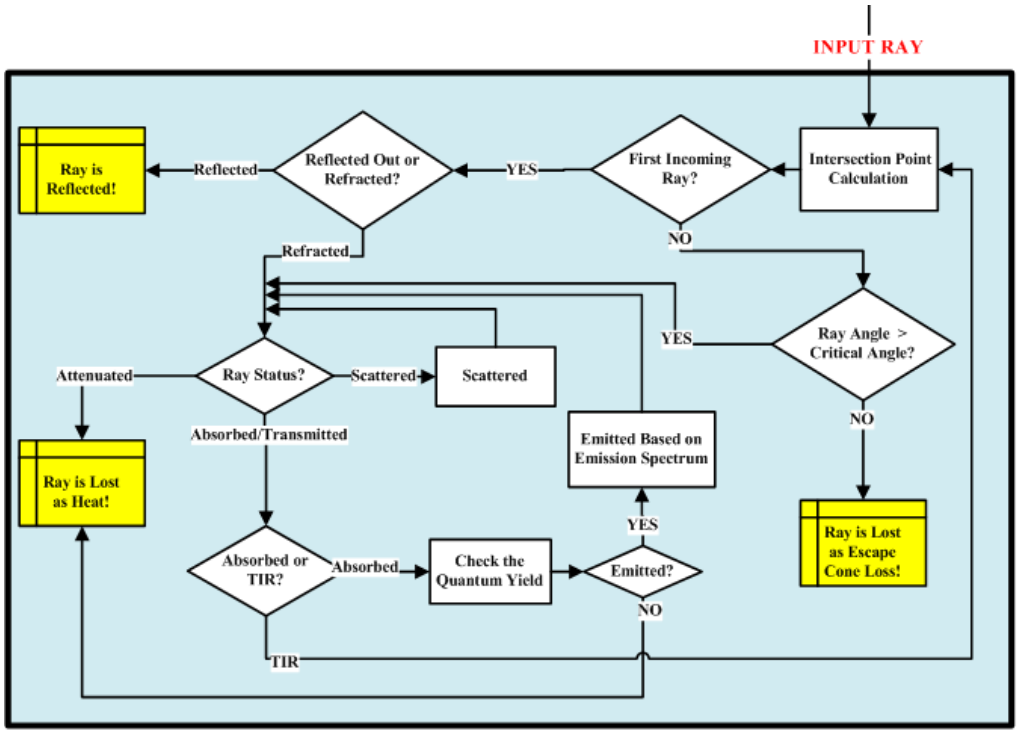

Fig. 2.12: Block diagram of ray tracing for a single incident ray in a LS device with no mirror or PV

For intersection point calculation, a ray is defined by its origin point ($I_0 : [X_0\ Y_0\ Z_0]$) and its normalized vector ($I_d : [X_d\ Y_d\ Z_d]$) as defined in $Eqn\ (2.16)$ (Glassner, 1989):

$$X_d^2 + Y_d^2 + Z_d^2 = 1 \qquad Eqn\ (2.16)$$

The ray vector with any length can be obtained by $Eqn\ (2.17)$:

$$I_L = I_0 + (I_d \times L) \qquad Eqn\ (2.17)$$

Where *L* is the distance between the vector and any plane ($[PL : [a_P\ b_P\ c_P\ DP]$) in space. The plane is defined by $Eqn\ (2.18)$ and $Eqn\ (2.19)$:

$$(a_P \times x) + (b_P \times y) + (c_P \times z) + DP = 0 \qquad Eqn\ (2.18)$$

$$a_P{}^2 + b_P{}^2 + c_P{}^2 = 1 \qquad Eqn\ (2.19)$$

DP is the distance of the plane from the coordinate system origin. It should be noted that the sign of the *DP* determines the side of the plane in comparison with the system origin. The unit vector normal ($N : [a_P\ b_P\ c_P\ ]$) of the plane is also defined as a vector indicating a direction perpendicular to the plane.

To obtain the distance (*L*) between the ray's origin and its intersection point on the plane *PL*, *Eqn* (2.17) is substituted into the plane equation (*Eqn* (2.18)); which resultes in $Eqn\ (2.20)$:

$$a_P \times (X_0 + X_d \times L) + b_P \times (Y_0 + Y_d \times L) + c_P \times (Z_0 + Z_d \times L) = -DP \qquad Eqn\ (2.20)$$

Then, the intersection points can be calculated using *L* and $Eqn\ (2.21)$:

$$r_i : [x_i\ \ y_i\ \ z_i] = [X_0 + X_d \times L \qquad Y_0 + Y_d \times L \qquad Z_0 + Z_d \times L] \qquad Eqn\ (2.21)$$

Fig. 2.13a shows the process of reflection. The angle between the *N* and the incident ray (*I*) is called the angle of incident (θ_i) while the ray is reflected (*R*) by the angle of reflection (θ_r). The reflected vector is calculated by $Eqn\ (2.22)$:

$$R = I - 2(N.I)N \qquad Eqn\ (2.22)$$

Fig. 2.13b illustrates the refraction process. As is shown, the transmitted light is indicated with the vector *T* which has the angle of refraction of θ_t with *N*. The relation between θ_t and θ_i is interpreted by Snell's Law in $Eqn\ (2.23)$ (Glassner, 1989):

$$\frac{sin\,\theta_i}{sin\,\theta_t} = \frac{\eta_t}{\eta_i} = \eta_{ti} = \frac{1}{\eta_{it}} \qquad Eqn\ (2.23)$$

η is the refraction index of the medium. Using the algebraic solution, the value of T is calculated by Eqn (2.24):

$$T = \eta_{it} I + \left[\eta_{it} C_i - \sqrt{1 + \eta_{it}^2 (C_i^2 - 1)}\right] N \qquad Eqn\ (2.24)$$

$C_i = cos(\theta_i)$. The TIR phenomenon is seen in Fig. 2.13c which is the basic mechanism of trapping and wave-guiding light inside a medium according to θ_c of the device which is calculated by Eqn (2.25) (Glassner, 1989):

$$\theta_c = sin^{-1} \frac{\eta_2}{\eta_1} \qquad Eqn\ (2.25)$$

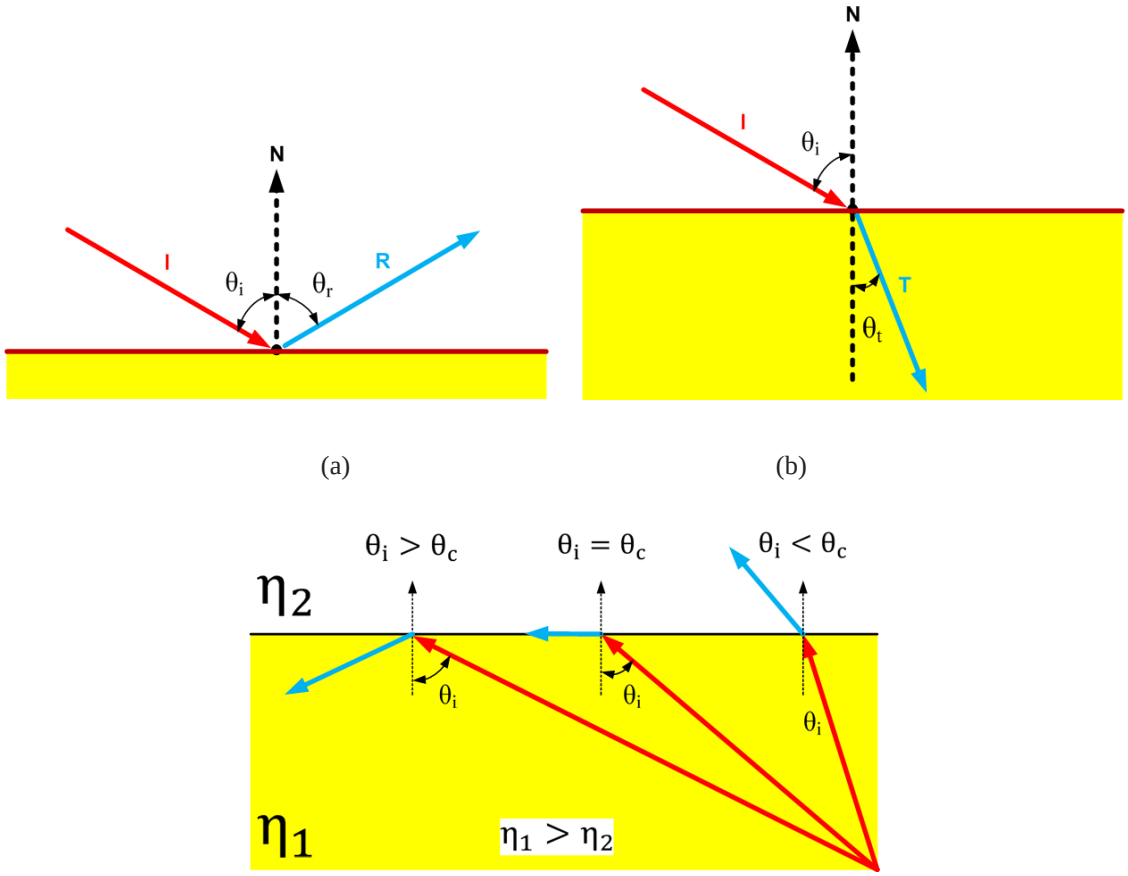

(a) (b)

(c)

Fig. 2.13: (a) Reflection and (b) Refraction of a photon striking a surface, and (c) Trapping mechanism of light inside a medium based on critical angle when the medium is denser than the outer environment (Glassner, 1989)

The probability of scattering in the algorithm is achieved by $Eqn\ (2.26)$(Kennedy, 2010):

$$PR_{scat} = 1 - e^{-d.\alpha_{Scat}} \qquad Eqn\ (2.26)$$

Where d is the thickness in cm and α_{Scat} is the scattering coefficient of the host material in 1/cm. The probability of host material attenuation is obtained by $Eqn\ (2.27)$:

$$PR_{atte} = 1 - e^{-d.\alpha_{Atte}} \qquad Eqn\ (2.27)$$

Where α_{Atte} is the attenuation coefficient of the host material in 1/cm. The probability of absorption of a ray by luminescent materials is calculated by $Eqn\ (2.28)$:

$$PR_{abs}^{L} = 1 - e^{-MC.d.\alpha_{Abs}} \qquad Eqn\ (2.28)$$

Where α_{Abs} is the absorption coefficient of the luminescent material in 1/cm. *MC* is the multiplication constant which is a factor used to apply different doping concentrations of the luminescent material to the algorithm. The absorption is obtained by $Eqn\ (2.29)$ from the Beer Lambert law (Klampaftis *et al.*, 2009, Abderrezek *et al.*, 2013, Şahin and Ilan, 2013):

$$Tran = 10^{-A} = e^{-\tau} \qquad Eqn\ (2.29)$$

Where *A* is the absorbance and *Tran* is the value of transmittance of the material. $\tau = MC.d.\alpha_{Abs}$ is the optical depth. Accordingly, the probability of being transmitted is calculated by $Eqn\ (2.30)$:

$$PR_{tran} = 1 - [PR_{abs}^{L} + PR_{atte} + PR_{scat}] \qquad Eqn\ (2.30)$$

Slooff et al., used the ray tracing algorithm to model a 5 × 5 × 0.5 cm LSC with mirror on its three edges and bottom while mc-Si solar cell was attached on one of LSC edges (Slooff *et al.*, 2006). They also used the ray tracing algorithm to model another 5 × 5 × 0.5 cm LSC (Slooff *et al.*, 2008). The ~10% differences between the modelling and experimental results were due to experimental errors such as LSC degradation (LSC used after one year) and also to non-optimal coupling of the LSC and solar cells.

Kennedy et al., used ray tracing algorithms to model four LSC configurations (6 × 6 × 0.3 cm) under different types of input solar radiation (Kennedy, 2010). The reason for discrepancy between experimental and modelling results was that the real materials and devices were non-homogenous and non-linear while they were modelled as homogenous and linear.

Bomm et al., fabricated five LSCs with different dimensions (Bomm *et al.*, 2011). Although the results obtained in the range of 600 nm closely matched the experimental results, there were vast differences at other wavelengths (~75%). This was due to not importing the host material characteristics and scattering effects to the model which can change the response of the model at longer wavelengths (above ~600 nm). They found it difficult to distinguish the exact reason for the discrepancy at short wavelengths (~300 nm to ~500 nm). It might be because the cell response is not linear in this region or the value of QY is not constant at all wavelengths (Bronstein *et al.*, 2015).

A Monte Carlo simulation was used to study the performance of a $2 \times 2 \times 0.2$ cm LSC including CdSe/CdS core/shell QD (Şahin *et al.*, 2011, Coropceanu and Bawendi, 2014). The model predicted the light which was reflected, lost and collected by the PV. The optical efficiency was estimated to be 49% which was a close match with the experimental result of 48%.

Alvaerz et al., used "Tracey" software (offered by PV Lighthouse Company) which uses ray tracing algorithms (PV-Lighthouse, 2017) to model different multi-layer LDS structures of different dyes, host materials and PV technologies (including CdTe, mc-Si and CIGS PV) (Alonso-Álvarez *et al.*, 2015). The reason of discrepancy (from ~64% to ~273% error) for such a commercial software was ignoring experimental errors such as the non-efficient optical coupling in the device which can affect the spectral characteristics and response of the devices in different wavelength ranges.

The main challenges in ray trace modelling are accuracy and simulation time. In order to achieve more accurate results, all details of the 3D device and specification of the used materials including different losses mechanisms (such as escape cone loss, reabsorption, reflection, attenuation and scattering) and non-linear parameters (such as QY) should be considered in the model. Adding all these parameters increase the complexity of the ray tracing algorithm. In addition, since the algorithm is executed based on the probability of different events for each incident ray, by increasing the number of the rays (iterations in the algorithm), the outcomes are more precise; so that, the model may be required to run for several million rays in order to achieve highly accurate results (Bronstein, 2015). On the other hand, since the ray tracing algorithm is based on applying different conditional statements and calculations related to the optical and physical events, it is a complex and time-consuming process. Thus, for an accurate model, the computational cost is high so that it may need powerful computers with several CPU

cores (Bronstein, 2015). All these challenges, limitations and sources of discrepancies in existing ray tracing models will be considered in next Chapters to develop a high-accurate 3D ray tracing algorithm for LS and pLS devices.

2.4. Finite Difference Time Domain (FDTD) Method for Metal Nanoparticle (MNP) Modelling in pLS Devices

Plasmonic coupling of MNP and luminescent material in pLS devices improves the optical properties and performance of the device (Chandra *et al.*, 2012, Chandra, 2013, El-Bashir *et al.*, 2013b, El-Bashir *et al.*, 2014, Ahmed *et al.*, 2017a, Geddes, 2017). Therefore, investigating the optical properties of MNPs is required in developing a model for pLS devices. FDTD method is used in this thesis for studying and modelling the plasmonic effect and optical properties of MNP.

2.4.1. Optical Properties of MNP

The optical properties of MNPs is due to the collective response of conductive electrons which form an electron cloud around the metal nuclei. When an electric field is applied, the electrons are pushed away from the nuclei which forces the electron cloud to be displaced and asymmetrical forming a dipole. This is known as the material polarization which creates restoring force. It results in oscillating the conduction electron cloud (plasma) which is characterized by the resonance frequency of the MNP (Ritchie, 1957). When the incident photon frequency is resonant with collective oscillation of the conduction electron cloud, it is referred as surface plasmon resonance (SPR).

The resonance frequency of MNP SPR can be tuned by their dimensions, shape, and their solvent material specifications (Efrima and Metiu, 1979, Aravind and Metiu, 1980, Gersten and Nitzan, 1980, Wang *et al.*, 1980, Mirkin and Ratner, 1997, Rampi *et al.*, 1998, Scaffardi *et al.*, 2004, Orendorff *et al.*, 2006, Haiss *et al.*, 2007). The strong SPR of these metals gives them the ability to absorb and scatter the light. Among the noble metals, the surface plasmon experiments are mostly implemented using gold and silver because their near-field effect is so high which is due to the very small imaginary part in their permitivity. In pLS devices, if a luminescent species is placed near Au NPs or Ag NPs (in the enhanced local electromagnetic field due to the SPR),

plasmonic effect will take place after illuminating the device which can improve the performance of the whole device (Ahmed *et al.*, 2016, Amendola *et al.*, 2017). In addition, they have several other advantages which makes them efficient for using in pLS devices (Ritchie, 1957, Metiu and Das, 1984, Moskovits, 1985, Raether, 1988, Collin, 1990, Alvarez *et al.*, 1997, Link and El-Sayed, 1999, Lyon *et al.*, 1999, Barnes *et al.*, 2003, Myroshnychenko *et al.*, 2008):

- They are inert chemically
- Their absorption band and SPR peak are in the visible part of the solar radiation
- They do not oxidize; while, the oxidation in other metals makes their SPR observation very hard.
- They can be easily attached to biomolecules using chemical linkers
- They can significantly amplify the irradiated light intensity

2.4.2. Maxwell's Equation

The behaviour of MNPs can be interpreted by Maxwell's equations (Taflove and Hagness, 1995, Schneider, 2010, Inan and Marshall, 2011) which are presented as four equations in their macroscopic electromagnetism form. The first one is Gauss law defined by $Eqn\ (2.31)$:

$$\nabla \cdot \overrightarrow{D} = \rho_v \qquad Eqn\ (2.31)$$

Where D is electric flux density in C/m^2 and ρ_v is volume charge density in C/m^3. The law means that the electric field is diverging from positive charge and converging in negative charge. Note that if there is no charge, electric fields form loops. The second law is the Gauss's law for magnetism defined by $Eqn\ (2.32)$:

$$\nabla \cdot \overrightarrow{B} = 0 \qquad Eqn\ (2.32)$$

Where B is magnetic flux density in Wb/m^2. Based on this law, magnetic fields always form loops. The third law is Ampere's law and defined as in $Eqn\ (2.33)$:

$$\nabla \times \overrightarrow{H} = \overrightarrow{J} + \frac{\partial \overrightarrow{D}}{\partial t} \qquad Eqn\ (2.33)$$

Where H is the magnetic field intensity in A/m and J is electric current density in A/m^2. This law indicates that the circulating magnetic fields induce currents and (or) time varying electric fields. Currents and (or) time varying electric fields induce circulating magnetic fields.

The fourth law is Faraday's law of induction defined by Eqn (2.34):

$$\nabla \times \overrightarrow{E} = -\frac{\partial \overrightarrow{B}}{\partial t} \qquad Eqn\ (2.34)$$

Where *E* is electric field intensity in V/m. This law says that the circulating electric fields induce magnetic fields which vary over time; moreover, time-varying magnetic fields induce electric fields which circulates.

Hence, Maxwell's equations include two divergence equations and two curl equations which produce fields. In addition, there are two constitutive relations found in Eqn (2.35) and Eqn (2.36) which describe how fields interact with materials:

$$\overrightarrow{D}(t) = [\varepsilon(t)] * \overrightarrow{E}(t) \qquad Eqn\ (2.35)$$

$$\overrightarrow{B}(t) = [\mu(t)] * \overrightarrow{H}(t) \qquad Eqn\ (2.36)$$

Where $\varepsilon(t)$ is permittivity in F/m and $\mu(t)$ is permeability in H/m. Note that * is convolution and [ ] means tensor. The refractive index of a material is used to make a meaningful description which can be calculated by Eqn (2.37):

$$\eta = \sqrt{\mu_r \varepsilon_r} \qquad Eqn\ (2.37)$$

The magnetic response in most of materials is negligible ($\mu_r = 1$); hence, refractive index can be simply estimated as $\eta = \sqrt{\varepsilon_r}$.

Another term which can declare the relation between the electric and magnetic fields of the wave through the material is the impedance which is a fundamental quantity causing the reflection and scattering in the medium and obtained by Eqn (2.38):

$$Z_m = Z_{m0}\sqrt{\frac{\mu_r}{\varepsilon_r}} \approx \frac{|\overrightarrow{E}|}{|\overrightarrow{H}|} \qquad Eqn\ (2.38)$$

Where $Z_{m0} = \sqrt{\frac{\mu_0}{\varepsilon_0}} \approx 376.74\ \Omega$. If we assume that there are no charges ($\rho_v = 0$) or current sources ($\vec{J} = 0$) and we assume linear, isotropic and dispersive materials, the Maxwell's equations can be written as Eqn (2.39) and Eqn (2.40):

$$\nabla \times \overrightarrow{E} = -\mu \frac{\partial \overrightarrow{H}}{\partial t} \qquad Eqn\ (2.39)$$

$$\nabla \times \overrightarrow{H} = \varepsilon \frac{\partial \overrightarrow{E}}{\partial t} \qquad Eqn\ (2.40)$$

Which are generally found in most of the literature. Hence, Maxwell's equation can predict electromagnetic waves based on two main equations of *E* and *H* which are perpendicular to each other and update each other continuously.

2.4.3. FDTD Equations and Terms

Finite difference time domain (FDTD) is a grid-based numerical method and one of the best methods to solve Maxwell's equations and obtain the optical properties of MNPs while they are modelled in a discrete space grid (Known as "Yee" grid) (Yee, 1966, Taflove, 1980). FDTD has been used to estimate the extinction spectra of MNPs by changing their size, shape and concentration (Linden *et al.*, 2001, Vial *et al.*, 2005, Grand *et al.*, 2006, Ghosh and Pal, 2007, Myroshnychenko *et al.*, 2008).

In order to use FDTD to simulate Maxwell's equations, the first-order finite-difference approximation is used which is defined as the mid-point between two points as can be seen in Fig. 2.14.

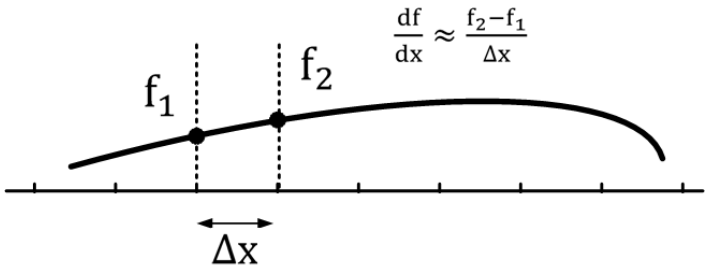

Fig. 2.14: Calculation of the first-order Finite-Difference approximation in FDTD method

The finite difference approximations of Maxwell's equations are in the form of $Eqn\ (2.41)$ and $Eqn\ (2.42)$ (Inan and Marshall, 2011):

$$H\,|_{t+\frac{\Delta t}{2}} = H|_{t-\frac{\Delta t}{2}} - \frac{\Delta t}{\mu}(C^E|_t) \qquad Eqn\ (2.42)$$

$$E\,|_{t+\Delta t} = E|_t + \frac{\Delta t}{\varepsilon}\left(C^H\,|_{t+\frac{\Delta t}{2}}\right) \qquad Eqn\ (2.42)$$

C^E and C^H terms are respectively the curl of electric and magnetic fields. By expanding these vector equations into scalar equations, the complete 3D Maxwell's equations and constitutive relations will be obtained in each axis (Taflove and Hagness, 1995). The final form of the update-equations and constitutive-relations for obtaining *H* field in only the *x*-axis are found in $Eqn\ (2.43)$:

$$H_x|_{t+\frac{\Delta t}{2}}^{i,j,k} = \left(m_{Hx1}|^{i,j,k}\right)H_x|_{t-\frac{\Delta t}{2}}^{i,j,k} + \left(m_{Hx2}|^{i,j,k}\right)C_x^E|_t^{i,j,k} + \left(m_{Hx3}|^{i,j,k}\right)I_{CEx}|_t^{i,j,k} + \left(m_{Hx4}|^{i,j,k}\right)I_{Hx}|_t^{i,j,k}$$

$$C_x^E|_t^{i,j,k} = \frac{E_z|_t^{i,j+1,k} - E_z|_t^{i,j,k}}{\Delta y} - \frac{E_y|_t^{i,j,k+1} - E_y|_t^{i,j,k}}{\Delta z}$$

$$I_{Hx}|_{t=\frac{\Delta t}{2}}^{i,j,k} = \sum_{T=\frac{\Delta t}{2}}^{t-\frac{\Delta t}{2}} H_x|_T^{i,j,k}$$

$$I_{CEx}|_t^{i,j,k} = \sum_{T=0}^{t} C_x^E|_T^{i,j,k}$$

$$m_{Hx0}|^{i,j,k} = \frac{1}{\Delta t} + \left(\frac{\sigma_y^H|^{i,j,k} + \sigma_z^H|^{i,j,k}}{2\varepsilon_0}\right) + \frac{\left(\sigma_y^H|^{i,j,k}\right)\left(\sigma_z^H|^{i,j,k}\right)\Delta t}{4\varepsilon_0^2}$$

$$m_{Hx1}|^{i,j,k} = \frac{1}{m_{Hx0}|^{i,j,k}}\left[\frac{1}{\Delta t} - \left(\frac{\sigma_y^H|^{i,j,k} + \sigma_z^H|^{i,j,k}}{2\varepsilon_0}\right) - \frac{\left(\sigma_y^H|^{i,j,k}\right)\left(\sigma_z^H|^{i,j,k}\right)\Delta t}{4\varepsilon_0^2}\right]$$

$$m_{Hx2}|^{i,j,k} = -\frac{1}{m_{Hx0}|^{i,j,k}}\frac{c_0}{\mu_{xx}|^{i,j,k}}$$

$$m_{Hx3}|^{i,j,k} = -\frac{1}{m_{Hx0}|^{i,j,k}}\frac{c_0\Delta t}{\varepsilon_0}\frac{\sigma_x^H|^{i,j,k}}{\mu_{xx}|^{i,j,k}}$$

$$m_{Hx4}|^{i,j,k} = -\frac{1}{m_{Hx0}|^{i,j,k}}\frac{\Delta t}{\varepsilon_0^2}\left(\sigma_y^H|^{i,j,k}\right)\left(\sigma_z^H|^{i,j,k}\right) \qquad Eqn\ (2.43)$$

The final form of the update equations and constitutive relations for *D* in the x-axis are found in $Eqn\ (2.44)$:

$$D_x|_{t+\Delta t}^{i,j,k} = \left(m_{Dx1}|^{i,j,k}\right)D_x|_t^{i,j,k} + \left(m_{Dx2}|^{i,j,k}\right)C_x^H|_{t+\frac{\Delta t}{2}}^{i,j,k} + \left(m_{Dx3}|^{i,j,k}\right)I_{CHx}|_{t-\frac{\Delta t}{2}}^{i,j,k} + \left(m_{Dx4}|^{i,j,k}\right)I_{Dx}|_{t-\Delta t}^{i,j,k}$$

$$C_x^H|_{t+\frac{\Delta t}{2}}^{i,j,k} = \frac{H_z|_{t+\frac{\Delta t}{2}}^{i,j,k} - H_z|_{t+\frac{\Delta t}{2}}^{i,j-1,k}}{\Delta y} - \frac{H_y|_{t+\frac{\Delta t}{2}}^{i,j,k} - H_y|_{t+\frac{\Delta t}{2}}^{i,j,k-1}}{\Delta z}$$

$$I_{Dx}|_t^{i,j,k} = \sum_{T=0}^{t} D_x|_T^{i,j,k}$$

$$I_{CHx}|_{t-\frac{\Delta t}{2}}^{i,j,k} = \sum_{T=\frac{\Delta t}{2}}^{t-\frac{\Delta t}{2}} C_x^H|_T^{i,j,k}$$

$$m_{Dx0}|^{i,j,k} = \frac{1}{\Delta t} + \left(\frac{\sigma_y^D|^{i,j,k} + \sigma_z^D|^{i,j,k}}{2\varepsilon_0}\right) + \frac{(\sigma_y^D|^{i,j,k})(\sigma_z^D|^{i,j,k})\Delta t}{4\varepsilon_0^2}$$

$$m_{Dx1}|^{i,j,k} = \frac{1}{m_{Dx0}|^{i,j,k}}\left[\frac{1}{\Delta t} - \left(\frac{\sigma_y^D|^{i,j,k} + \sigma_z^D|^{i,j,k}}{2\varepsilon_0}\right) - \frac{(\sigma_y^D|^{i,j,k})(\sigma_z^D|^{i,j,k})\Delta t}{4\varepsilon_0^2}\right]$$

$$m_{Dx2}|^{i,j,k} = \frac{c_0}{m_{Dx0}|^{i,j,k}}$$

$$m_{Dx3}|^{i,j,k} = \frac{1}{m_{Dx0}|^{i,j,k}} \frac{c_0\, \Delta t\, \sigma_x^D|^{i,j,k}}{\varepsilon_0}$$

$$m_{Dx4}|^{i,j,k} = -\frac{1}{m_{Dx0}|^{i,j,k}} \frac{\Delta t}{\varepsilon_0^2}\left(\sigma_y^D|^{i,j,k}\right)\left(\sigma_z^D|^{i,j,k}\right) \qquad Eqn\ (2.44)$$

(10)

Afterwards, the final form of the update equations and constitutive relations for *E* field in *x*-axis are obtained by $Eqn\ (2.45)$:

$$E_x|_{t+\Delta t}^{i,j,k} = \left(m_{Ex1}|^{i,j,k}\right) D_x|_{t+\Delta t}^{i,j,k}$$

$$m_{Ex1}|^{i,j,k} = \frac{1}{\varepsilon_{xx}|^{i,j,k}} \qquad Eqn\ (2.45)$$

Using the same interoperation, the final form of the updated equations and constitutive relations for other axis (*y* and *z*) can also be achieved. Note that, in the above equations, the terms are defined in 3D matrices in which *i*, *j* and *k* indicate the grid cell location (in *x*, *y* and *z* vectors respectively) in a 3D Yee grid. Δt is the time step in seconds, "*m*" terms are constitutive relations. "σ" terms are including all conductivity and loss values in the grid. "*I*" terms are integration terms which are the summation of curl (*C*) terms.

The algorithm which can be used in programming for solving these equations is illustrated in Fig. 2.15. It includes three main stages namely; (1) Pre-processing, (2) FDTD Main Loop and (3) Post-processing. As illustrated, each update equation has four terms including terms of the next time step, terms of the previous time step, update coefficient and curl term of other field at an intermediate time step. Maxwell's equations are solved in a leapfrog procedure which means the electric field is solved for one time instant and the magnetic field is updated and solved at the next time instant. To optimize the procedure and increase the speed of the loop, the update coefficients should be calculated before the loop in the Pre-processing stage. After ending the loop, the program enters the post-processing step in which the power flow, amount of reflection, transmission, extinction and other parameters can be calculated in the frequency and wavelength domain.

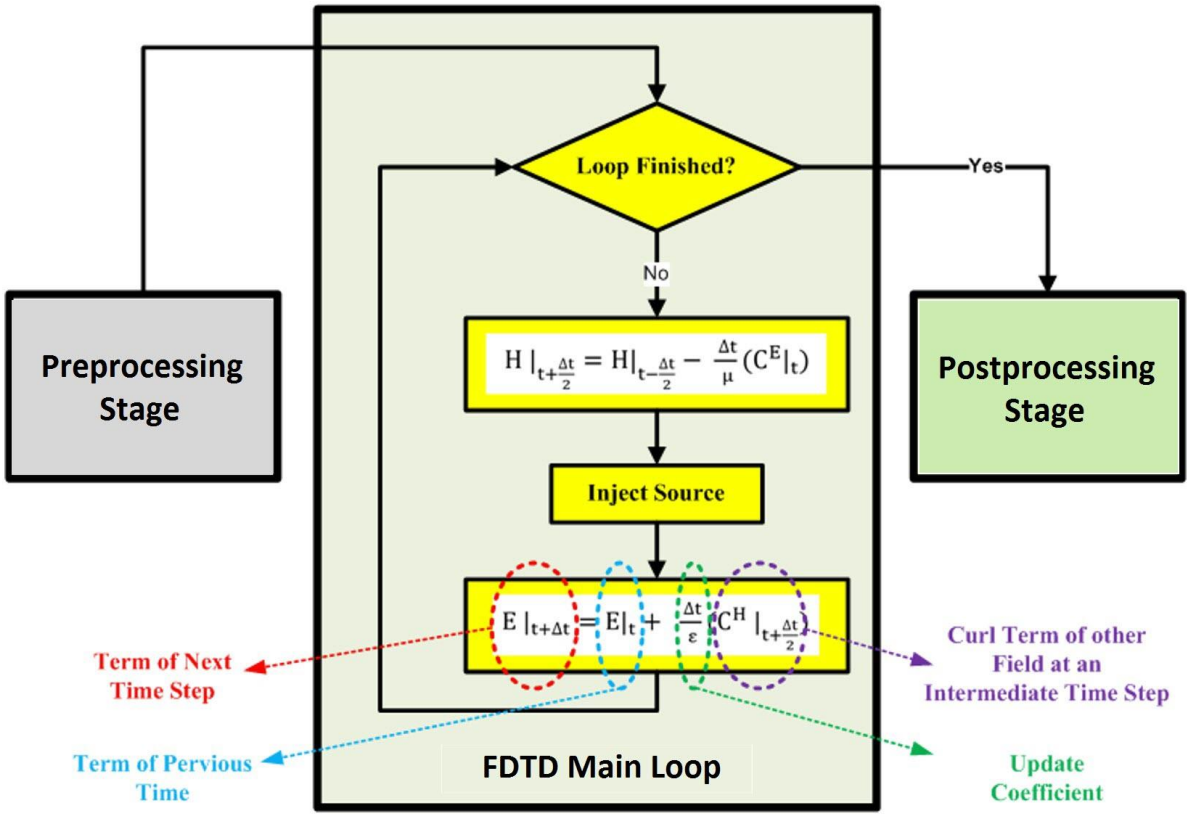

Fig. 2.15: General Block Diagram for FDTD Algorithm (Taflove and Hagness, 1995, Schneider, 2010, Inan and Marshall, 2011)

2.4.4. Implementing FDTD in Practice

Fig. 2.16 illustrates the complete process for the FDTD algorithm. In the Pre-processing stage, parameters such as grid structure, resolution, time step and total number of iterations are designed. During the FDTD main loop process, Maxwell's equations are solved. Finally, in the post-processing stage the power flow and the final results will be analysed and obtained. Results can be exported to an excel file and can also be visualised.

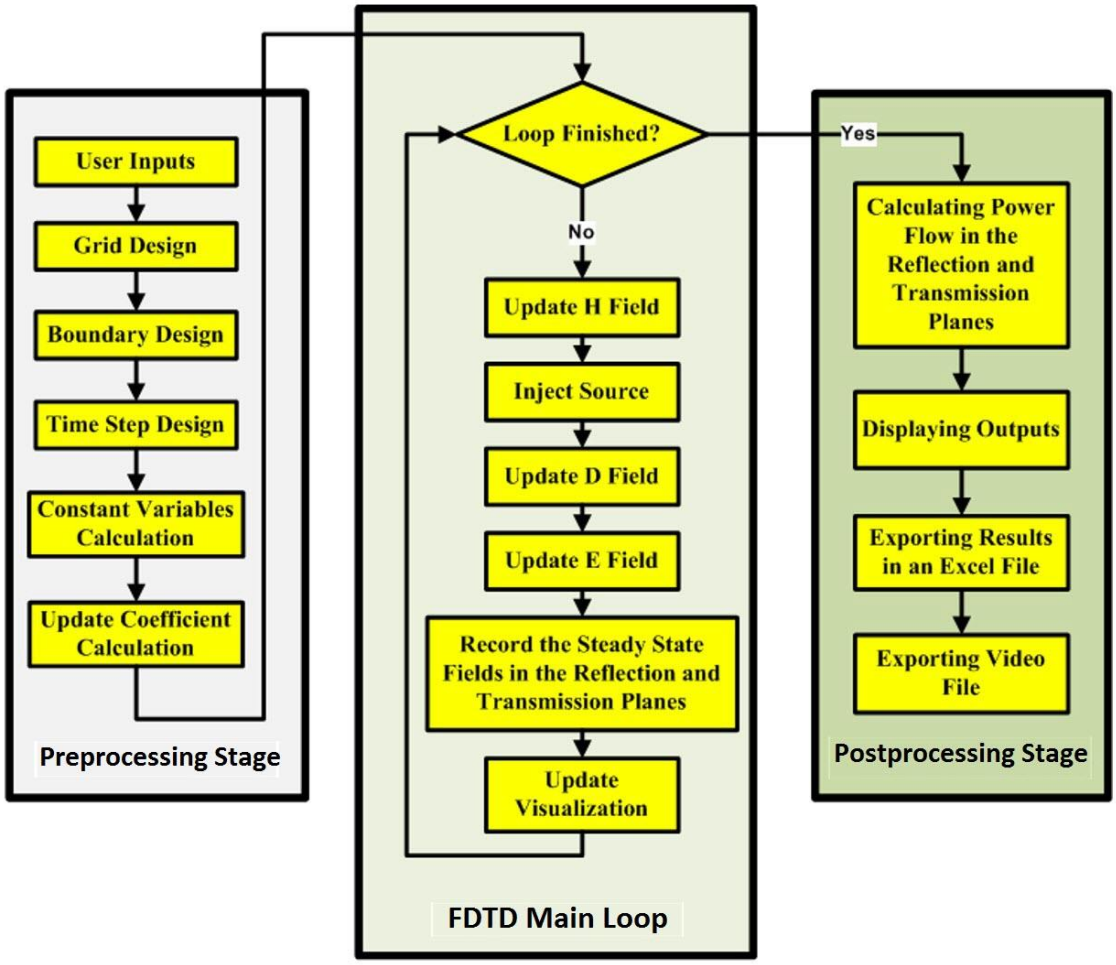

Fig. 2.16: Block Diagram for FDTD Algorithm

2.4.4.1. Yee Grid Designing

The Yee grid and components can be created as 1D, 2D and 3D. Fig. 2.17a simply shows a 1D grid. As can be seen, each grid consists of a number of cells. The simulated structure is designed and placed in the middle of the grid where two spacer regions (buffers) are placed around the component. The size of the buffer is designed so that it can cover the longest wavelength during the simulation. The source of the input is placed in a cell referred as the source injection point. Two points at the beginning and the end of the grid are added to record the reflected and transmitted energy. The boundary conditions are required to be defined in the endpoints of the grid which determine the condition of the fields at the edges of the Yee grid. Two types of boundary conditions can be defined in the grid's edges: periodic boundary condition (PBC) and absorbing boundary condition (ABC) as presented in Fig. 2.17b and Fig. 2.17c respectively. In PBC, the field amount in the last cell (shown in green) will be used as a boundary condition for the first cell and vice versa. The ABC is using a perfectly matched layer (PML) by which the field in the boundaries will be terminated gradually using a loss function such as $Eqn\ (2.46)$:

$$\sigma(x) = \frac{\varepsilon_0}{2\Delta t}\left(\frac{x}{L_{PML}}\right)^3 \qquad Eqn\ (2.46)$$

Where L_{PML} is PML length in metre.

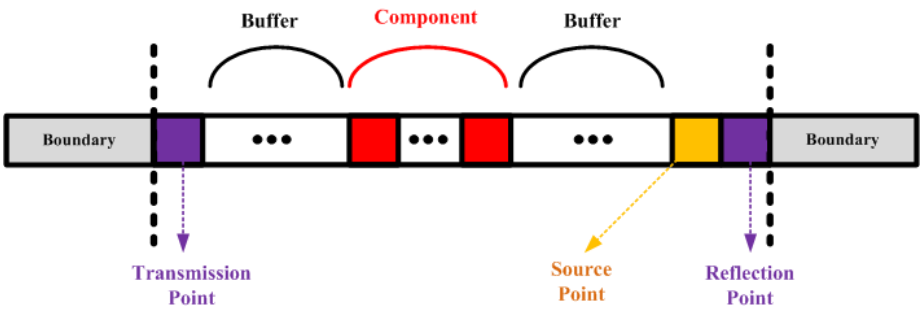

(a)

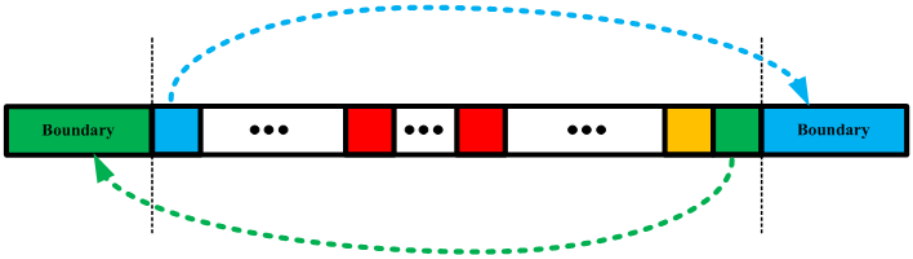

(b)

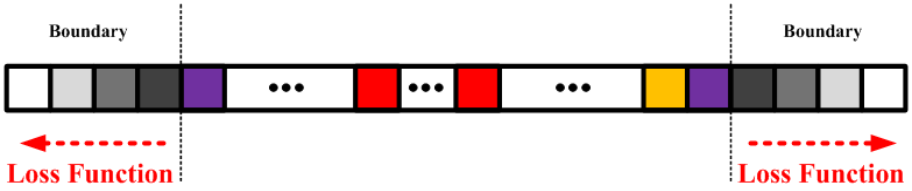

(c)

Fig. 2.17: (a) General structure for 1D Yee grid with (b) Periodic boundary condition and (c) Absorbing boundary condition using perfectly matched layer

The first step toward the grid design is computing the grid resolution based on the shortest wavelengths obtained by Eqn (2.47):

$$\lambda_{min} = \frac{c_0}{f_c\, \eta_{max}} \qquad Eqn\ (2.47)$$

Where η_{max} is the largest refraction index in the grid and f_c *i*s the maximum frequency. The larger resolution constant (N_{res}) in the grid, the more accurate component will be created. The grid cell's size is calculated by Eqn (2.48):

$$\Delta d = \frac{\lambda_{min}}{N_{res}} \qquad Eqn\ (2.48)$$

For a 3D grid, $\Delta x = \Delta y = \Delta z = \Delta d$ can be considered. The total number of grid cells in one direction is given by $Eqn\ (2.49)$:

$$N_d = \frac{L_d}{\Delta d} + N_{BUF} + N_{PML} + N_{SRC} + N_{Records} \qquad Eqn\ (2.49)$$

Where L_d is the length of the component in that direction, $N_{BUF} = \frac{2 \times BUF}{\Delta x}$ is the number of cells required for the buffers, $N_{PML} = \frac{2 \times PML}{\Delta x}$ is the number of cells required for the PMLs, N_{SRC} is the number of the source injection point and $N_{Records}$ is the number the record points.

2.4.4.2. Time Step, Iteration Calculation and Injecting Source

The Courant stability condition (Courant *et al.*, 1967) is therefore used to design the time step in $Eqn\ (2.50)$:

$$\Delta t \leq \frac{1}{c_0 \sqrt{\frac{1}{(\Delta x)^2} + \frac{1}{(\Delta y)^2} + \frac{1}{(\Delta z)^2}}} \qquad Eqn\ (2.50)$$

After obtaining the time step, the total iteration in the simulation loop will be calculated by $Eqn\ (2.51)$:

$$N_{Iteration} = round\ (\tfrac{T_t}{\Delta t}) \qquad Eqn\ (2.51)$$

T_t is the total simulation time.

While updating Maxwell's equations, the input source radiation spectrum is added to the system. The incident electric field of the source radiation spectrum is only polarised in *x-y* plane (Taflove and Hagness, 2005); therefore, it is imported to grid as $Eqn\ (2.52)$:

$$E_x^{src}|_t^{i,j,k_{src}} = P_x cos(\omega t - k_0 \eta_{inc} z)$$

$$E_y^{src}|_t^{i,j,k_{src}} = P_y co\ s(\omega t - k_0 \eta_{inc} z) \qquad Eqn\ (2.52)$$

Where *P* terms are calculating from the polarization vector ($\overrightarrow{P} = \overrightarrow{P_x} + \overrightarrow{P_y}$), $k_0 = \frac{2\pi}{\lambda_0}$, is the radiation's free space wavelength which is constant and η_{inc} is the refraction index of the

incident source perimeter. The incident source magnetic field is achieved using the Maxwell's curl equation ($\nabla \times \overrightarrow{E} = -\mu \frac{\partial \overrightarrow{H}}{\partial t}$) and is defined as Eqn (2.53):

$$H_x^{src}|_t^{i,j,k_{src}} = -P_y \sqrt{\frac{\varepsilon_{inc}}{\mu_{inc}}} cos(\omega t - k_0 \eta_{inc} z)$$

$$H_y^{src}|_t^{i,j,k_{src}} = P_x \sqrt{\frac{\varepsilon_{inc}}{\mu_{inc}}} co\, s(\omega t - k_0 \eta_{inc} z) \qquad Eqn\ (2.53)$$

2.4.4.3. Real (Frequency Dependent) Material Modelling

The electromagnetic characteristics of materials are frequency dependent (Maier, 2007). Therefore, it is important to modify FDTD models to be able to model real materials such as MNPs.

By applying an electric field to MNPs and material polarization as seen in Fig. 2.18, the nucleus starts oscillating based on its resonance frequency and radiates an electric field. This plasma model is similar to the mechanical motion model in Eqn (2.54) (Maier, 2007):

$$M_m \frac{\partial^2 \vec{r}}{\partial t^2} + M_m f_d \frac{\partial \vec{r}}{\partial t} + M_m f_0^2 \vec{r} = -q\vec{E} \qquad Eqn\ (2.54)$$

Where M_m is the mass in kg, r is the vector of position, f_d is damping rate in loss per second and f_0 is natural frequency of the system in hertz.

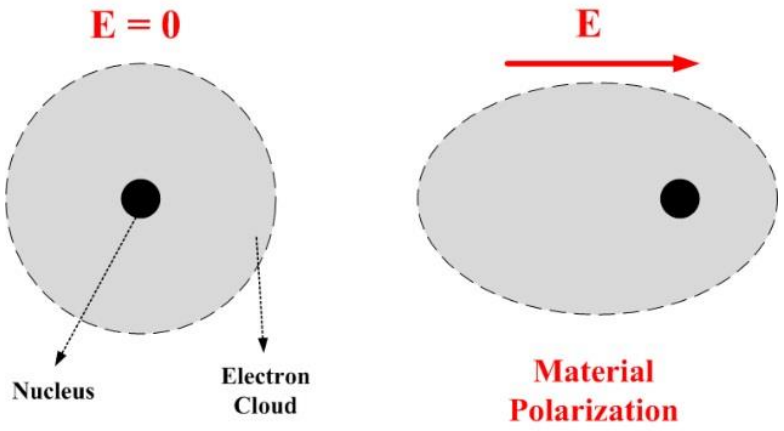

Fig. 2.18: Material polarization in atomic scale

MNP polarization under electric field irradiation is due to the changes in the permittivity over frequency which was experimentally measured for several metals by Johnson and Christy (Johnson and Christy, 1972). The measured data was fitted mathematically through the "Lorentz-Drude Model" using $Eqn\ (2.55)$ (Maier, 2007):

$$\tilde{\varepsilon}_r(\omega) = \varepsilon_r(\infty) + \sum_{u=1}^{U} \frac{S_u {\omega_P}^2}{\omega_{0,u}^2 + j\Gamma_u\omega - \omega^2} \qquad Eqn\ (2.55)$$

Where U is the number of resonators, S_u is the strength of the resonator u. $\omega_{0,u}$ and Γ_u are respectively the natural frequency and the damping rate of the resonator u, ω_P is the plasma frequency and all are in electron-volts (eV). $\varepsilon_r(\infty)$ in F/m is the offset value of permittivity of the host material where the metal is solved. Table 2-2 shows the value of Lorentz-Drude parameters for Au NPs and silver nano particles (Ag NPs). The permittivity of Au NPs using this information can be found in Fig. 2.19 at different frequencies. As is shown, the value of permittivity is a complex value and it is frequency dependent.

Table 2-2: Lorentz-Drude parameters for Au NPs and Ag NPs (Schneider, 2010)

Au NP		
$\omega_P = 9.03\ ev$	$\varepsilon_r(\infty) = 1\ F.m$	
$\omega_0 = 0\ ev$	$S_0 = 0.76$	$\Gamma_0 = 0.053\ ev$
$\omega_1 = 0.415\ ev$	$S_1 = 0.024$	$\Gamma_1 = 0.241\ ev$
$\omega_2 = 0.83\ ev$	$S_2 = 0.01$	$\Gamma_2 = 0.345\ ev$
$\omega_3 = 2.969\ ev$	$S_3 = 0.071$	$\Gamma_3 = 0.87\ ev$
$\omega_4 = 4.304\ ev$	$S_4 = 0.601$	$\Gamma_4 = 2.494\ ev$
$\omega_5 = 13.32\ ev$	$S_5 = 4.384$	$\Gamma_5 = 2.214\ ev$
Ag NP		
$\omega_P = 9.01\ ev$	$\varepsilon_r(\infty) = 1\ F/m$	
$\omega_0 = 0\ ev$	$f_0 = 0.84$	$\Gamma_0 = 9.01\ ev$
$\omega_1 = 0.816\ ev$	$f_1 = 0.065$	$\Gamma_1 = 0.053\ ev$
$\omega_2 = 4.481\ ev$	$f_2 = 0.124$	$\Gamma_2 = 3.886\ ev$
$\omega_3 = 8.185\ ev$	$f_3 = 0.011$	$\Gamma_3 = 0.065\ ev$
$\omega_4 = 9.083\ ev$	$f_4 = 0.84$	$\Gamma_4 = 0.916\ ev$
$\omega_5 = 20.29\ ev$	$f_5 = 5.646$	$\Gamma_5 = 2.419\ ev$

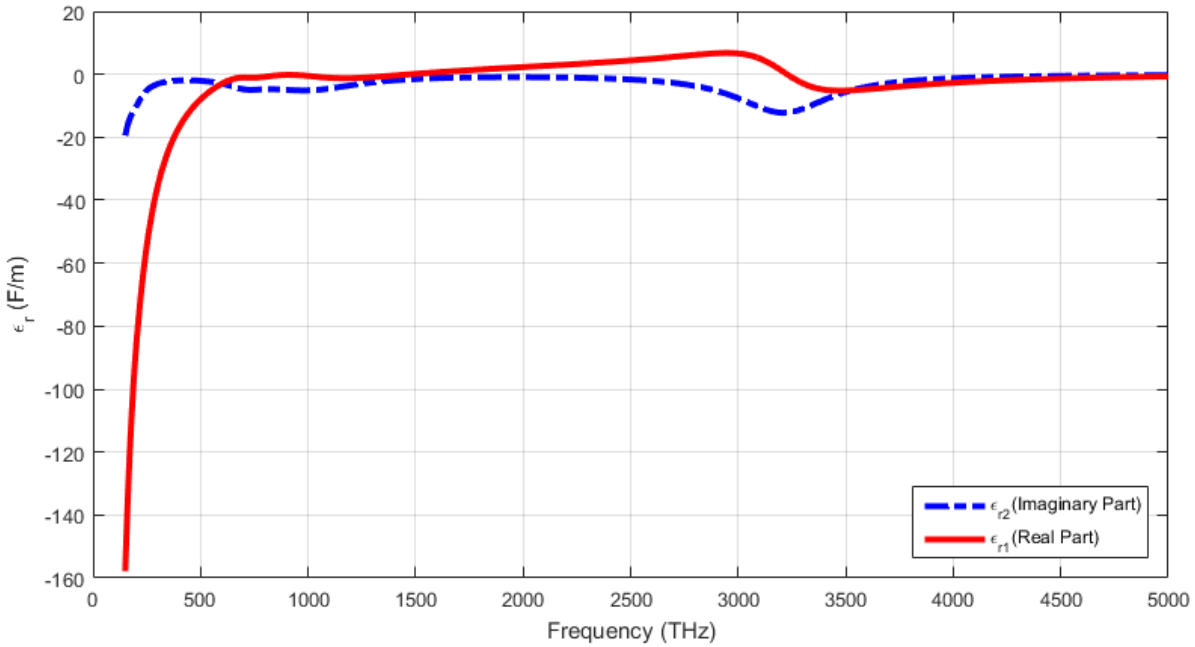

Fig. 2.19: The permittivity function of Au NPs at different frequencies

By applying the Lorentz-Drude permittivity model into the FDTD algorithm and importing the Lorentz-Drude parameters, the optical properties of Au NPs and Ag NPs including their plasmonic effect can be modelled.

To model and analyse pLS devices, the achieved optical properties of MNP, as well as the characteristics of luminescent material must be imported as inputs in a comprehensive ray tracing algorithm which is able to model the interaction between luminescent material and MNP in pLS devices.

2.5. Conclusion

In this Chapter, the main characteristics and specifications of LS device were discussed and reviewed. The optical behaviour algorithm of LS devices (LDS and LSC) is the same from modelling perspective; however, this thesis mostly studies the LSC and pLSC devices. Therefore, small and large scale LSCs and pLSCs were critically reviewed. LSC technology is an economical approach to increase PCE through concentrating and converting solar radiation

spectrum into the wavelength band where the PV solar cells are more efficient. Their manufacturing process is straightforward due to simple structure and they are compatible with large-scale PV applications such as the façade of modern buildings. Their drawback however is associated with their loss mechanisms such as escape cone, re-absorption, attenuation and scattering losses which is magnified by increasing their geometric gain.

Host material in an ideal LSC must be highly transparent (95%-100%) to decrease attenuation and scattering losses. Using high-QY luminescent material boosts the flux of concentrated photons increasing OE. However, for achieving maximum PCE, emission band of the luminescent material should match PV spectral response and EQE. Doping concentration of luminescent material should be optimised. Although increasing the doping concentration increases the LSC absorption and emission rate, it boosts re-absorption losses. LSC losses are also characterised by its shape and size (geometric gain). Planar devices are more common than other shapes as they suggest low fabrication cost due to their simple structure. Increasing geometric gain and path-length in LSC increase re-absorption and thermal losses. Various luminescent materials and techniques have been proposed during recent years to increase QY and also overcome the re-absorption losses through Stokes-shift engineering. This resulted in achieving luminescent materials exhibiting near-unity QY and zero-re-absorption loss. All these recent breakthroughs have been along with introducing various LSC generations.

LSC-cavity, advanced pLSC and QD-based tandem LSC exhibit promising optical performance based on the reviewed devices. Among these, QD-based tandem LSCs offer a simple structure, acceptable PCE (~7%) and high compatibility with BIPV systems; however, LSC-cavity and pLSC provide higher PCE (up to ~77%). LSC-cavity cannot be considered as an option for (semi-)transparent BIPV systems but it can be used as an efficient non-transparent facade component. LSC-cavity and pLSC manufacturing process seem to be more complex than tandem LSC. Advanced pLSCs provide remarkable performance (~50% enhancement in PCE) and offer high compatibility with BIPV systems; however, their optimisation have found to be complex due to challenges in tuning the doping concentration of MNP. Evaluating the final development costs of different LSC generations would be also helpful to select the best LSC configuration for a particular application.

Modelling of LS devices was found crucial to optimize the device characteristics such as dimensions, luminescent materials and their doping concentration. Therefore, developing a fast

and precise ray tracing algorithm which can model all characteristics of the device and loss mechanisms, is an important step toward minimizing the time and cost of the fabrication procedure.

In pLS device modelling, the optical properties and plasmonic effect of coupled MNP must be investigated as well. The FDTD method was reported to be a robust, accurate, and straightforward method which has been extensively used to model and study the optical response of MNPs. However, the accuracy of FDTD modelling, its memory requirement and simulation time are all dependent on the Yee grid resolution. Therefore, FDTD requires optimization to decrease the computational cost.

The aforementioned modelling limitations and challenges are considered in model development in Chapter 3 (for ray tracing) and Chapter 4 (for FDTD) to improve their performance and accuracy. Both models need to be developed as their achievements are required in the final comprehensive algorithm to model pLS devices where MNP plasmonic optical properties are achieved through FDTD and used as inputs in a 3D ray tracing algorithm to model pLS device.

Chapter 3: Development of “Ray Tracer” 3D Model

The commercial ray tracing-based software which are available in the market cannot be used for modelling plasmonically enhanced luminescent solar (pLS) devices. As discussed in Chapter 2, the combination of both ray tracing and finite difference time domain (FDTD) algorithms can be used to achieve the optical properties and performance of pLS devices. This Chapter studies the development of a ray tracing algorithm from the scratch. Ray tracing algorithms are one of the most common methods for modelling optical devices including luminescent solar (LS) devices. However, as discussed in Section 2-3, one of the main challenges in the existing ray tracing models is accuracy.

To achieve more accurate results, LS devices are modelled in 3D using Monte Carlo ray tracing (MCRT) algorithm; where specification of the used materials including different loss mechanisms such as escape cone loss, reabsorption, reflection, attenuation and scattering are considered in the model. For this research a MCRT model has been developed as an interactive software (referred as “Ray Tracer”). Meanwhile, due to LS device development requirements, the program was developed with the ability to model and optimise both single and multi-layer LS devices.

In the developed Ray Tracer program, solar radiation is represented by photons (rays) and the designed MCRT algorithm determines the fate of each incident ray based on the probability of different optical procedures such as reflection, absorption, scattering, attenuation.

3.1. Ray Tracer Development

In this MCRT algorithm, the Monte Carlo method (Jacques and Wang, 1995, Joy, 1995, Şahin *et al.*, 2011, Şahin and Ilan, 2013) is used which has various applications in modelling of fluids, solids, optics and physics where the behaviour of the input parameters in problems are non-linear and have uncertainty. The inputs in these types of problems can be interpreted by probabilities and they cannot be solved by traditional mathematical methods. Monte Carlo has a statistical nature and the results are obtained by random sampling which make it an ideal method for LS device modelling.

MCRT simulation can be a complex, lengthy and time-consuming process. The time of the simulation is largely dependent on the number of incident photons, hence the number of iterations in the model. In previous studies such as (Roth, 1982, Bomm *et al.*, 2011, Rothemund, 2014), in order to reduce the complexity and computational cost of the MCRT model, loss mechanisms (such as scattering and attenuation) were not considered which resulted in reduced accuracy. However, in the developed Ray Tracer, loss mechanisms were included in the model. In addition, the advanced version of the developed program can model multi-layer devices comprising different layers of host and luminescent materials attached to each other. The developed Ray Tracer software interacts with the user through a Graphical User Interface (GUI) with two versions for modelling single layer devices (SLD) and multi-layer devices (MLD) which are referred as Ray Tracer-SLD and Ray Tracer-MLD respectively discussed in the following sections.

3.1.1. Development of Model for Single Layer Device (SLD)

Optical and physical procedures (including reflection, refraction, absorption, scattering, attenuation, wave-guiding and transmission) in LS devices explained in Chapter 1 and Section 2-1 in details. In summary, in ray tracing, each incident ray (with specific wavelength and angle of direction) is traced in LS device until its fate is detected. From a physical procedure perspective, the incident ray strikes the top plane of the luminescent solar device at the intersection point where it may be reflected or refracted. When refraction occurs, the ray may be attenuated or scattered by the host material. Furthermore, it may be (re-)absorbed by the luminescent material and (re-)emitted isotropically based on the value of the quantum yield (QY) and according to emission spectra of luminescent material both of which are either given by the manufacturer or measured experimentally. Otherwise, the ray is transmitted in the waveguide. During transmission, the behaviour of rays is described by the total internal reflection (TIR) phenomenon where the ray may strike internal boundaries and if its incident angle is less than the critical solid angle θ_c of the medium, it exits the device and is lost as escape cone loss.

Here, the algorithm of the model is focused and discussed. The algorithm flowchart of the developed Ray Tracer-SLD is shown in Fig. 3.1.

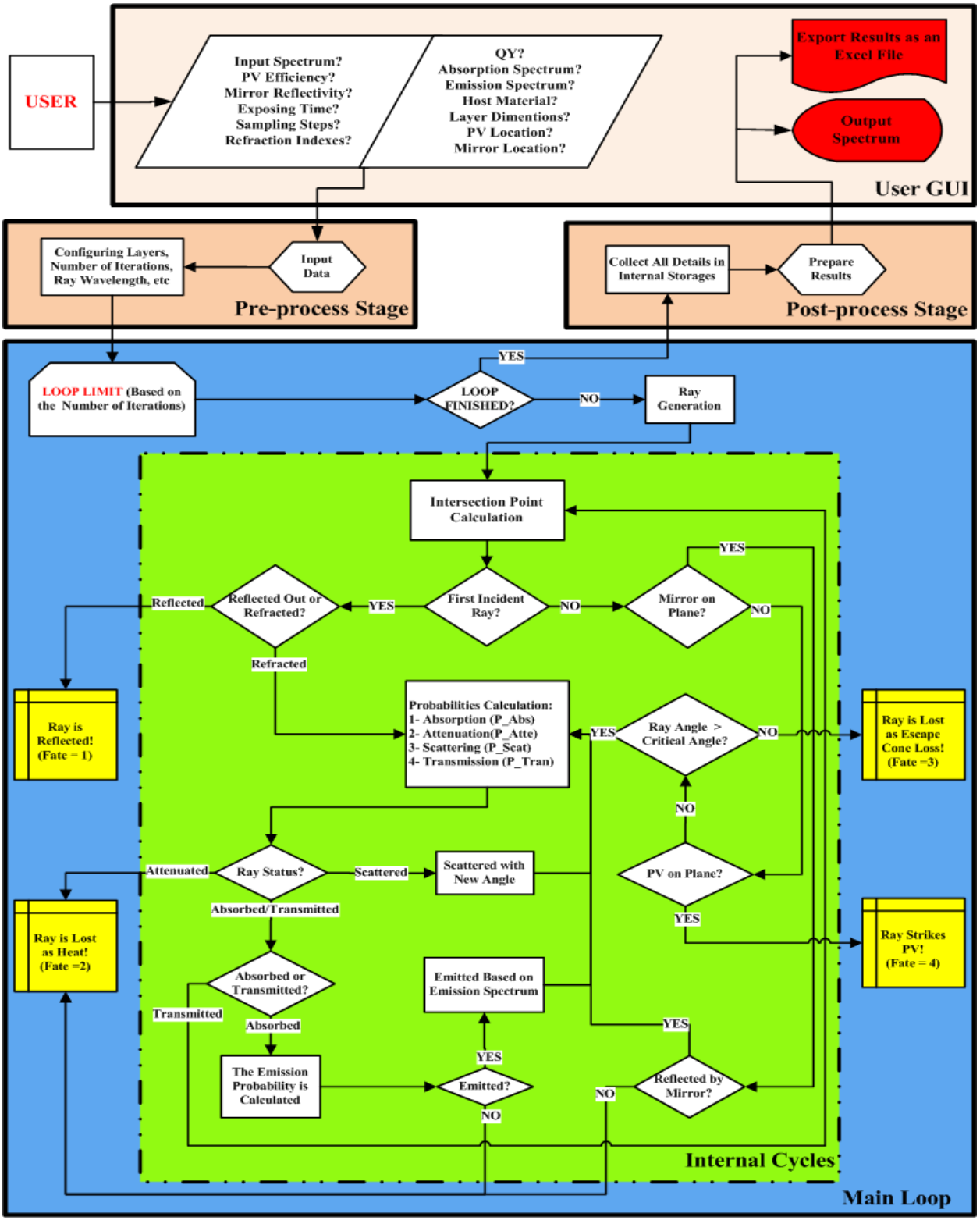

Fig. 3.1: Flowchart of the algorithm developed for Ray Tracer-SLD showing different stages of the program: "GUI", "Pre-Processing, "Post-Processing" and "Main Loop" including a internal cycles' loop

The algorithm was developed in MATLAB (MATLAB, 2017). As can be observed, the algorithm includes four main stages:

1- "Importing Input to GUI": interface used for Ray Tracer for inputs of LS configuration
2- "Pre-Processing": used to conFig. the device parameters which are defined by the user
3- "Main Loop": where the implementation of MCRT simulation takes place in several "Internal Cycles"
4- "Post-Processing": where the outcomes and spatial tracing data are collected.

In the "Importing" step of the algorithm, the user inputs the configuration of LS device. This includes solar radiation spectrum (such as global standard solar radiation spectrum (AM1.5G) (NREL, 2019)), refractive index (η) and device dimensions, type of host material, quantum yield (QY), absorption and emission spectra of the luminescent material.

Based on the configuration, the LS device is developed as a 3D structure through the Pre-Processing stage of the algorithm. Note that, the structure is modelled by different planes ($PL: [a_P \ b_P \ c_P \ DP]$) and boundaries in a 3D tracing-space. Moreover, the number of incident rays (which also determines the number of modelling iterations) is calculated using incident photon energy as in Eqn (3.1):

$$N_{Ray} = N_{Iteration} = \sum_{\lambda=\lambda_{min}}^{\lambda_{max}} \left(\frac{E_{P_{IN}}(\lambda)}{E_P(\lambda)} \right) \qquad Eqn\ (3.1)$$

The summation is implemented in the range of wavelength λ_{min} to λ_{max} , where $E_P(\lambda)$ is the energy in joules (J) of photon calculated by *Eqn* (2.7). $E_{P_{IN}}(\lambda)$ is the incident solar radiation energy (J) at wavelength of λ_i which is calculated by Eqn (3.2) using incident solar radiation power i.e. $P_{in}(\lambda)$ in W.m^{-2}.nm^{-1}:

$$E_{P_{IN}}(\lambda) = P_{in}(\lambda) \times A_{APR} \times \lambda \times t_{ex} \qquad Eqn\ (3.2)$$

Where t_{ex}(s) is the incident exposing time and A_{APR} (m^2) is area of LS device aperture where it receives the input solar radiation.

Afterwards, the algorithm enters the "Main Loop" (shown in the blue box, Fig. 3.1) where N_{Ray} Rays are generated and radiated on the top surface of the device. Each ray is defined by two parameters: wavelength (λ) and 3D ray vector (*I*). λ is extracted from the input solar radiation

spectrum. *I* is a normalized vector and its angle determined based on the type of the radiation spectrum (such as global standard solar radiation (AM1.5G) (NREL, 2019)). The main loop is iterated for each incident ray until their final fate (shown in the yellow boxes, Fig. 3.1) is detected.

The main loop includes a loop for the "Internal Cycles" (shown in the green box, Fig. 3.1) where the probability of optical procedures (such as reflection, absorption, scattering, attenuation and transmission) taking place in LS device is calculated. The allocated probabilities were defined based on the wavelength and angle of the incident ray, the host and luminescent materials, and configuration of the device as discussed in section 2-3. In the first internal cycle of the algorithm, the intersection point of the incident ray at the top surface of the luminescent device is calculated by *Eqn* (2.20) and *Eqn* (2.21) and using the "SOLVE" function in MATLAB (which is a function using symbolic variables to find the solution of the equation (MATLAB, 2017)). For the incoming incident ray, after the intersection point calculation, the probability of reflection and refraction are checked by Fresnel equation (Şahin and Ilan, 2013, Ishihara *et al.*, 2016). If $\eta_1 < \eta_2$, the probability of reflection is calculated by Eqn (3.3) to Eqn (3.5):

$$PR_r = \frac{PR_{r1} + PR_{r2}}{2} \qquad Eqn\ (3.3)$$

$$PR_{r1} = \left[\frac{\eta_1\ cos(\theta_1) - \eta_2\ cos(\theta_2)}{\eta_1\ cos(\theta_1) + \eta_2\ cos(\theta_2)}\right]^2 \qquad Eqn\ (3.4)$$

$$PR_{r2} = \left[\frac{\eta_1\ cos(\theta_2) - \eta_2\ cos(\theta_1)}{\eta_1\ cos(\theta_2) + \eta_2\ cos(\theta_1)}\right]^2 \qquad Eqn\ (3.5)$$

Where η_1 is the refraction index of the outside medium (such as air) and η_2 is the refraction index of the host material of the device. θ_1 is the angle of incident radiation and θ_2 is the angle of refraction. To apply each event based on its probability, a random number (*k)* is generated in the range of 0 - 1 and compared with the calculated PR_r value. If $k < PR_r$, the ray will be "Reflected" (Fate=1, Fig. 3.1), otherwise it will be refracted.

In the next internal cycle of the algorithm, if the ray is refracted, it may be scattered, attenuated by host material, absorbed by luminescent materials or transmitted. The probability of each optical procedure is calculated based on the wavelength and angle of each photon, as well as the dimensions of the device, host material attenuation and scattering coefficient , absorption and emission spectrum of the luminescent material using *Eqn* (2.26) to *Eqn* (2.30).

In the next internal cycle of the algorithm, if the ray label is "Attenuated" by the host material, it is "Lost as Heat" (Fate=2, Fig. 3.1). If the ray label is "Scattered", it will be scattered with a new angle and re-enter the algorithm process.

If the ray is "Absorbed" by the luminescent material in the next internal cycle of algorithm, the probability of emission is calculated using the QY of the luminescent material which is either given by the material manufacturer or measured experimentally. If the ray is not emitted, it is "Lost as Heat" (Fate=2, Fig. 3.1). Otherwise, it is emitted, and its new wavelength is determined by the weighted probability according to the emission spectrum of the luminescent material. Note that, the emission direction has been considered to be isotropic due to the nature of luminescent material; however, anisotropic emission can also be modelled if needed.

If the ray is "Transmitted" in the next internal cycle, the next intersection point of the ray with its new facing front plane is calculated. If there is a mirror on new plane, the ray is either reflected by the mirror based on its reflectivity or it is absorbed by the mirror and "Lost as Heat" (Fate=2, Fig. 3.1). If the plane is coupled to a PV cell, the ray "Strikes PV" (Fate=4, Fig. 3.1). In the absence of a mirror or PV cell, the angle of the ray (θ_i) is compared with value of the critical angle (θ_c). If $\theta_i \leq \theta_c$, the ray exits the device and "Lost as Escape Cone Loss" (Fate=3, Fig. 3.1); otherwise, the ray is reflected back into the device and is trapped and enters the algorithm process again.

In each step of the internal cycles' loop of the algorithm, spatial tracing data such as the wavelength, vector and position of the ray in the 3D tracing-space are stored in matrices as 3D parameters. After determining the fate of the ray, the outcomes for the ray are saved and the loop is iterated for the next incident ray. After finishing the main iterative loop, the detailed outcomes and the 3D spatial tracing data are entered into the Post-Processing stage where they are used to calculate the final detailed results including the total rate of the reflection, losses (such as heat and escape cone loss), output emission and energy spectrum, optical efficiency, solar concentration ratio, simulation time and current density of the PV. In the final stage, all the results enter the GUI and are shown to the user and exported as an excel file (shown in the red boxes in Fig. 3.1).The developed user-friendly GUI of this version of the program is presented in Fig. 3.2 in which the user can find a "Help" button for each section. The designed GUI includes three main panels of "Input Configuration", "Summary/Results" and "Graphs" which are described in Appendix 1.

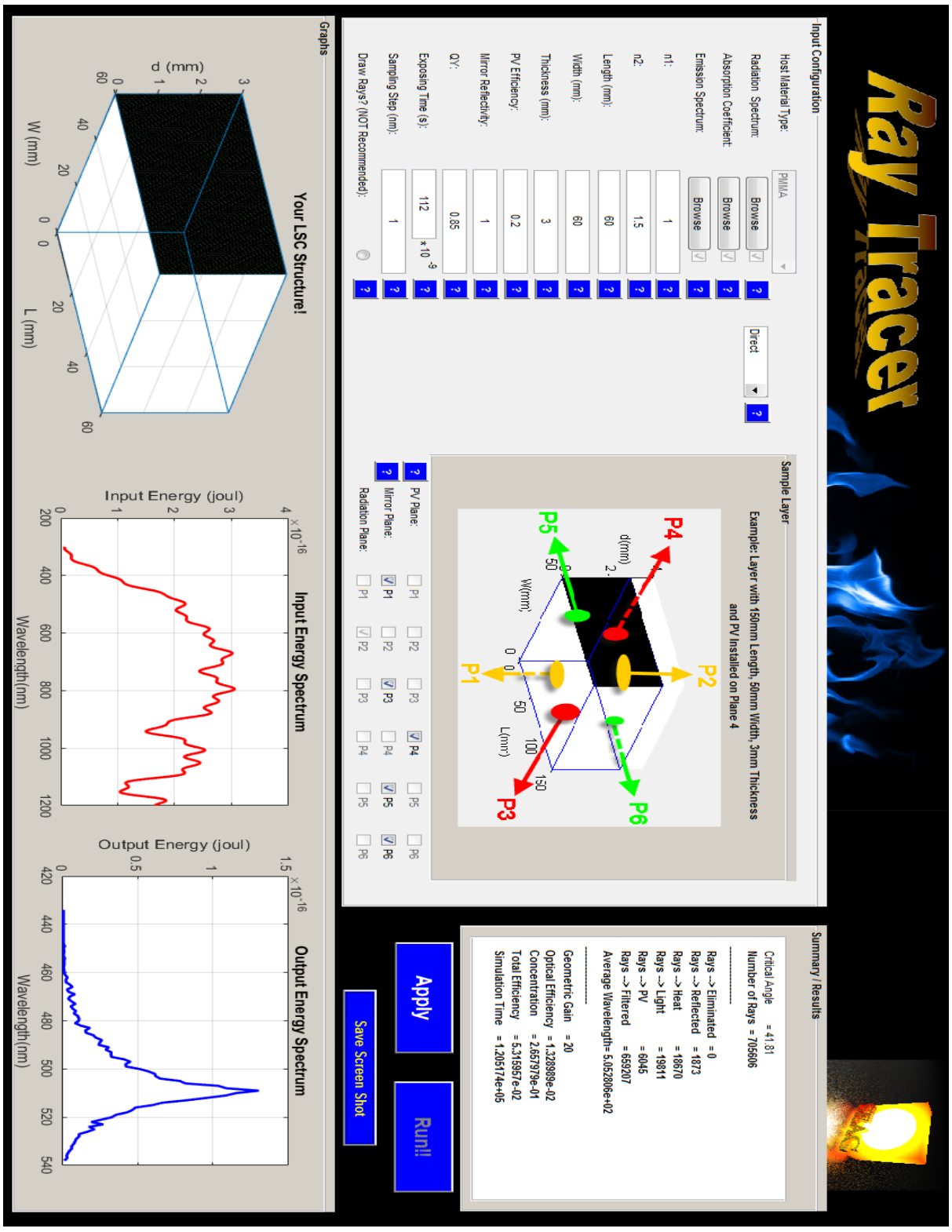

Fig. 3.2: Designed GUI for the developed Ray Tracer-SLD

3.1.2. Development of Model for Multi-Layer Device (MLD)

As it was reviewed and discussed in Section 2.1.1, multi-layer device (MLD) can be used to harvest broader band of solar radiation where each layer of LS device can absorb and waveguide a particular band of incident light. To model such structures, Ray Tracer-MLD was also developed.

In MLDs, the incident ray's fate is characterised by optical properties of luminescent species and host material of several layers coupled to one another. The ray incident angle is re-modified at boundary of intermediate layers based on their refraction indices and Snell's law. Therefore, although the main algorithm of the Ray Tracer-MLD and SLD were similar and the same optical procedures were implemented in each layer, there were some differences in the "Internal Cycles" of algorithm to model the optical interaction between each incident ray and intermediate layers which are detailed in Fig. 3.3.

As is seen, the behaviour of rays in the intermediate planes (reflection and refraction at the boundary of different intermediate layers) has been considered in this version to check whether the ray at the intersection point is a first-incident coming ray or the incident ray wave-guided from other layers of the LS device.

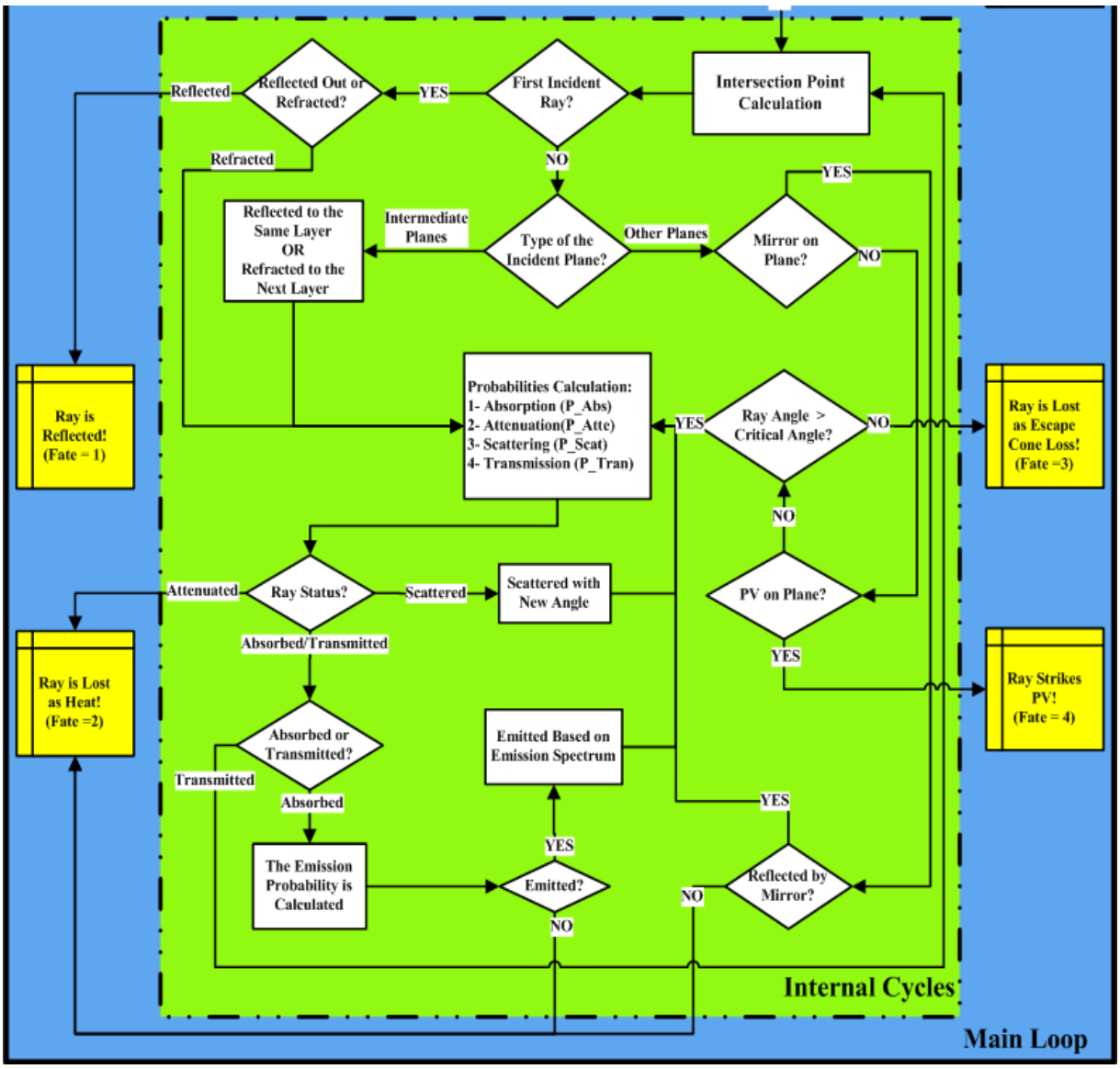

Fig. 3.3: Flowchart of the algorithm for Ray Tracer-MLD

The GUI of the Ray Tracer-MLD is shown in Fig. 3.4. As is seen, the user is able to configure several independent layers of multilayer devices. In addition, in this version, the range of the wavelength in the imported spectra can be defined by the user and it is not restricted to start from 300 to 1200 nm as in former SLD versions (See Appendix 1 for more details). Moreover, the user can define the measurement unit of the input spectrum. This is an important feature because the unit of the input spectrum is given in $W.m^{-2}.nm^{-1}$ in some experiments and more often is given as intensity of the solar radiation (number of photons).

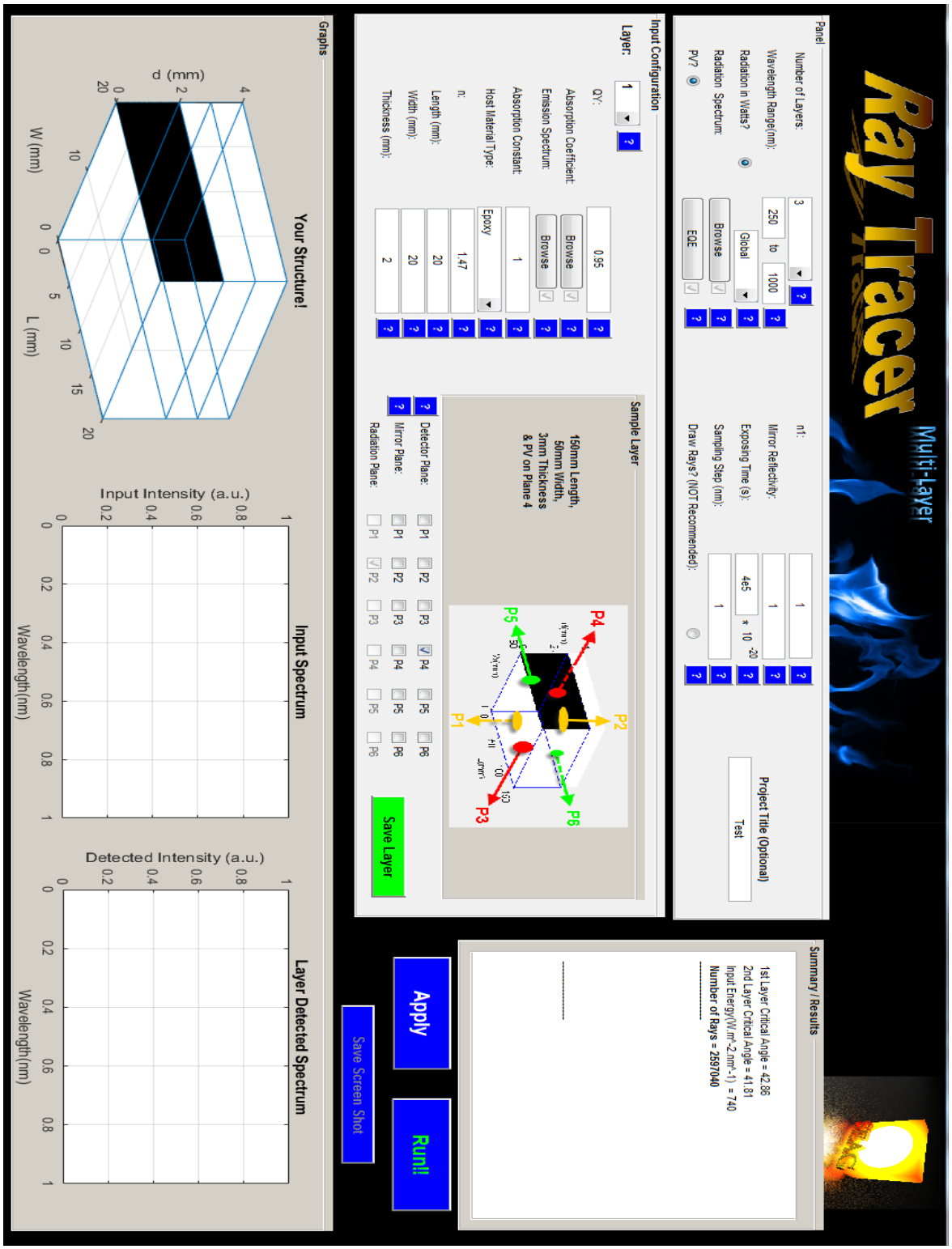

Fig. 3.4: GUI of the Ray Tracer-MLD while modelling a LSC with 3 independent layers

3.2. Ray Tracer Validation

3.2.1. Visualization of Model

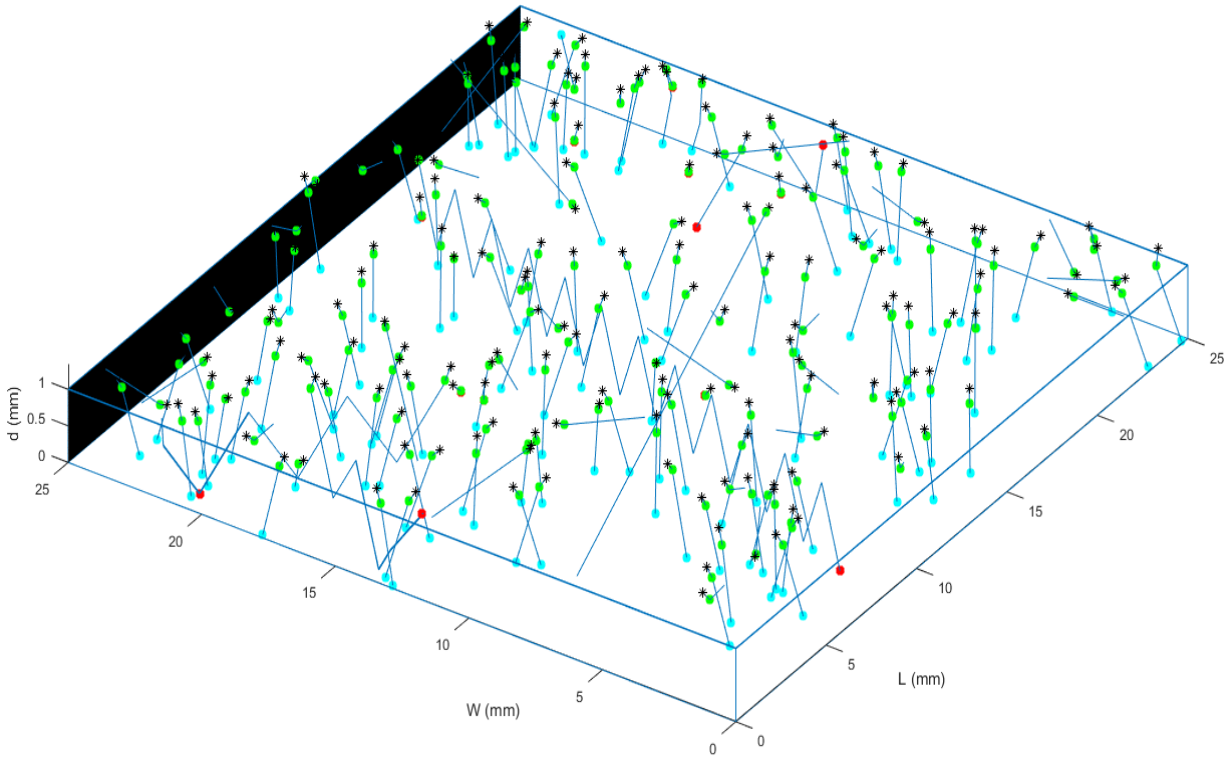

Fig. 3.5: Visual validation of Ray Tracer software under 160 rays: A 60 × 60 × 3 mm LSC device in a 3D tracing-space including a PV cell on one edge (black plane) and mirror on the other edges and bottom. The black spots show the light source, the green spots show the first intersection point of the input rays with the top plane. Red spots were the rays which were lost as heat due to the reabsorption or attention of the host material. The cyan spots illustrate the rays which were lost as the escape cone loss

The model behaviour was visually checked while running the model for 160 rays. This can be observed in Fig. 3.5 which shows colour-coded fates of each incident ray and various optical procedures taking place in a LSC of dimensions 25 × 25 × 1 mm. A PV solar cell (detector) is attached to one edges. The device was illuminated by AM1.5G solar radiation. The structures comprised epoxy resin as a host material doped with CdSe/Zns Green QDs with QY = 85 % (Kennedy *et al.*, 2008).

3.2.2. LS Device Modelling by Ray Tracer

Ray Tracer was used to model an LSC device (Rafiee *et al.*, 2017b) doped with Near-Infrared QDs (NIR-QD) (Rowan, 2007, Kennedy *et al.*, 2008, Kennedy *et al.*, 2009, Kennedy, 2010). The specifications of the LSC can be found in Table 3-1. A PV solar cell was attached to one of the edges and mirrors were attached to the other edges. Direct solar radiation (AM1.5D) shown in Fig. 3.6 was used as an incident spectrum. The emission and absorption spectra of the NIR QDs is shown in Fig. 3.7.

Table 3-1: Specifications of the LSC doped with NIR QDs (Rowan, 2007, Kennedy *et al.*, 2008, Kennedy *et al.*, 2009, Kennedy, 2010)

Radiation Type	AM1.5D
Host Material Type	Epoxy
η_1	1
η_2	1.5
Length(mm)	60 mm
Width(mm)	60 mm
Thickness(mm)	3 mm
Mirror Reflectivity	~1
QY	~0.85

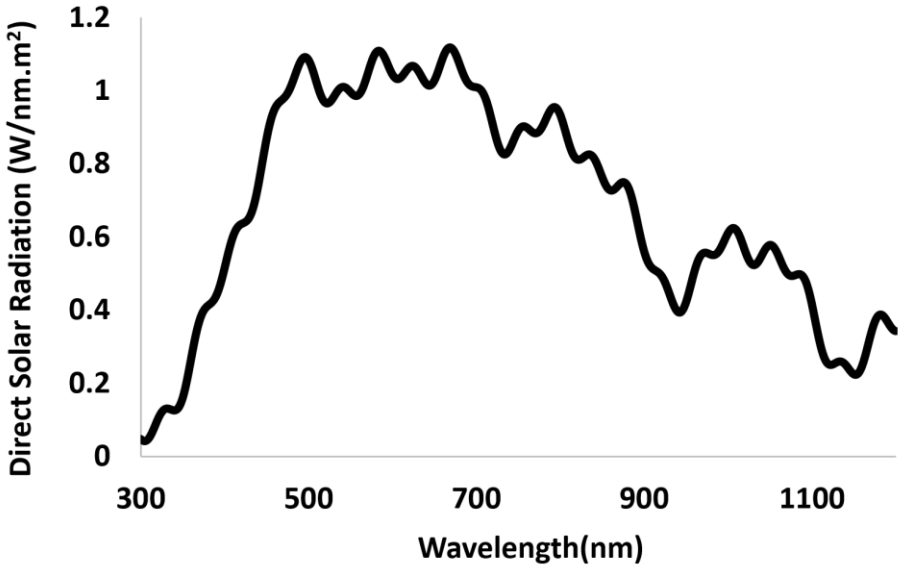

Fig. 3.6: Direct solar radiation (AM1.5D) (Rowan, 2007, Kennedy *et al.*, 2008, Kennedy *et al.*, 2009, Kennedy, 2010)

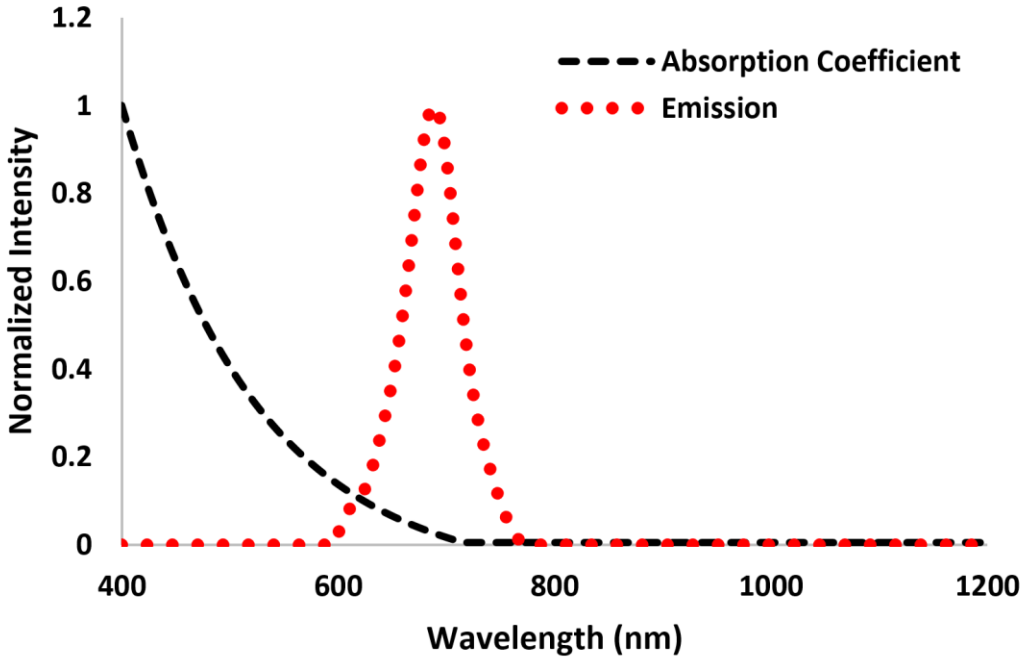

Fig. 3.7: Normalized absorption coefficient and emission spectra for NIR QD (Rowan, 2007, Kennedy *et al.*, 2008, Kennedy *et al.*, 2009, Kennedy, 2010)

The results of Ray Tracer and the comparison of the obtained optical efficiencies with the reference value are reported in Table 3-2. ~4% of the incident rays were reflected back from the

top surface of the device due to the difference in refraction indices between air and epoxy host material. The rest of the rays were refracted; however, ~8% was lost due to thermal losses including attenuation and reabsorption losses. ~81% of the rays exited the device as escape cone loss due to the reflection of the mirror at the bottom of the device. ~6.5% reached the PV cell at the edge. As was found, by increasing the number of rays (iterations), the obtained optical efficiency (OE = 7.47%) was closer to the reference OE (7.59%); however, increasing the iterations significantly increased the calculation costs and simulation time from 424,933s (~5 days) to 1,283,918s (~2 weeks).

Table 3-2: Comparison and validation of the results obtained by Ray Tracer and the reference result for an LSC with NIR QD

	Test 1	**Test 2**
Initial Number of Rays	125,989	261,392
Reflected Rays (%)	4.12	4.04
Refracted Rays (%)	95.88	95.96
Thermal Losses (%)	8.02	8.00
Exited the Device (%)	81.36	81.35
Rays Reached PV (%)	6.50	6.61
OE (%)	(Reference OE=7.59%) (Rowan, 2007, Kennedy *et al.*, 2008, Kennedy *et al.*, 2009, Kennedy, 2010)	
	7.33	7.47
Simulation Time (s)	424,933.3	1,283,918.1

3.3. Conclusion

Ray Tracer was developed as a 3D tool to model reflection, refraction, absorption, scattering, attenuation, wave-guiding and transmission in LS devices. This was undertaken through an algorithm which determined whether an incident ray striking the top plane is reflected or refracted based on the assigned probability governed by angle of the incident ray and refraction

index of host material. When refraction occurred, the ray was either attenuated or scattered by the host material based on the optical properties of host material such as attenuation and scattering profiles. Furthermore, it can be (re-)absorbed by the luminescent material and (re-)emitted at longer wavelength (based on the value of the QY) and according to emission spectra of luminescent material. Otherwise, the ray was transmitted in the waveguide through TIR process.

Two versions of the "Ray Tracer" were developed to model single and multilayer LS devices. All optical losses including reabsorption, non-unity QY, attenuation, scattering and escape cone losses were considered in the modelling resulting in ~98% validation accuracy overcoming the main challenges in the existing ray tracing models as it was discussed in Section 2-5. Validation was undertaken by comparing the modelling and experimental results. It was observed that by increasing the number of rays (number of iterations in the main loop) in the program, the simulation time increased; however, the modelling and experimental results were closer. The accurate model can be used to optimise LS devices before fabrication which can reduce the manufacturing costs.

To achieve more accurate results, details of 3D structure and specifications of LS device including different losses mechanisms must be considered in the model. In addition, since the algorithm is based on the probability of different optical processes for each incident ray, increasing the number of the rays (iterations) is required to improve the modelling accuracy. Moreover, the MCRT algorithm is complex and based on applying many calculations and conditional statements for each incident ray. All these requirements increase the simulation time of MCRT modelling which is another challenging issue. In Chapter 5, optimization approaches are introduced and validated to overcome this disadvantage of MCRT.

Chapter 4: Development of "Plasmon" 3D Model

In plasmonically enhanced luminescent solar (pLS) devices, the optical properties of metal nanoparticle (MNP) is also required to investigate the plasmonic interaction between luminescent material and MNP. Therefore, in addition to the ray tracing model (detailed in Chapter 3), the optical properties of MNP also needs to be modelled in pLSC. This is undertaken using the finite difference time domain (FDTD) method in this thesis. FDTD is chosen as it is one of the best methods to solve Maxwell's equations and obtain the optical properties of MNPs (as discussed in Section 2-4). In this research, an FDTD program; referred to as "Plasmon", has been developed to model periodical homogeneous structures doped with MNP in 3D Yee grid. Modelling accuracy can be enhanced by increasing FDTD grid resolution; however, the resolution and size of the grid are limited by the memory and computational requirements. Using conventional FDTD, the impact of this limitation was clearly observed in MNP plasmonic modelling where a relatively high grid resolution was required. To overcome this limitation, a 3D optimized FDTD (OFDTD) was developed which introduced new FDTD approximation terms based on the physical events occurring during the plasmonic oscillations of MNP. The validation of the developed FDTD and OFDTD methods were undertaken by comparing simulation and experimental results (Linden *et al.*, 2001, Ahmed, 2014) which were found to be in close agreement.

4.1. Development and Validation Based on Conventional FDTD Model

Before developing the OFDTD model and assessing its performance, a conventional FDTD model was developed based on FDTD algorithm discussed in Section 2.4.

A periodical MNP device (Linden *et al.*, 2001) was used in order to validate and compare the performance of the developed FDTD model. The device shown in Fig. 4.1a, was fabricated in different samples including ellipsoidal Au NPs on top of an indium tin oxide (ITO) coated glass substrate.

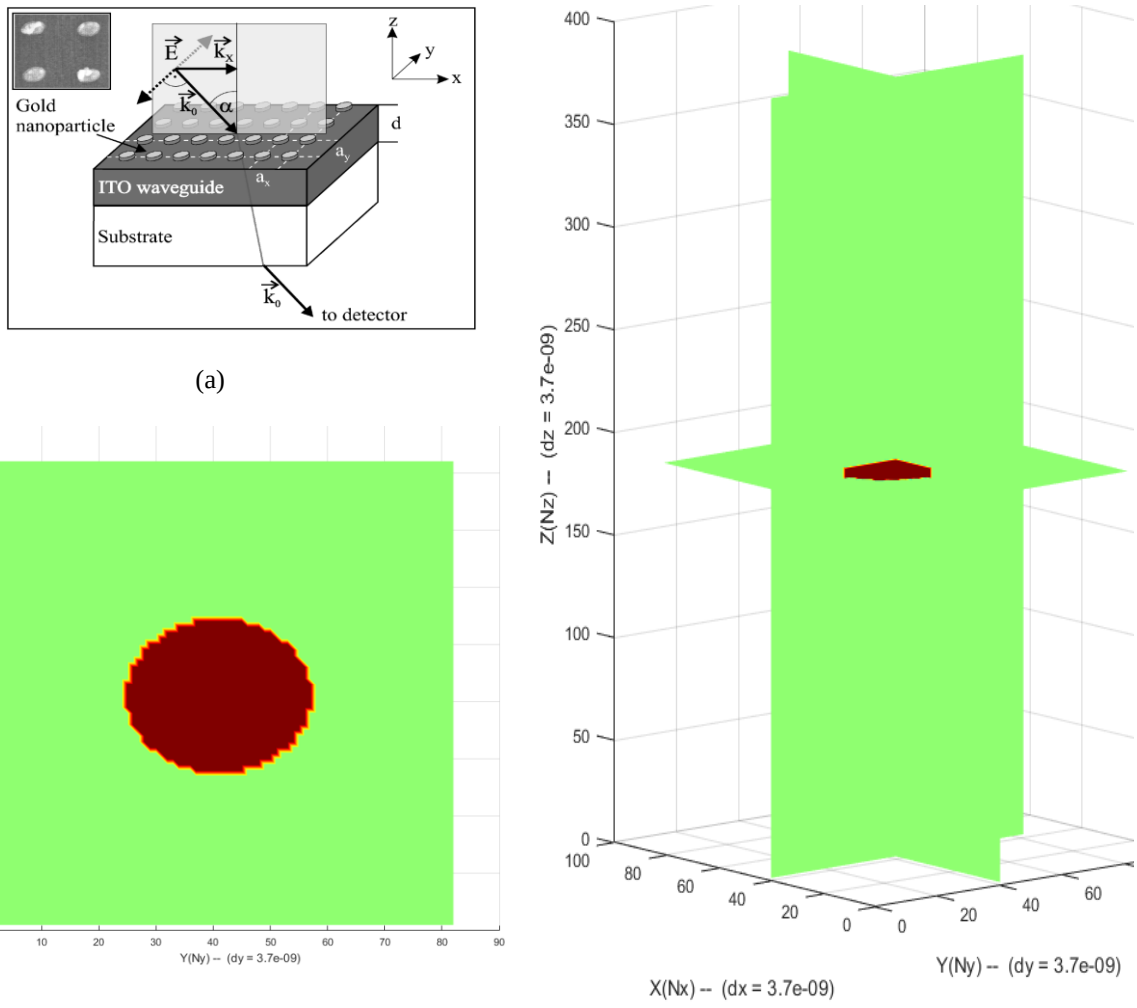

(a)

(b)

(c)

Fig. 4.1: (a) The periodical Au NP device (taken from (Linden *et al.*, 2001)). (b) Top view and (c) 3D view of the designed Yee grid model in Plasmon for the experimental sample with radius of 60 nm along the longer axis, 50nm along the shorter axis and height of 20 nm and the array's centre to centre distance of 300 nm in both x and y directions

Fig. 4.1b and c show the Au NP particle in a 3D FDTD Yee grid with grid discretization of 3.7 nm. The modelled Au NPs had a radius of 60 nm along the longer axis, 50 nm along the shorter axis, height of 20 nm with an array centre to centre distance of 300 nm in both x and y directions. The total grid size was 82 × 82 × 381 cells calculated by *Eqn* (2.49). The time step ($\Delta t = 7.13 \times 10^{-18}$s) was calculated using *Eqn* (2.50) based on the courant stability condition. The value of permittivity were 3.8, 2.1 and 1 for ITO, glass and air respectively. Since the device is periodic in x and y axis, the modelling of one particle was sufficient under well-designed boundary

conditions in all directions. Therefore, periodic boundary conditions (PBC) were defined in the x and y axis of the grid; while, absorbing boundary conditions (ABC) were defined at the z axis by placing a perfectly matched layer (PML) at both ends of the grid in z axis. PML length was designed so that it was able to absorb and terminate the total field striking the absorbing boundary and for this model was 50 cells (length = 185 nm).

To achieve the optical properties and frequency response of MNP under solar radiation, the device was illuminated by a gaussian electric field (with the frequency covering AM 1.5G solar radiation spectrum) which was injected as a plane wave and propagated in the z-direction while it was polarized along the x-y plane. Fig. 4.2 shows the sample under the simulation.

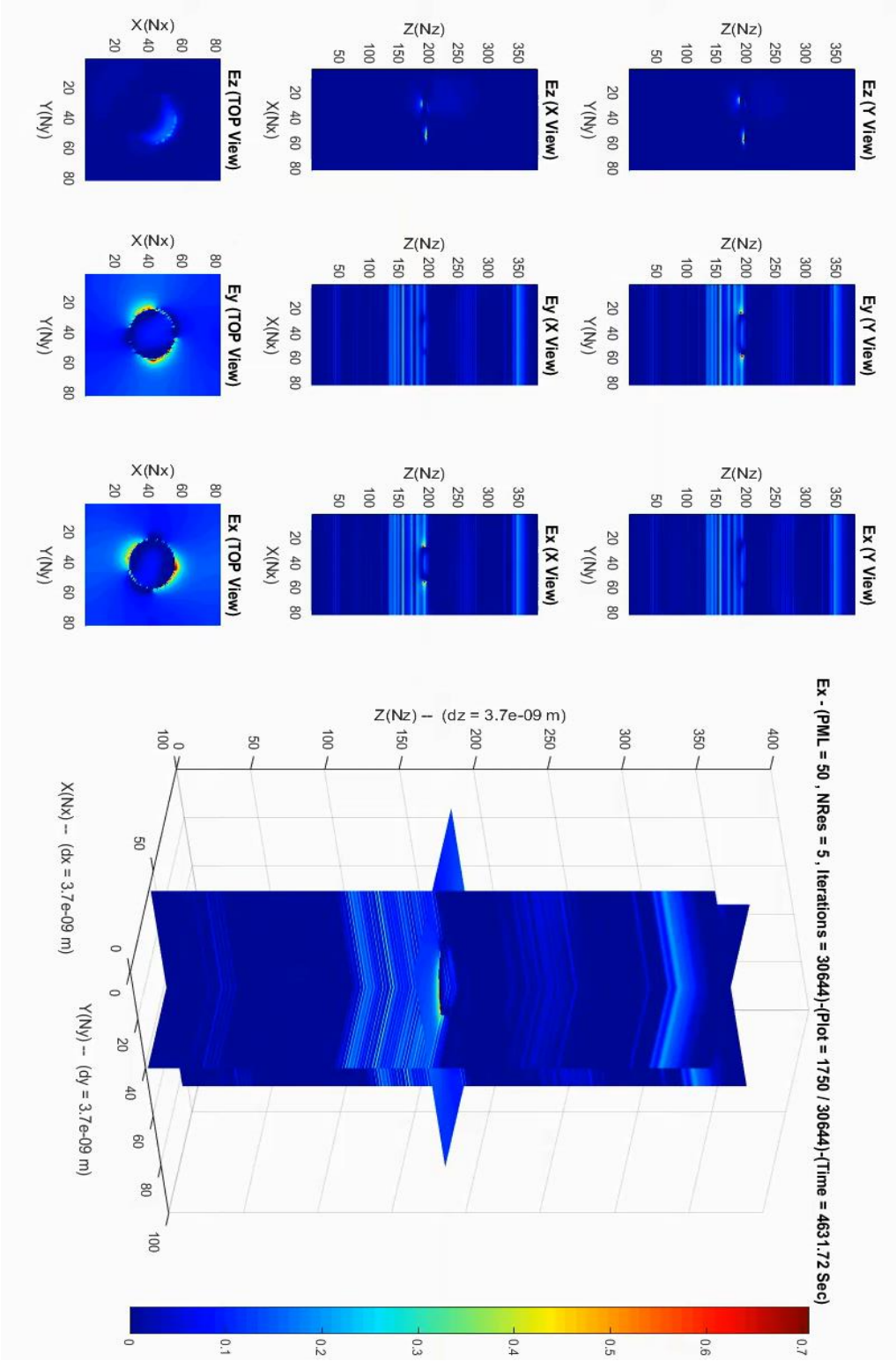

Fig. 4.2: Electric field distribution in the Yee grid of the sample while the “Plasmon” simulation is running

In each time step, the electric field was recorded at the top of the particle where the record plane was placed in the boundary of the study-space and the PML layer. After ending the FDTD main loop, the extinction spectrum of the device was achieved using fast Fourier transform (FFT) and the recorded time-domain electric fields.

Fig. 4.3 shows the normalized experimental extinction spectra for Au NPs sample and that obtained by the novel Plasmon model. The position of Surface Plasmon Resonance (SPR) energy (E_{SPR}) obtained by the model was 1.965 eV (630.97 nm) while it was reported as ~1.95 eV (635 nm) for the experimental sample which is in close agreement.

However, as is shown, the experimental and modelling extinction spectra did not completely overlap. Increasing FDTD grid resolution was required to compensate this and enhance the modelling accuracy, however, this increased modelling memory and calculation requirements. In the next section, a new algorithm is described which has been developed to solve this FDTD limitation.

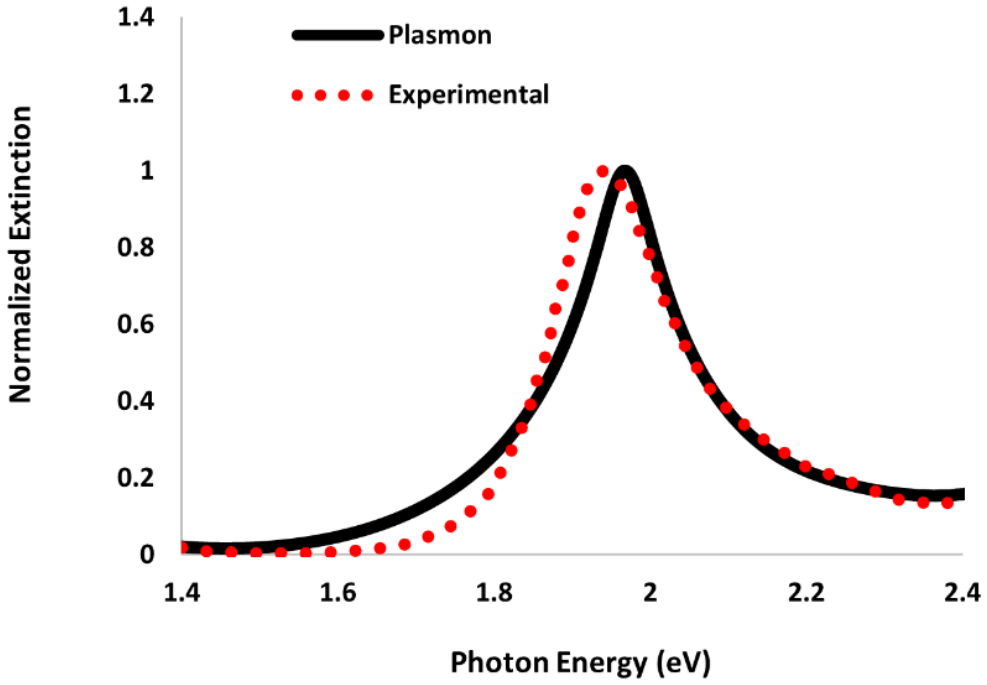

Fig. 4.3: Normalized extinction spectra resulted from the Plasmon model and the experimental sample

4.2. Development and Validation of a Cost-Effective Optimized 3D FDTD Method

All of the 3D FDTD terms including "*m*", "σ", "*I*", "*C*" , "*E*", "*H*", "*D*", "ε" and "μ" were defined as 3D matrices in *x, y* and *z* directions (see Chapter 2, Section 2-4 for more details). The size of the 3D matrices was equal to the size of the designed Yee grid which was expanded by increasing the resolution and/or the size of the modelled component. Conductivity ($\sigma(1/\Omega)$) was used to introduce the amount of losses inside the grid. By considering an isotropic medium in MNP, σ could be considered identical at all vectors of 3D grid. Therefore, in the matrix group of "σ", all terms for *H* and *D* fields in *x, y* and *z* could be same which is introduce here as $\sigma_{xyz}^{HD}|^{i,j,k}$ in Eqn (4.1):

$$\sigma_{xyz}^{HD}|^{i,j,k} = \sigma_x^H|^{i,j,k} = \sigma_y^H|^{i,j,k} = \sigma_z^H|^{i,j,k} = \sigma_x^D|^{i,j,k} = \sigma_y^D|^{i,j,k} = \sigma_z^D|^{i,j,k} \qquad Eqn\ (4.1)$$

The charge which was required to generate electric flux in the polarisation ($\overrightarrow{\mathrm{P}}$) of each grid cell was identical in all vectors. This resulted in an identical polarised damping rate (Γ_u) for each grid cell in all vectors. The Γ_u characterised the losses in MNP and determined the SPR oscillations and decay frequency in the polarised direction of MNP. For MNP, the permittivity and permeability of the metal can be treated as isotropic; therefore, the permittivity (ε terms) of each grid cell was considered to be identical in *x*, *y* and *z* in the polarisation of MNP. The polarised MNPs were considered to be aligned with *x*, *y* and *z* vectors as well. In addition, relative permeability (μ terms) is equal to 1 for MNPs in all vectors. Under the aforementioned conditions, $\varepsilon_{xyz}|^{i,j,k}$ and $\mu_{xyz}|^{i,j,k}$ 3D matrices were introduced as Eqn (4.2):

$$\varepsilon_{xyz}|^{i,j,k} = \varepsilon_{xx}|^{i,j,k} = \varepsilon_{yy}|^{i,j,k} = \varepsilon_{zz}|^{i,j,k}$$

$$\mu_{xyz}|^{i,j,k} = \mu_{xx}|^{i,j,k} = \mu_{yy}|^{i,j,k} = \mu_{zz}|^{i,j,k} \qquad Eqn\ (4.2)$$

And therefore, the primary $\tilde{\varepsilon}_r = \begin{bmatrix} \varepsilon_{xx}|^{i,j,k} & \varepsilon_{xy}|^{i,j,k} & \varepsilon_{xz}|^{i,j,k} \\ \varepsilon_{yx}|^{i,j,k} & \varepsilon_{yy}|^{i,j,k} & \varepsilon_{yz}|^{i,j,k} \\ \varepsilon_{zx}|^{i,j,k} & \varepsilon_{zy}|^{i,j,k} & \varepsilon_{z\square}|^{i,j,k} \end{bmatrix}$ and $\tilde{\mu}_r = \begin{bmatrix} \mu_{xx}|^{i,j,k} & \mu_{xy}|^{i,j,k} & \mu_{xz}|^{i,j,k} \\ \mu_{yx}|^{i,j,k} & \mu_{yy}|^{i,j,k} & \mu_{yz}|^{i,j,k} \\ \mu_{zx}|^{i,j,k} & \mu_{zy}|^{i,j,k} & \mu_{zz}|^{i,j,k} \end{bmatrix}$ for each grid cell can be optimised to Eqn (4.3):

$$\tilde{\varepsilon}_r = \begin{bmatrix} \varepsilon_{xyz}|^{i,j,k} & 0 & 0 \\ 0 & \varepsilon_{xyz}|^{i,j,k} & 0 \\ 0 & 0 & \varepsilon_{xyz}|^{i,j,k} \end{bmatrix}$$

$$\tilde{\mu}_r = \begin{bmatrix} \mu_{xyz}|^{i,j,k} & 0 & 0 \\ 0 & \mu_{xyz}|^{i,j,k} & 0 \\ 0 & 0 & \mu_{xyz}|^{i,j,k} \end{bmatrix} \qquad Eqn\ (4.3)$$

By applying these new terms, the primary FDTD updated coefficients (see Chapter 2, Section 2-4 for more details) were optimised and reduced to new terms for the OFDTD algorithm as presented in $Eqn\ (4.4)$ where Table 4-1 classifies the new OFDTD terms and the matrix groups:

$$m_{HDxyz0}|^{i,j,k} = m_{Hx0}|^{i,j,k} = m_{Hy0}|^{i,j,k} = m_{Hy0}|^{i,j,k} = m_{Dx0}|^{i,j,k} = m_{Dy0}|^{i,j,k} =$$

$$m_{Dz0}|^{i,j,k} = \frac{1}{\Delta t} + \sigma_{xyz}^{HD}|^{i,j,k}\left(\frac{1}{\varepsilon_0} + \frac{\sigma_{xyz}^{HD}|^{i,j,k}\Delta t}{4\varepsilon_0^2}\right)$$

$$m_{HDxyz1}|^{i,j,k} = m_{Hx1}|^{i,j,k} = m_{Hy1}|^{i,j,k} = m_{Hy1}|^{i,j,k} = m_{Dx1}|^{i,j,k} = m_{Dy1}|^{i,j,k} =$$

$$m_{Dz1}|^{i,j,k} = \frac{1}{m_{HDxyz0}|^{i,j,k}}\left[\frac{1}{\Delta t} - \sigma_{xyz}^{HD}|^{i,j,k}\left(\frac{1}{\varepsilon_0} + \frac{\sigma_{xyz}^{HD}|^{i,j,k}\Delta t}{4\varepsilon_0^2}\right)\right]$$

$$m_{Hxyz2}|^{i,j,k} = m_{Hx2}|^{i,j,k} = m_{Hy2}|^{i,j,k} = m_{Hy2}|^{i,j,k} = -\frac{1}{m_{HDxyz0}|^{i,j,k}}\frac{c_0}{\mu_{xyz}|^{i,j,k}}$$

$$m_{Hxyz3}|^{i,j,k} = m_{Hx3}|^{i,j,k} = m_{Hy3}|^{i,j,k} = m_{Hy3}|^{i,j,k} = -\frac{1}{m_{HDxyz0}|^{i,j,k}}\frac{c_0\Delta t}{\varepsilon_0}\frac{\sigma_{xyz}^{HD}|^{i,j,k}}{\mu_{xyz}|^{i,j,k}}$$

$$m_{HDxyz4}|^{i,j,k} = m_{Hx4}|^{i,j,k} = m_{Hy4}|^{i,j,k} = m_{Hy4}|^{i,j,k} = m_{Dx4}|^{i,j,k} = m_{Dy4}|^{i,j,k} =$$

$$m_{Dz4}|^{i,j,k} = -\frac{1}{m_{HDxyz0}|^{i,j,k}}\frac{\Delta t}{\varepsilon_0^2}\left(\sigma_{xyz}^{HD}|^{i,j,k}\right)^2$$

$$m_{Dxyz2}|^{i,j,k} = m_{Dx2}|^{i,j,k} = m_{Dy2}|^{i,j,k} = m_{Dz2}|^{i,j,k} = \frac{c_0}{m_{HDxyz0}|^{i,j,k}}$$

$$m_{Dxyz2}|^{i,j,k} = m_{Dx2}|^{i,j,k} = m_{Dy2}|^{i,j,k} = m_{Dz2}|^{i,j,k} = \frac{c_0}{m_{HDxyz0}|^{i,j,k}}$$

$$m_{Dxyz3}|^{i,j,k} = m_{Dx3}|^{i,j,k} = m_{Dy3}|^{i,j,k} = m_{Dz3}|^{i,j,k} = \frac{1}{m_{HDxyz0}|^{i,j,k}}\frac{c_0\Delta t}{\varepsilon_0}\,\sigma_{xyz}^{HD}|^{i,j,k}$$

$$m_{Exyz1}|^{i,j,k} = m_{Ex1}|^{i,j,k} = m_{Ey1}|^{i,j,k} = m_{Ez1}|^{i,j,k} = \frac{1}{\varepsilon_{xyz}|^{i,j,k}} \qquad Eqn\ (4.4)$$

Table 4-1: OFDTD terms and the matrix groups

I	Type of the Matrix Group	Equal Matrix Group	Alternative Matrix	Optimization Factor of Matrix Group (f_i^{OPT})	Memory Deduction (%) of Matrix Group (1-f_i^{OPT})×100
1	"σ" terms	$\sigma_x^H\|^{i,j,k}$, $\sigma_y^H\|^{i,j,k}$, $\sigma_z^H\|^{i,j,k}$ $\sigma_x^D\|^{i,j,k}$, $\sigma_y^D\|^{i,j,k}$, $\sigma_z^D\|^{i,j,k}$	$\sigma_{xyz}^{HD}\|^{i,j,k}$	$\frac{1}{6}$	84%
2	*H* and *D* update coefficient "*m0*" terms	$m_{Hx0}\|^{i,j,k}$, $m_{Hy0}\|^{i,j,k}$, $m_{Hz0}\|^{i,j,k}$, $m_{Dx0}\|^{i,j,k}$, $m_{Dy0}\|^{i,j,k}$, $m_{Dz0}\|^{i,j,k}$	$m_{HDxyz0}\|^{i,j,k}$	$\frac{1}{6}$	84%
3	*H* and *D* update coefficient "*m1*" terms	$m_{Hx1}\|^{i,j,k}$, $m_{Hy1}\|^{i,j,k}$, $m_{Hz1}\|^{i,j,k}$, $m_{Dx1}\|^{i,j,k}$, $m_{Dy1}\|^{i,j,k}$, $m_{Dz1}\|^{i,j,k}$	$m_{HDxyz1}\|^{i,j,k}$	$\frac{1}{6}$	84%
4	*H* update coefficient "*m2*" terms	$m_{Hx2}\|^{i,j,k}$, $m_{Hy2}\|^{i,j,k}$, $m_{Hz2}\|^{i,j,k}$	$m_{Hxyz2}\|^{i,j,k}$	$\frac{1}{3}$	67%
5	*H* update coefficient "*m3*" terms	$m_{Hx3}\|^{i,j,k}$, $m_{Hy3}\|^{i,j,k}$, $m_{Hz3}\|^{i,j,k}$	$m_{Hxyz3}\|^{i,j,k}$	$\frac{1}{3}$	67%
6	*H* and *D* update coefficient "*m4*" terms	$m_{Hx4}\|^{i,j,k}$, $m_{Hy4}\|^{i,j,k}$, $m_{Hz4}\|^{i,j,k}$, $m_{Dx4}\|^{i,j,k}$, $m_{Dy4}\|^{i,j,k}$, $m_{Dz4}\|^{i,j,k}$	$m_{HDxyz4}\|^{i,j,k}$	$\frac{1}{6}$	84%
7	*D* update coefficient "*m2*" terms	$m_{Dx2}\|^{i,j,k}$, $m_{Dy2}\|^{i,j,k}$, $m_{Dz2}\|^{i,j,k}$	$m_{Dxyz2}\|^{i,j,k}$	$\frac{1}{3}$	67%
8	*D* update coefficient "*m3*" terms	$m_{Dx3}\|^{i,j,k}$, $m_{Dy3}\|^{i,j,k}$, $m_{Dz3}\|^{i,j,k}$	$m_{Dxyz3}\|^{i,j,k}$	$\frac{1}{3}$	67%
9	*E* update coefficient "*m*" terms	$m_{Ex1}\|^{i,j,k}$, $m_{Ey1}\|^{i,j,k}$, $m_{Ez1}\|^{i,j,k}$	$m_{Exyz1}\|^{i,j,k}$	$\frac{1}{3}$	67%
10	"$\tilde{\varepsilon}_r$" terms	$\varepsilon_{xx}\|^{i,j,k}$, $\varepsilon_{yy}\|^{i,j,k}$, $\varepsilon_{zz}\|^{i,j,k}$	$\varepsilon_{xyz}\|^{i,j,k}$	$\frac{1}{3}$	67%

In the matrix group of "σ", FDTD terms for *H* and *D* fields in *x*, *y* and *z* were replaced with one single alternative 3D matrix ($\sigma_{xyz}^{HD}|^{i,j,k}$) in the OFDTD algorithm. This resulted in a reduction of 84% of the required memory for σ matrix group. For $\tilde{\varepsilon}_r$ matrix group, the three permittivity terms were replaced with a single 3D matrix ($\varepsilon_{xyz}|^{i,j,k}$) in OFDTD which led to ~67% deduction in the required memory for the relative permittivity group. The same optimisation process was applied for the updated coefficient matrix groups ("*m*" terms). For example, "*m0*" updated coefficients for *D* and *H* fields could be replaced with an alternative matrix, $m_{HDxyz0}|^{i,j,k}$, in OFDTD. This resulted in 84% reduction in the memory required for these matrix groups. Moreover, during the simulation process, the "*m0*" terms were calculated only once instead of six times (see Chapter 2, Section 2-4 for more details) which significantly reduced the computational (calculation) requirement.

The estimated rate of the total required memory which was deducted and saved using the OFDTD algorithm can be calculated by Eqn (4.5):

$$\Delta MEM_{Total} = \frac{MEM_{Total} - \sum_{i=1}^{M} f_i^{OPT} \times MEM_i}{MEM_{Total}} \times 100 \qquad Eqn\ (4.5)$$

Where MEM_{Total} is the total memory size which is used in the 3D FDTD algorithm, "*M*" is the total number of equal matrix groups (which is 10 here), "*i*" is the index of each matrix groups. MEM_i is the total memory size required for each matrix group. f_i^{OPT} is the optimization factor for the matrix group "*i*" which can be calculated by Eqn (4.6) using the total number of matrices in each matrix group (N_i^G):

$$f_i^{OPT} = \frac{1}{N_i^G} \qquad Eqn\ (4.6)$$

OFDTD requires less calculation costs in comparison with LSC (quantified by ΔMEM_{Total}). This allows MNP to be modelled with higher resolution of the Yee grid resulting in higher accuracy in the modelling outputs.

Experimental results (Ahmed *et al.*, 2016) were used to validate and compare the performance of the FDTD and OFDTD methods. Scanning electron microscopy (SEM) images of the fabricated sample using spherical Ag NPs (with diameter of ~50 nm) can be seen in Fig. 4.4a. Fig. 4.4b shows the modelled Ag NP in a 3D FDTD Yee grid where discretization was $\Delta d =$ 5.56 nm and the total grid size was 10×10×330. The time step was $\Delta t = 1.070 \times 10^{-17}$s. PBC

were defined at *x* and *y* axis; while, ABC were defined at *z* axis by placing PML at both ends of the grid in *z* axis. PML was designed using the field termination (loss) function obtained by $Eqn\ (4.7)$:

$$\sigma(z) = \frac{\varepsilon_0}{2\Delta t}\left(\frac{z}{L}\right)^3 \qquad Eqn\ (4.7)$$

Where Δt is the time step in second, L is the length of the PML in m and $\varepsilon_0 \approx 8.86 \times 10^{-12}$ F/m is free-space permittivity. The length of the PML (280 nm) was designed to absorb and terminate the total field striking the absorbing boundary.

Primary FDTD method was unable to run the simulation for higher resolution (i.e. grid with $\Delta d < 5$ nm) due to the memory limitations of the computer which caused the simulation to crash. However, the OFDTD was able to model the MNP with a resolution ($\Delta d = 0.877$ nm) ~7 times higher than FDTD as observed in Fig. 4-4-c. Under this circumstance, the total grid size was 62×62×1530 cells and time step was $\Delta t = 1.68 \times 10^{-18}$s.

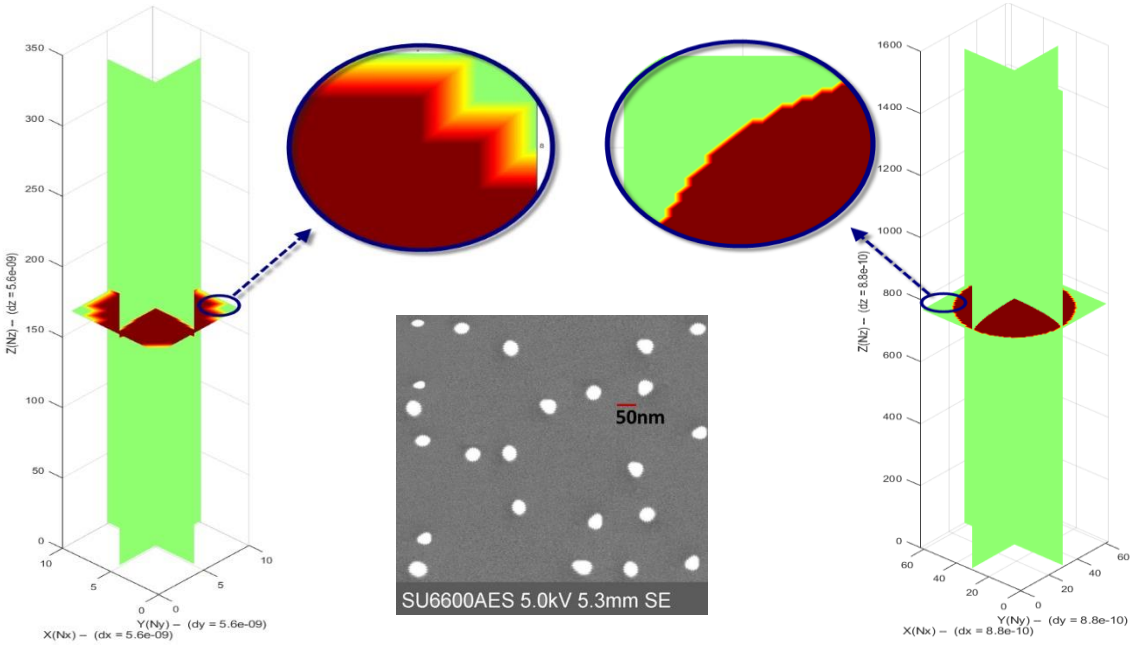

(b) (a) (c)

Fig. 4.4: (a) SEM image of synthesised 45 ± 5 nm Ag NP in water (Ahmed, 2014). (b) 3D cross-section view of a modelled Ag NP by the FDTD Yee grid discretization of 5.56 nm and total grid size of 28×28×330 and (c) by OFDTD Yee grid discretization of 0.877 nm and total grid size of 62×62×1530

Both FDTD and OFDTD models were implemented using MATLAB R2018b installed on a PC with Core i-5@3.30GHz CPU and 16GB RAM. The modelled samples were illuminated again by a gaussian electric field. In each time step, electric field was recorded at the top of the particle where the record plane was placed in the boundary of the study-space and PML layer. After terminating the irradiation and ending the FDTD main loop, the extinction spectrum of the Ag NP device was achieved using FFT and the recorded time-domain electric fields.

Fig. 4.5 shows the MNP under Plasmon simulation and Fig. 4.6 shows the normalized extinction spectra obtained by FDTD and OFDTD methods comparing with the experimental spectrum. As can be observed, the FDTD model result did not match with the reference data due to the low resolution (large Δd) of the model. SPR peak wavelengths (λ_{SPR}) obtained by FDTD model was at 455 nm while experimentally was reported at 435 nm. When it was obtained by the OFDTD with the same resolution ($\Delta d = 5.56$ nm), it was found to be at the same wavelengths of 455 nm. However, by increasing the resolution to $\Delta d = 0.877$ nm, the OFDTD model and the experimental results were found to be in close agreement (λ_{SPR} = ~435 nm).

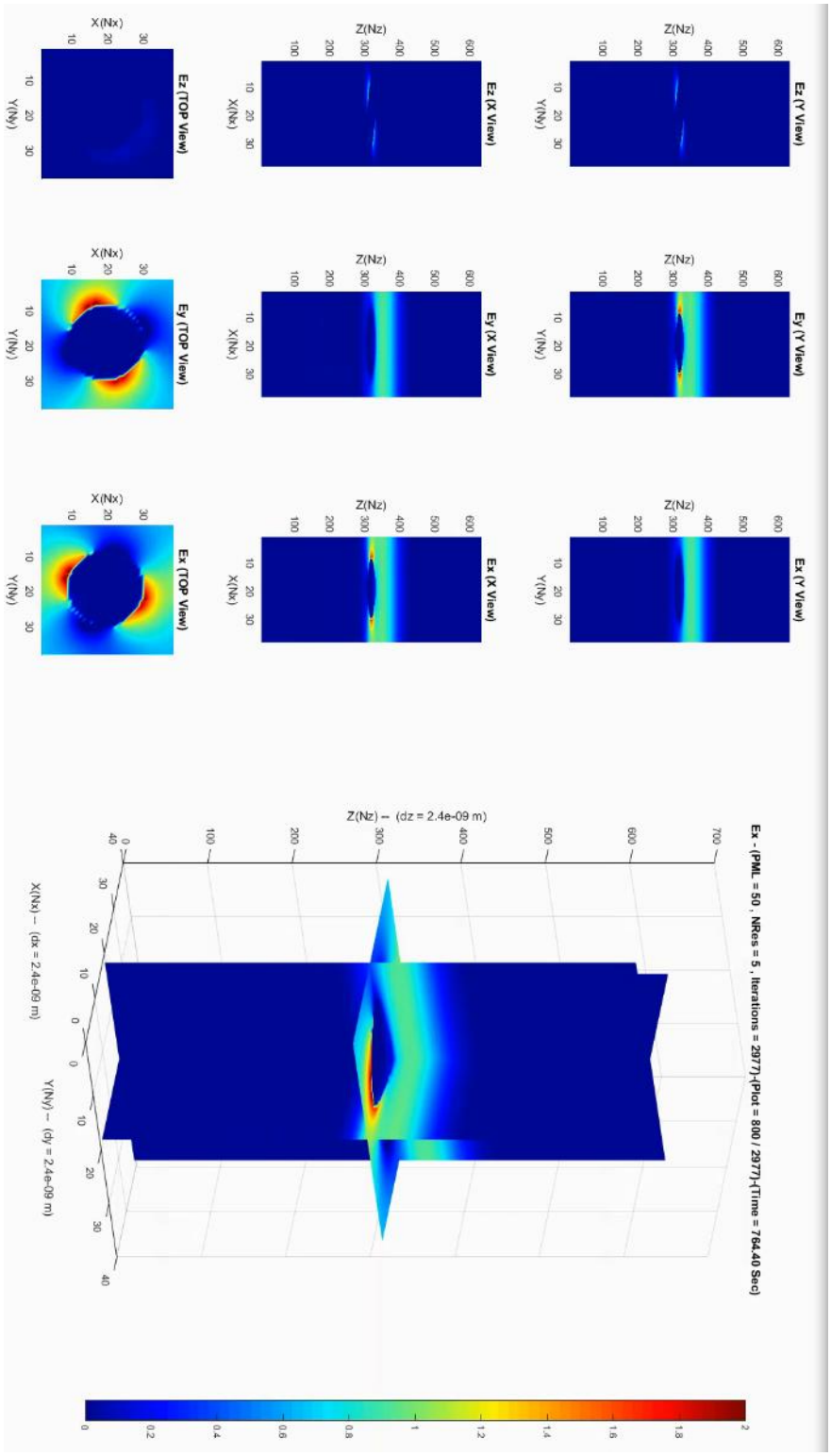

Fig. 4.5: 50 nm Ag NP under Plasmon simulation

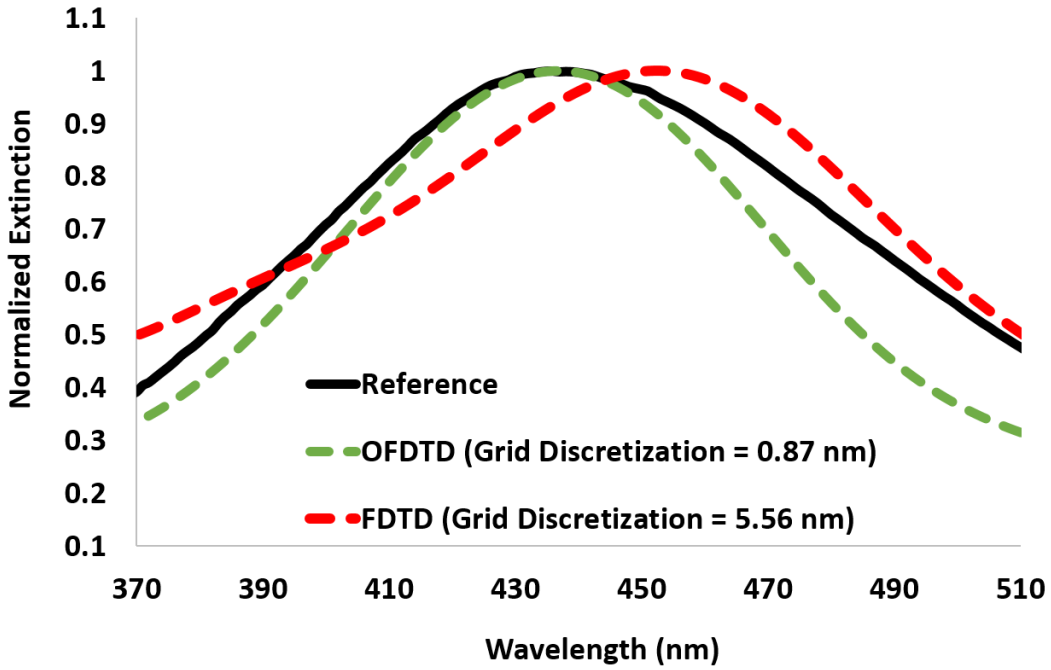

Fig. 4.6: Normalised extinction spectra: comparison of FDTD, OFDTD and reference results

Detailed and statistical modelling results are presented in Table 4-2. It can be observed that by decreasing the grid discretization from 5.56 nm to 0.877 nm, the number of iterations inside the main loop increased from 1505 to 2743 changing the simulation time. The results of FDTD and OFDTD models were the same at low resolution (5.56 nm); however, when a high resolution (0.877 nm) was used, the FDTD model crashed. Experimental results were closely matched to the OFDTD high-resolution results. Using OFDTD, the λ_{SPR} discrepancy was enhanced by 17 nm. It was observed that the total amount of memory consumed by OFDTD was ~52% less than the FDTD model. In addition, optimization steps used in OFDTD gave ~9 % reduction in the simulation time in comparison with FDTD.

Table 4-2: Comparison of statistical results obtained by FDTD, OFDTD and experimental results

$\Delta\lambda$ (nm)	**Low Resolution Condition**		**High Resolution Condition**	
	5.56		0.877	
Method	**FDTD**	**OFDTD**	**FDTD**	**OFDTD**
Total Yee Grid size ($X \times Y \times Z$)	10×10×330	10×10×330	Simulation Crashed Due to Lack of Memory (reaching 100% memory usage limitation point)	62×62×1530
Total Iterations of Main Loop (Simulation Time/Time Step)	1505	1505		2743
λ_{SPR}(nm) (Reference = 435)	455	455		438
λ_{SPR} Discrepancy (nm)	-20	-20		+3
Simulation Time (Hour)	0.74	0.67		121.85
Required Memory (%)	89	42		93
Deduction in Simulation Time When OFDTD was Used (%)	~ 9.4			
ΔMEM_{Total} When OFDTD was Used (%)	~ 52.8			

Although promising modelling results are obtained from OFDTD, it can be observed that OFDTD and experimental results are not completely matched. The reason of discrepancy between the experimental and modelling results may be due to the fact that Lorentz-Drude relative permittivity spectrum did not perfectly match the experimental data achieved by Johnson and Christy (Johnson and Christy, 1972, Rakić *et al.*, 1998) for Ag NPs. The best

approach to compensate this would be increasing the FDTD grid resolution. Moreover, MNPs were considered to have same shape and size in the model which were periodically distributed; however, in the experiment, the shape and size of particles were different and randomly distributed inside the device. In addition, MNP were modelled in cubic discrete grid cells; therefore, the curved edges might not be modelled perfectly and continuously.

4.3. Conclusion

The novel Plasmon model was developed based on 3D FDTD algorithm to model optical response of the MNPs. The model was run for homogeneous devices with a periodical structure. Although the FDTD method is an excellent numerical algorithm to solve Maxwell's equations, its memory demand, calculation costs and accuracy are dependent on the Yee grid properties of the modelled device. The impact of this on implementation is observed clearly for MNP modelling in which high grid resolution and precise modelling results are required. Here, by introducing the developed 3D OFDTD method, 3D parameters of the model, whose value were the same and/or constant, were detected based on the physical events occurring during the MNP plasmonic effect and SPR oscillations. The detected similar terms were then eliminated from the program and replaced with single alternative parameters. Thus, OFDTD has not only decreased the total memory requirement by ~52% but also decreased the modelling calculations by ~9%. The released memory was then allocated to increase the modelling Yee grid resolution which resulted in enhanced accuracy of the results. The performance of the developed FDTD and OFDTD methods were validated by comparing the simulation and experimental results of a sample with 50 nm spherical Ag NPs. The 3D FDTD could not get reasonable accuracy due to low grid resolution. However, the extinction spectrum and the position of SPR wavelength were in close agreement with the experiment results (~435 nm) when OFDTD modelled the device in high resolution.

Chapter 5: Development of "PEDAL" 3D Model

The performance improvement in plasmonically enhanced luminescent solar (pLS) devices is due to the plasmonic coupling of metal nanoparticle (MNP) and luminescent material (Chandra *et al.*, 2012, Chandra, 2013, El-Bashir *et al.*, 2013b, El-Bashir *et al.*, 2014, Ahmed *et al.*, 2017a, Geddes, 2017). This Chapter presents the proposed configuration and mathematical model for pLS devices. The mathematical model is used in development of the novel PEDAL program (named after PEDAL project: Plasmonic Enhancement and Directionality of Emission for Advanced Luminescent Solar Devices) which is a comprehensive modelling tool to simulate not only pLS device but also LS devices.

PEDAL is developed based on developed Ray Tracer program, the 3D Monte Carlo ray tracing (MCRT) algorithm. However, not only does it require the optical properties of host material and luminescent species as input parameters, but it also needs the optical properties of coupled MNP to be able to model pLS devices. MNP optical properties can be obtained through the optimised finite difference time domain (OFDTD) developed in Chapter 4. In PEDAL development, the limitations of ray tracing have been also improved by applying some optimisation techniques to the program. The developed model has been validated through three stages; (1) PEDAL was validated for LS device modelling; (2) a mathematical method was introduced and validated to convert MNP doping concentration unit from ppm (mg/L) to number of particle per litre (N/L) required in the PEDAL program; (3) PEDAL was validated for pLS devices by comparing the modelling and experimental results of nine samples where epoxy host material was doped with different concentrations of gold nanoparticles (Au NP) coupled with quantum dots (QD).

5.1. PEDAL Development

5.1.1. Proposed Configuration for pLS device

As discussed in Chapter 2, plasmonic enhancement in luminescent material-MNP coupling is controlled by photon density enhancement factor (PDEF) and emission quenching as parameters which are mainly governed by factors such as distance between MNP-luminescent

material, chemical interface damping and spectral overlap between the emission spectrum of luminescent material and absorption of MNP (Geddes, 2017).

Fig. 5.1 shows enhancement factor as a function of distance between luminescent molecule and MNP. In the far-field region where the distance in between two particles is more than ~50 nm (Region 3), the luminescent molecule is poorly affected by MNP because there is a weak interaction between the particles. In near-field region where the distance is ~20 nm to ~50 nm (Region 2), PDEF increases where radiative decay (Γ_{rM}) is dominant with respect to non-radiative decay (Γ_{nr}) of coupling (i.e. $\Gamma_{rM} > \Gamma_{nr}$). Within the distance of ~20 nm (Region 1), Γ_{nr} is dominant (i.e. $\Gamma_{nr} > \Gamma_{rM}$) which decreases PDEF due to the increase in non-radiative dissipation and emission quenching (Geddes, 2017).

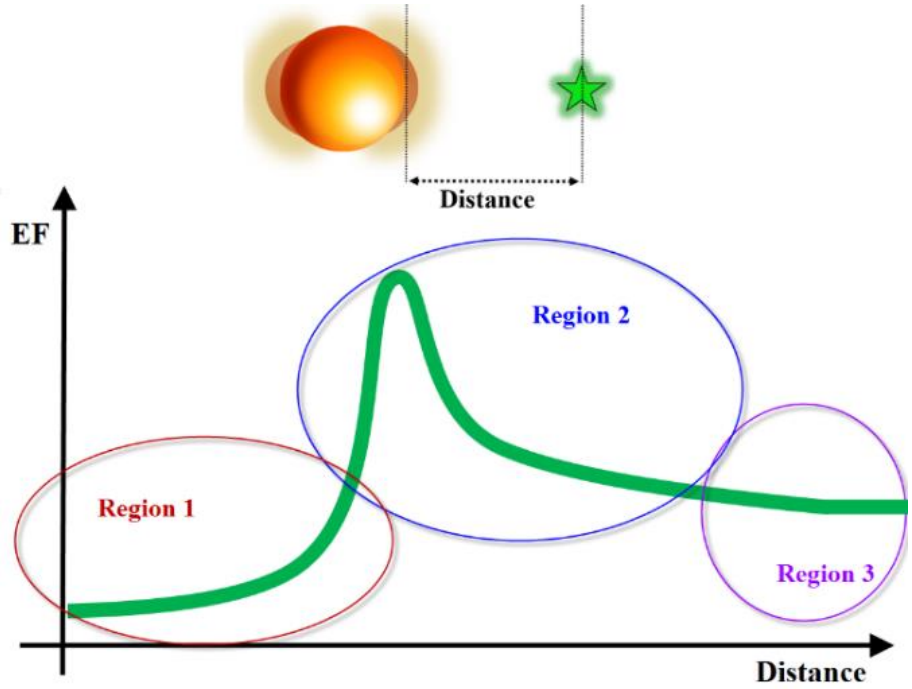

Fig. 5.1: Enhancement factor as the function of distance between luminescent molecule and MNP

Based on these interactions between MNP and luminescent material, the configurations for pLS devices including plasmonically enhanced luminescent solar concentrator (pLSC) and down shifting (pLDS) are proposed in Fig. 5.2. As is exhibited, almost the same optical processes (from a modelling point of view) occur in both pLS devices. The configurations were used to

develop the PEDAL mathematical model. The proposed model was then applied to each incident ray as can be seen in PEDAL schematic in Fig. 5.3.

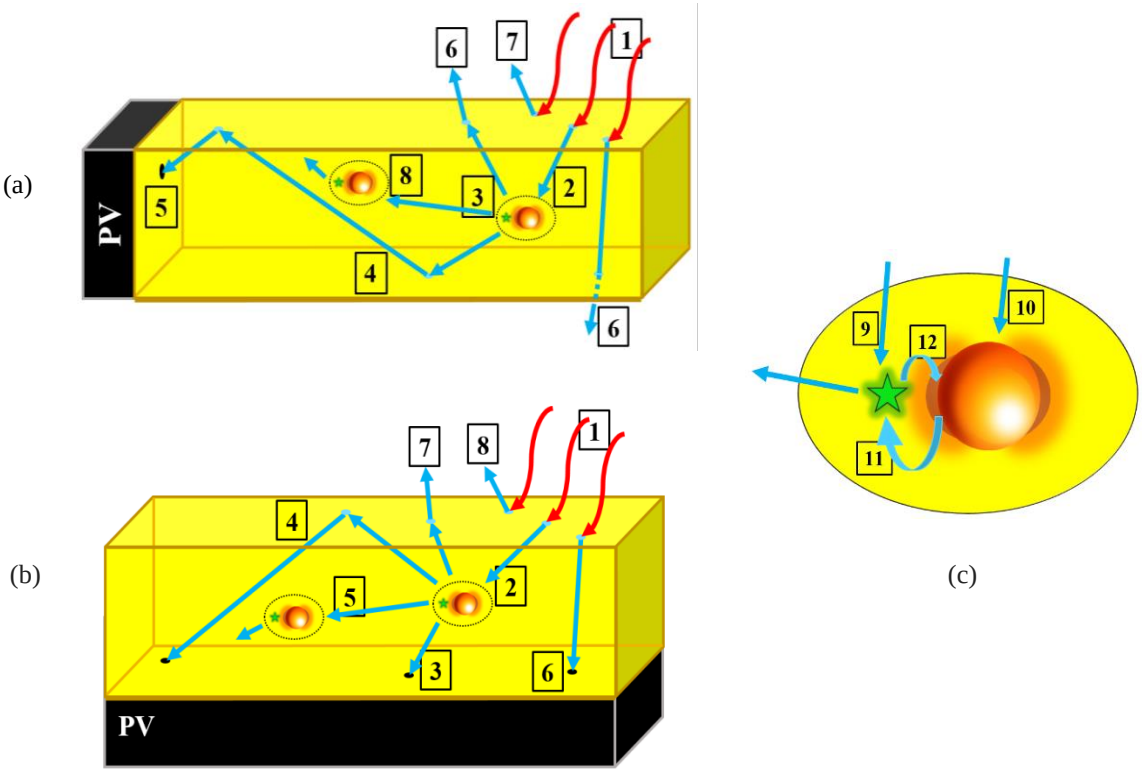

Fig. 5.2: Proposed configuration for pLS devices including: (a) pLSC device which shows: 1- incident photon strikes the pLSC, 2- absorbed by the coupled luminescent-MNP particles, 3- re-emitted at longer wavelengths, 4- wave-guided by total internal reflection (TIR), 5- reaches the PV cell at the edge of the device. Losses include: 6- front surface reflection, 7- escape cone loss and 8-emitted light which is reabsorbed by other particles. (b) pLDS device which shows: 1- incident photon strikes the pLDS, 2- absorbed by the coupled luminescent-MNP particles and emitted at longer wavelength. The emitted photon is either 3- reaches the PV cell directly or 4- it is wave-guided to the PV cell by TIR or 5- re-absorbed by other particles and re-emitted. 6- Some photons directly reach the PV cell without red-shifting. The losses include: 7- escape cone loss and 8- front surface reflection. (c) Procedures taking place in luminescent-MNP coupling: Based on the spectral overlap and properties of coupled luminescent-MNP, some photons are absorbed by 9- luminescent molecule or 10- MNP resulting in SPR generation energy and contributing in characterisation of excitation and emission efficiencies explained in introduction (11 and 12) and emitted based on PDEF and QF of the coupling. Note that, other loss mechanisms are not shown here including: photons scattered or attenuated by the host material, those lost due to multi-scattering of light with multi-MNPs and self-quenching of MNPs

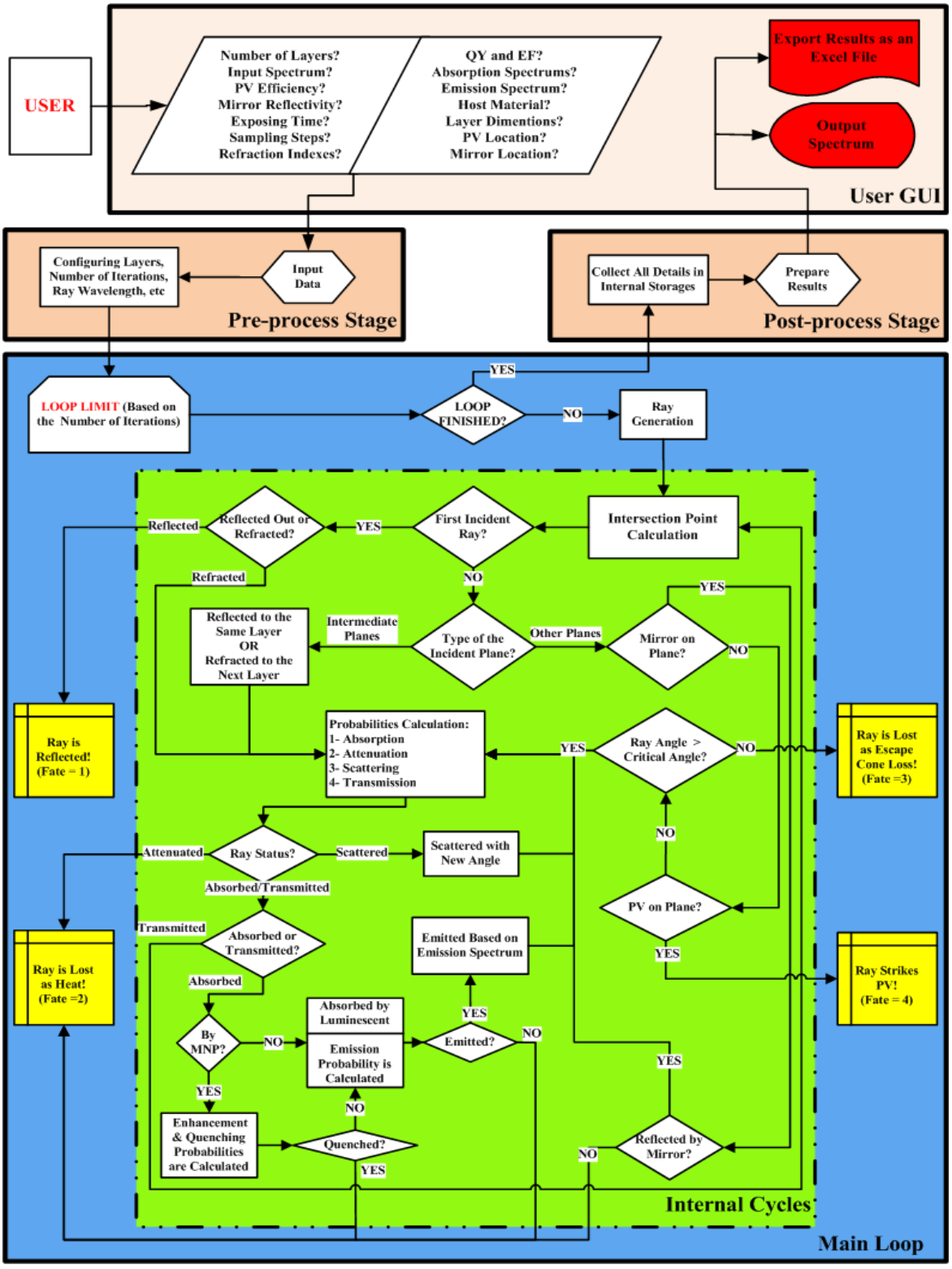

Fig. 5.3: Flowchart of the MCRT algorithm developed for PEDAL program showing different stages of the program: “GUI”, “Pre-Processing”, “Post-Processing” and “Main Loop” including internal cycles’ loop

5.1.2. Proposed Mathematical Model for pLS device

All physical and optical phenomena were included using separate mathematical functions based on their occurrence weighted probability (*PR*). As calculated by Eqn (5.1), some portion of the incident solar radiation power ($P_{in}(\lambda)$) is reflected from the top surface of the device ($P_{reflect}(\lambda, \theta_i, \eta_{out}, \eta_{host})$) while the rest is refracted:

$$P_{reflect}(\lambda, \theta_i, \eta_{out}, \eta_{host}) = PR_r(\theta_i, \eta_{out}, \eta_{host}) \times P_{in}(\lambda)$$

$$P_{refract}(\lambda, \theta_i, \eta_{out}, \eta_{host}) = [1 - PR_r(\theta_i, \eta_{out}, \eta_{host})] \times P_{in}(\lambda) \qquad Eqn\ (5.1)$$

Where $PR_r(\theta_i, \eta_{out}, \eta_{host})$ is the reflection probability of device as a function of incident angle (θ_i), refraction indices of the device host material (η_{host}) and the outer environment (η_{out}). For simplicity $P_{refract}(\lambda, \theta_i, \eta_{out}, \eta_{host})$ are denoted as $P_{refract}(\lambda)$.

Some part of $P_{refract}(\lambda)$ directly reaches the PV ($P_{direct}(\lambda)$) mounted to the device. The rest of the rays may be trapped ($P_{trap}(\lambda)$) and wave-guided inside the device. The non-trapped rays are lost as escape cone loss ($P_{cone}(\lambda)$) and exit the device.

Trapped rays can be (i) directly absorbed by luminescent material based on the absorbance spectrum of luminescent material ($PR^{L}_{abs}(\lambda)$); (ii) absorbed by the MNP ($PR^{MNP}_{abs}(\lambda)$) based on the extinction spectrum of the MNP generating SPR energy ($P_{SPR}(\lambda)$). SPR energy is then radiated to the coupled luminescent species based on the coupling PDEF as a function of distance between the MNP and luminescent material ($PR_{PDEF}(di)$) and absorbed by them. This is also governed by the quenching factor (QF) of the MNP-luminescent coupling ($PR_{QF}(di)$). Therefore, absorbed energy by luminescent material is given as Eqn (5.2):

$$P^{L}_{abs}(\lambda, di) = \begin{bmatrix} (P_{trap}(\lambda) \times PR^{L}_{abs}(\lambda)) \\ + \\ \left(P_{trap}(\lambda) \times PR^{MNP}_{abs}(\lambda) \times PR_{PDEF}(di) \times PR_{QF}(di)\right) \end{bmatrix}$$

$$= P_{trap}(\lambda) \times PR^{L}_{T.abs}(\lambda, di) \qquad Eqn\ (5.2)$$

Where, $PR^{L}_{T.abs}(\lambda, di)$ is the luminescent material total absorption probability for pLS devices. The total absorbed energy by the luminescent material in the device is obtained by Eqn (5.3):

$$P_{T.abs}^{L} = \sum_{\lambda=\lambda_{min}}^{\lambda_{max}} [P_{abs}^{L}(\lambda, di)] \qquad Eqn\ (5.3)$$

The summation is applied in the wavelength range of interest; i.e. λ_{min} to λ_{max}. The absorbed energy is emitted based on the emission spectrum ($PR_{emit}(\lambda)$) and QY of luminescent molecule (PR_{QY}) and written by Eqn (5.4):

$$P_{emit}(\lambda, di) = P_{abs}^{L}(\lambda, di) \times PR_{emit}(\lambda) \times PR_{QY} \qquad Eqn\ (5.4)$$

The rest of the absorbed energy is wasted as thermal loss through Eqn (5.5) due to non-unity QY:

$$P_{NQY}(\lambda, d) = P_{abs}^{L}(\lambda, d) \times \left(1 - PR_{QY}\right) \qquad Eqn\ (5.5)$$

The total energy emitted by the luminescent material in the device is obtained by Eqn (5.6):

$$P_{T.emit} = \sum_{\lambda=\lambda_{min}}^{\lambda_{max}} [P_{emit}(\lambda, di)] \qquad Eqn\ (5.6)$$

The non-absorbed and the emitted radiation are transmitted through total internal reflection (TIR) inside the device which can be written as Eqn (5.7):

$$P_{trans}(\lambda, di) = \left[P_{trap}(\lambda) \times (1 - PR_{T.abs}^{L}(\lambda, di))\right] + P_{emit}(\lambda, di)) \qquad Eqn\ (5.7)$$

$P_{trans}(\lambda, di)$ may be absorbed by other MNP-luminescent coupling or lost by other thermal loss mechanisms including reabsorption, host material attenuation and scattering losses. Reabsorption loss can be calculated as Eqn (5.8):

$$P_{re-abs}(\lambda, di, Dim) = P_{trans}(\lambda, di) \times PR_{re-abs}(\lambda, Dim) \qquad Eqn\ (5.8)$$

Host material attenuation and scattering losses are obtained by Eqn (5.9):

$$P_{atte}(\lambda, di, Dim) = P_{trans}(\lambda, di) \times PR_{atte}(\lambda, Dim)$$

$$P_{scat}(\lambda, di, Dim) = P_{trans}(\lambda, di) \times PR_{scat}(\lambda, Dim) \qquad Eqn\ (5.9)$$

As can be observed, the probabilities of all loss mechanisms are also a function of the device dimension including its size and shape *(Dim)*. Moreover, reabsorption ($PR_{re-abs}(\lambda, Dim)$) depends on the stokes-shift between the absorption and emission spectra of luminescent material. Attenuation ($PR_{atte}(\lambda, Dim)$) and scattering ($PR_{scat}(\lambda, Dim)$) are characterized by

the optical properties of host material which can be obtained experimentally using a spectrometer. The total thermal loss $P_{lost}(\lambda, di, Dim)$ of device includes reabsorption, escape cone, attenuation and scattering losses. Therefore, total output energy reaching the PV written is as in Eqn (5.10):

$$P_{out}(\lambda, di, Dim) = [P_{trans}(\lambda, di) - P_{lost}(\lambda, di, Dim)] + P_{direct}(\lambda) \qquad Eqn\ (5.10)$$

Output energy ($P_{out}(\lambda, di, Dim)$) is a function of many complex, nonlinear and uncertain parameters characterised by non-linear optical properties of pLS devices. This is the reason why it cannot be estimated by conventional mathematical methods and MCRT algorithm is required.

The developed graphical user interface (GUI) of PEDAL is presented in Fig. 5.4 in which the user is able to import the input parameters and use "Help" button for filling each section. As can be observed, the designed GUI includes four main sections including "Panel", "Input Configuration", "Summary/Results" and "Graphs" which are described in Appendix 2.

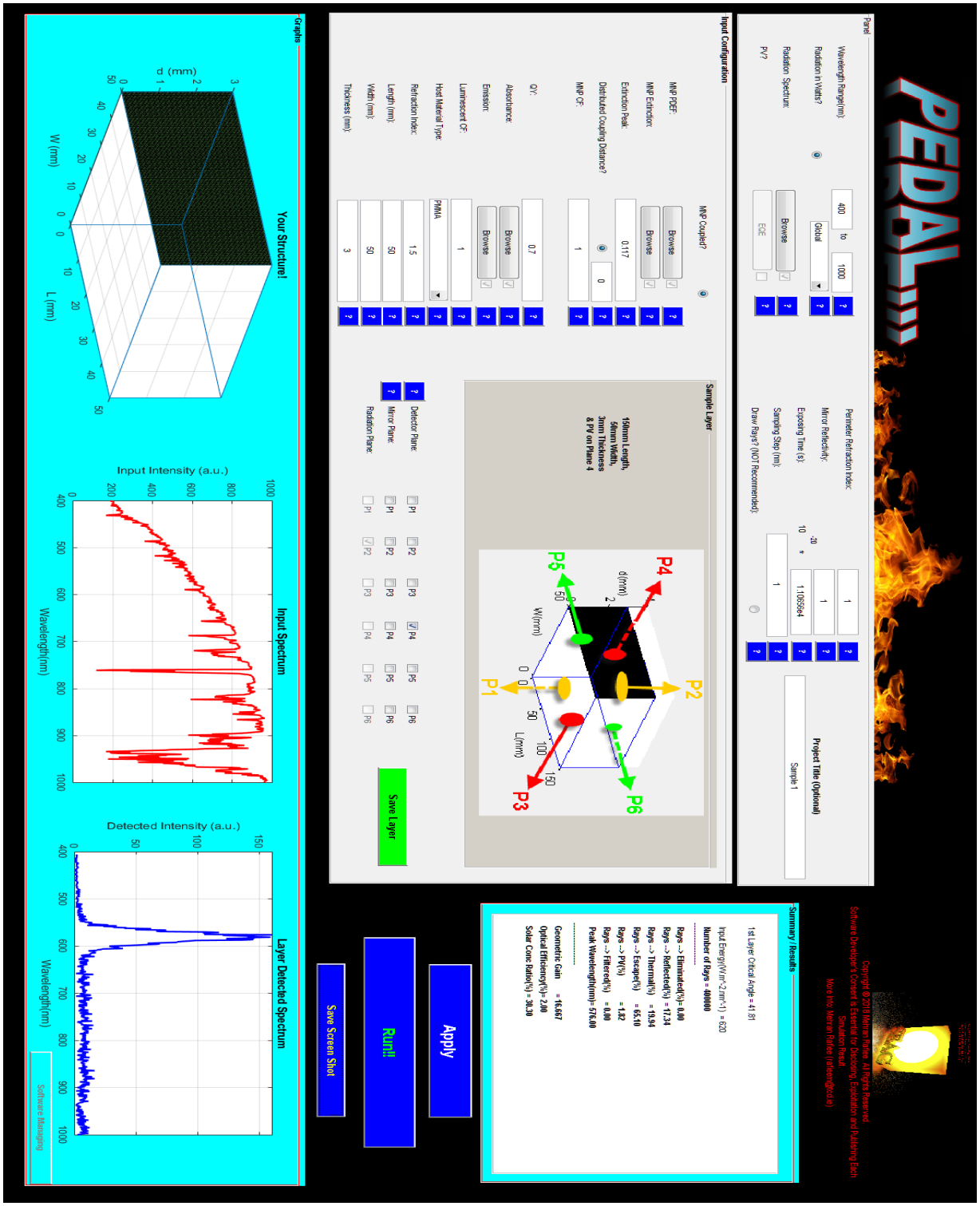

Fig. 5.4: GUI for the novel PEDAL program which can be used for modelling both pLS devices and LS devices

5.2. Enhancing PEDAL Accuracy and Performance

As concluded in Chapter 3, MCRT algorithm is based on applying complex calculations and conditional statements which require long simulation times to achieve reasonable accuracy for LS devices. MCRT algorithm used in PEDAL is more complex than Ray Tracer due to the non-linear functions related to MNP-luminescent plasmonic coupling. Therefore, the simulation time in PEDAL is relatively longer than Ray Tracer depending on the structure and configuration of pLS device. In this section, two approaches are introduced to develop the optimized versions of PEDAL to enhance modelling performance and reduce simulation time:

5.2.1. Modelling pLS Device using an Adaptive Filter Approach

One method was to reduce the number of rays which decreases the number of iterations, hence the simulation time (Roth, 1982, Hall and Greenberg, 1983, Kajiya, 1986, Whitted, 2005). For this, an adaptive filter (AFI) is added to PEDAL algorithm as illustrated in Fig. 5.5, shown in the black box was placed after "Pre-Processing" and before starting the "Main Loop". The filter was designed to decrease the number of iterations without reducing the number of rays incident on the device. For each incident ray, the filter prioritised the optical process (event) such as reflection, absorption, scattering and attenuation based on its probability. A dominant factor, f_{d_K}, was defined (in the range 0 - 1) based on the priority of the *Kth* event for the incident ray so that the event with highest probability was considered dominant. For a single ray, if $f_{\mathrm{d_K}} \approx 1$ for one of the energy loss events such as attenuation and it had a small value (≈ 0) for the other optical processes; then, attenuation event was considered as the final fate of that ray. The fate of this ray would be labelled as "Lost (Filtered)". Therefore, the fate of the ray was foreseen without running waveguiding process (before starting the internal cycles, Fig. 5.5) and there was no need to consume time and run the loop for the ray. This proposed technique decreased the number of iterations and calculations; and accordingly, reduced the simulation time.

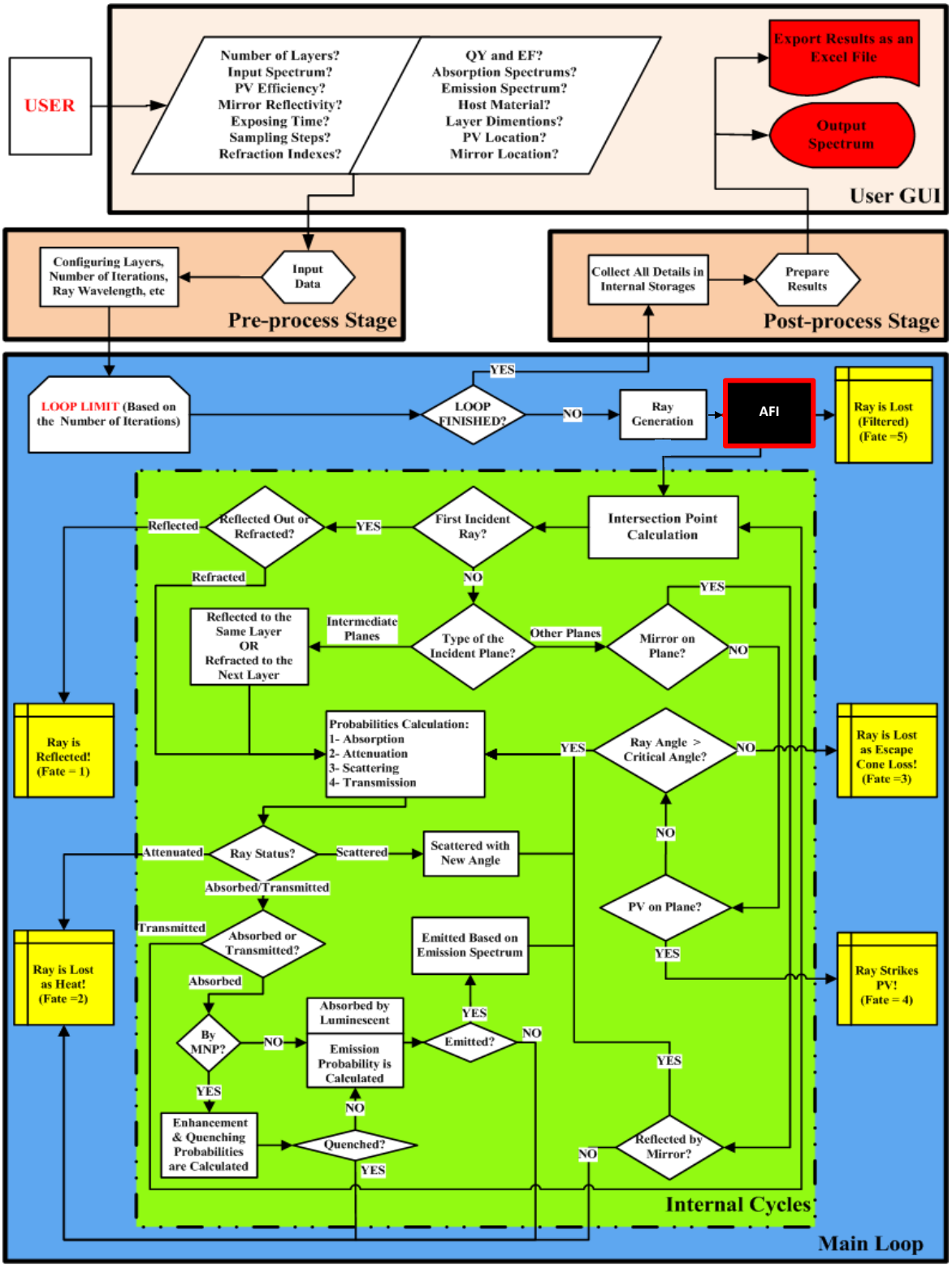

Fig. 5.5: PEDAL flowchart optimised by AFI approach

For example, the attenuation coefficient (α_{Atte}) of epoxy resin (Kennedy, 2010) is high below 300 nm as is shown in Fig. 5.6. Thus, the probability of attenuation (PR_{atte}) of rays with wavelengths below 300 nm is calculated very high. Hence, attenuation is the dominant event and is the fate for these rays (with $f_{d_{Atte}} \approx 1$). For other events, f_{d_K} can be considered as zero ($f_{d_{Abs}} = f_{d_{Trans}} = f_{d_{Scat}} = 0$). Therefore, the fate of the ray simply is foreseen without running the rest of the processes.

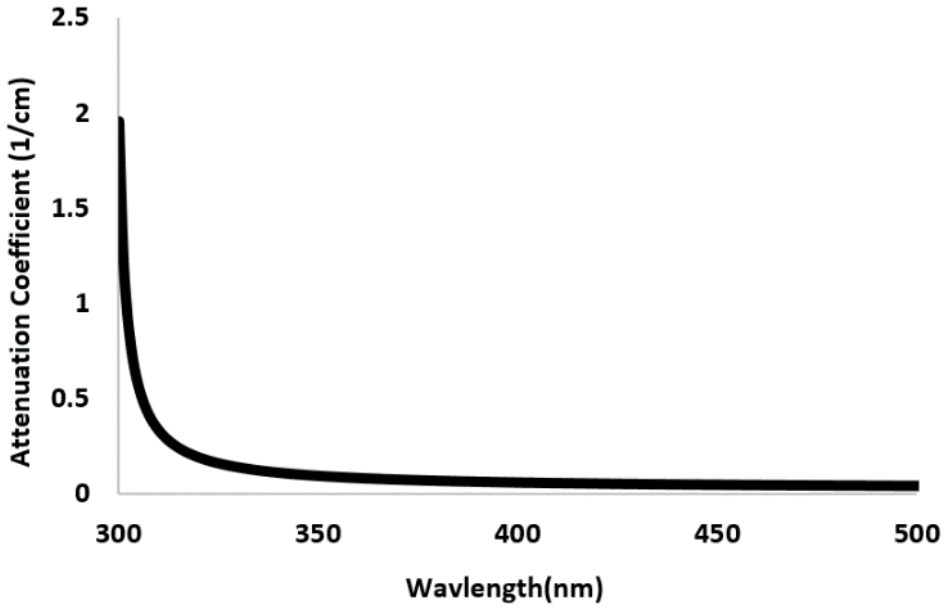

Fig. 5.6: Attenuation coefficient of epoxy resin host material (Kennedy, 2010)

5.2.2. Modelling pLS Device using a High-Performance Coding Approach

While AFI approach decreased the number of iterations and simulation time, program accuracy decreased by ~12% (detailed results are shown in Section 5-3-1). Therefore, instead of using the AFI, high-performance coding (HPC) techniques were used which could significantly reduce simulation time and improve accuracy. The presented techniques were introduced in the following sections.

5.2.2.1. Minimize Repetitive Parameter Calculations

Minimizing repetitive parameter calculations was undertaken by finding the parameters whose values were the same in various iterations of the processing loop, e.g., when calculating the refraction angle (θ_t) in *Eqn* (2.23), it had the same values for all the rays incident at the same angle of incidence (θ_i). Thus, this calculation only needs to be implemented once for all rays which results in reducing calculation time. In MCRT algorithm, the incident angle θ_i is a random number ranging between 0 - 90 degrees. The weighted probability for θ_i is equal for all angles inside this range. Thus, the estimated number of the refracted rays with similar calculations is obtained by Eqn (5.11):

$$N_{R_S} = \frac{N_{R_{tot}}}{f_{op}} \quad , \quad f_{op} = 90 \times \Delta\theta \qquad Eqn\ (5.11)$$

Where $N_{R_{tot}}$is the total number of refracted rays and $\Delta\theta$ is the ray angle step, f_{op} is the optimization factor indicating the optimized number of calculations required to optimize the system. For example, consider a pLSC model where 1,000,000 rays with random angles were refracted to the pLSC. If the angle step is $\Delta\theta = 1$ ($\theta_i = [1\ 2\ ...\ 90]$), $f_{op} = 90$ and $N_{R_s} \approx 11111$ for each θ_i. As a result, in the optimized condition, θ_t can be calculated only once for each θ_i instead of 11,111 times which dramatically decreases the number of calculations and hence simulation time. The same optimization method is applied in calculating other vectors and parameters (such as reflection and transmission) which significantly reduces duplicating calculations.

5.2.2.2. Optimizing the Process of Parameter Storage

Calculating and storing every array in 3D spatial tracing matrices are based on the type of host material and the ray's location in the 3D tracing-space. Therefore, conditional statements (such as IF statements) had to be used in order to fill spatial tracing matrices. The number of these conditional statements is increased in the modelling of multilayer devices where tracing-space comprised different media and boundaries with different host and luminescent materials. Conditional statements take more time in comparison with non-conditional statements because they need more time to survey the conditions and decision making (MATLAB, 2017). The total

amount of time that was consumed in order to survey the conditions to fill the arrays of the 3D spatial tracing matrices is calculated by $Eqn\ (5.12)$:

$$T_{Fill} = N_L \times t_C \times \sum_{i=1}^{N_m} (i \times Sz_i) \qquad Eqn\ (5.12)$$

Where t_C is the time consumed when a conditional statement is used, N_L is the number of layers with different materials in pLS device (which indicates the number of the conditions which must be surveyed), Sz_i is the total size of the *i*th 3D spatial tracing matrix and N_m is the total number of 3D spatial tracing matrices used.

To decrease simulation time, 3D tracing-space of the device was divided and labelled into different sections based on the type of host materials and boundaries. Then, 3D spatial tracing matrices were filled based on the labelled sections in an iterative statement (such as a FOR loop) which consumes less time in comparison with a conditional statement. Using this idea, T_{Fill} decreased which is calcualted by $Eqn\ (5.13)$:

$$T_{Fill} = N_L \times N_m \times t_{ITR} \qquad Eqn\ (5.13)$$

Where t_{ITR} is the time consumed when the iterative statement is used.

Table 5-1 includes an example comparing two scripts in which the value of a small 3D spatial matrix size of (100,100,100) was updated in a loop with only 1000 iterations when an iterative statement was used. As can be seen, several conditions were applied in order to fill different regions (rows and columns) of the matrix. In the first script, the conditions were applied using a conditional statement (IF); however, in the second script, different regions were labelled and a technique with iterative statements was used in order to fill the matrix so that no conditional statement was applied. Both scripts were run in MATLAB R2018b installed on a PC with Core i-5@3.30GHz CPU with 16GB RAM. Although the results of both scripts were the same, the simulation time decreased from 14.06 seconds to 12.47 seconds when the code was executed with the optimized method using iterative statements.

Table 5-1: Two sample codes with the same output but different simulation time: A small 3D matrix with the size of (100,100,100) was updated with and without "Conditional Statement"

	With "Conditional Statement"	With "Labelling" method and "Iterative Statement"

Script	Nx=100;
	Ny=100;
	Nz=100;
	A = zeros(Nx,Ny,Nz);
	tic
	for i=1:1000
	for nx = 1 : Nx
	for ny = 1 : Ny
	for nz = 1 : Nz
	if (ny <= Ny-1)&&(nz <= Nz-1)
	A(nx,ny,nz) = i+1;
	end
	if (ny <= Ny-1)&&(nz == Nz)
	A(nx,ny,nz) = i+2;
	end
	if (nz <= Nz-1)&&(ny == Ny)
	A(nx,ny,nz) = i+3;
	end
	if (nz == Nz)&&(ny == Ny)
	A(nx,ny,nz) = i+4;
	end
	end
	end
	end
	end
	consumed_time=toc
		Nx=100;
		Ny=100;
		Nz=100;
		A = zeros(Nx,Ny,Nz);
		tic
		for i=1:1000
		for nx = 1 : Nx
		for ny = 1 : Ny-1
		for nz = 1 : Nz-1
		A(nx,ny,nz) = i+1;
		end
		A(nx,ny,Nz) = i+2;
		end
		for nz = 1 : Nz-1
		A(nx,Ny,nz) = i+3;
		end
		A(nx,Ny,Nz) = i+4;
		end
		end
		consumed_time=toc

Time (s)	14.06	12.47

5.2.2.3. Event Prioritizing Based on Probability

In each internal cycle of the main loop, the probability of all simultaneous events such as attenuation, absorption, scattering and transmission was surveyed by conditional statements and then the event with the highest probability was selected for the ray. The conditional statements consumed time; moreover, the number of iterations in the internal cycles' loop (N_{int}) was more than the number of the iterations of the main loop (N_{ITR}) because a single ray may internally be scattered or wave-guided by TIR several times in the loop of the internal cycles. Hence, the total time consumed for surveying and finding the ray status in internal cycles' loop is calculated by Eqn (5.14):

$$T_{Staus} = N_{ITR} \times N_{int} \times \sum_{K=1}^{N_K} t_{C_K} \qquad Eqn\ (5.14)$$

Where N_K is the total number of events in the internal cycles, t_{C_k} is the time consumed when a conditional statement is used for the *Kth* ray tracing event. The idea to optimize the process was defining the priority (f_{d_K}) for each event based on the weight of its probability; so that, the event

with highest probability received the dominant priority. Then, the process of checking the conditions was commenced by the event with the dominant priority (highest f_{d_K}). As a result, the optimized T_{Staus} could be calculated by Eqn (5.15) and reduced to:

$$T_{Staus_{OPT}} = N_{ITR} \times N_{int} \times \sum_{K=1}^{N_K} f_{d_K} \times t_{C_K} \qquad Eqn\ (5.15)$$

From the coding point of view, this idea can be applied using Switch-Case conditional statements instead of IF conditional statements. Table 5-2 illustrates two simple scripts in which a parameter was assigned different values in different conditions in a loop with only 100,000 iterations. One of the scripts was executed by IF statement; while, the other one used Switch-Case statement. Although the results of both scripts were same, it was clear that Switch-Case Statement was less time consuming, decreasing the simulation time from 0.0129 seconds to 0.0075 seconds.

Table 5-2: Two sample codes with the same output but different simulation time: A parameter is assigned using "IF Conditional Statement" and "Switch-Case Statement"

	With "IF Conditional Statement"	With "Switch-Case Statement"

Script	tic
	for i=1:100000
	
	if i==1
	a=i*1;
	elseif i==2
	a=i*5;
	elseif i==3
	a=i*15;
	elseif i==4
	a=i*20;
	elseif i==5
	a=i*25;
	elseif i==6
	a=i*30;
	elseif i==7
	a=i*35;
	elseif i==8
	a=i*40;
	elseif i==9
	a=i*45;
	elseif i==10
	a=i*50;
	else
	a=i*100;
	end
	end
	consumed_time=toc
		tic
		for i=1:100000
		
		switch i
		case 1
		a=i*1;
		case 2
		a=i*5;
		case 3
		a=i*15;
		case 4
		a=i*20;
		case 5
		a=i*25;
		case 6
		a=i*30;
		case 7
		a=i*35;
		case 8
		a=i*40;
		case 9
		a=i*45;
		case 10
		a=i*50;
		otherwise
		a=i*100;
		end
		end
		consumed_time=toc

Time (s)	0.0129	0.0075

5.2.2.4. Optimizing Intersection Point Calculation

In MCRT, the device was modelled by different planes and boundaries. Also, the heart of the program was based on the calculation of intersection point of the ray and planes. Since a single refracted ray might scatter or be wave-guided by TIR inside the pLS device and strike different planes, the total number of iterations of the internal cycles' loop and intersection point calculations is much more than the total number of the iterations of the main loop. Therefore, optimizing the process of the intersection point calculation could significantly enhance the performance of the program and decrease the simulation time. In order to obtain the intersection point (r_i) of the ray which originated at $I_0 : [X_0\ Y_0\ Z_0]$ and direction vector of $I_d : [X_d\ Y_d\ Z_d]$, with the plane of $PL : [a_P\ \ b_P\ c_P\ \ DP]$, the ray equation is substituted in a plane equation in the first step. In the next step, the distance (L) between the ray origin and the plane is obtained by solving the substituted *Eqn* (2.20). The value of L was then used to calculate the exact intersection point by *Eqn* (2.21). The total time for calculating the intersection point in the whole ray tracing algorithm can be obtained by Eqn (5.16):

$$T_{Intersection} = N_{ITR} \times N_{int} \times t_S \qquad Eqn\ (5.16)$$

Where t_S is the time consumed by the mathematical method used to calculate the intersection point. Generally, the "SOLVE" function (MATLAB, 2017) is used in order to solve equations in MATLAB software. However, after comparing the "SOLVE" and direct method in calculation of *Eqn* (2.20), it was observed that the measured consumed time was dramatically reduced from 1.1526 seconds for "SOLVE" method to 2.12×10^{-4} seconds in the direct method. The detail of the comparison is presented in Table 5-3 including the calculation of intersection point for a single ray and pLS device plane. Using a direct method for intersection point calculation significantly enhances the performance of the program and reduces the calculation time.

Table 5-3: The calculation of L only for one particular ray and plane by two methods of using "SOLVE" function and with using "Direct" Calculations

	With "SOLVE" function	With "Direct" Calculations

Script	x0=0;
	y0=0;
	z0=0;
	
	xd=0.5774;
	yd=0.5774;
	zd=0.5774;
	
	aP=0;
	bP=0;
	cP=1;
	DP=2;
	
	tic
	
	syms P
	
	eqn = (aP*(x0+(P*xd))) + (bP*(y0+(P*yd))) + (cP*(z0+(P* zd)))-DP;
	
	L = double (solve(eqn, P));
	
	ri = [x0+(xd *L) y0+(yd *L) z0+(zd *L)];
	
	consumed_time=toc
		x0=0;
		y0=0;
		z0=0;
		
		xd=0.5774;
		yd=0.5774;
		zd=0.5774;
		
		aP=0;
		bP=0;
		cP=1;
		DP=2;
		
		tic
		
		L =((aP*x0)+(bP*y0)+(cP*z0)+DP) / ...
		((aP* xd)+(bP* yd)+(cP* zd));
		
		ri = [x0+(xd *L) y0+(yd *L) z0+(zd *L)];
		
		consumed_time=toc

Time (s)	1.1526	2.12×10^{-4}

5.2.2.5. Using Look Up Tables

In order to speed up the processes inside the iterative loop and reduce calculations, a "look up table" (MSDN, 2017) of the constant parameters such as scattering coefficient and attenuation coefficient and θ_c in the iterative loop was used instead of calculating them inside the loop. The constant parameters were calculated out of the program and their values were placed in matrix as a "look up table". Then, inside the iterative loop, the values of the parameters can be called and read from the look up table whenever they are required. Therefore, there is no need to directly calculate them inside the program which decreases the computational time.

Table 5-4 illustrates two scripts in which the attenuation coefficient (α_{Atte}) was obtained for a wavelength (350nm). In the first script, the value of α_{Atte} is directly calculated by the attenuation function while in the second script, the value of α_{Atte} is read from a look up table (LUT_data) which was filled out of the program including the values of attenuation coefficients for all

wavelengths. As reported, the measured consumed time decreased by ~75% from 22.79×10^{-5} to 5.51×10^{-5} seconds.

Table 5-4: Obtaining attenuation coefficient for one particular wavelength by "Calculation" and using "Look Up Table"

	Using "Calculations" inside the loop	Using "Look Up Table" inside the loop

Script	wavelength=350;
	
	tic
	
	a = 8201;
	b = -0.03294;
	c = 0.05316;
	d = -0.0005568;
	α_Atte = a*exp(b*wavelength) + c*exp(d*wavelength);
	
	consumed_time=toc
		wavelength=350;
		
		tic
		
		α_Atte = LUT_data (wavelength);
		
		consumed_time=toc

Time (s)	22.79×10^{-5}	5.51×10^{-5}

5.3. PEDAL Validation

In this section, the performance of PEDAL to model both LS and pLS device is investigated. Results were compared and validated with experimental results. In addition, a conversion correlation is discussed and validated for various sizes and shapes of MNP to convert the doping concentration unit from ppm (mg/L); which is used in experiment, to N/L which is used in modelling. This provides the ability to compare the modelling and experimental results obtained from MNPs.

5.3.1. PEDAL Validation for LS Devices

PEDAL results (Rafiee *et al.*, 2017c) were compared with results of an LSC reported by Kennedy et.al. (Rowan, 2007, Kennedy *et al.*, 2008, Kennedy *et al.*, 2009, Kennedy, 2010) with 6 × 6 × 0.3 cm dimensions and epoxy host material doped with CdSe/Zns Green QDs which had a QY of 85%. A PV solar cell was coupled to one of the edges and mirrors were attached at the other edges. Emission and absorption spectra of CdSe/Zns QDs are shown in Fig. 5.7 with solar radiation AM1.5D was used.

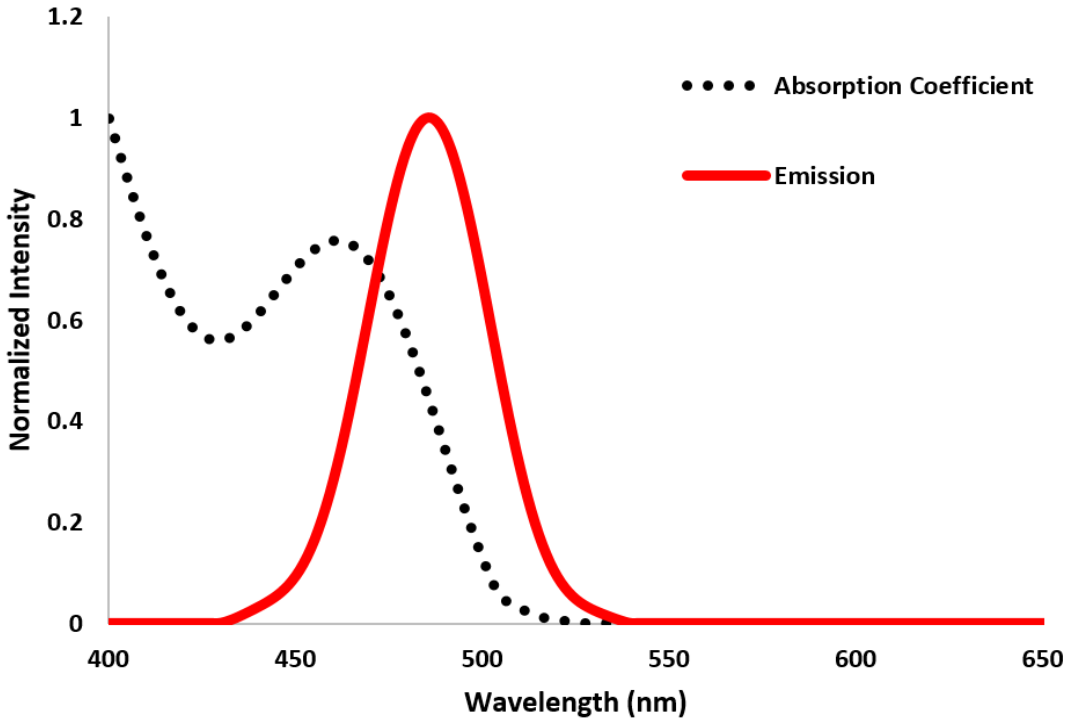

Fig. 5.7: Normalized absorption coefficient and emission spectra for CdSe/Zns Green QDs (Rowan, 2007, Kennedy *et al.*, 2008, Kennedy *et al.*, 2009, Kennedy, 2010)

The results of different PEDAL versions and the comparison of the optical efficiencies obtained with the reference value (1.63%) can be found in Table 5-5.

At first, PEDAL was run for 125,989 input rays. As reported in table 5-5, ~3.9% of the irradiated rays were reflected from the top surface of the device. The rest of the rays (96.1%) were refracted inside the LSC. ~5.2% of rays were lost as heat inside the LSC which were either absorbed by the host material or absorbed by the QD and lost due to non-unity QY. ~89% of the rays exited the LSC and were lost due to the escape cone. A small portion of rays (~1%) were wave-guided to the edge of the device and detected by the PV solar cell. Simulation time was found to be 385,462 seconds (~4.5 days). Optical efficiency was calculated as 1.56% while it had -4.3% discrepancy error ($\Delta\eta_{opt}$) with the measured optical efficiency of 1.63%. The value of the discrepancy error presented the accuracy of the modelling results in comparison with the experimental outcomes. In order to achieve an accurate value of optical efficiency and emission spectrum that were closely matched to the reference values, the number of iterations (input rays)

had to be increased which further increased the simulation time; thus, it was found as a serious limitation on the model.

Table 5-5: Comparison and validation of results obtained by PEDAL models

Version	**PEDAL**	**PEDAL Optimised by AFI Approach**	**PEDAL Optimised by HPC Approach**	
Initial Number of Rays	125,989	125,989	125,989	1,061,392
Filtered Rays (%)	-----	92.89	-----	-----
Reflected Rays (%)	3.90	0.30	3.90	3.98
Refracted Rays (%)	96.10	6.81	96.10	96.02
Thermal Loss (%)	5.18	2.94	5.21	5.27
Escape Cone Loss (%)	89.90	2.95	89.87	89.71
Reached to PV (%)	1.02	0.92	1.02	1.04
OE (%)	(Reference η_{opt}=1.63%) (Rowan, 2007, Kennedy *et al.*, 2008, Kennedy *et al.*, 2009, Kennedy, 2010)			
	1.56	1.43	1.56	1.60
$\Delta\eta_{opt}$ *(%)*	-4.3	-12.3	-4.3	-1.8
Simulation Time(s)	385462.5 **(~6425 Minutes)**	7271.9 **(~121 Minutes)**	138.5 **(~2.2 Minutes)**	3970.9 **(~66 Minutes)**

Secondly, PEDAL optimised using an AFI approach (described in Section 5-2-1) was run for the LSC with the same number of rays. As presented in table 5-5, ~92.89% of the rays were filtered and did not enter the iterative loop which decreased the simulation time to ~7,272 seconds (~2h). However, since in this version of the program, the fate of the filtered rays was not determined by the MCRT algorithm and were estimated based on their dominant priority, the accuracy decreased. The value of optical efficiency obtained was 1.43% and $\Delta\eta_{opt} = -12.3\%$.

Third, PEDAL optimised using HPC approach (described in Section 5-2-2) was run for the device with the same number of rays. As shown in table 5-5 (fourth column), almost the same statistical results and accuracy were obtained (similar to the first run of PEDAL). However, the simulation time decreased significantly from ~385,462 seconds to only ~138 seconds when HPC approach was used.

Finally, PEDAL using HPC approach, was run for 1,061,392 rays to increase the accuracy of the results. As observed in table 5-5 (fifth column), the simulation time was 3,970 seconds (~1 hour) and the optical efficiency obtained was 1.60%. This is a close match to the reference value, 1.63%. By increasing the number of incident rays, the accuracy of the program was enhanced and $\Delta\eta_{opt}$ of 1.8% was obtained. The model was also run for more than 1000 K rays; however, no enhancement was observed in the accuracy and the discrepancy error remained constant, $\Delta\eta_{opt} \approx 1.7$. PEDAL using HPC approach was then used for all modelling in this research.

5.3.2. Computational Method to Convert MNP Doping Concentration from ppm to N/L

The doping concentration of MNP is an important parameter in pLS device fabrication. Although the performance of pLS device is enhanced by plasmonic coupling of MNP and luminescent material, increasing MNP doping concentration increases the probability of energy quenching. Therefore, estimating the correct MNP doping concentration is a crucial task for PEDAL. The unit of MNP doping concentration in modelling is based on number of particles per litre (N/L). In this section, a computational method is used to convert the experimental unit of doping concentration (ppm) to the modelling unit (N/L) so the experimental and modelling

results can be compared. The method is validated for both nano-sphere (NS) and nano-rod (NR) particles (Sethi and Rafiee *et al.*, 2019).

In the validation process, a scanning electron microscope (SEM) was used to determine the size and shape distribution of MNP (Sethi, 2017). Moreover, the concentration of MNP can be obtained through the inductively coupled plasma optical emission spectroscopy (ICP-OES) (Sethi, 2017).

Doping concentration can be obtained by Eqn (5.17) (Kittler *et al.*, 2015):

$$c_{MNP} = \frac{N_{Au}}{N_{Au/MNP} \times V_{Sample} \times N_A} \qquad Eqn\ (5.17)$$

Where $N_A = 6.022 \times 10^{23}\ \frac{1}{Mol}$ is Avogadro number and V_{Sample} is the volume (L) of the sample used in the ICP-OES test process. N_{Au} is the number of gold atoms calculated by Eqn (5.18):

$$N_{Au} = \frac{c_{ICP-OES} \times V_{Tot} \times N_A}{M_{Au}} \qquad Eqn\ (5.18)$$

Where $c_{ICP-OES}$ is the concentration of gold ions in ppm (mg/L) obtained from ICP-OES test, V_{Tot} is the total volume (L) of the primary sample used ICP-OES measurements and $M_{Au} = 196.96657\ \frac{g}{Mol}$ is the molar mass of gold. $N_{Au/MNP}$ is the number of gold atoms in one MNP obtained by Eqn (5.19):

$$N_{Au/MNP} = \frac{4 \times V_{MNP}}{V_{UC}} \qquad Eqn\ (5.19)$$

Where $V_{UC} = 6.78\ \times\ 10^{-29} m^3$ is the volume of a unit cell which includes four Au atoms. V_{MNP} is the volume of the MNP which is $\frac{4}{3}\pi . r^3$ for NS and $\pi . r^2 . h$ for NR particles.

For validation, the experimental results of four Au NS samples with different concentrations have been used which can be seen in Fig. 5.8 (Sethi, 2017). The concentration of each sample was obtained by ICP-OES and was 50±10%, 33±10%, 61±10% and 37±10% ppm for sample A1, A2, B1 and B2 respectively.

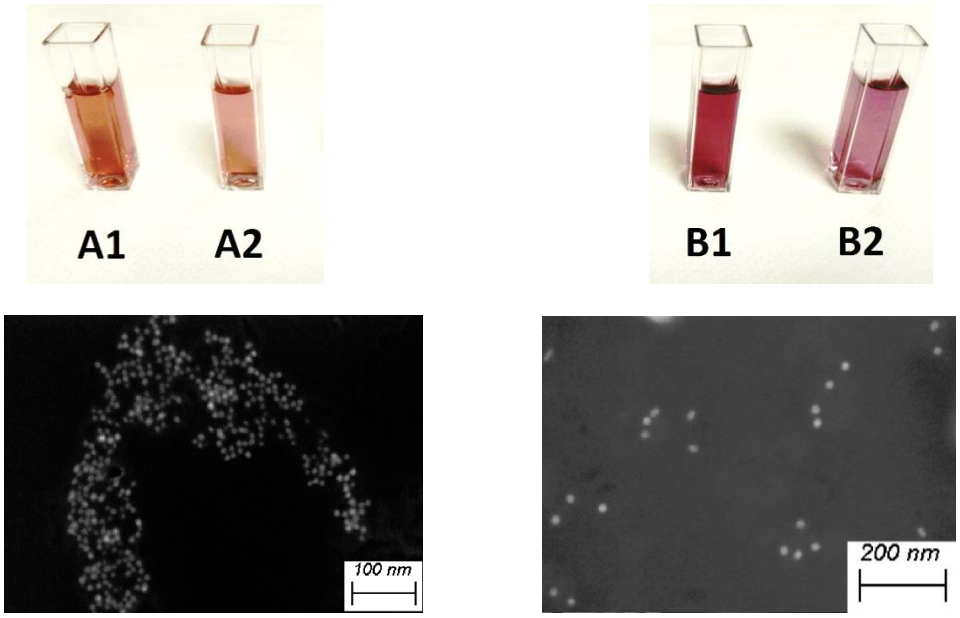

(a) (b)

Fig. 5.8: Synthesized and SEM image of Au NS samples: (a) A1 (50±10% ppm) and A2 (33±10% ppm) and (b) B1(61±10% ppm) and B2 (37±10% ppm) (Sethi, 2017)

The sample size distribution can be found in Fig. 5.9. The majority of Au NS particles in A1 and A2 samples had a radius of ~5-6 nm. The radius of particles in B1 and B2 were ~10-11nm.

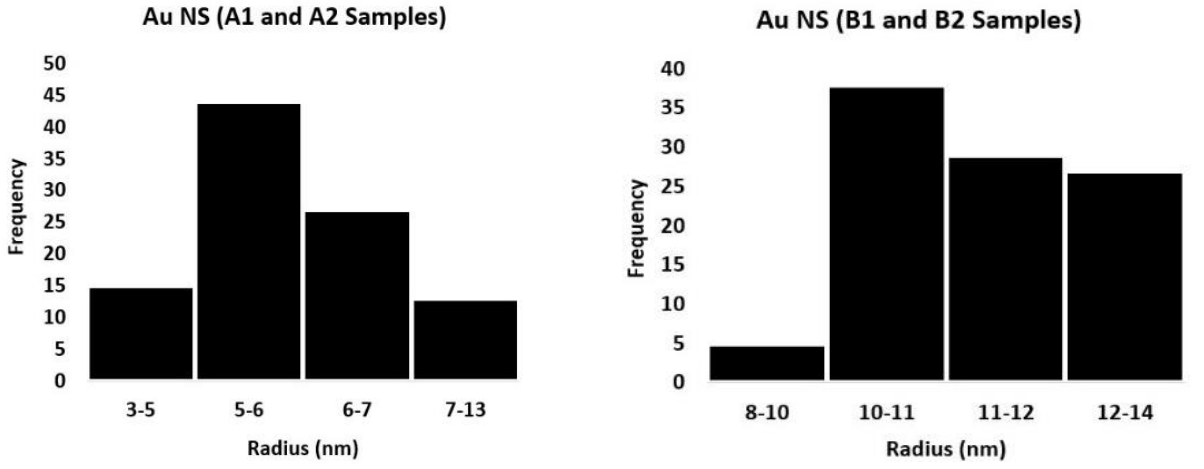

(a) (b)

Fig. 5.9: Size distribution of Au NS samples: (a) A1 and A2 and (b) B1 and B2 (Sethi, 2017)

In the modelled devices, 5.5 nm and 10.5 nm radii were selected for samples A and B respectively. Fig. 5.10 compares the modelling and experimental extinction spectra of samples A1 and A2. Au NS concentration has been described in both units of ppm and N/L using the computational method and were found to be in close agreement. The estimated concentration for sample A1 was 51.3 ppm which was a close match to the experimental results (50±10% ppm). Regarding sample A2, the modelling concentration was 36.1 ppm which was close to the experimental results (33±10% ppm). The modelling and experimental peaks of the extinction spectra were perfectly matched at ~524 nm; however, there were some differences in the shapes of the spectra. The reason was that in the experimental samples other sizes of NS were also present; but, when modelling, all NS particles were the same size and shape and dispersed in a homogenous structure.

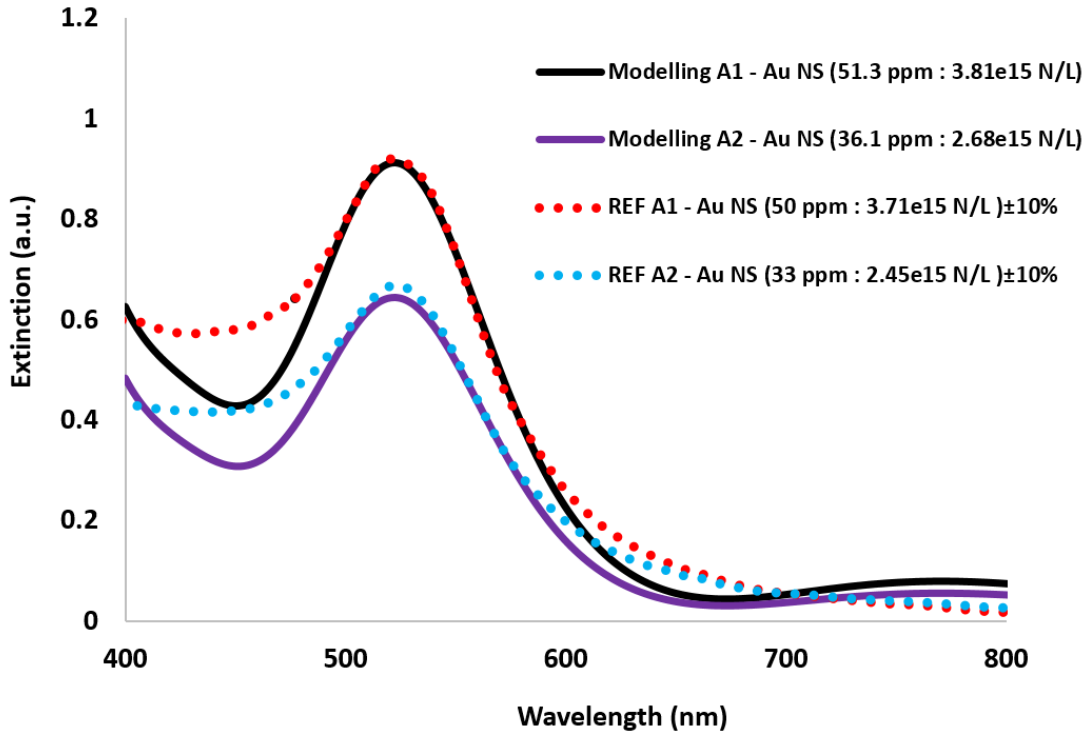

Fig. 5.10: Experimental and modelling extinction spectra for different Au NS-A concentrations (in ppm and N/L units)

Fig. 5.11 compares modelling and experimental extinction spectra of samples B1 and B2. Modelling and experimental extinction peaks are at ~527 nm and in perfect agreement. The

modelling concentrations were 63.2 ppm and 38.1 ppm for sample B1 and B2 respectively which were closely matched to the experimental results of 61±10% ppm and 37±10% ppm.

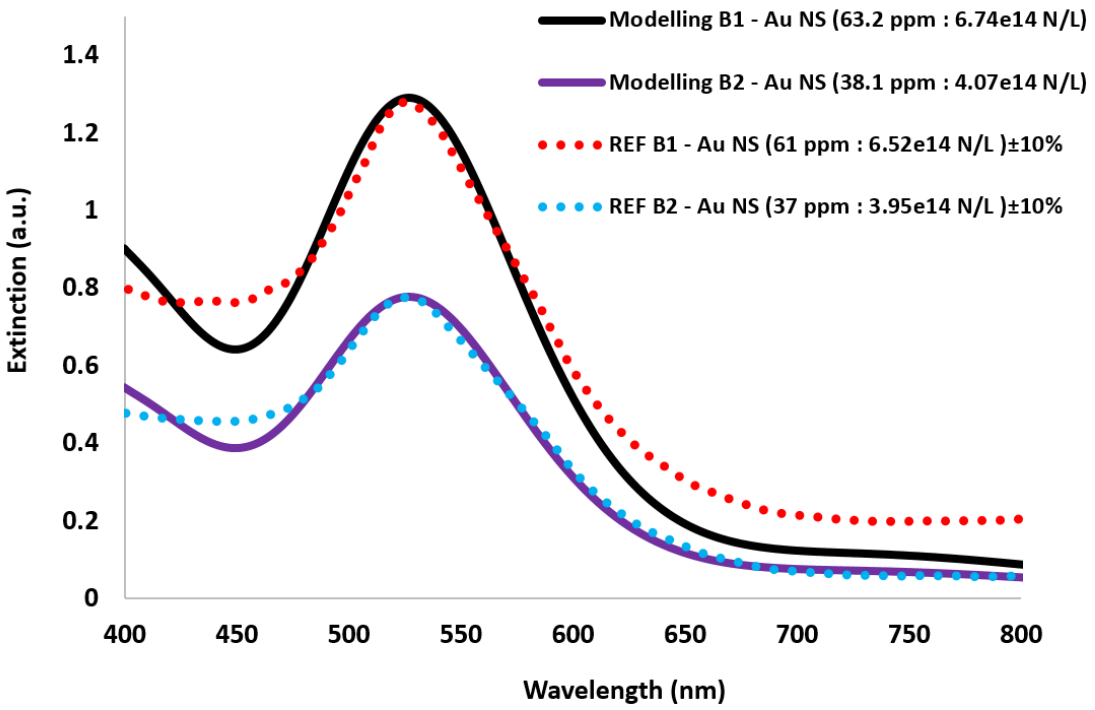

Fig. 5.11: Experimental and modelling extinction spectra for different Au NS-B concentrations (in ppm and N/L units)

The model can accurately predict the experimental results while converting the concentration in ppm to N/L. Fig. 5.12 shows the conversion correlation between these parameters for both sample A and B obtained by the computational method and used for PEDAL. As can be seen, the slope of the conversion graph is different for different sizes of NS particles depending on the weight of the particle which can be estimated by Fig. 5.13 which was obtained from experimental ICP-OES and SEM measurements and through the conversion equations *Eqn* (5.17) to *Eqn* (5.19). The weight for A and B particles were $1.34 \times 10^{-11}\,\mu g$ and $9.35 \times 10^{-11}\,\mu g$ respectively.

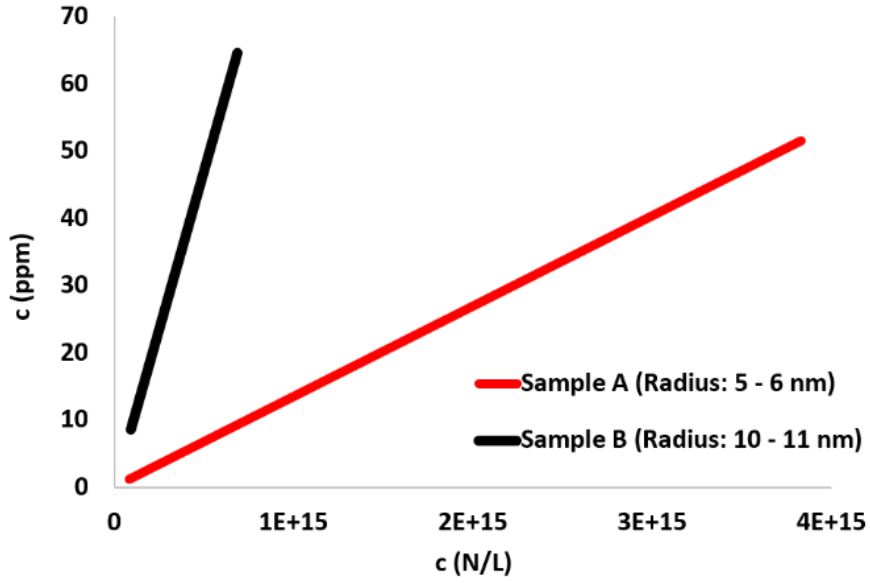

Fig. 5.12: Conversion graph of concentration (ppm) to (N/L) for sample A and B

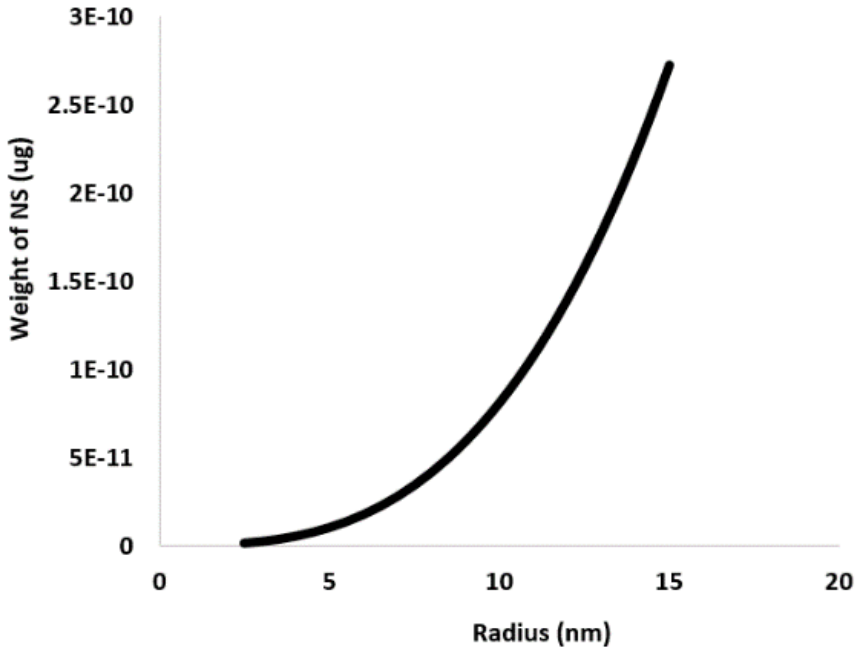

Fig. 5.13: Weight of Au NS particle in Sample A and B over its radius

In the next step, the experimental results obtained from Au NR (Sethi, 2017) was used to validate the computational method used for PEDAL. Size distribution and SEM image of the sample on

Si wafer can be found in Fig. 5.14. As can be observed, Most NRs have a length of ~20-25 nm with an aspect ratio (AR) of the particles of ~2.9±0.4.

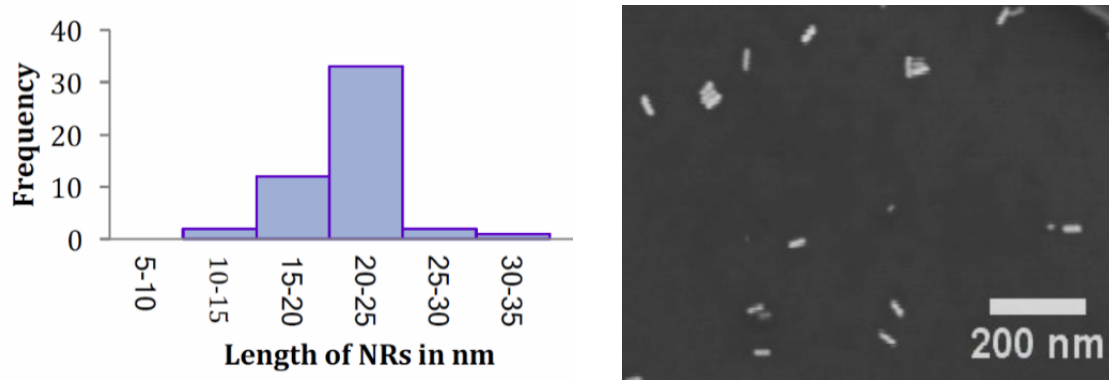

Fig. 5.14: Size distribution and SEM image of the Au NR sample on Si wafer (Sethi, 2017)

Doping concentration of the Au NR sample was ~87±10% ppm which was obtained through the ICP-OES measurement. From Fig. 5.15, the best modelling results was achieved for Au NR with 22 nm length and AR=2.8 and concentration of 82 ppm where the extinction spectrum peak was found to closely match the experimental results (0.82). The results have been shown in both ppm and N/L units obtained using the conversion computational method developed. As the experimental results had an error bar of ~10%, modelling results were also obtained for 80, 90 and 100 ppm to study the effect of concentration changes on the extinction peak. By increasing the concentration from 80 to 100 ppm, the extinction peak increases from ~0.80 to 0.99.

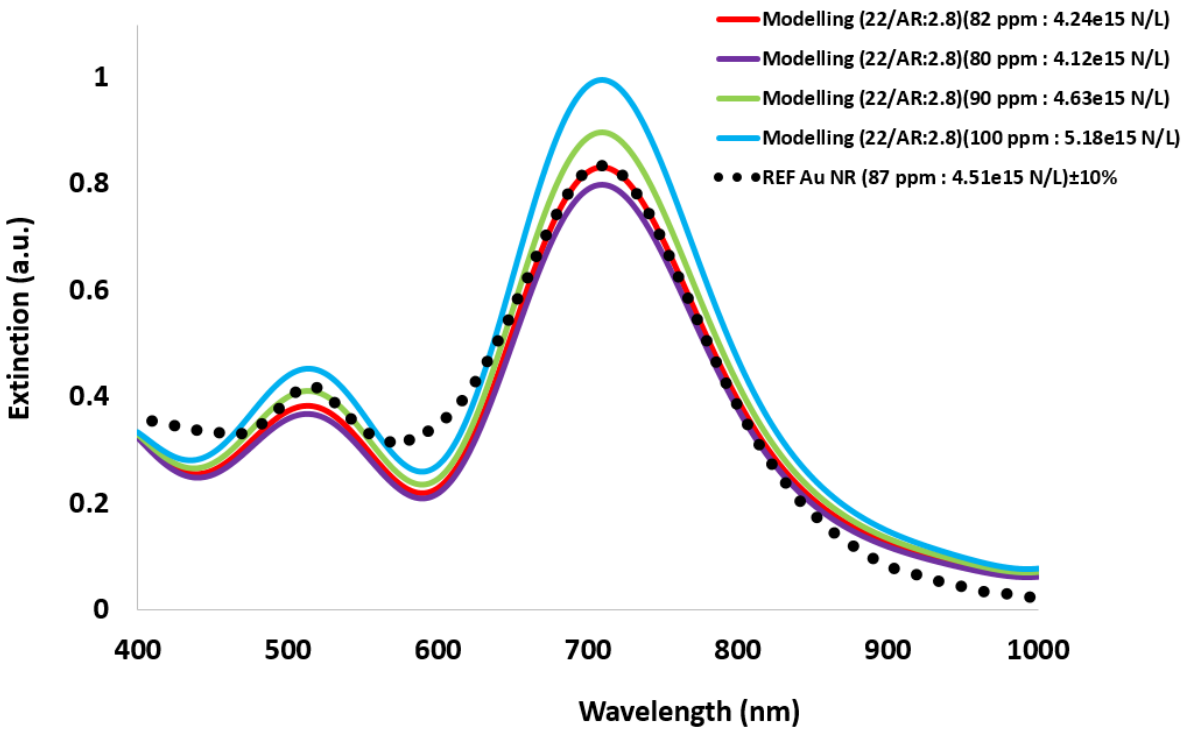

Fig. 5.15: Experimental and modelling extinction spectra for different Au NR concentration (in ppm and N/L)

Fig. 5.16 shows the concentration (ppm) to (N/L) conversion graph for the modelled samples obtained by the computational method and used for PEDAL. The slope of the conversion graph is different for different sizes of NR particles depending on the volume of the particle which can be found by Fig. 5.17. The volume and weight for the best matched sample (22nm/AR:2.8) was $9.98 \times 10^{-25} m^3$ and $1.93 \times 10^{-11} \mu g$ respectively.

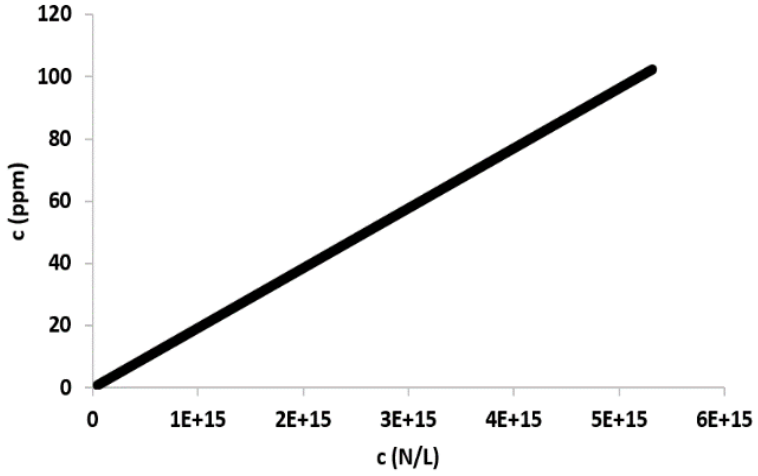

Fig. 5.16: Conversion graph of concentration (ppm) to (N/L) for Au NR sample

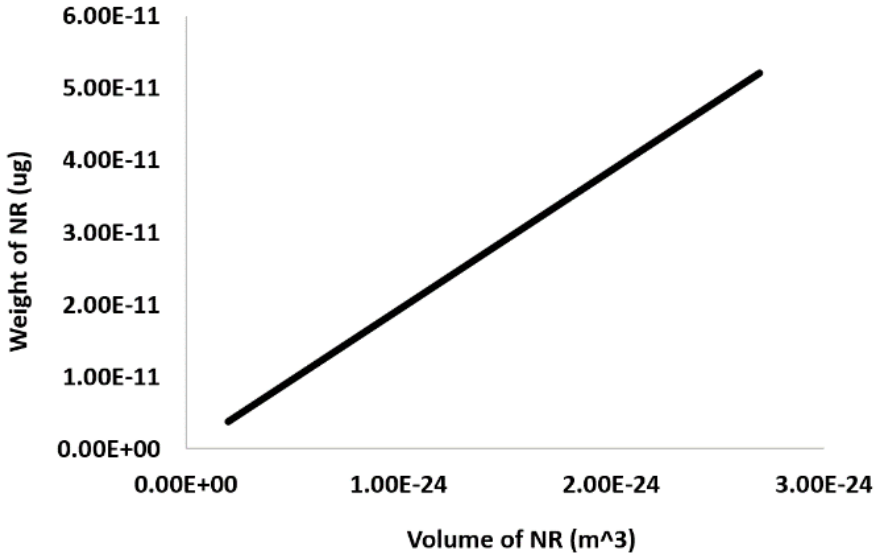

Fig. 5.17: Weight of Au NR over its volume

5.3.3. PEDAL Validation for pLS Devices

Nine pLS devices with different concentrations of MNP and luminescent material (reported by (Chandra, 2013)) were modelled using the developed PEDAL program. Specifications of the modelled devices are presented in Table 5-6 where all devices are in 20 × 10 × 10 mm cuvettes (10 mm pathlength). Host material was epoxy resin doped with 0.008 wt% and 0.01 wt% of core-

shell CdSe/ZnS QDs (QD 575) with ~50% QY (Plasmachem, Germany) and different concentration of Au NS with ~5 nm radius.

Table 5-6: Parameters and configuration of pLS devices

Device	**D1**	**D2**	**D3**	**D4**	**D5**	**D6**	**D7**	**D8**	**D9**
Au NS Concentration (ppm)	0	1	2	2.5	3.5	0	1	1.5	2
Concentration of QD575 (wt%)	0.008					0.01			
Au NS Radius (nm)	~5								
Device Dimension (mm)	20 × 10 × 10								
Host Material Type	Epoxy Resin ($\eta = 1.5$)								
QD575 QY (%)	~50								

QD concentration was 0.008 wt% in D1 to D5 and 0.01 wt% in D6 to D9. Emission and absorption spectra of QD 575 is shown in Fig. 5.18. QD exhibited a single emission peak of ~570-575 nm and a wide absorption band with a peak at ~555 nm resulting in ~20 nm stokes-shift contributing in reabsorption losses.

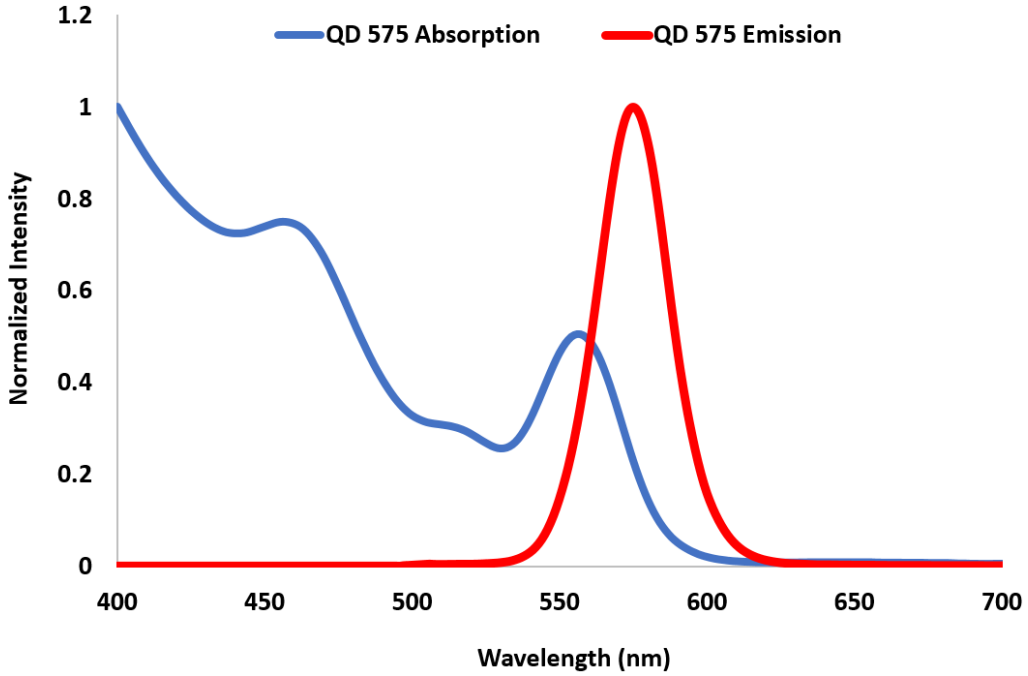

Fig. 5.18: Emission and absorption spectra of QD 575

Normalized extinction spectrum of Au NS can be seen in Fig. 5.19. The peak of Au NS in epoxy resin host material was at ~545 nm which was close to the absorption peak of the coupled QD. This resulted in the absorption enhancement of the whole device allowing the device to achieve higher emission based on the PDEF profile of the Au NS-QD coupling.

Optical properties of Au NS including PDEF and extinction spectrum were obtained using "Plasmon" (detailed in Chapter 4). In modelling, devices were considered to be homogeneously dispersed with Au NS particles of 5 nm radius. This might not be achieved experimentally which results in some discrepancies between the modelled and experimental results. All experimental and modelling discrepancy sources will be discussed in detail in Section 5-4.

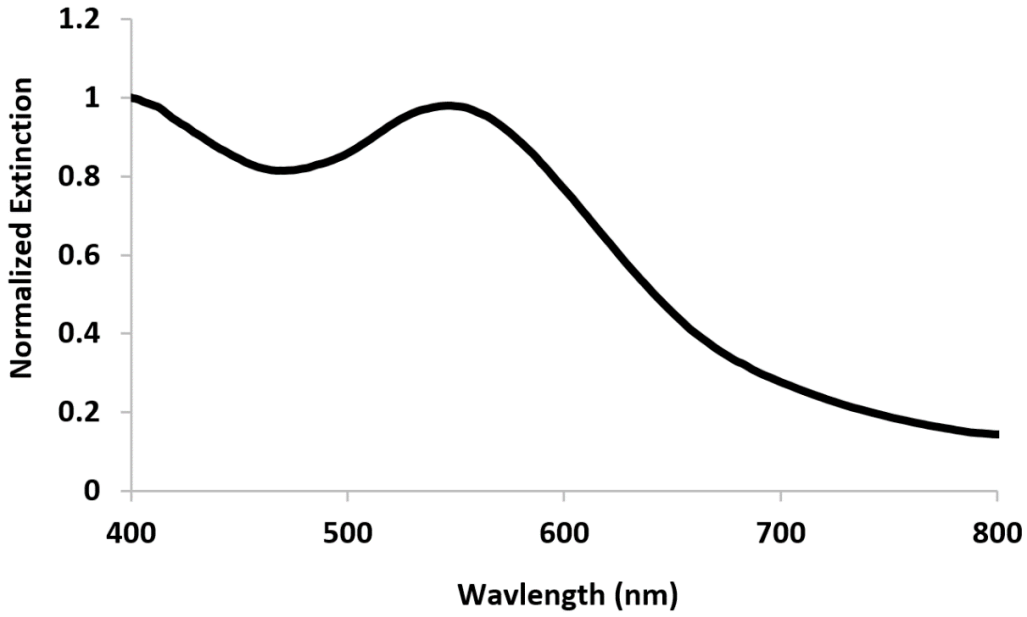

Fig. 5.19: Normalized extinction spectra for Au NS with 5nm radius in epoxy resin

Fig. 5.20a and b show the modelled Au NS in epoxy placed in the 3D FDTD Yee grid with resolution of 15 and a grid discretization of 1.4 nm. In Fig. 5.20, the spacing between the particle and the x-y boundaries is 15 nm. As discussed in Chapter 4, by modelling a single particle, defining well-designed inter-particle spacing and boundary conditions in all directions, different concentration of Au NS could be modelled.

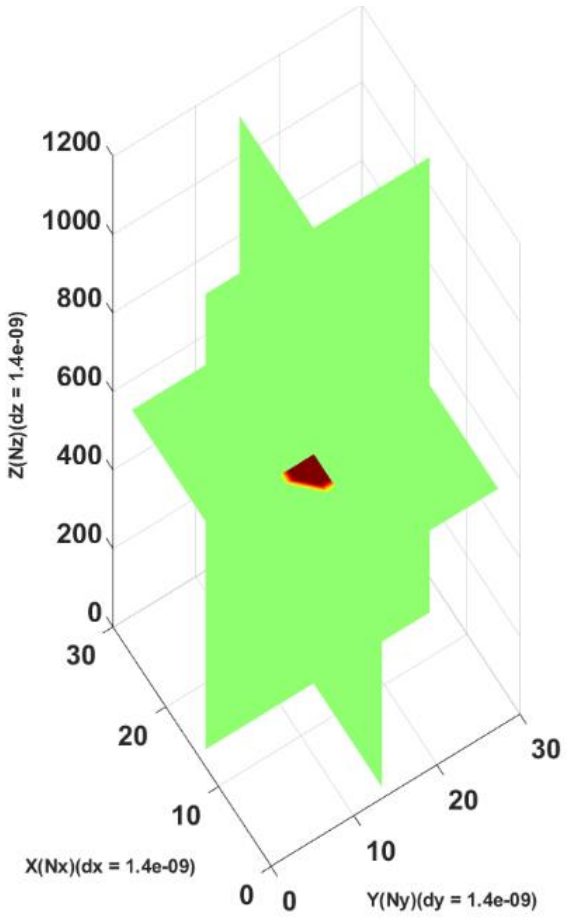

Fig. 5.20: 3D view of the Yee grid including 5nm radius Au NS particles modelled in "Plasmon" program

The modelled particle was irradiated by a gaussian electric field which was injected as a plane wave and propagated in the z-direction while it was polarized along the x-y plane. Fig. 5.21 shows the electric field in all vectors (E_x, E_y, and E_z) and views (x, y, z and 3D) under the simulation. As can be observed, the electric field was enhanced on the boundary of Au NR due to SPR. Once the field was terminated in the grid, Fast Fourier Transform (FFT) was used to achieve the extinction spectra and electric field enhancement of the device from the time domain response of the particle collected from the grid.

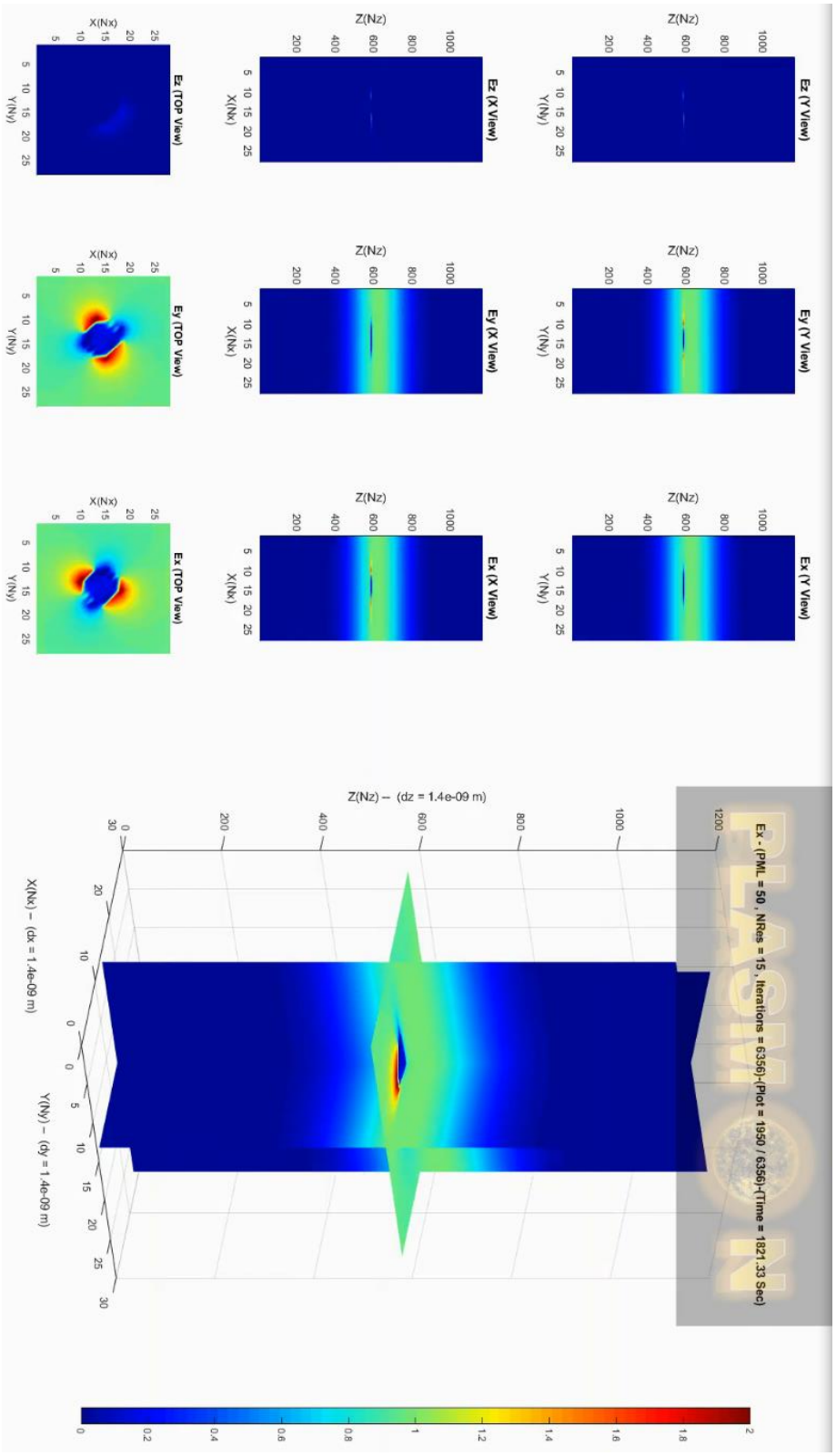

Fig. 5.21: Au NR under Plasmon simulation: electric field distribution in all vectors and views (x, y, z and 3D)

Fig. 5.22a shows the electric field enhancement of the modelled Au NS over time and its location (x view) in the grid. The field enhancement maximum value is ~4.7 on the particle boundary which exponentially decreases to 1 (background energy level) as a function of distance from the particle's surface. PDEF obtained from the field enhancement can be found in Fig. 5.22b which was used as an input parameter for PEDAL.

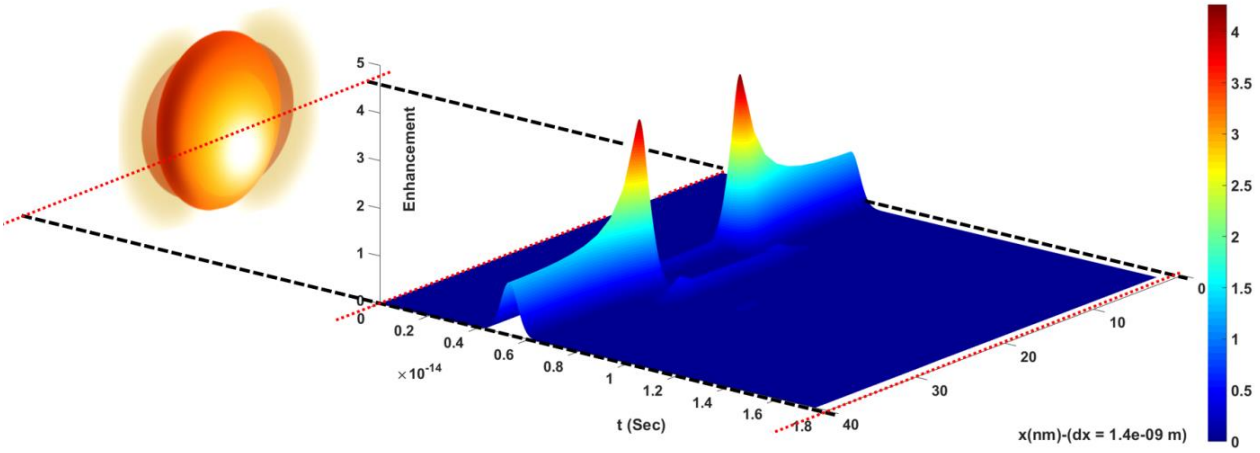

(a)

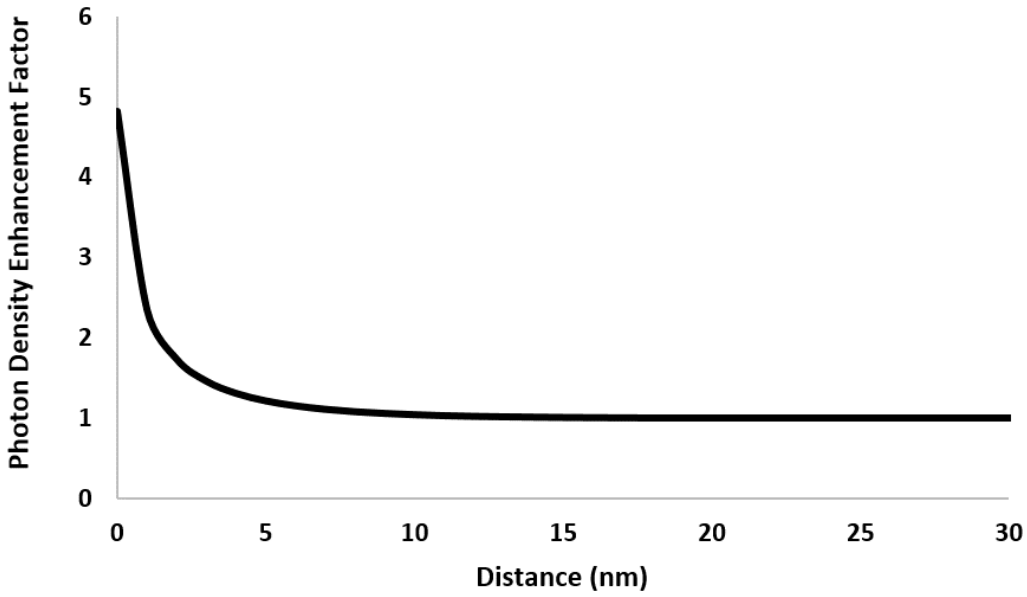

Fig. 5.22: (a) Electric field enhancement over time and its location (x view) for the modelled Au NS (b) PDEF input for PEDAL

The next input required for the PEDAL is the extinction spectra of the Au NS. Fig. 5.23a compares the extinction spectra of the Au NS of different concentrations obtained by changing the spacing between the particle and PBC in the Yee grid. The peaks are at ~545 nm (in close agreement with experimental extinction peak). Doping concentration conversion graph (ppm to N/L units) can be found in Fig. 5.23b. The conversion graph was obtained using the weight of 5 nm radius sphere ($\sim 1.01 \times 10^{-11} \mu g$) and through the validated method presented in Section 5-3-2. As can be seen in Fig. 5.23c, the extinction spectrum peak linearly decreases by reducing the concentration. Fig. 5.23c was used in the model to generate the extinction spectra for any concentration required for D1 to D9.

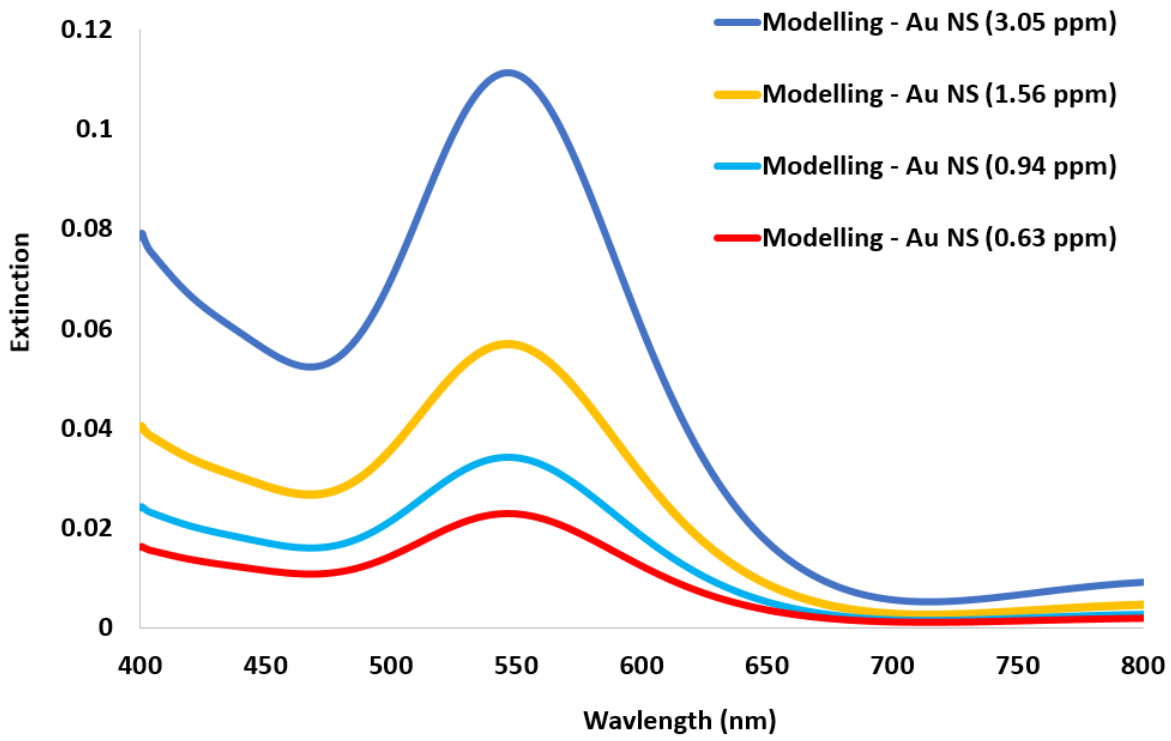

(a)

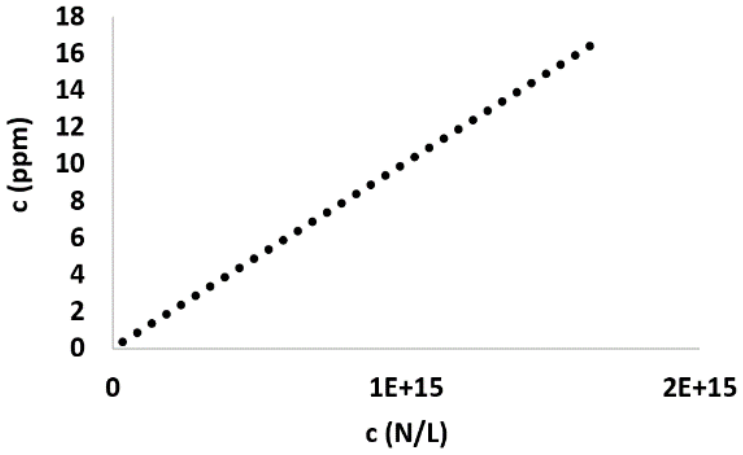

(b)

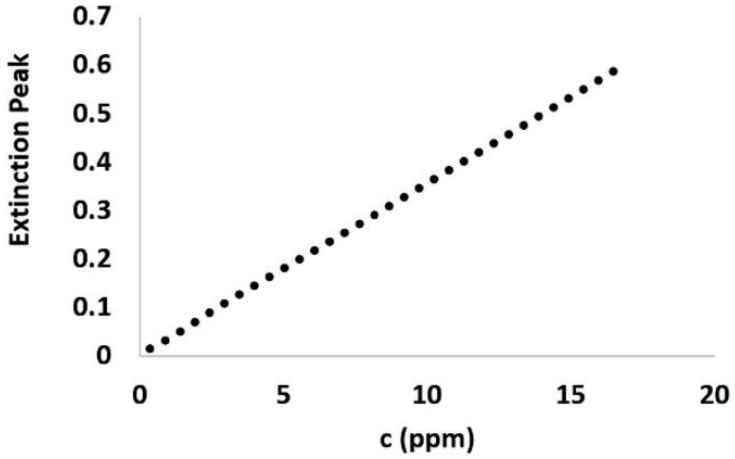

(c)

Fig. 5.23: (a) Extinction spectra of Au NS (R=5 nm) for several doping concentrations.(b) Concentration conversion graph. (c) The extinction peak is linearly changed by changing the concentration. This function is used in modelling to generate the extinction spectra with the concentration of interests required for D1 to D9

The input parameters of all devices obtained for QD and Au NS were imported to PEDAL. QD doping concentration was 0.008 wt% for D1-D5 and 0.01 wt% for D6-D9. Fig. 5.24 shows a visual structure for simulated device (D2) under the radiation of ~350 rays on top surface of the device.

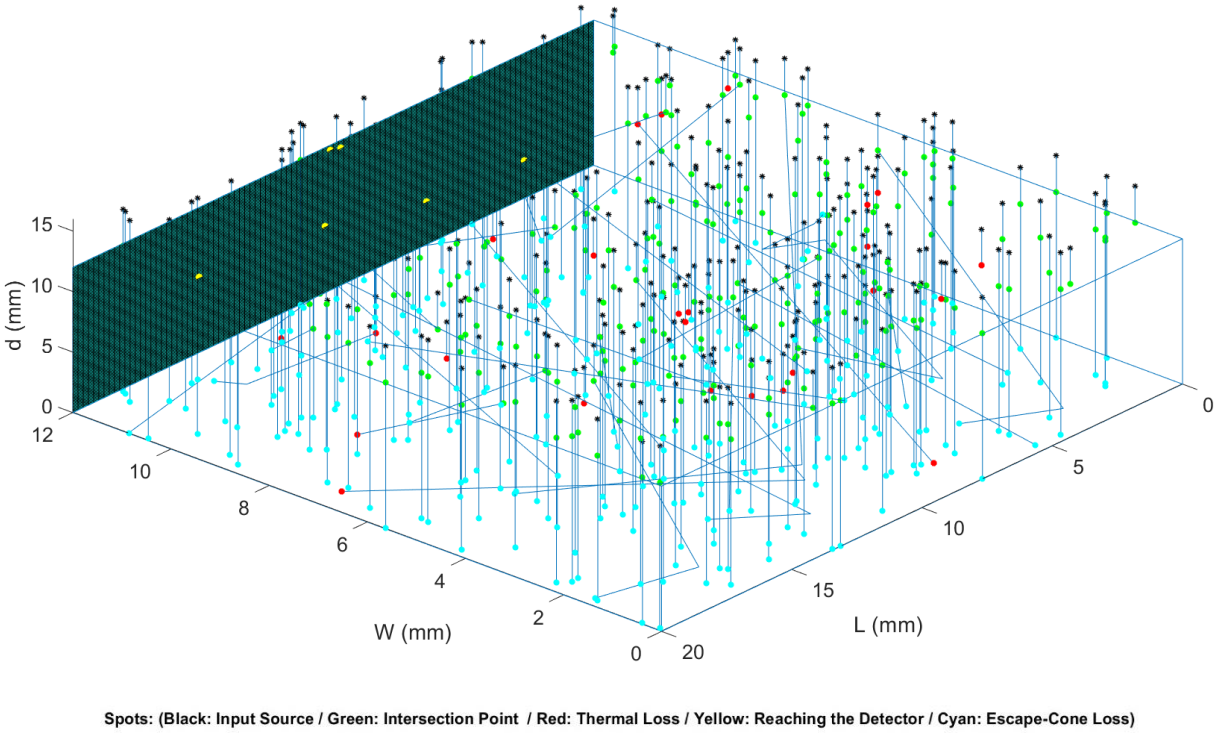

Fig. 5.24: Simulation visualization where the device was irradiated by ~350 rays

The model was run for 1,000,000 incident rays to guarantee the program accuracy and also decrease the noise in the emitted spectrum reaching the detector at the edge of the device. For each QD concentration (0.008 wt% and 0.01 wt%), the concentration of Au NS was increased from 0 to 6.5 ppm.

Fig. 5.25a shows the emission spectra for 0.008 wt% QD concentration. By increasing the concentration of Au NS from 0 to 2.3 ppm, the emission peak increased from 577 a.u. to 953 a.u. where the maximum enhancement was observed. Further increase in concentration of Au NS, increased the rate of quenching which reduced the emission spectra peak. At 6.5 ppm, the emission peak decreased to 452 a.u. which was even less than the emission in the device with 0 ppm Au NS.

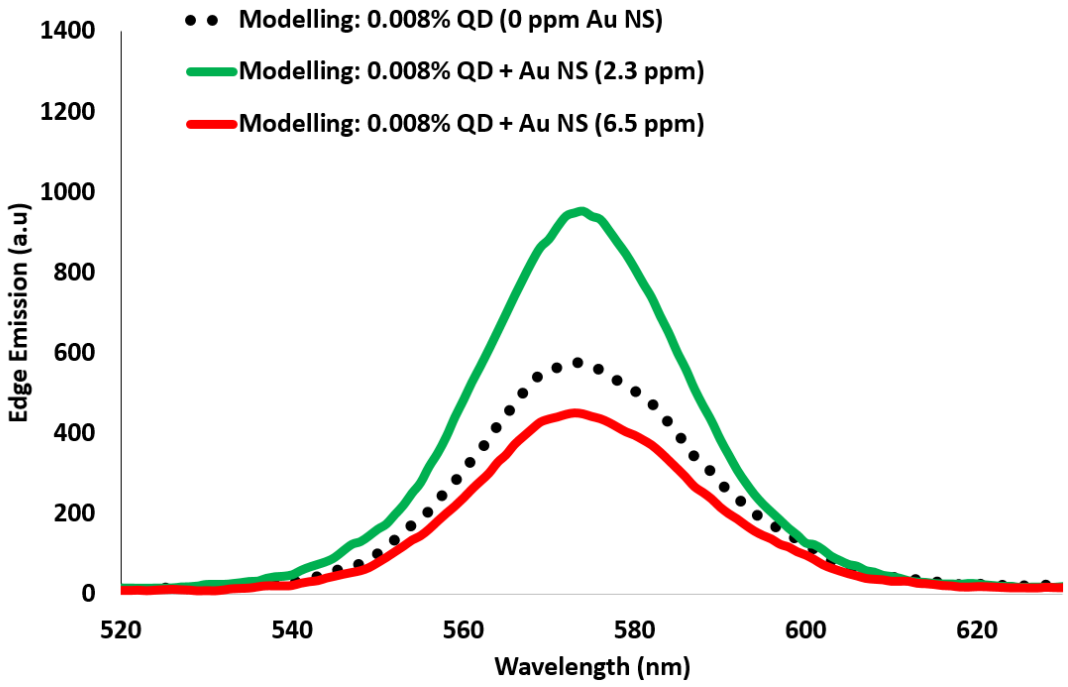

(a)

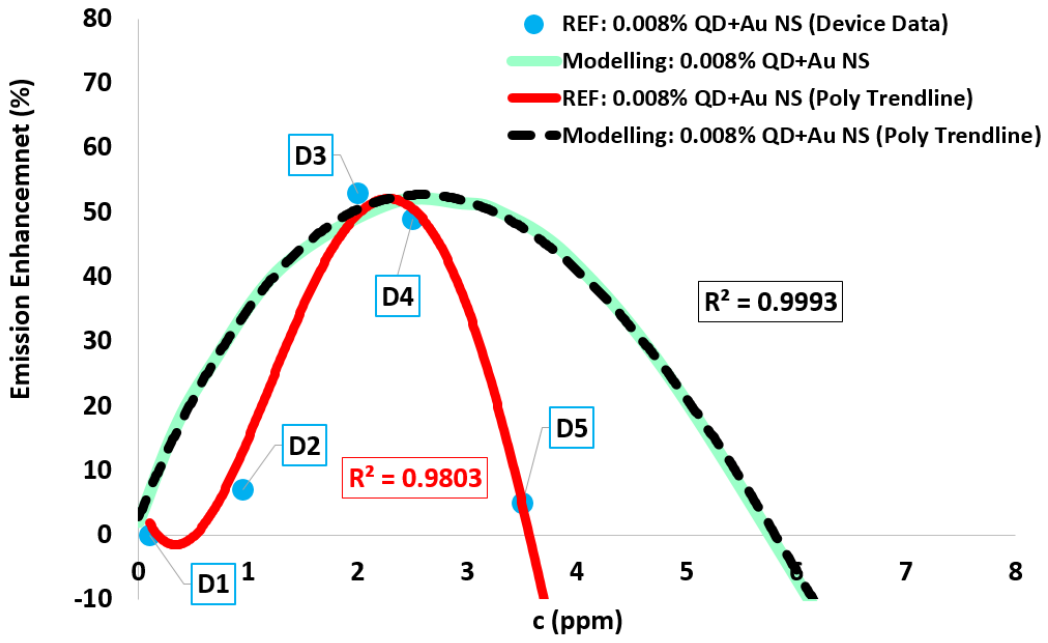

(b)

Fig. 5.25: (a) PEDAL emission spectra for the best and worst concentration of Au NS compared with the 0.008 wt% QD device (0 ppm Au NS). (b) Comparison of the modelled and experimental emission enhancement trend for D1 to D5

The emission enhancement for D1 to D5 predicted in modelling was compared to experimental results in Fig. 5.25b. The model could achieve the emission enhancement peak of 53.06% (at 2.3 ppm) which was in close agreement with experimental results of D3 with 53% emission enhancement peak at 2 ppm. Poly-trend fitted lines were also drawn to compare the trend of the modelling and experimental results over variation of Au NS doping concentration.

Table 5-7 shows the statistical modelling results achieved for the best and worst pLS devices. The results are also compared to D1 which is a conventional QD device without Au NS. ~4% of the incident rays were reflected back from the top surface of all devices due to mismatching of air and epoxy refraction index (1.5). The rest of the rays (~96 %) were refracted inside the devices.

In the best case scenario where pLS device was doped with 2.3 ppm Au NS, escape cone loss decrease from ~84% (in QD device) to ~80%. The total thermal losses increased from ~9% to ~12% due to increasing the energy quenched in Au NS-QD coupling. However, since the coupling plasmonic enhancement was the dominant process in comparison with the quenching effect, the number of the rays waveguiding and reaching the detector increased from 2.45% (in QD device) to 3.75% (in QD+Au NS device). Therefore, the optical efficiency also increased from 2.79% to 4.36% where the device achieved 53% enhancement in the total integrated emission. This was closely matched with experimental results of D3.

In the worst case scenario where 6.5 ppm of Au NS was used in the device, energy quenching increased resulting in the total thermal loss rate of ~18%. Under this condition, the quenching effect was the dominant event which decreased the rate of rays reaching the detector from 2.45% (in QD device) to ~1.9%. Accordingly, the total optical efficiency also dropped from 2.79% to 2.18%. The performance of the device was even ~22% less than the QD device in this case.

Table 5-7: Detailed statistical PEDAL results for devices with 0.008 wt% QD 575 and different concentrations of Au NS

Initial Number of Rays (Iteration)	1,000,000		
Doped Material	QD	QD + Au NS	
		Best Case	Worst Case
QD Concentration (wt %)	0.008	0.008	0.008
Au NS Concentration (ppm)	0	2.3 ***(REF=2)***	6.5
Reflected (%)	4.01	3.93	4.01
Refracted (%)	95.99	96.07	95.99
Total Thermal Loss (%)	9.51	12.36	17.89
Escape Cone Loss (%)	84.03	79.96	76.2
Reach at Detector (%)	2.45	3.75	1.90
Total Input Energy ($W.m^{-2}.nm^{-1}$)	619.68	619.68	619.68
Total Output Energy ($W.m^{-2}.nm^{-1}$)	19.55	30.08	14.91
Geometric Gain	1	1	1
OE (%)	2.79	4.36	2.18
Solar Concentration Ratio (%)	2.45	3.75	1.90
Integrated Emission Enhancement (%)	-------	+53.06 ***(REF=53)***	-22.44
Simulation Time (s)	3725.45	3896.92	4472.54

Fig. 5.26 shows rate of rays reaching the detector (to total incident ray) over different Au NS concentrations. The graph shows the comparison with 0 ppm device to obtain the enhancement and quenching regions. Above ~5.7 ppm Au NS concentration, the device enters the quenching region where quenching in the Au NS-QD coupling is more dominant than enhancement.

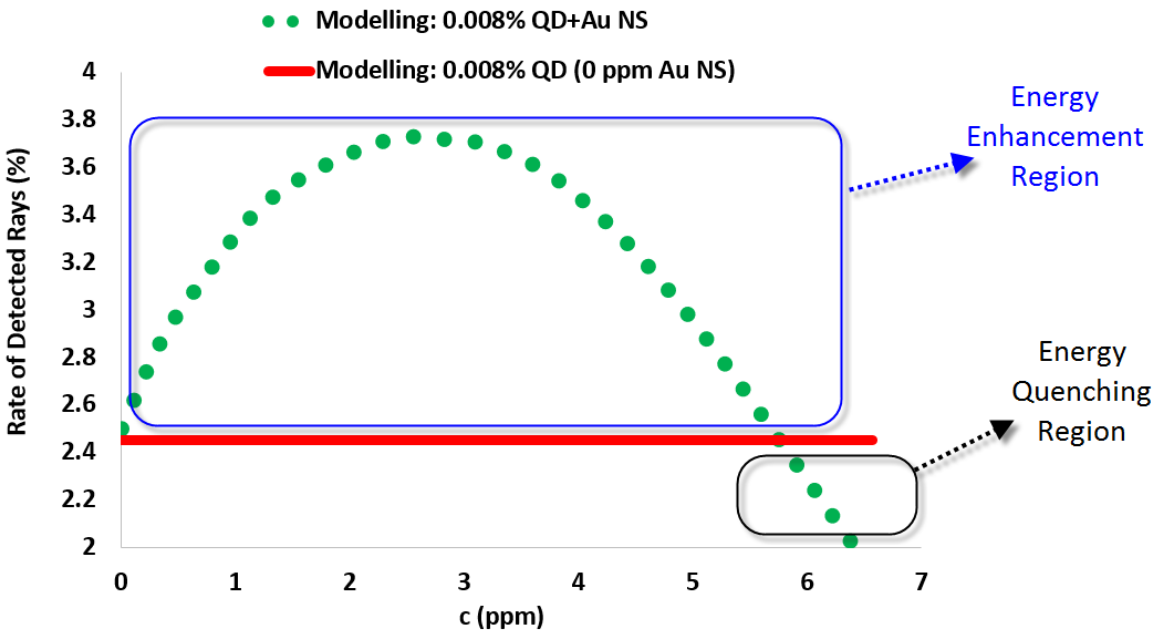

Fig. 5.26: Enhancement and quenching regions of Au NS concentration in the devices with 0.008 wt% QD concentration

Fig. 5.27a shows emission spectra for the devices with 0.01 wt% QD concentration (D6 to D9). By increasing concentration of Au NS from 0 to 2.20 ppm, emission peak increased from 938 a.u. to 1106 a.u. where the maximum enhancement was observed. Further increase in concentration of Au NS, resulted in increasing the rate of quenching and thermal loss which reduced emission spectra peak. At 6.5 ppm, emission peak decreased to 680 a.u. The complete trend of emission enhancement achieved in modelling is compared to experimental results for D6 to D9 and shown in Fig. 5.27b. As can be seen, modelling and experimental emission enhancement peaks were respectively 17.27% (at 2.2 ppm) and 16.8% (at 2 ppm for D9) and found to be in close agreement.

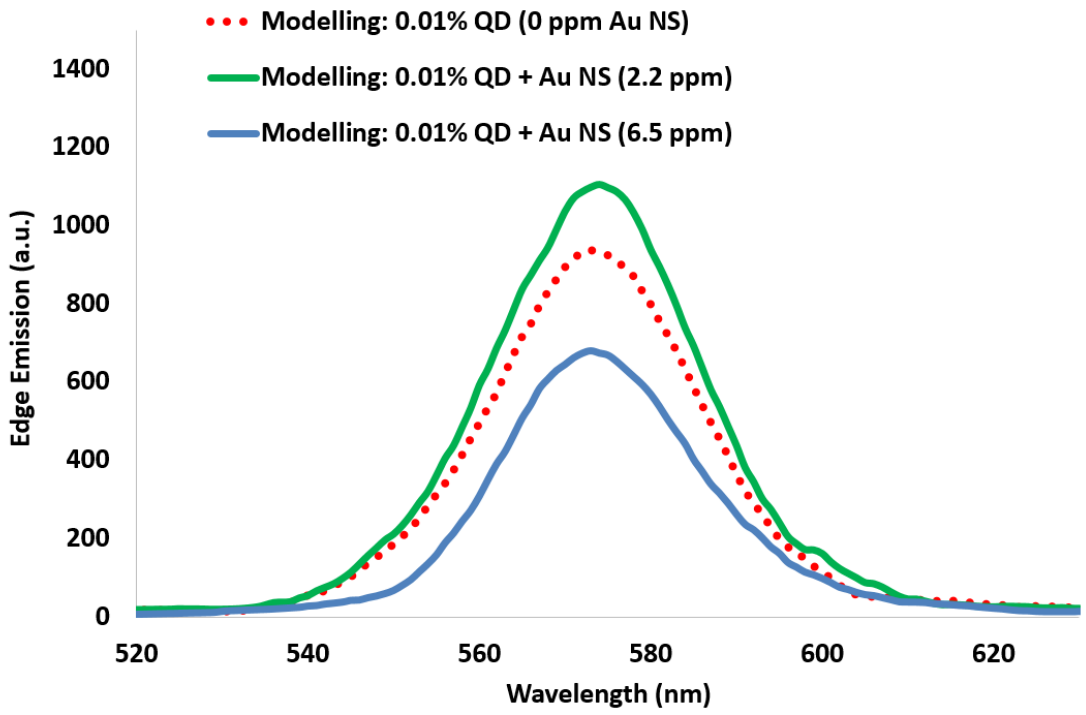

(a)

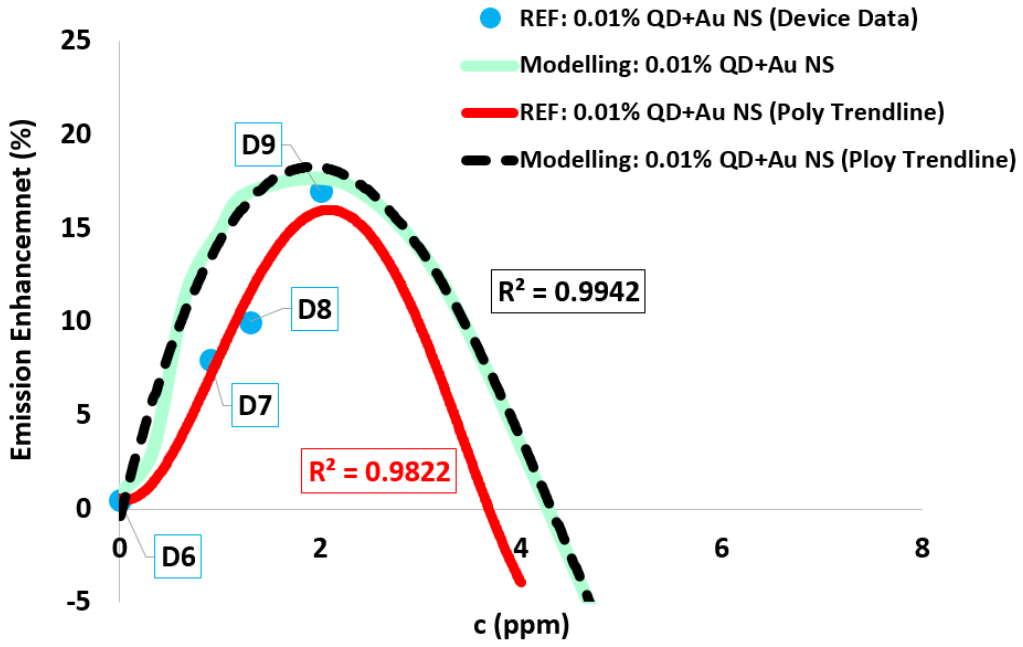

(b)

Fig. 5.27: (a) PEDAL Emission spectra for the best and worst concentration of Au NS compared with 0 ppm Au NS device (b) Comparison of the modelling and experimental emission enhancement trend (for D6 to D9)

Table 5-8 shows the detailed statistical PEDAL results for plasmonically enhanced devices with 0.01 wt% QD concentration compared with the conventional device. As presented, ~4% of the irradiated rays were reflected from the top surface and the rest of the rays (~96 %) were refracted inside the devices. When the device was doped with 2.2 ppm Au NS (Best Case), escape cone loss decreased from ~78% to ~74%. Total thermal losses increased from ~14% to ~17% due to the quenching effect. The rate of rays reaching the detector increased from 3.59% to 4.21% which increased the total output energy from ~28 $W.m^{-2}.nm^{-1}$ to ~33 $W.m^{-2}.nm^{-1}$. The optical efficiency also increased from 4.15% to 4.89% which enhanced the device integrated emission to 17.27% (close to the experimental enhancement of 16.8%).By increasing Au NS concentration to 6.5 ppm (Worst Case), thermal losses increased to ~24%. This decreased the rate of rays reaching the detector to ~2.61%. Total output energy also reduced to ~19.41 $W.m^{-2}.nm^{-1}$ which decreased optical efficiency to 2.85%. Total integrated emission rate decreased by ~27%.

Table 5-8: Detailed statistical PEDAL results for devices with 0.01 wt% QD 575 and different concentration of Au NS

Initial Number of Rays (Iteration)	1,000,000		
Doped Material	QD	QD + Au NS	
		Best Case	Worst Case
QD Concentration (wt %)	0.01	0.01	0.01
Au NS Concentration (ppm)	0	2.2 ***(REF=2)***	6.5
Reflected (%)	4.00	4.00	4.09
Refracted (%)	96.00	96.00	95.91
Total Thermal Loss (%)	14.18	17.11	24.17
Escape Cone Loss (%)	78.23	74.68	69.13
Reach at Detector (%)	3.59	4.21	2.61
Total Input Energy ($W.m^{-2}.nm^{-1}$)	619.68	619.68	619.68
Total Output Energy ($W.m^{-2}.nm^{-1}$)	28.71	33.83	19.41
Geometric Gain	1	1	1
OE (%)	4.15	4.89	2.85
Solar Concentration Ratio (%)	3.59	4.21	2.61
Integrated Emission Enhancement (%)	-------	+17.26 ***(REF=16.8)***	-27.58
Simulation Time (s)	3410.21	3839.61	4241.26

Fig. 5.28 shows the rate of rays reaching the detector over all concentrations of Au NS compared with the reference device of 0 ppm MNP. As can be observed, above ~4.2 ppm Au NS concentration, the device enters the quenching region.

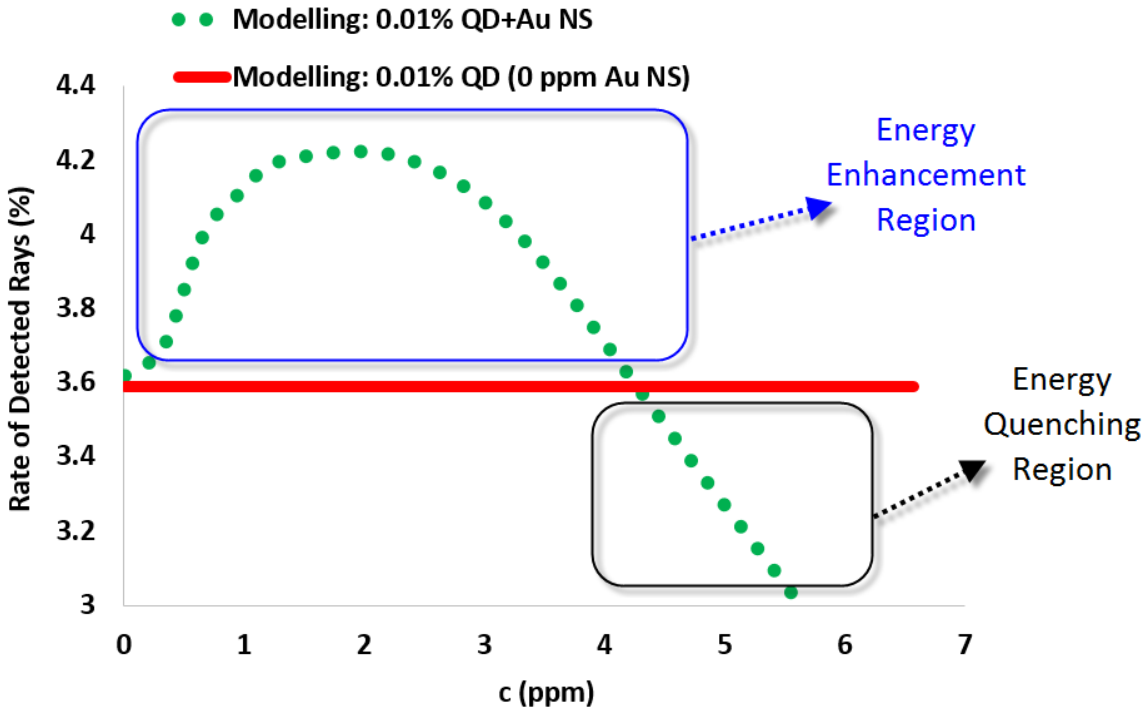

Fig. 5.28: Enhancement and quenching regions in the devices with 0.01 wt% QD concentration

Fig. 5.29 compares the emission enhancement of devices with different concentration of QD and Au NS. As it is shown, by decreasing QD concentration from 0.01 wt% to 0.008 wt%, Au NS concentration range which was required to keep the device in the enhancement region (positive side of the curve) was extended by ~35% from 0-4.2 ppm to 0-5.7 ppm. Moreover, the enhancement rate increased from ~17% (at 2.2 ppm) to ~53% (at 2.3 ppm). It has been observed that, by decreasing QD concentration, relative distance between QD and Au NS particles increased which decreased the probability of energy quenching. This can also be observed by comparing the third columns of Table 5-7 and 5-8 (Best Cases) where the rate of thermal loss decreased from ~17% (for 0.01 wt% device) to ~12% (for 0.008 wt% device).

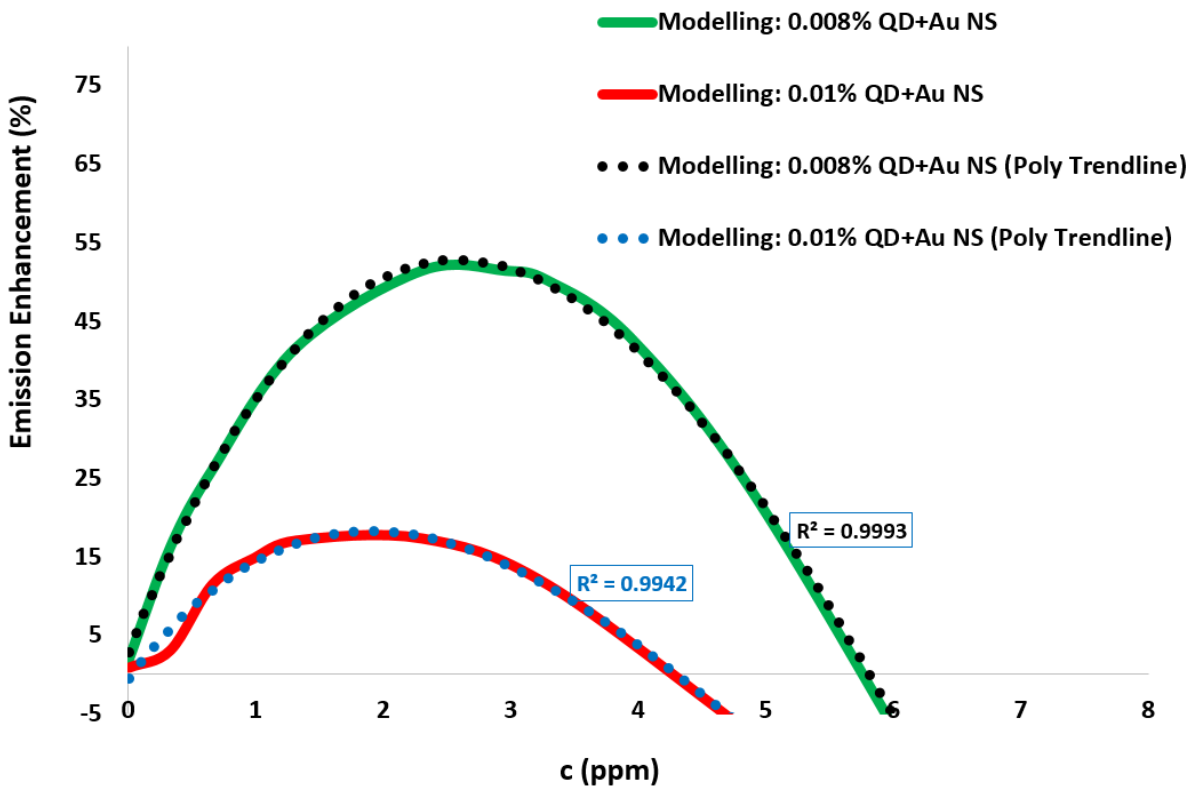

Fig. 5.29: Comparisons of device performance for 0.008 wt% and 0.01 wt% QD concentration

5.4. Sources of Discrepancy in Experimental and Modelling Results

The discrepancy between the modelling and experimental results is due to several factors such as measurement, human and fabrication errors as well as modelling.

- All equipment involved in the measurements have limitations and accuracy ranges. For example, in several concentration measurements using ICP machine, ~ ±10% error was observed. Almost the same trend was seen in SEM imaging where only a small random area (~1000nm×1000nm) of the whole device is focused and studied. This causes some measurement errors because the real device may not be homogeneously dispersed; therefore, results from different areas may not be the same.
- In SEM imaging, even the laboratory conditions such as interference (electric field) of other instruments and small vibrations could affect the accuracy of the results.

- In modelling, particles are considered to have exactly the same size, shape and orientation which may differ in fabricated devices. Different sizes and shapes of MNP generate different SPR energy levels in different wavelengths. This changes the optical properties of MNP (including the extinction spectra and PDEF) which ultimately changes the optical properties of the modelled pLS device.
- The coupling of device and detector in experimental measurements might not be implemented optimally which can also affect the results and cause discrepancy between the modelling and experimental results. For example, a study on quality of coupling (the details will be discussed in Chapter 6) showed that only 0.5 mm airgap between the device and detector results in intensity reduction of ~20% and ~ 35% for LDS and LSC, respectively.
- The surfaces of devices are not perfectly smooth in reality. However, all surfaces were considered with no roughness in the model. This might have resulted in further discrepancies between the experimental and modelling results.
- Some non-linear parameters could not be modelled. For example, chemical interference are not considered in the model which may non-linearly change the optical properties of the device.
- In addition, the effect of temperature changes and material degradation are not considered in the model.
- QY of luminescent species are changed as a function of host material and wavelength (Bronstein, 2015); however, QY is considered as a constant number over all wavelengths in the model
- Ray tracing is based on only the particle model of light. Note that the light has been described by either Wave or Particle model; however, the nature of light is more complex and none of the models are completely correct (Glassner, 1989).

5.5. Conclusion

This Chapter presented the proposed configuration and mathematical model for pLS devices used in the PEDAL development process. PEDAL was developed as a comprehensive tool to 3D model both LS and pLS device. The achievement of both ray tracing algorithm and FDTD

method have been combined and used in PEDAL algorithm. To decrease the simulation time and improve the performance of PEDAL, two techniques were introduced and validated:

First, using an AFI which reduces the number of iterations by filtering some portion of incident rays. Although simulation time was decreased significantly by this method (from 385463 to 7272 seconds for a LS device doped with CdSe/Zns Green QDs), the value of the accuracy was also reduced by ~12.3% due to the error of estimations.

The second technique was applied to model the device with high speed and accuracy at the same time. This version of PEDAL significantly decreased the simulation time (from 385463 to 139 seconds for the same device). The simulation results showed an excellent agreement with the experimental results with discrepancy error of ~1.7%.

A computational method was introduced and tested to convert the experimental unit of concentration from ppm to the modelling unit (N/L). The method was used for Au NS and Au NR particles and the modelling results were found to be in very close agreement with the experimental outputs. Using the validated method, a conversion graph was obtained for use in PEDAL which could convert concentration from ppm to N/L based on the shape and size of the particle.

PEDAL was validated for pLS device by comparing the modelling and experimental results of 9 samples with different Au NS and QD doping concentration. Average modelling accuracy of ~96% was observed in estimating the device enhancement. The results showed that by decreasing the QD concentration from 0.01 wt% to 0.008 wt%, the Au NS concentration band (where enhancement is occurring) was extended by ~35%. The enhancement rate also increased by ~34%. This is due to the relative distance between the QD and Au NS particles been increased which reduced the probability of energy quenching. This resulted in decreasing the rate of thermal loss from ~17% (for 0.01 wt% device) to ~12% (for 0.008 wt% device).

Chapter 6: Modelling and Optimisation

This Chapter models and studies a variety of configurations and structures of luminescent solar (LS) devices using PEDAL. This included modelling of new LS device configurations such as multi-layer thin-film luminescent solar concentrator (LSC), LSCs with near-unity quantum yield (QY) and complex configurations such as LSC cavity coupling to photonic selective mirrors (optical filter). Due to environmentally unfriendly impact of poly(methyl methacrylate) (PMMA) (Council, 2018), an LSC with polydimethylsiloxane (PDMS) host material was also modelled and validated. The model predicted results were compared with experimental results, which have been found to be in close agreement.

Although this thesis focuses more on PEDAL's abilities to model and investigate conventional and plasmonically enhanced LSC devices, it is also able to model luminescent down shifting (LDS) layers which is shown in modelling various configurations of single and multi-layer LDS devices.

The impact of nano rod (NR) alignment directionality on its optical properties was also studied. The technique can be used to characterise and optimise NR extinction spectrum and surface plasmon resonance (SPR) which can be used in optimisation of plasmonically enhanced luminescent solar (pLS) device.

6.1. Multi-Layer Thin-Film LSC

In this section, a two-layer LSC structure is modelled whose specifications are presented in Table 6-1 (Chandra *et al.*, 2018). It is a 25 × 25 mm structure consisting of 1 mm blank glass at the bottom layer and 10 μm epoxy thin film doped with Perylene based Lumogen F Red305 dye (BASF, Germany). The input solar radiation is downshifted through the thin film and then wave guided to the edges through the glass. Only one of the edges includes a detector and there is no mirror in the structure. Direct radiation was used in the experiment and modelling whose spectrum is illustrated in Fig. 6.1 showing intensity over wavelength. The experiment and simulation were applied for different doping concentrations of dye (0.1, 0.3, 0.5, 0.7 and 0.9 wt %) whose absorption coefficient can be observed in Fig. 6.2 with a peak at ~575 nm. The

emission spectra of the thin film can be seen in Fig. 6.3 whose peak is at ~610 with a stokes-shift of ~35 nm.

Table 6-1: Specifications of the two-layer LSC structure

Prosperities	Bottom Layer	Top Layer
Host Material Type	Glass	Epoxy
η	1.5	1.5
Length (mm)	25	25
Width (mm)	25	25
Thickness (mm)	1	0.010
Luminescent Material	-----	F Red305 dye
QY (%)	----	95

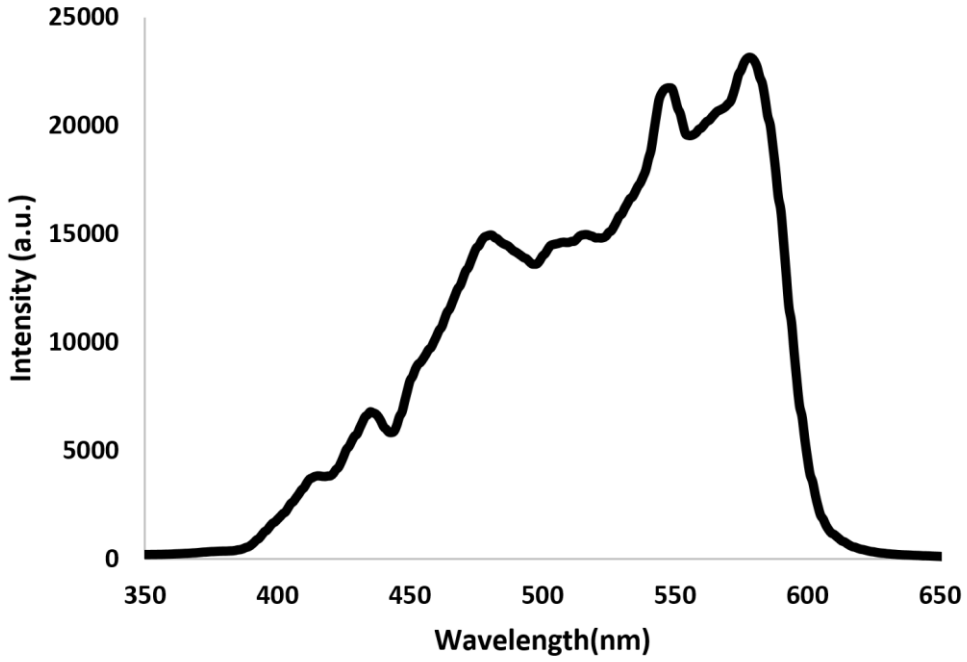

Fig. 6.1: Direct solar radiation spectrum used in the experiment and modelling

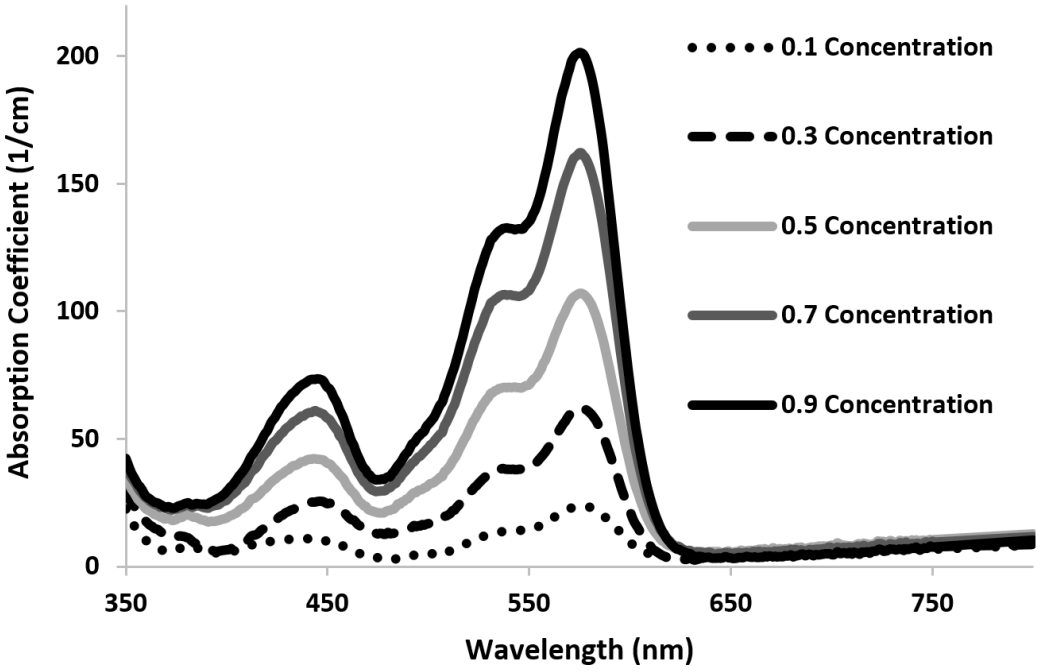

Fig. 6.2: Absorption coefficient for different dye doping concentrations of the thin film

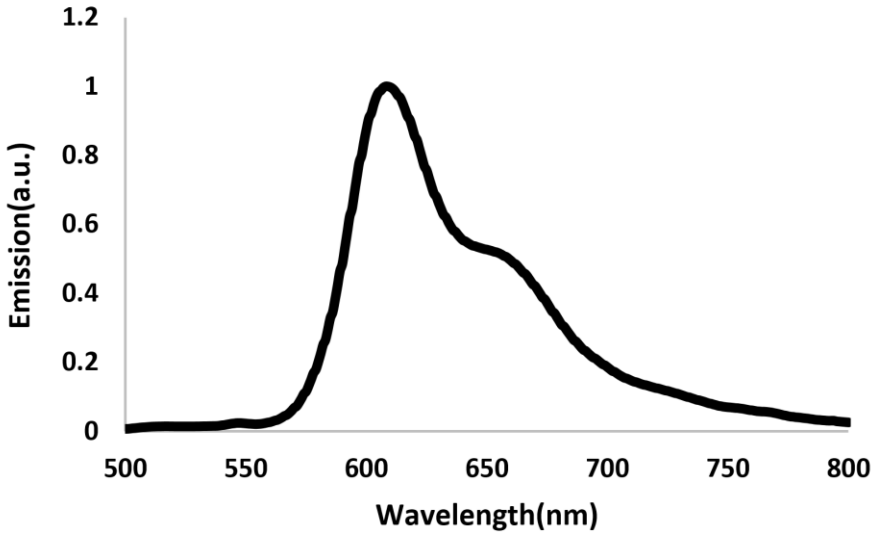

Fig. 6.3: Emission spectra of the thin film

Fig. 6.4 shows the visual configuration of the LSC structure while it was simulated under only 100 rays. There is no mirror used in the structure's planes and the detector was placed at the device edge.

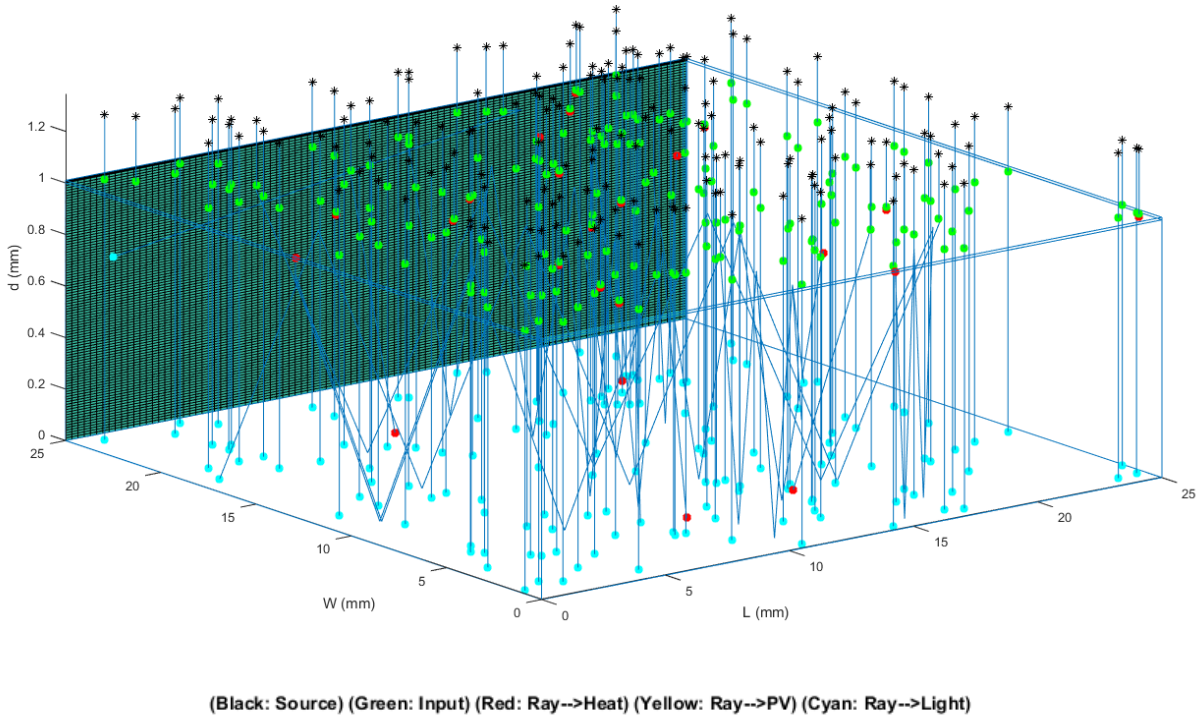

Fig. 6.4: Structure of the two-layer LSC under simulation of 100 rays

The program was run for ~5 million rays. Then, simulation and experimental results were compared for different dye doping concentrations (Fig. 6.5). The modelling and experimental results are in close match. Table 6-2 reports the statistical detail of modelling results. ~4% of rays were reflected from the top surface due to the mismatch of the refraction indices of air and the epoxy layer (η = 1.5). The rest of the rays were refracted (~96%) into the structure. By increasing the doping concentration, the absorption of the device increased which reduced the rate of escape cone loss and increased thermal losses. This also resulted in the highest value of optical efficiency (10.22%) at 0.7 wt% concentration. However, further increase in dye doping concentration reduced the performance of the device due to increasing the rate of re-absorption and thermal losses.

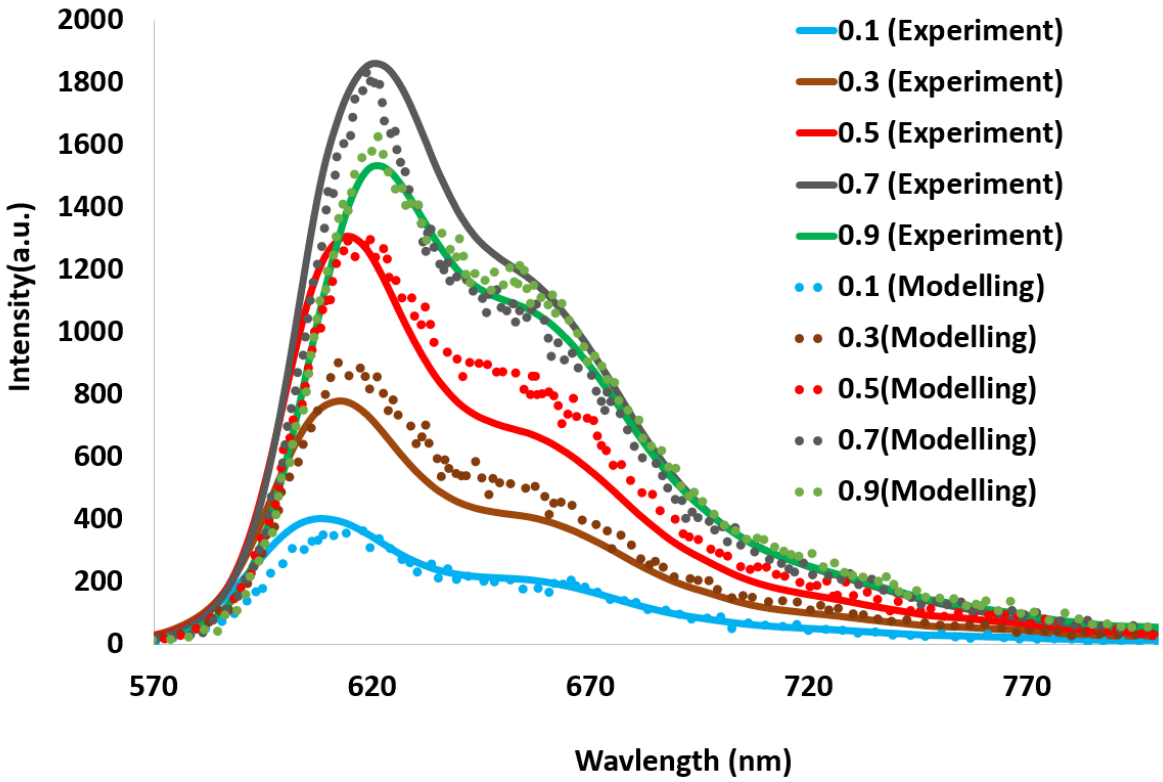

Fig. 6.5: Comparison of the simulation and experimental results in the Two-Layer LSC for different concentrations (wt%)

Table 6-2: Statistical Results achieved by the PEDAL modelling

Concentration (wt%)	**0.1**	**0.3**	**0.5**	**0.7**	**0.9**
Reflected (%)	4.01	3.98	4.01	3.99	3.98
Refracted (%)	95.99	96.02	95.99	96.01	96.02
Thermal Loss (%)	13.69	21.05	27.77	29.21	34.49
Exited the Edges (%)	80.88	71.65	63.33	55.93	55.65
Reached PV (%)	1.42	3.32	4.89	10.87	5.88
***OE* (%)**	1.03	2.66	4.08	10.22	5.14

6.2. LSC Devices with Near-Unity QY

6.2.1. LSC with PV Mounted at Four Edges

PEDAL was used to model a LSC where 86% QY was achieved for CdSe/CdS core/shell by optimizing the QD shell thickness (Coropceanu and Bawendi, 2014). QD was dissolved in transparent host material which was a mixture of monomeric precursor (lauryl methacrylate) and a cross-linker (ethylene glycol dimethacrylate) to fabricate a 2 × 2 × 0.2 cm LSC. The emission peak of the QD was at ~650 nm. The optical properties of the real device were obtained using an integrating sphere where the integrated emission of the device with covered edges (using black carbon paint) was subtracted from the integrated emission of the original device. This resulted in obtaining the integrating emission of the edges alone which was ~48% at 400 nm. In PEDAL, the edge emission was directly obtained by defining the detectors at the edges of the device. Fig. 6.6 shows the visualization of the modelled device under 100 direct rays.

Modelling results obtained under 1,000,000 input rays can be found in Fig. 6.7 where ~4% of input spectrum was reflected from the top surface of the device due to mismatching in refraction indices of air and polymer host material. The rest of the rays (~96%) were refracted inside the device. ~16% of radiation was lost due to escape cone loss. ~32% of rays were lost through thermal losses including the attenuation of host material, reabsorption and non-unity QY of QD. ~49% of rays reached the detector at the edges of the device which was in close agreement with experimental results (48%).

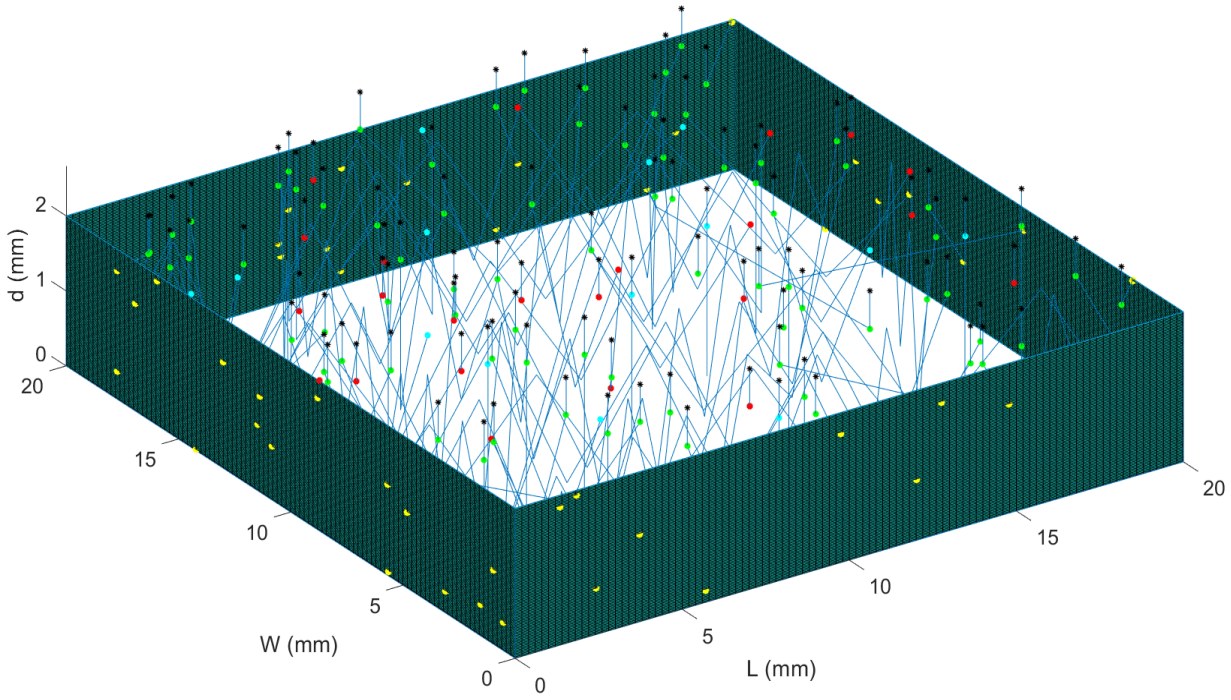

Fig. 6.6: Configuration of the modelled device under only 100 rays

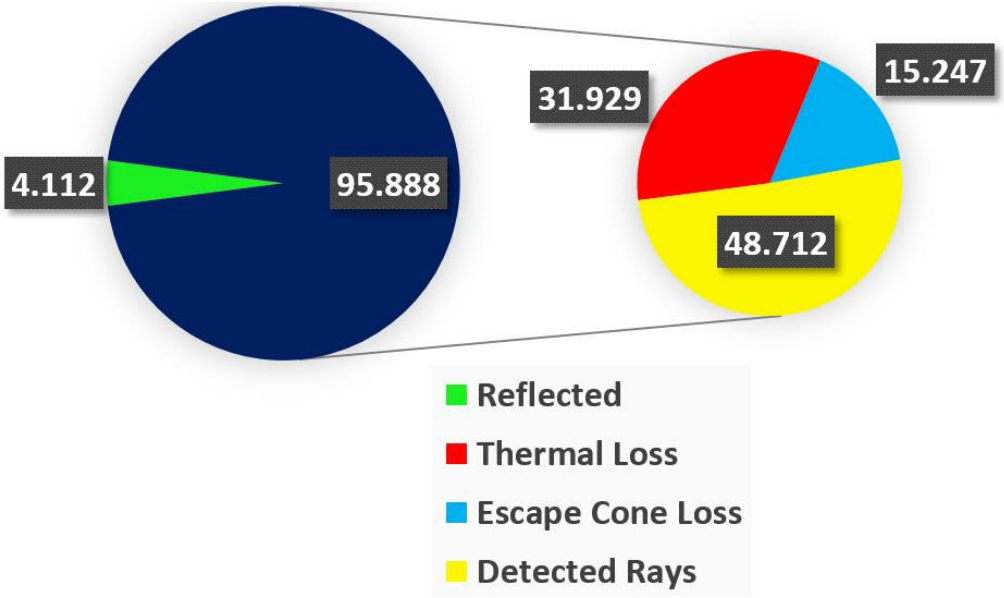

Fig. 6.7: Statistical modelling results for device under 1,000,000 incident rays (400 nm)

6.2.2. Optimization of LSC Cavity Coupled with Photonic Selective Mirror

To decrease the rate of escape cone loss and to trap more radiation inside LSC, Bronstein et al., 2015 introduced a cavity using a photonic mirror. The device comprised of a 30 μm polymer (poly[lauryl methacrylate] (PLMA)) with refraction index of 1.4 doped with CdSe/Cds QDs on top of a 180 μm quartz plate with a refraction index of 1.5 (Bronstein *et al.*, 2015). LSC had a width and length of 38 mm (1.5 inch). A silicon PV solar cell with dimensions of 1500×100×30 μm was installed inside the polymer acting as a detector. The side and bottom surfaces were covered by a mirror with high reflectivity (~0.99). Reflectance of the top wavelength-selective photonic mirror was a function of both incident angle and wavelength matched with the peak of emission spectrum of QD (~600 nm) (Bronstein, 2015).

Absorption of QD was below 500 nm. The mirror accepted high energy blue incident radiation from 350 nm to 520 nm with average transmission of ~90%. Over QD emission range (~600 nm), average reflectance of the photonic mirror was ~98% which resulted in trapping the emitted radiation. Due to using the photonic mirror, more red-shifted radiation was wave-guided in the device which increased the rate of rays reaching the PV solar cell. The configuration of the modelled device can be seen in Fig. 6.8.

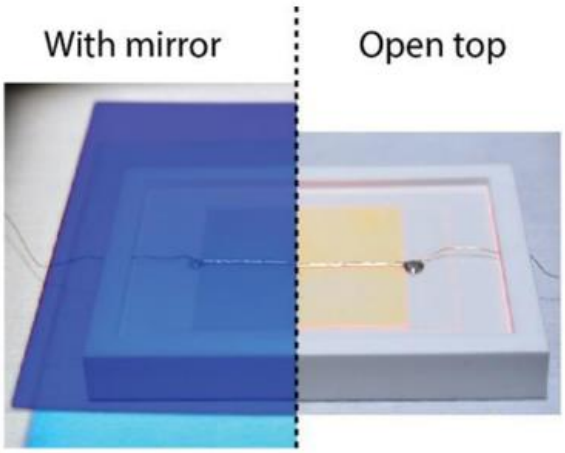

(a)

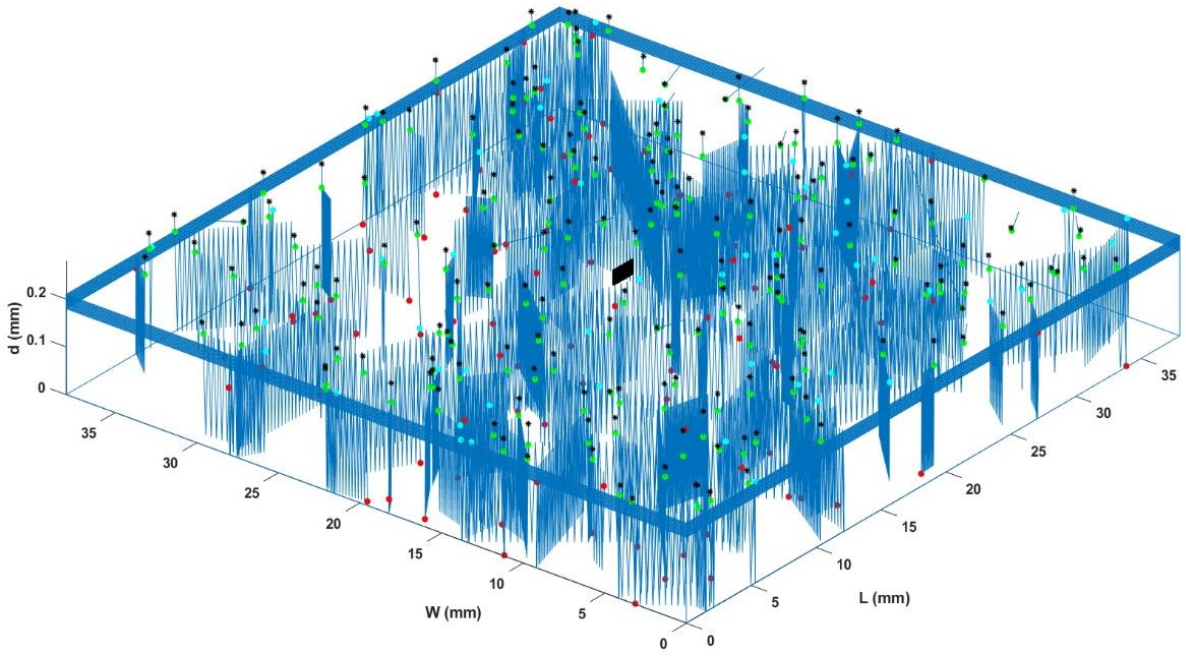

(b)

Fig. 6.8: (a) Configuration LSC cavity covered by photonic mirror which (b) was the modelled by PEDAL. The tiny silicon PV cell (black cube) was installed at the middle of the device acting as a detector

Both Open-Top and With-Mirror structures were modelled under 450 nm incident radiation matched with absorption range of QD where top mirror transmission is also high (~90%).

In the first stage, the model was used to obtain the optimised geometric gain (G_g) for the Open-Top device. While the optical depth (obtained from *Eqn* (2.29)) was kept constant (τ = 0.5), G_g was increased by changing the top aperture area. As can be observed in Fig. 6.9, increasing G_g, enhanced total solar concentration ratio (C); however, further than the optimum point (G_g = 60), no enhancement was seen in the performance of the device due to increasing the rate of thermal losses. Modelling results for optimum geometric gain closely matched the experimental results (G_g = 61).

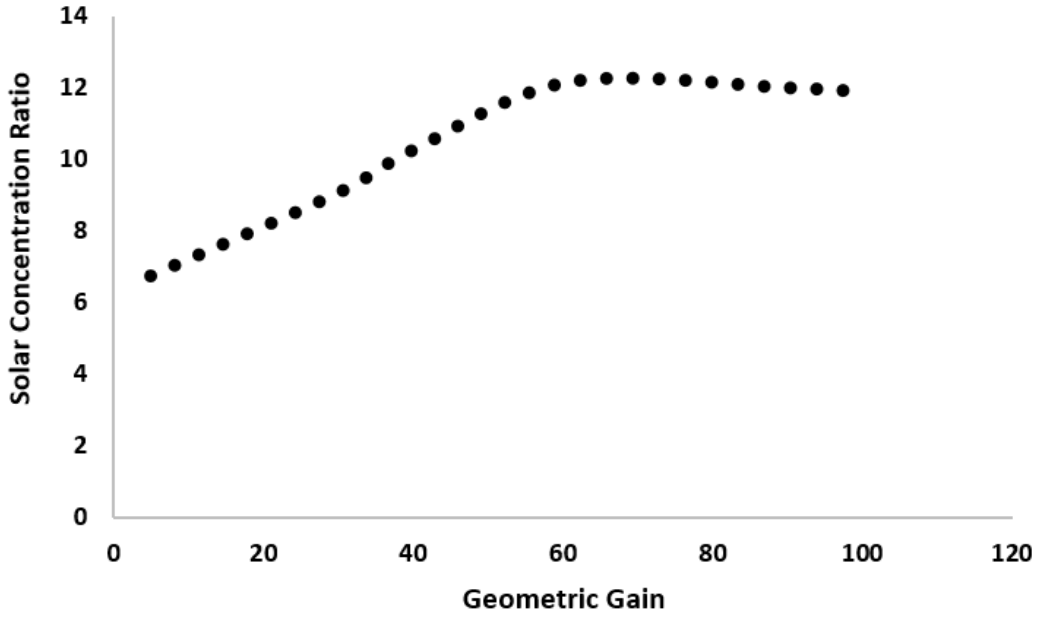

Fig. 6.9: Solar concentration ratio over geometric gain variation (for *QD* = 0.5)

By considering the optimised geometric gain (G_g = 60), the model was used to optimise QD concentration of both Open-Top and With-Mirror structures. As shown in Fig. 6.10, modelling and experimental *C* over τ were compared and found to be in close agreement.

In both devices, increasing τ from 0 to 0.65 increased *C* which was due to the increase in the rate of QD absorption and emission. However, for further values of τ, *C* mitigated because the density of doped QDs increased which increased the probability of non-unity QY and reabsorption losses. It appears that With-Mirror structure presented better performance in comparison with Open-Top device and could achieve ~30 *C* which was only ~15 for the Open-Top LSC.

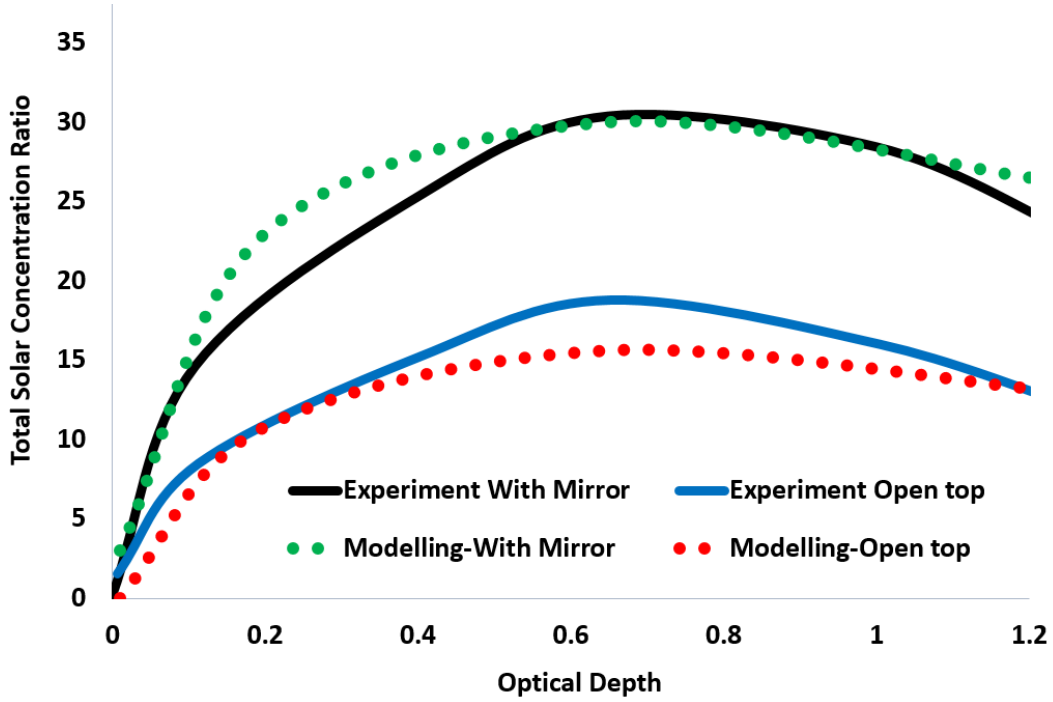

Fig. 6.10. *C* over τ for Open-Top and With-Mirror LSC under 450 nm incident radiation

Table 6-3 compares more statistical results obtained for both Open-Top and With-Mirror structures under 450 nm incident radiation. Using the photonic mirror on top of LSC resulted in decreasing escape cone losses from ~50% (in Open-Top) to 2% (in With-Mirror) which was due to high reflectance (~98%) of the top selective mirror at QD emission peak (~600 nm) resulting in trapping incident rays. Trapping more rays increased the rate of internal reflections (and photon path length) which mainly increased non-unity QY, attenuation and scattering losses inside the host material. This resulted in increasing thermal losses from ~12% in Open-Top to 43% in With-Mirror configuration. However, ~47% of rays reached the PV solar cell resulted in C≈30.

As thermal losses are quite high in LSC cavity (~43%), one method to increase the performance can be to use more transparent host materials which reduces attenuation losses.

Table 6-3: Statistical results achieved from the "Open-Top" and "With-Mirror" structure under τ of 0.65 and geometric gain of 60 under 450 nm incident radiation

	Best Results in: τ= 0.65 G_g=60	
	With-Mirror	**Open-Top**
Initial Incident Rays	1,000,000	
Reflected Ray (%)	10.00	15.83
Refracted Ray (%)	90.00	84.17
Escaped Rays (%)	1.8	49.92
Thermal Loss (%)	42.17	11.21
Reached PV (%)	46.03	23.04
C	29.28	14.51

6.3. Optimisation of LSC with Silicon PDMS Host Material

PDMS host material can be a future alternative for PMMA to reduce the environment impact (Council, 2018). In this section, an LSC with Silicon PDMS host material doped with red dye (Sethi, 2019) is modelled and optimised using PEDAL. LSC specifications can be seen in Table 6-4. Size of LSC is 45 × 45 × 3 mm and it includes no mirror while the detector is at one of the edges (shown in Fig. 6.11). The absorption and emission spectra of the luminescent material is shown in Fig. 6.12. The absorption peak is at ~550 nm and the emission peak is at ~600 nm with stokes-shift of ~50 nm.

Table 6-4: Specification of the LSC with Silicon PDMS host material doped with red dye

Host Material Type	Dimension (mm)	Luminescent Material	QY
Silicon PDMS	45 × 45 × 3	Red Dye	0.95

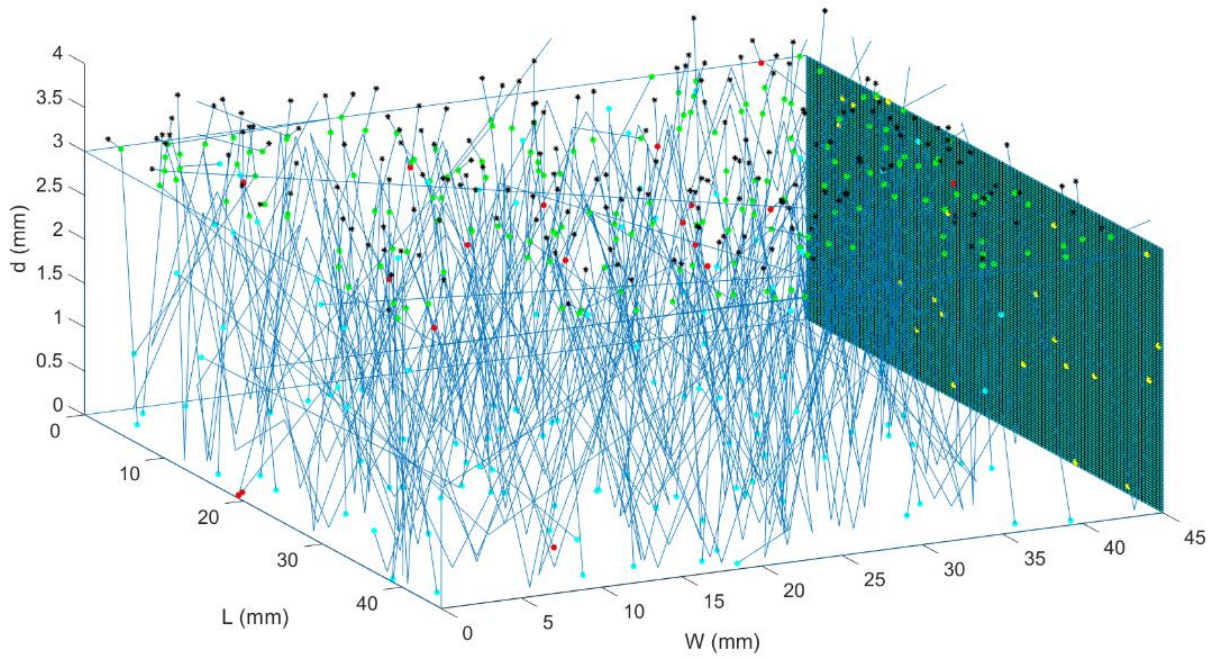

Fig. 6.11: Modelled LSC structure in the program while only 200 rays were irradiated to the device

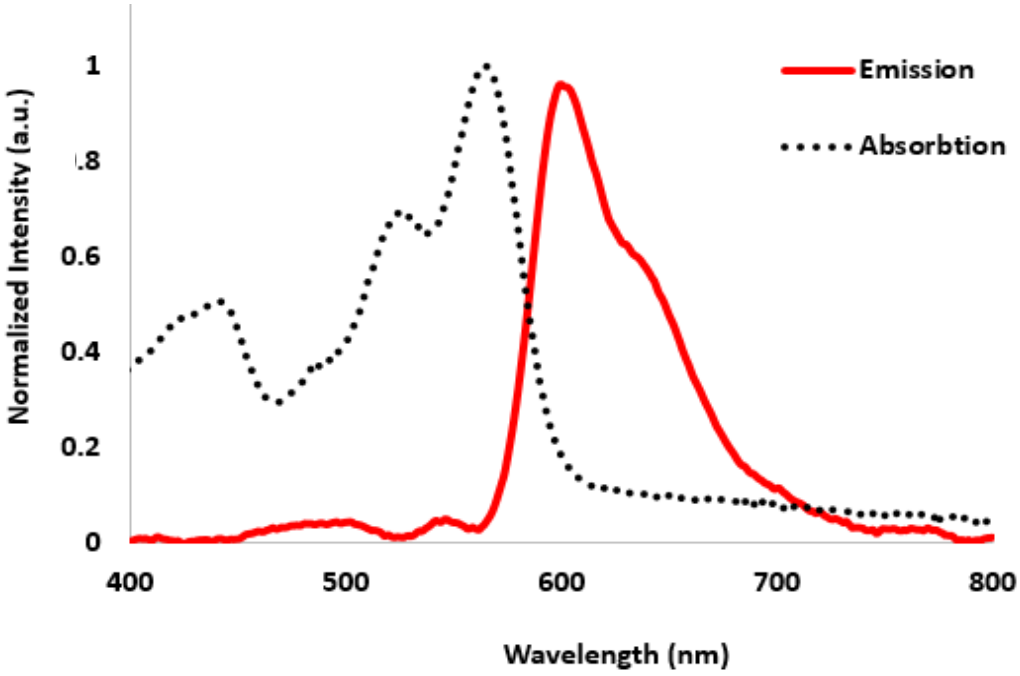

Fig. 6.12: Normalized emission and absorption spectra of red dye

LSC was modelled for dye doping concentrations of 10, 30, 70 and 100 ppm. Fig. 6.13 shows the comparison of experimental and modelling emission spectra at the edge of the LSC for different concentrations. By increasing the dye doping concentration from 10 to 100 ppm, peak of emission intensity increased. However, further increase in concentration, increased in the probability of re-absorption. Higher reabsorption increased the rate of thermal losses which reduced the performance of the device. This can be seen in detail in Fig. 6.14 showing the modelled and experimental integrated emission of the device over dye doping concentration. The modelled and experimental results are in close agreement. The device with ~70-100 ppm dye concentration was found to be the optimized device reaching the highest emission peak. Further increase in dye concentration could not enhance the performance and efficiency of the device due to increase in reabsorption losses.

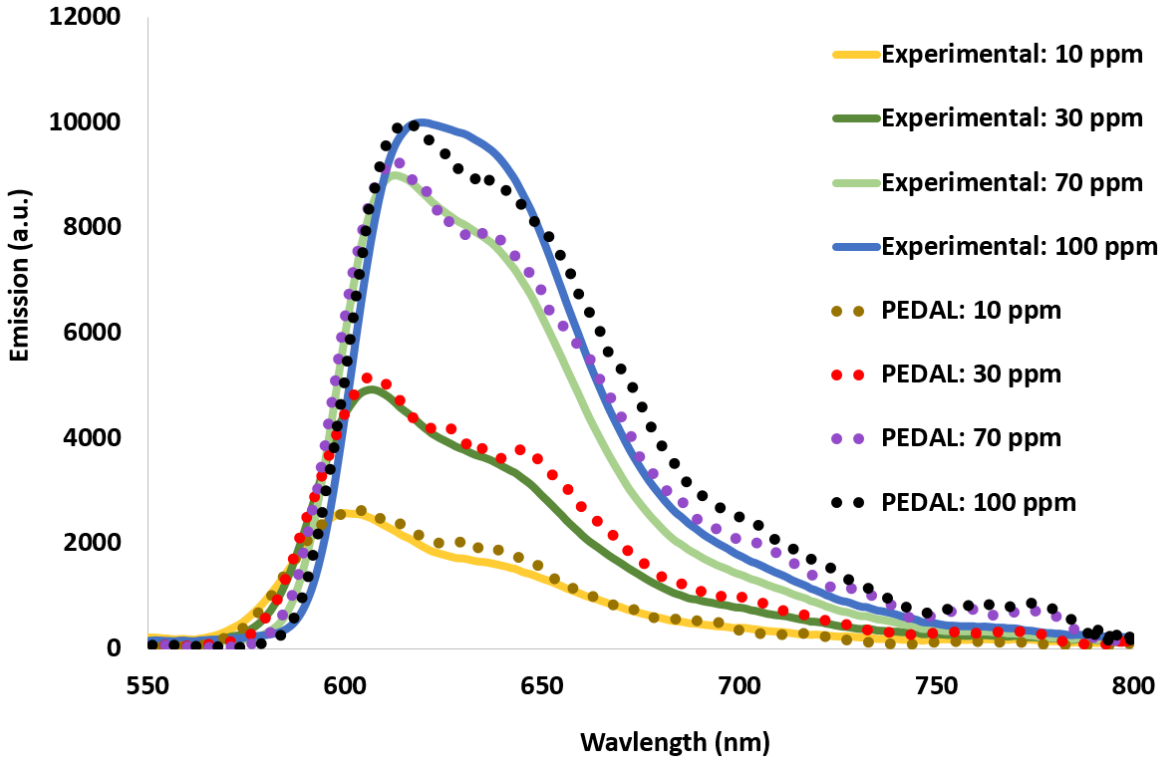

Fig. 6.13: Comparison of experimental and modelling emission spectra detected at the edge of the LSC for different doping concentration of dye

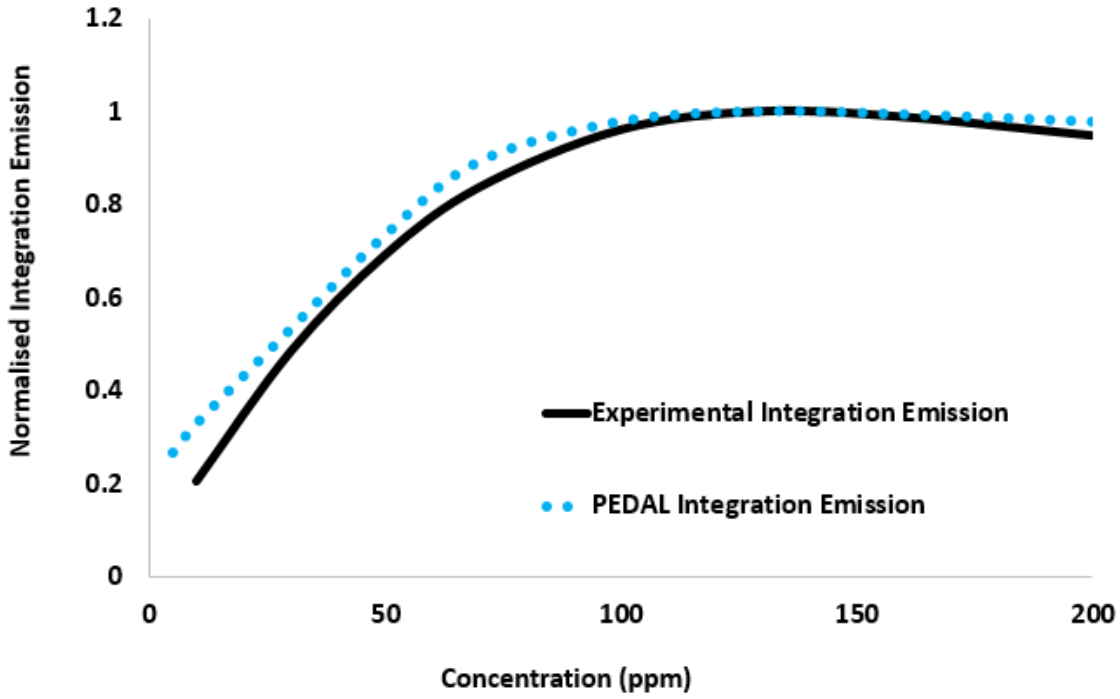

Fig. 6.14: Comparison of the normalized experimental and modelling integration emission at the edge of the LSC for different concentration of dye

Table 6-5 presents detailed statistics of modelling results. ~16% of rays were reflected from the top surface due to mismatched refraction indices of air and PDMS layer in all configurations. The rest of the rays were refracted (~84%) into the structure. By increasing the dye concentration from 10 to 100 ppm, the rate of thermal loss has increased from ~1.3% to ~8% due to the increase in non-unity QY and re-absorption losses. Best performance was observed for the device with 100 ppm dye concentration with optical efficiency of ~8.25%.

Table 6-5: Statistical results achieved by the PEDAL model for the LSC

Concentration (ppm)	10	30	70	100
Reflected (%)	15.90	15.74	15.91	15.90
Refracted (%)	84.10	84.26	84.09	84.10
Thermal Loss (%)	1.29	2.46	4.34	8.30
Escape Cone Loss (%)	76.64	73.28	69.51	64.47
Reached PV (%)	6.17	8.52	10.24	11.33
Geometric Gain	15			
OE (%)	4.78	6.42	7.57	8.25

6.4. PEDAL for Luminescent Down Shifting (LDS) Layer Analysis

This thesis mostly focuses on using PEDAL for modelling and investigating various types of LSC and pLSCs. However, PEDAL is also capable of modelling and investigating different configurations of LDS and pLDS devices which were not studied here due to time limitations and lack of enough experimental data required for validation. To show the capability and reliability of PEDAL for this application, various configurations of LDS devices are presented in the following sections.

6.4.1. Multi-Layer LDS Device Modelling

PEDAL was used to model an LDS device (Klampaftis and Richards, 2011) in which mc-Si PV encapsulated by a poly-ethylene vinyl acetate (EVA) was doped with Lumogen-F violet 570 dye (BASF).

The specification of the LDS device is presented in Table 6-6. It is a two-layer 77 × 77 mm device including 0.5 mm EVA encapsulation layer with refraction index of 1.51 covered by 3.3

mm glass with η = 1.5. Absorption and emission spectra of the doped luminescent material is presented in Fig. 6.15.

Table 6-6: Configuration mc-Si PV cell with encapsulated layer doped with violet dye (Klampaftis and Richards, 2011)

Prosperities	Encapsulation Layer	Top Layer
Host Material Type	EVA	Glass
η	1.51	1.5
Length (mm)	77 mm	77 mm
Width (mm)	77 mm	77 mm
Thickness (mm)	0.5 mm	3.3 mm
Used Luminescent Material	Lumogen-F violet 570 dye	-----
Quantum Yield (QY)	90%	-----

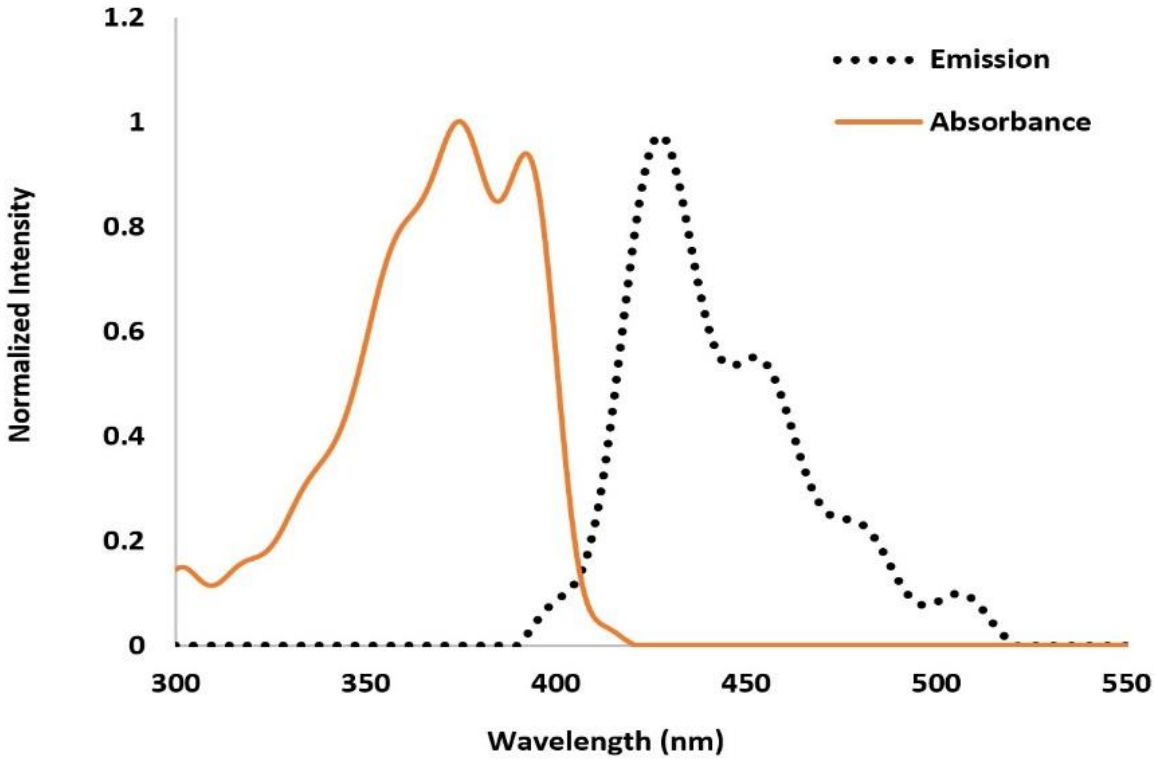

Fig. 6.15. Normalized emission and absorbance spectra of Lumogen-F violet 570 dye used for the enhanced PV device

PEDAL used AM1.5 global solar radiation (NREL, 2019). Fig. 6.16 shows the visualization of the simulation for 100 incident rays and their final fate inside the device (Rafiee *et al.*, 2018a).

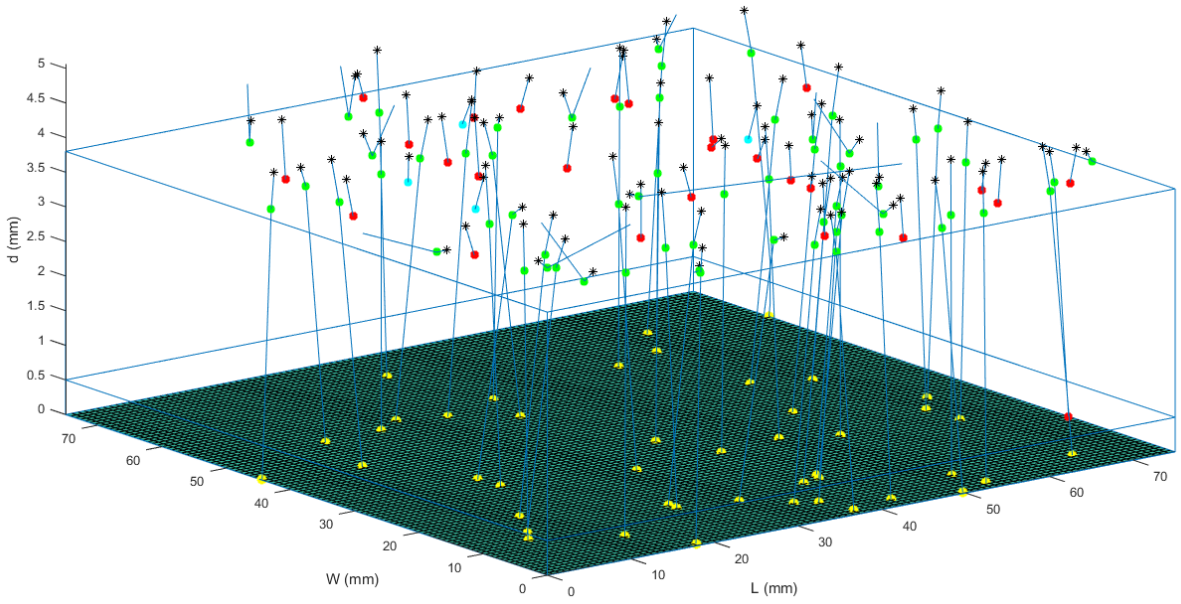

Fig. 6.16. Multi-layer LDS device under simulation of 100 rays: PV is the black plane at the bottom of the structure. The black spots show the solar radiation source, the green spots show the first intersection point of the input rays with the top plane. Red spots were the rays which were lost as heat due to the reabsorption or attenuation of the host material. The yellow spots show the rays which reached the PV and the cyan spots illustrate the rays which were lost as the escape cone loss

The number of incident rays increased to enhance modelling accuracy. Table 6-7 shows the statistical results predicted by PEDAL for 1,000,000 incident rays (AM 1.5G). ~18% of rays were reflected due to angular difference between the incident rays and normal vector of top surface (θ_i); moreover, mismatch of the refraction indices of air and the glass layer. The rest of the rays were refracted (~83%) into the structure where ~7% of them were lost due to the loss mechanisms such as escape cone and thermal losses such as attenuation, scattering and reabsorption losses. The rest of the rays (~76%) were detected by the PV cell. Due to using luminescent material inside the encapsulation layer, current density (J_{SC}) of PV was increased from 31.30 to 31.38 mA/cm^{-2} and resulted in increasing the solar cell efficiency from 14.93% to 15.07%. Moreover, it can be observed that the modelling and reference results for J_{SC} are closely matched and the discrepancy error was less than 1%.

Table 6-7: Statistical Results achieved by the PEDAL modelling

Parameter		Quantity
Number of Irradiated Photons		1,000,000
Reflected (%)		17.29
Refracted (%)		82.71
Thermal Loss (%)		0.15
Escape Cone Loss (%)		6.11
Reached PV (%)		76.45
J_{SC} (mA/ cm^{-2}) (Bare PV Solar Cell)	Reference(Klampaftis and Richards, 2011)	31.30
	31.33	
J_{SC} (mA/ cm^{-2}) (LDS-PV Device)	Reference(Klampaftis and Richards, 2011)	31.38
	31.37	

Fig. 6.17 compares the modified external quantum efficiency (EQE) of the LDS device with the reference EQE of the bare mc-Si PV solar cell. As is exhibited, the modelling and reference spectra are in close agreement. The LDS layers increased EQE from 25% to 35% at 300 nm, and by 15% in the region between 300 to 400 nm.

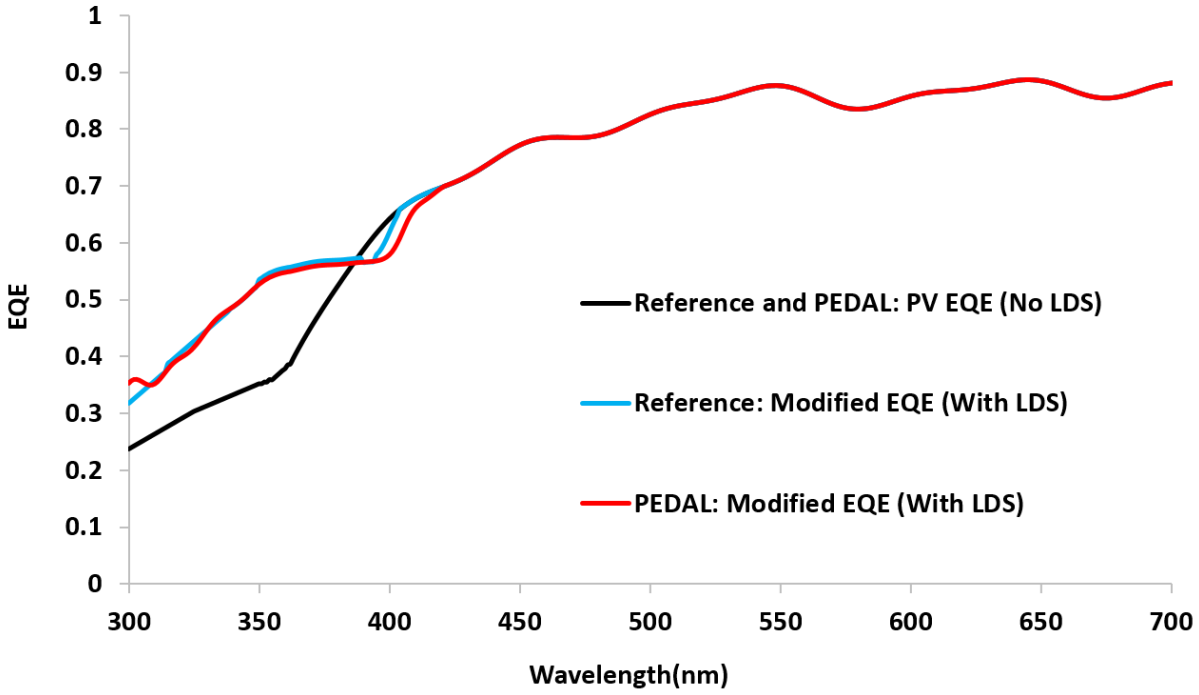

Fig. 6.17. Comparison of modified EQE of the enhanced device with EQE of a bare PV cell

6.4.2. Investigating the Effect of Loss Mechanisms on LDS Device Performance

In this section, an LDS doped with EU^{3+} complex (Liu *et al.*, 2013a) is modelled (Rafiee *et al.*, 2017a). Absorption and emission spectra of the luminescent material is presented in Fig. 6.18 where absorption spectrum covers 250-400 nm and the emission peak is at ~610 nm which provides a large stoke-shift of ~260 nm. The size of the LDS layer is 156 cm^2 with 0.15 mm thickness, deposited on top of c-Si PV. The solar radiation used in the experiment and modelling was AM 1.5 global solar radiation. The doping concentration of the EU^{3+}complex was 1%.

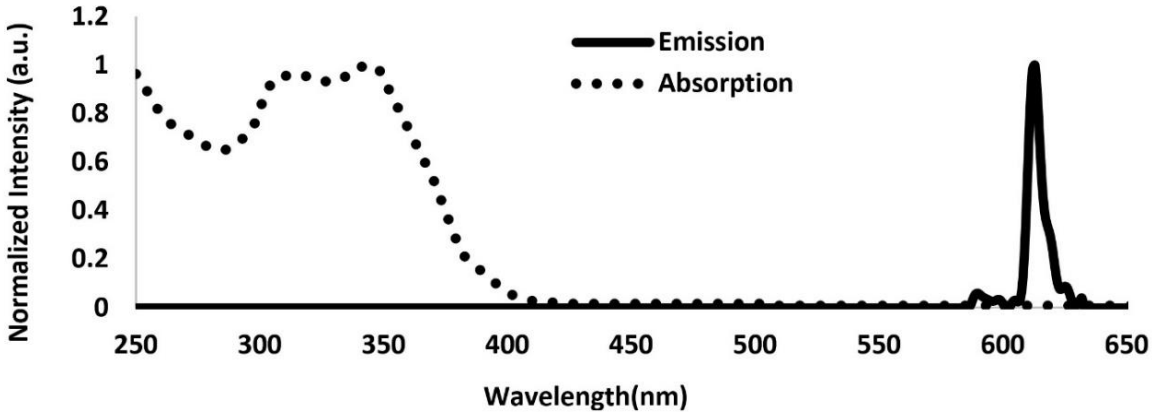

Fig. 6.18: Normalized emission and absorption spectra for EU complex (Liu *et al.*, 2013a)

LDS based PVA layer was simulated under 250,000 rays while all loss mechanisms were considered in the model. Fig. 6.19a shows the simulation and experimental output spectra of the LDS (in arbitrary units) which are compared with the input solar radiation of the LDS layer. The output spectrum of the LDS layer has a peak at ~610 nm which is due to the emission peak of the EU^{3+} complex. It is also red-shifted by 60 nm (from 300 nm to 360nm) in comparison with AM 1.5G solar radiation due to the absorption band of the EU^{3+} complex. Fig. 6.19b shows the simulation and the experimental EQE_{LDS} sprectra in comparison with the *EQE* of uncoated PV. EQE of the PV is significantly improved by ~46% in the wavelength range of 300-365 nm by LDS layer

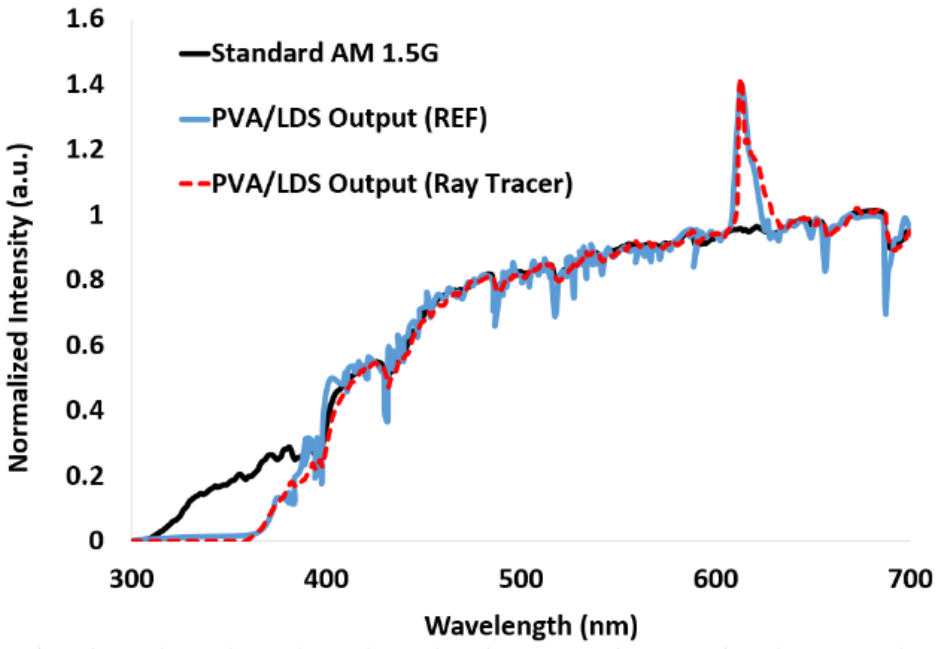

(a)

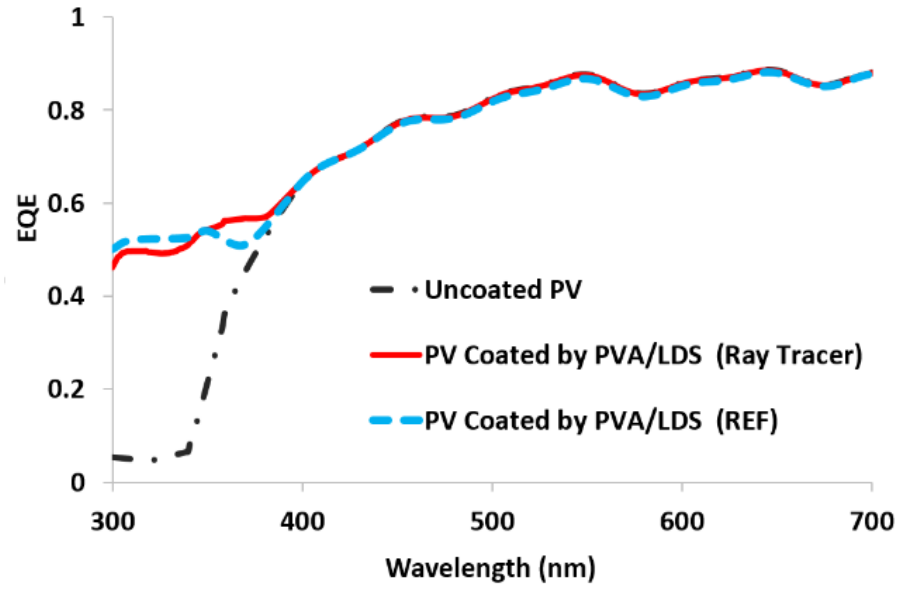

(b)

Fig. 6.19: (a) Output spectrum of the LDS based PVA layer obtained from modelling (red) and experimental (blue) in comparison with the input solar radiation spectrum (black). The spectra are normalised to AM1.5G solar radiation. (b) Modelling (red) and experimental (blue) EQE curves in comparison with the EQE of uncoated c-Si PV cell (black)

LDS layer was also modelled without counting the loss mechanisms of the PVA matrix material such as attenuation and scattering losses. As can be seen in Fig. 6.20, the modelling and experimental spectra are not well-matched in this case. This clearly shows the effect of including material losses in the LDS modelling.

In the next step, LDS based epoxy, glass and PMMA were simulated under the same conditions for the LDS layer (Fig. 6.21). The trend and position of peaks in all layers are similar; however, red-shifting and peak values are different. This is due to different attenuation and scattering losses caused by different host materials.

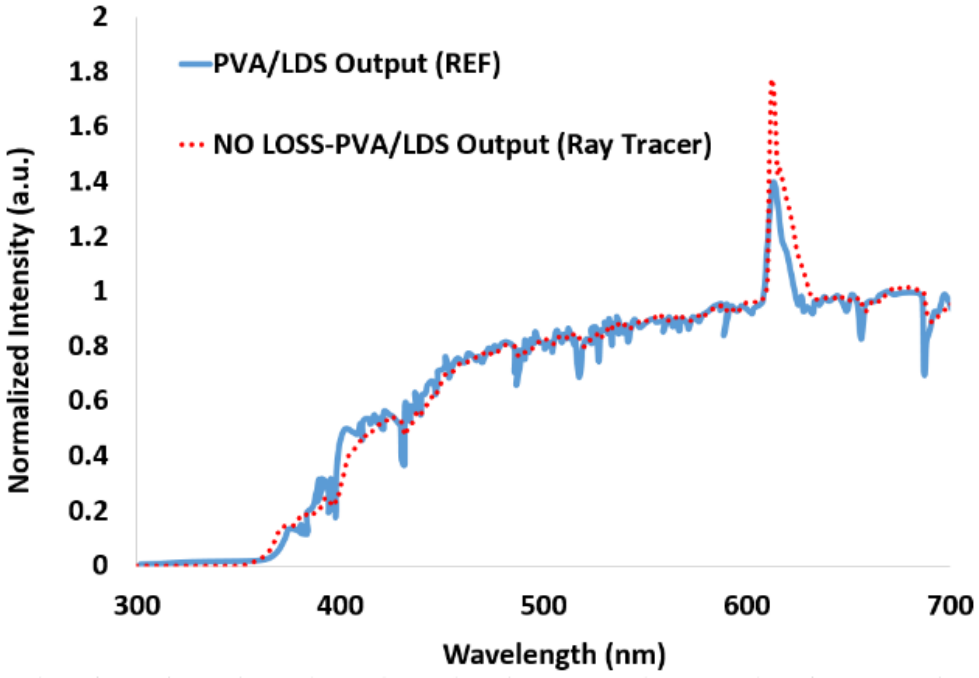

Fig. 6.20: Output spectrum of the LDS based PVA layer obtained from modelling (red and no loss mechanisms is counted) and experimental (blue). The spectra are normalised to AM1.5G solar radiation

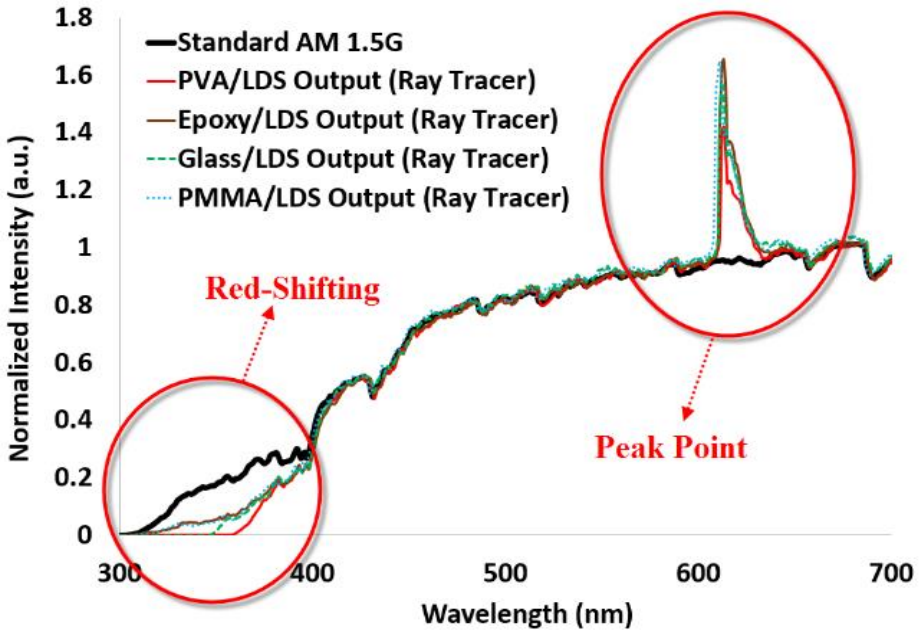

Fig. 6.21: Output spectrums of LDS layers based, epoxy, glass, PMMA and PVA compared to the solar radiation spectrum. The spectra are normalised to AM1.5G solar radiation

The statistical modelling results are summarised in Table 6-8. In the LDS based PVA modelling, ~17% of rays are reflected after striking the top surface of the LDS layer due to different θ_i and mismatching in refraction index of air (1) and the PVA film (1.49). It has been found that, 2.7% of rays were lost as thermal losses which is due to either attenuation loss of the PVA matrix material or non-unity QY of the luminescent material. Majority of rays (~80%) reached the PV cell at the bottom layer which resulted in approximately 79% optical efficiency and a 31.39 $\mathrm{mA.\,cm^{-2}}$ current density. It is observed that by including the loss mechanisms, the model is validated and the simulation results are in excellent agreement with experiments (maximum 2.2% discrepancy error in peak). In the case where no attenuation or scattering losses were included, the rate of thermal losses decreased from 2.69% (in PVA modelling) to 1.01%. This resulted in the final optical efficiency of 81%, current density of 31.41 $\mathrm{mA.\,cm^{-2}}$ and discrepancy error of ~27%. Using epoxy as the matrix material of LDS, the lowest rate of thermal loss (0.87%) was achieved in comparison with other host materials. This resulted in the highest optical efficiency (81.52%) and current density (31.41 $\mathrm{mA.\,cm^{-2}}$).

Table 6-8: Statistic results for LDS devices modelled with different matrix materials

Modelled Matrix Material	**PVA**	**Without Loss**	**Glass**	**Epoxy Resin**	**PMMA**
Reflected (%)	17.03	16.86	17.05	16.99	16.92
Refracted (%)	82.97	83.14	82.95	83.01	83.08
Thermal Loss (%)	2.69	1.01	2.44	0.87	1.02
Exited the Edges (%)	0.01	0.01	0.003	0.01	0.01
Reached PV (%)	80.27	82.12	80.50	82.13	82.05
OE (%)	79.45	81.31	79.85	81.52	81.43
$\mathbf{J_{sc}}$ $(\mathbf{mA.cm^{-2}})$	For Uncoated PV : 31.19 mA. cm^{-2}				
	31.39	31.41	31.39	31.41	31.40
Red-Shifting (nm)	In REF: 63nm				
	60	53	48	15	18
Discrepancy Error in Peak Point in Comparison with the REF PVA Layer (%)	2.2	27.34	13.77	19.57	18.84

6.4.3. Optical Coupling Sensitivity Study

LSC of 60 × 60 × 3 mm and LDS of 100 × 100 × 0.01 mm with epoxy and PMMA host material, respectively were modelled with PEDAL (Rafiee *et al.*, 2020). The specifications of the devices are summarized in Table 6-9. AM1.5 global solar radiation (NREL, 2019) was used to generate the incident photon flux for modelling. Both devices were doped with CdSe/ZnS QDs with QY of 85%. QD emission and absorbance spectra are shown in Fig. 6.22. QDs absorbed solar radiation below 500 nm with an absorbance peak at 460 nm. Emission of the QD was a gaussian spectrum in the region between 430 to 530 nm with a peak at ~485 nm which resulted in a stokes-shift of ~ 25 nm.

Table 6-9: Configuration of the modelled LSC and LDS devices

	LSC Device	LDS Thin Film
Radiation Type	AM1.5G	AM1.5G
Host Material Type	Epoxy	PMMA
Length (mm)	60 mm	100 mm
Width (mm)	60 mm	100 mm
Thickness (mm)	3 mm	0.01 mm
Geometric Gain	20	1
CdSe/ZnS QY	0.85	0.85

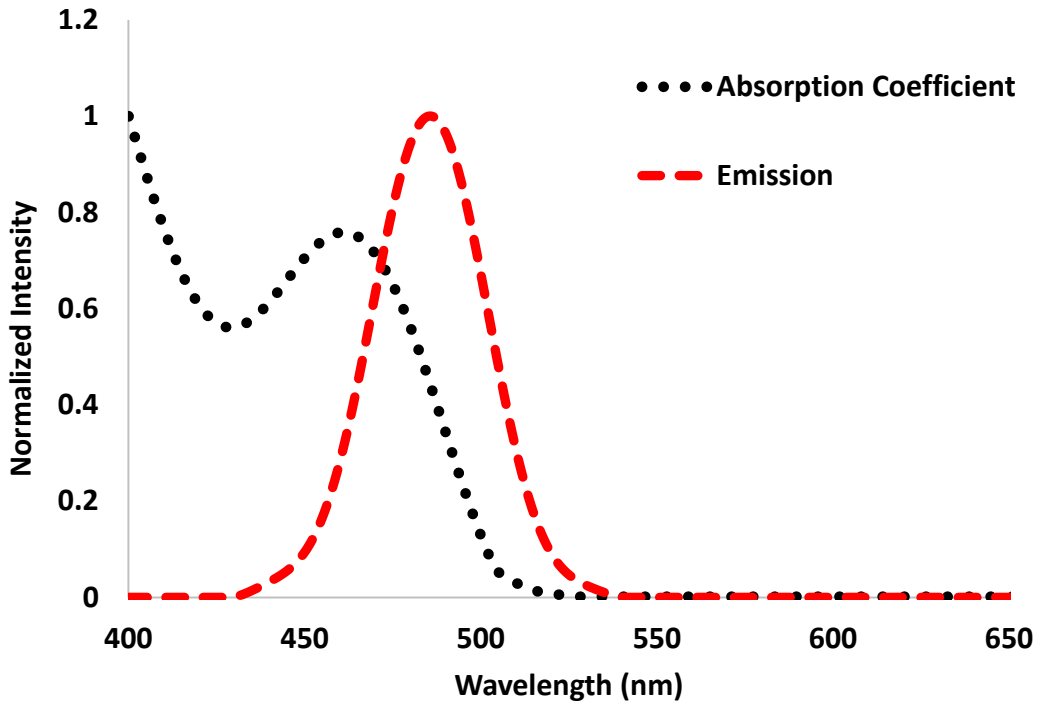

Fig. 6.22: Normalized absorption coefficient and emission spectra for CdSe/ZnS QD (Kennedy, 2010)

Both devices (shown in Fig. 6.23) were modelled under similar conditions and inputs. Top surface reflection was ~17% for both devices due to the close refraction indices of host materials

($\eta \approx 1.5$). The rest of the photons (~82%) were refracted into the layers. The devices were modelled for different airgap thicknesses (G = 0 to 2 mm) between the luminescent layer and PV solar cell.

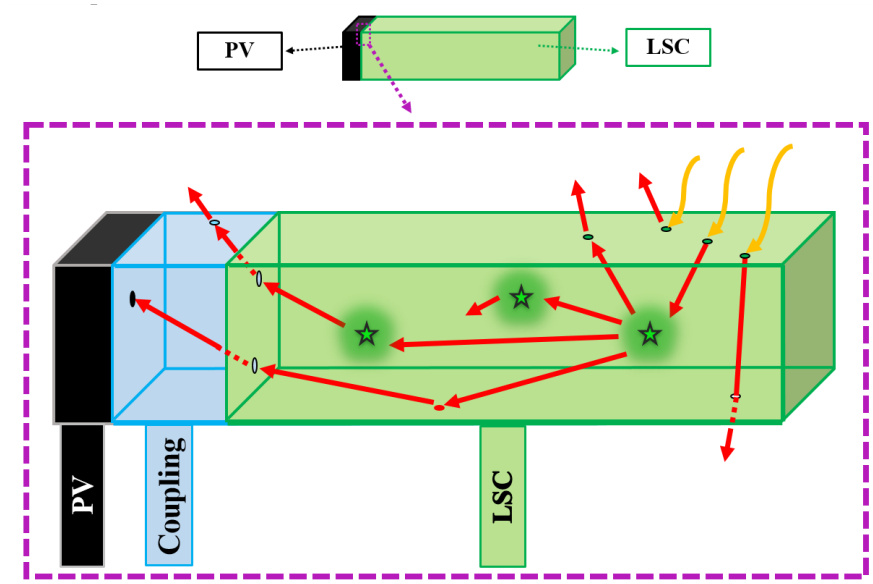

(a)

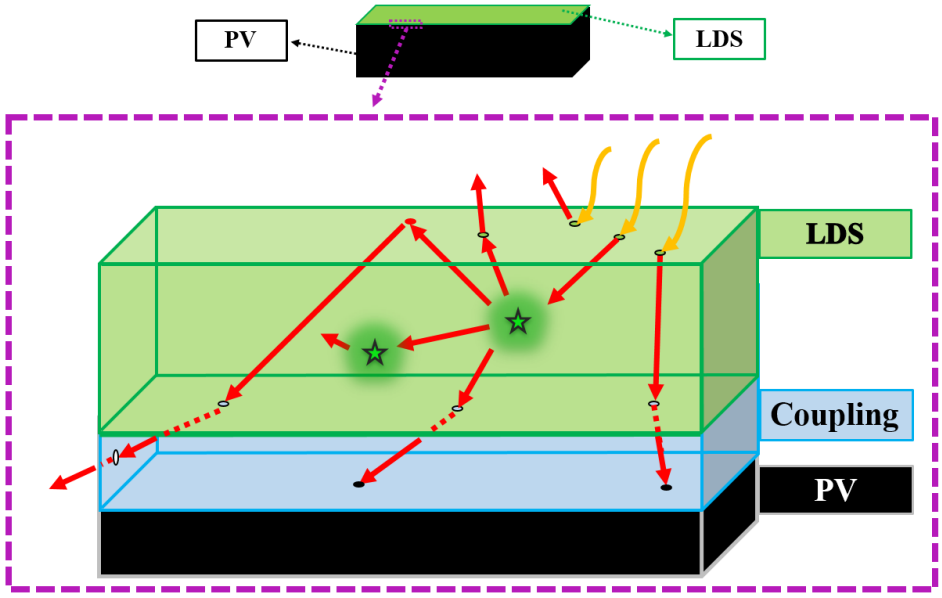

(b)

Fig. 6.23: Configuration of an (a) LSC and (b) LDS devices modelled to study the optical coupling impacts – you need to explain the numbers in the figure

.

Fig. 6.24a shows the total optical efficiency (OE) over the airgap variations for the LDS device. Overall, the airgap between the LS devices and PV solar cell should be kept as small as possible. OE significantly decreased from ~82% to 76% when *G* increased by only 0.1 mm. Further increase in *G* from 0.1 to 2 mm, resulted in OE decreasing smoothly to ~66%.

The initial fall in the optical efficiency of the LSC with air gap thickness was significantly less steep for the LSC than the LDS device (Fig. 6.24b), under perfect optical coupling conditions (*G* = 0 mm), OE was ~2.79% which decreased to 2.16% when *G* increased to 0.5 mm. Above *G* = 0.5 mm, OE decreased with less steep slope and reached 1.85 at *G* = 2 mm.

Table 6-10 presents detailed statistical modelling results where it can be seen that for LDS, by increasing the airgap from 0 to 2 mm, 15.5% increase was found in the rate of the photons exiting the edges. Moreover, thermal losses increased by ~0.32%. Increase in the edge losses was due to the photon deviation in the airgap as a result of refraction index differences. The increase in thermal losses was because of the increase in photon pathlength resulting in higher attenuation losses inside the airgap. These losses decreased the rate of photons reaching the bottom-mounted PV from ~82% to 66%. As a result, ~19% deduction ($\Delta\eta_{opt}$) was observed in the performance of the device. For the modelled LSC, increasing the airgap resulted in ~0.27% increase in thermal and 0.43% increase in edge losses. Therefore, the rate of the photons reaching the PV cell at the side-edge decreased from 2.46 to 1.77. The total solar concentration ratio decreased from 56% to 36% which resulted in ~37% performance deduction.

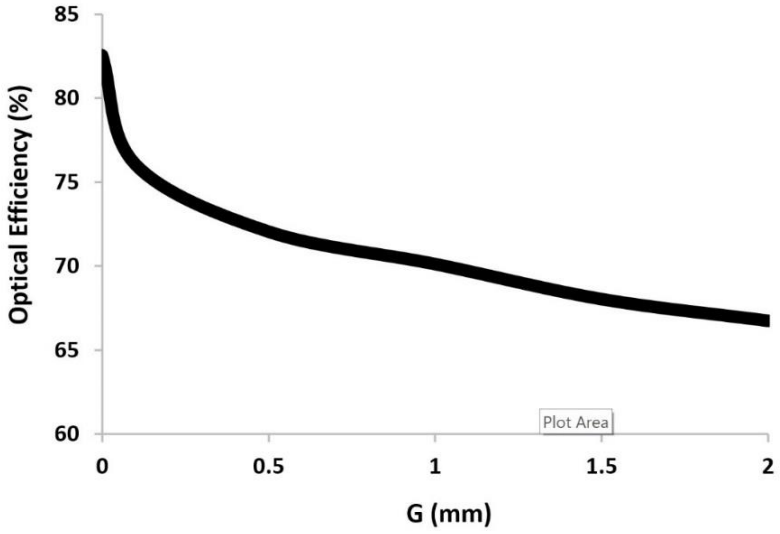

(a)

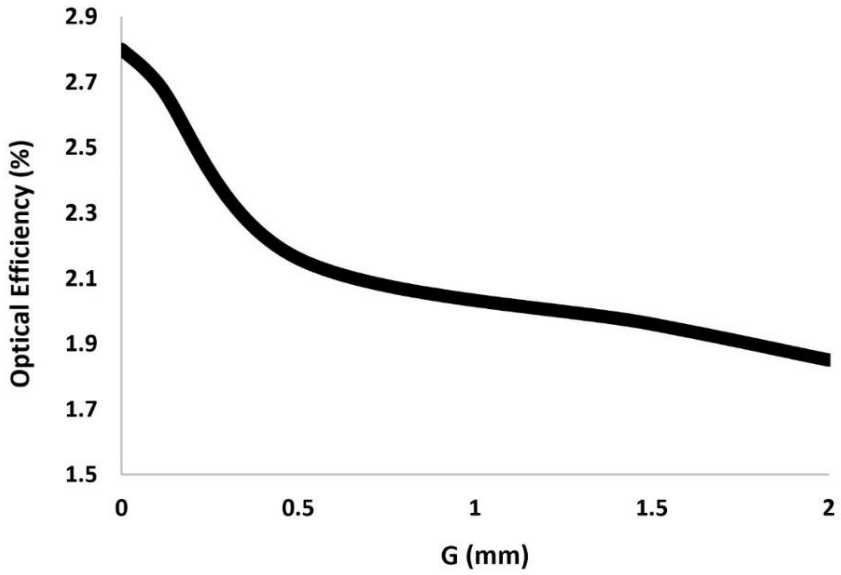

(b)

Fig. 6.24: Optical efficiency over airgap variations for the modelled: a) LDS and b) LSC

Table 6-10: Investigating the performance of the modelled devices by changing the airgap thickness

LPV Device	**LDS**		**LSC**	
***G* (mm)**	0	2	0	2
Reflected (%)	17.42	17.43	17.54	17.53
Refracted (%)	82.58	82.57	82.46	82.47
Thermal Loss (%)	0.02	0.34	4.24	4.51
Exited the Edges (%)	0.0003	15.50	75.76	76.19
Reached PV (%)	82.55	66.73	2.46	1.77
***OE* (%)**	82.56	66.74	2.79	1.85
$\Delta\eta_{opt}$ ***(%) - Between G = 0 to 2mm***	-19.17%		-36.67%	

6.5. Impact of Nano Rod (NR) Alignment on their Optical Properties

NR optical properties can be changed based on the polarization of incident light and direction of NR (van der Zande *et al.*, 1999). When NRs are oriented randomly, optical response includes both transverse and longitudinal resonances. In the case of NR alignment, two events may occur: if the incident light polarization (E) is parallel to the longitudinal direction of NR, longitudinal resonance will be dominant in characterising the optical properties. Similarly, if the incident light polarization is perpendicular to the longitudinal direction of NR, transverse resonance will govern the optical properties.

NRs alignment is undertaken by applying electric field experimentally; however, it is hard to get full alignment between all NRs (van der Zande *et al.*, 1999). Here, the developed model is used to study and estimate the effect of both longitudinal and transverse alignments on optical properties of the same Au NR used in section 5-3-2 (22 nm length and aspect ratio=2.8) (Sethi, 2017). Fig. 6.25 shows NR under simulation for both longitudinal resonance and transverse cases. As it is observed in Fig. 6.25a, the incident polarization is in parallel with longitudinal direction of NR (x direction) while it is propagated in z direction. Regarding transverse case (Fig. 6.25b), as it was not possible to change the incident propagation direction in the program, the particle has been relocated and placed in parallel with the direction of propagation (z).

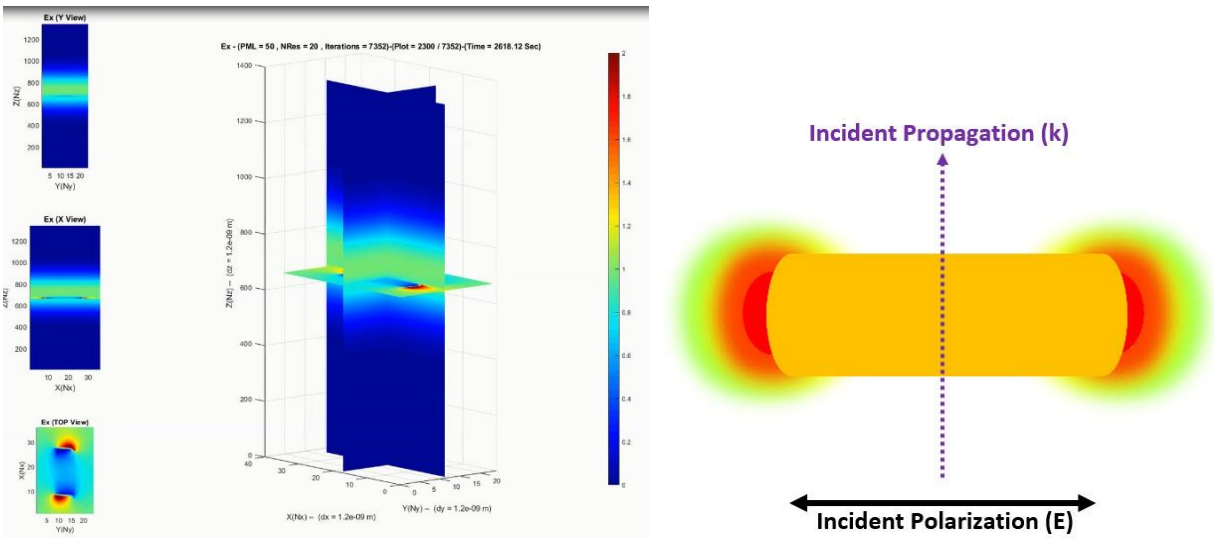

(a)

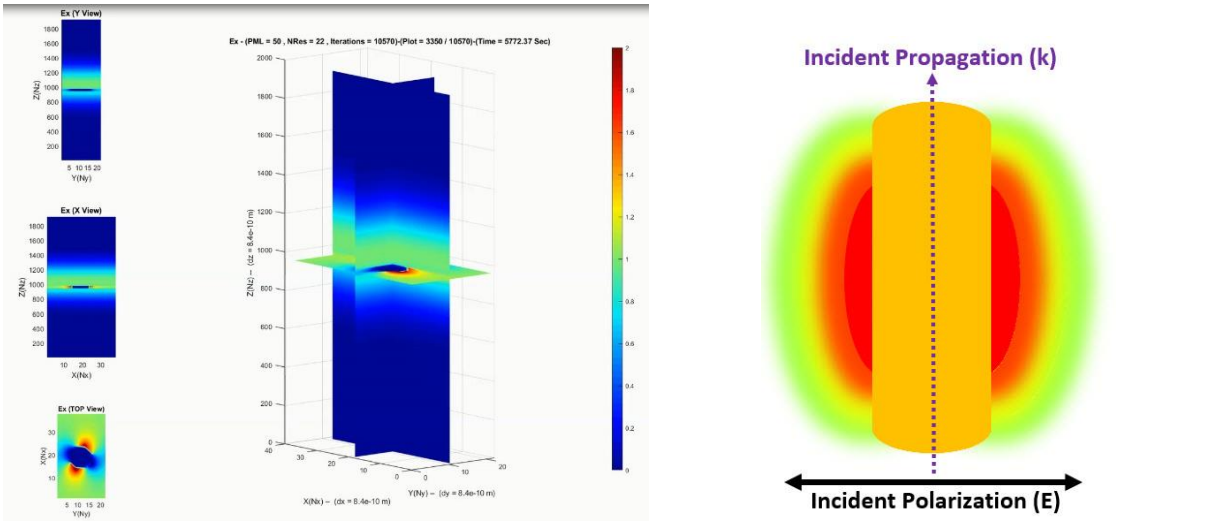

(b)

Fig. 6.25: Au NR under Plasmon simulation for different directions of alignment: (a) Longitudinal resonance and (b) Transverse resonance

The extinction spectra of Au NR for both longitudinal and transverse cases can be seen and compared in Fig. 6.26. The longitudinal resonance peak is at ~700 nm while the transverse peak is at ~550 nm.

As is shown, by aligning the NRs in the direction of interest, their optical properties and extinction spectra can be tuned within a wide range. In terms of application in pLS device design

and optimization, this gives the chance to spectrally match the coupled NR and luminescent material to enhance the pLS device performance. This will be investigated in the Chapter 7.

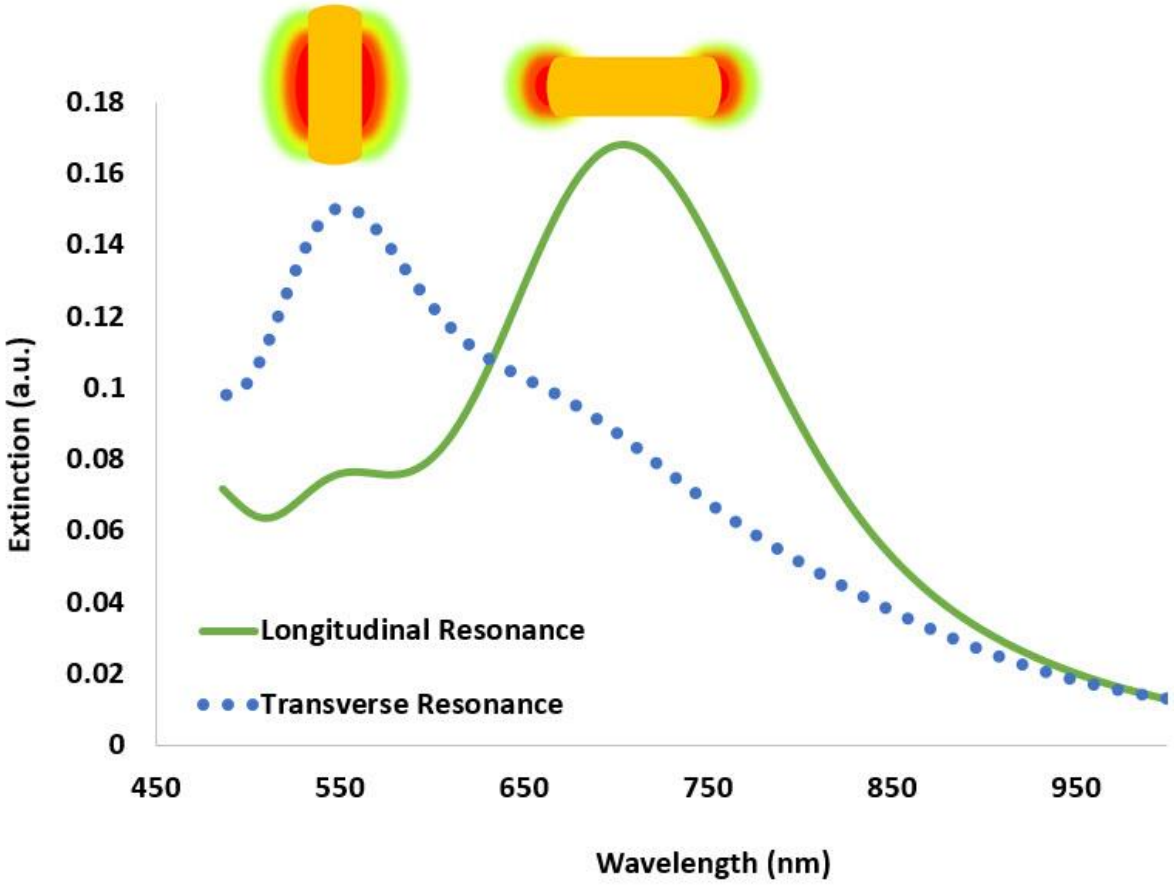

Fig. 6.26: Extinction spectra of Au NR showing both longitudinal and transverse resonances

6.6. Conclusion

This Chapter modelled and studied different configurations of luminescent solar devices to show more validation results and capabilities of PEDAL. This included modelling new device configurations such as multi-layer thin-film LSC, devices with near-unity QY, LSC cavity and LSC with PDMS host material. PEDAL results were found to be in close agreement with experimental outputs. This was mainly due to considering all optical processes in LS devices such as reflection, refraction, absorption, emission, enhancement, transmission and also loss

mechanisms such as reabsorption, non-unity QY, quenching, attenuation, scattering and escape cone losses in the modelling algorithm.

Although PEDAL was mostly used to model and study various configurations of LSC and pLSC devices in this thesis, it was also able to model LDS devices. This was shown through modelling results of various configurations of LDS devices where the results were in close agreement with experimental outcomes.

In modelling a multi-layer LDS, EQE improved by 15% due to doping EVA with violet dye. This occurred in the region between 300 to 400 nm where the dye has the highest absorbance. This indicates that the absorbance of dye should match the lower-efficiency region of EQE spectrum for improved performance. Dye emission peak should be where the PV EQE is highest so it red-shifts the absorbed energy to the region where PV is relatively more efficient.

In modelling an LDS layer of EU^{3+} doped in PVA film, it was found that, when loss mechanisms such as attenuation and scattering are counted in the model algorithm, the model's discrepancy, in comparison with the experimental results, is significantly improved from ~27% to 2%. By considering the losses, an excellent agreement has been achieved between the experimental and the model results. Using the developed model, the LDS layer achieved 79% optical efficiency and 31.39 $mA.\,cm^{-2}$ current density. In addition, the EQE of the PV was significantly improved by ~46% in the wavelength range of 300-365nm.

In addition, in modelling of the performances of LDS based glass, epoxy and PMMA layers, the best results were achieved by LDS based epoxy layer with ~82% optical efficiency and 31.41 $mA.\,cm^{-2}$ current density. Different degrees of red-shift were observed in the modelled LDS layers when compared to the solar radiation spectrum. Therefore, the selection of the matrix material is very important when designing the LDS layer. The matrix material must be a suitable environment for the luminescent species and should exhibit a high transmittance and low scattering over the LDS operating wavelength, 300-500 nm. Also, the matrix materials should be highly transparent in the region where the PV cell is efficient so that it does not attenuate the incident rays in this region. It has been observed that, all used matrix materials are transparent after ~300nm; however, their optical response in the region between 300-400nm can significantly change the response and optical properties of LDS layer.

In studying the effects of optical coupling quality on device efficiency, the performance of LSC decreased by increasing G from 0 to 0.5 mm; while, the performance of LDS was more significantly affected at low air gaps. However, over the studied air-gap range, the LSC efficiency was affected more than that of LDS. ~19% performance reduction was observed for the LDS when G increased from 0 to 2 mm; while, the performance of the LSC reduced by ~37% under the same conditions. This indicated that the LSC was more sensitive to the quality of optical coupling than LDS.

The impact of NR directionality on its optical properties was also investigated in this Chapter. Although fully aligning NRs and studying their optical properties are quite challenging experimentally, the developed model was able to study and estimate the effect of both longitudinal and transverse alignments on optical properties of NRs. The modelling results showed that the resonance frequency can be tuned by NR alignment. E.g. for Au NR (with 22 nm length and aspect ratio=2.8), the longitudinal resonance peak is occurring at ~700 nm the transverse resonance peak is taking place at ~550 nm. This can be an interesting feature in optimising pLS devices and matching the optical properties of NR and luminescent material which is discussed in the next Chapter.

Chapter 7: Novel Structures and Upscale of pLS Device

This Chapter uses PEDAL as a tool to model, estimate and study the performance of a large scale plasmonically enhanced Luminescent Solar (pLS) device to develop a large scale building integrated photovoltaic (BIPV) component. The impact of gold nano rod (Au NR) alignment and directionality on pLS device performance is also studied. The achievements give valuable knowledge for design and optimising pLS device in terms of selecting suitable optically-matched material (metal nano particle, luminescent, host material and solar cell), their doping concentration, size and performance of the device. The idea of using a stem component (SC) in fabricating large scale pLS devices is also proposed whose specifications and advantages are discussed.

7.1. Material Specifications and Optical Properties

Specifications of the modelled plasmonically enhanced luminescent solar concentrator (pLSC) is presented in Table 7-1. The initial configuration of the device is doped with ZnCuInSZnS QD (QD 700) and has the size of 45 × 45 × 3 mm which was optimised experimentally for LSC (Ben Sexton, Sexton, 2018). The same Au NR discussed in Section 6-5 (22 nm length and AR=2.8) (Sethi, 2017) was used in the pLSC to separately study the impact of both longitudinal and transvers surface plasmon resonance (SPR) peaks on pLSC performance. The absorption and emission (peak at ~700 nm) spectra of QD 700 is shown in Fig. 7.1a. The device was modelled under global, direct and diffuse solar radiation spectrum (NREL, 2019) in the range of 300 nm-1000 nm shown in Fig. 7.1b.

Table 7-1: Specifications of each pLSC doped with QD 700 and Au NR

Host Material Type	Predefined Dimension (mm)	Luminescent Material	QY	Au NR Size (nm)
PMMA	45 × 45 × 3	QD 700	0.5	length=22 (AR=2.8)

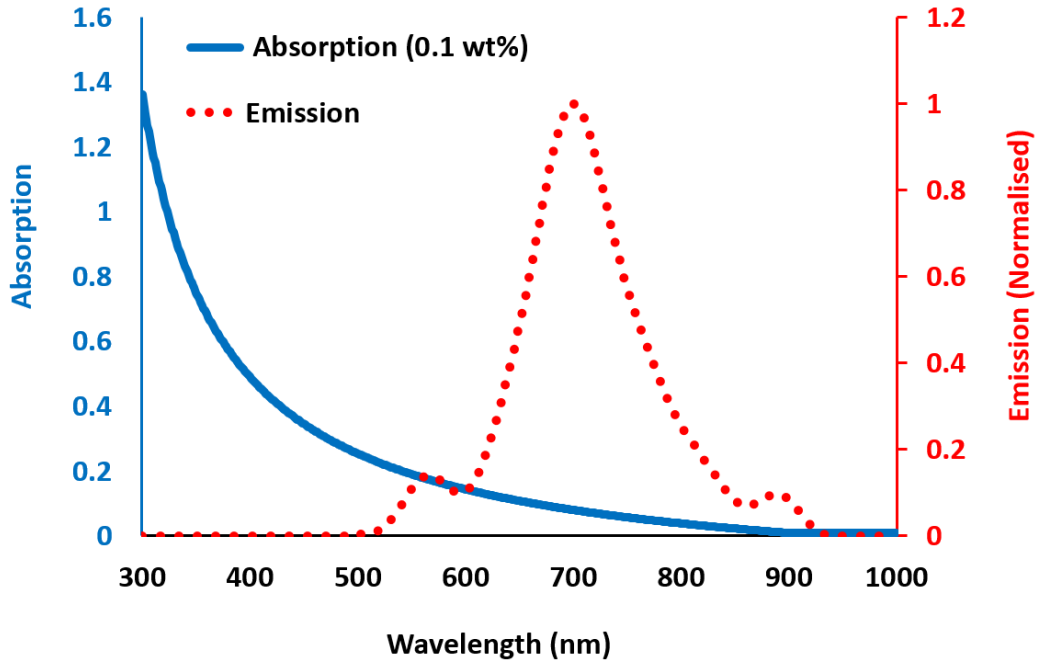

(a)

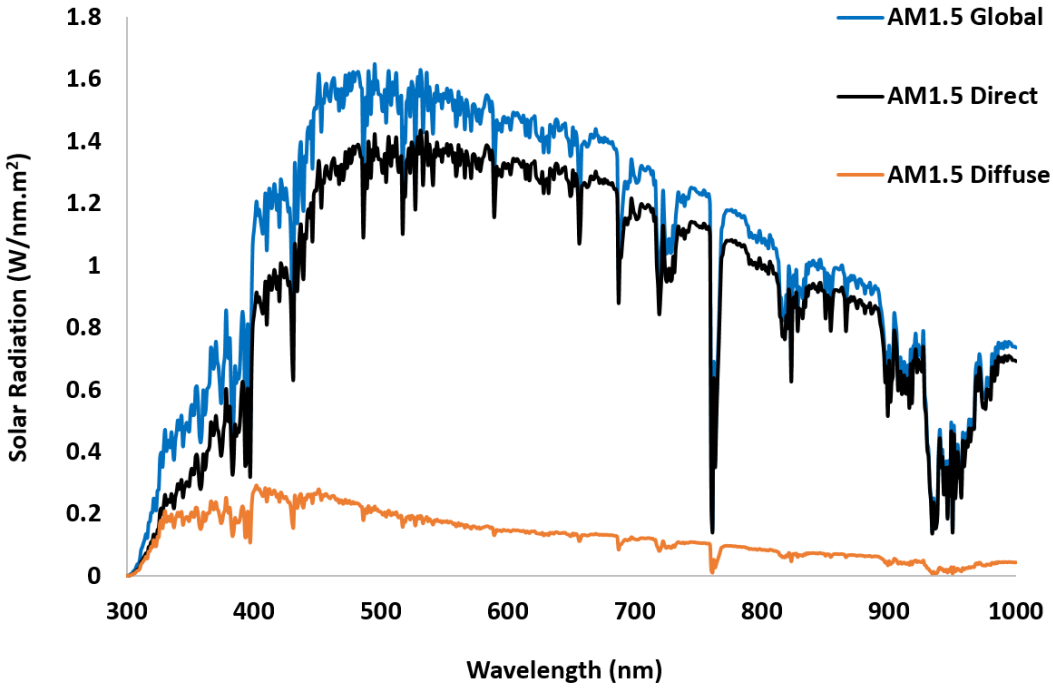

(b)

Fig. 7.1: (a) Emission and absorption spectra of QD 700 and (b) Global, Direct and Diffuse solar radiation Spectra (NREL, 2019)

The design and optimisation of this device was undertaken by PEDAL through the following methodology:

- QD concentration is optimised in the small scale LSC (45 × 45 × 3 mm)
- Au NR is coupled to QD in the optimised LSC to model small scale pLSC and optimising its NR doping concentration.
- NR alignment impact is also studied on the optical performance of pLSC.
- The sgeometric gain (G_g) of pLSC is optimised to obtain large scale device
- The suitable photovoltaic (PV) solar cell is chosen whose external quantum efficiency (EQE) is spectrally overlapped the edge-emission spectrum of the pLSC.

7.2. LSC Optimization

7.2.1. Optimization of QD Doping Concentration

The configuration of the modelled small-scale device (45 × 45 × 3 mm) can be seen in Fig. 7.2. The lateral edges of the device has been covered by PV detectors. The device has been modelled for different QD doping concentration from 0.01 wt% to 0.13 wt% under different solar radiation inputs.

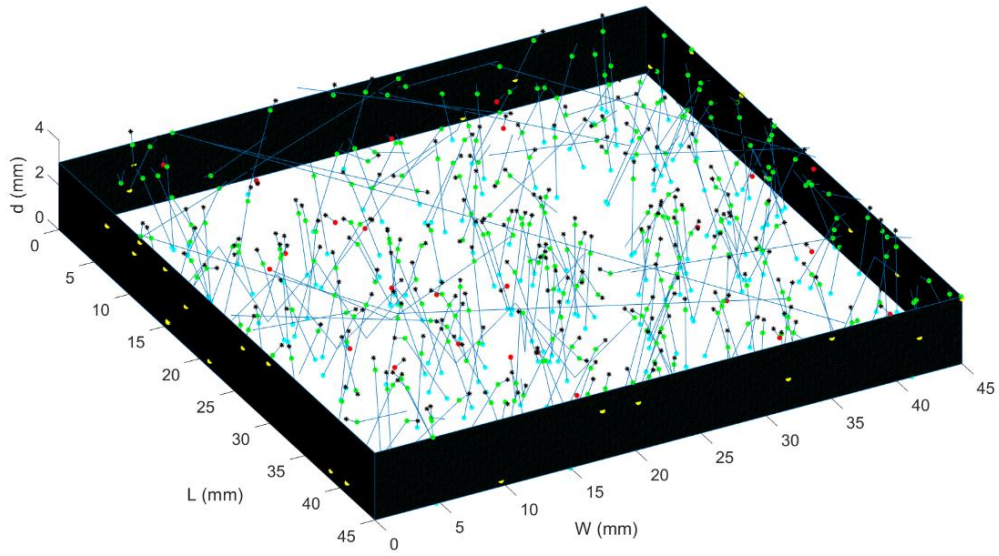

Fig. 7.2: Modelled small scale LSC in the program while ~300 rays were applied to the device

Fig. 7.3 shows the optical efficiency (OE) of the device achieved under global, direct and diffuse solar radiation. OE peak for all cases was obtained at ~ 0.09 wt% QD doping concentration (optimised case). Under global solar radiation, thermal losses increased by increasing the doping concentration of QD (from 0.01 wt% to 0.09 wt%) due to the increase in reabsorption and non-unity QY of QD. However, the escape cone losses reduced from ~79% to ~64% which increased the waveguiding and OE from 5.37% (in 0.01 wt %) to 7.86% (in 0.09 wt %).

Although the results obtained under global solar radiation are considered for the device optimisation process, the highest OE was achieved under diffuse solar radiation which is discussed in Section 7.2.2 in more detail.

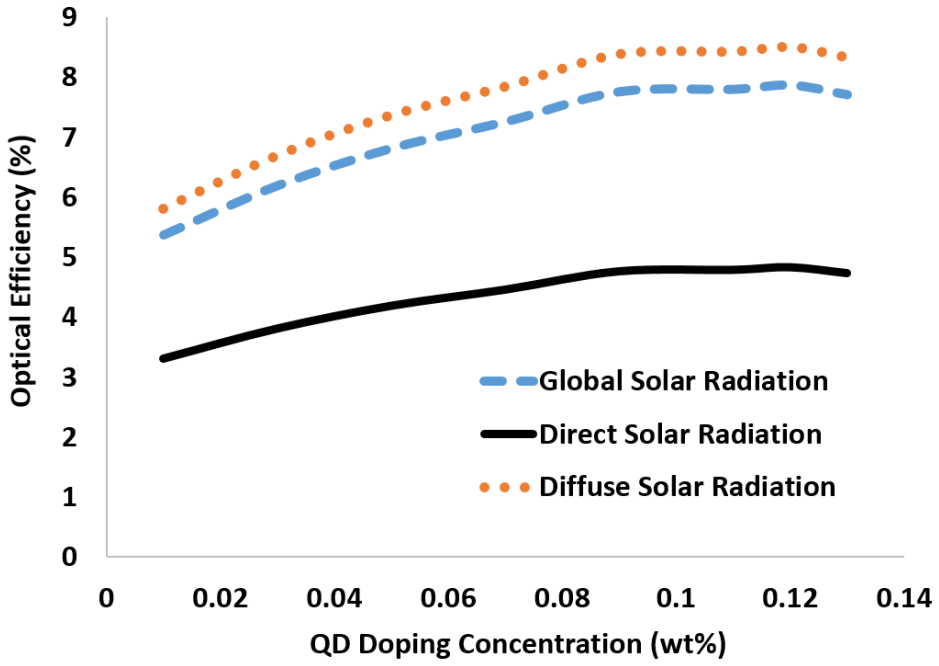

Fig. 7.3: Optical efficiency of small scale LSC (45 × 45 × 3 mm) over various QD doping concentration and solar radiation types

7.2.2. Impact of Diffuse and Direct Solar Radiation on LSC Performance

Fig. 7.4 can be used to estimate the optical performance of LSCs based on the ratio of diffuse and direct solar radiation. In Table 7-2, the best performance of the device was obtained under diffuse solar radiation where the device could reach the OE of ~8.50% under optimised condition (doping concentration of 0.09 wt%) which was ~75% more than OE peak obtained

under direct solar radiation (~4.8%). Under diffuse solar radiation, LSC could achieve 9.90% waveguide efficiency which was almost double that of the device under direct light (5.09%). This was mainly due to the decrease in escape cone losses from ~79% (under direct solar radiation) to ~58% (under diffuse solar radiation). Surface reflection was 2.7% under direct radiation (due to perpendicular angle of incident ray) which was much less than the surface reflection under diffuse light (~16%).

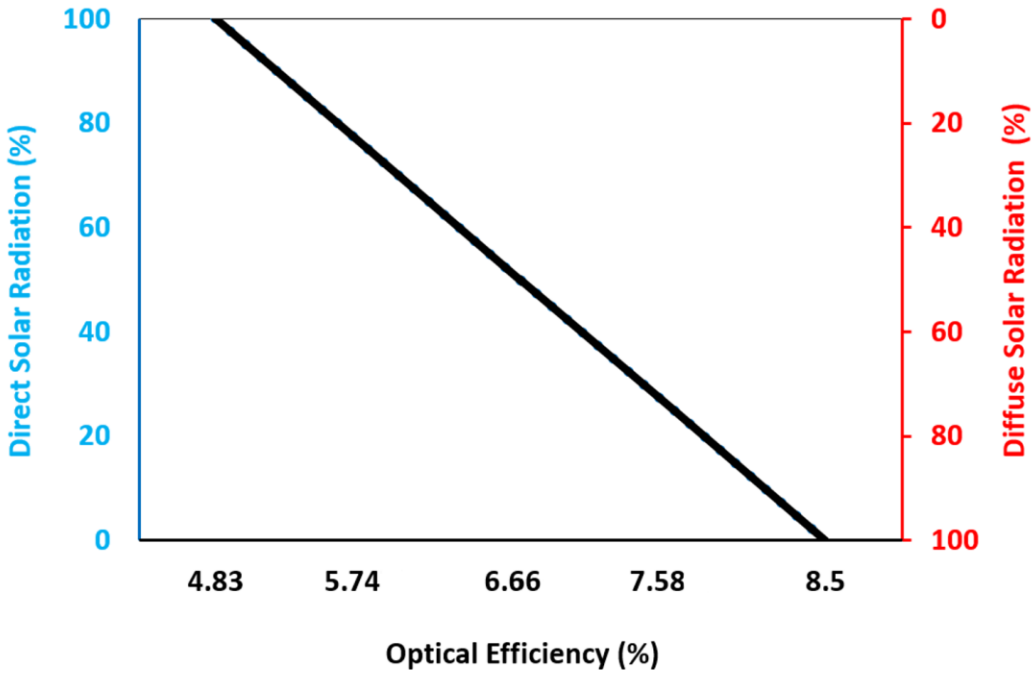

Fig. 7.4: OE of the optimised small LSC based on the rate of local diffuse and direct solar radiation

Table 7-2: Statistical results achieved by PEDAL for LSC with various doping concentration of QD 700

Solar Radiation Type	Global			Direct	Diffuse
Doping Concentration (wt%)	0.01	0.07	0.09 (Optimised)		
Reflected (%)	15.75	15.79	15.67	2.70	15.64
Refracted (%)	84.25	84.21	84.33	97.3	84.36
Thermal Loss (%)	1.25	7.27	12.10	13.47	16.75
Escape Cone Loss (%)	77.55	69.31	63.84	78.74	57.71
Reached PV (%)	5.45	7.63	8.39	5.09	9.90
G_g	3.75				
OE (%)	5.37	7.25	7.86	4.83	8.50

7.3. Impact of NR Alignment on pLSC Performance

The results of the optimised LSC in the last section under global solar radiation (~740 $W.m^{-2}.nm^{-1}$) were used to optimise small-scale pLSC by coupling QD to both Au NR configurations (with longitudinal and transverse alignment) which were discussed in section 6-5. Au NR doping concentration increased from 0 ppm to 2 ppm. Fig. 7.5 and Table 7-3 compare OE of LSC and pLSC devices. The best OE of 9.8% was obtained for the pLSC with Au NR doping concentration of ~1 ppm (with transverse alignment). This was ~25% more than the OE of LSC.

As it might be very hard to achieve full NR alignment experimentally (van der Zande *et al.*, 1999), OE was also estimated for randomly oriented Au NR in pLSC which resulted in ~9.28% maximum OE.

As is presented, in longitudinal alignment, although Au NR resonance frequency (extinction peak) matched QD emission peak (which enhances the coupling emission efficiency), pLSC achieved less OE (~8.9%) than transverse alignment. As can be seen in Fig. 7.6, this can be due

to overlapping Au NR resonance frequency (extinction peak) with low-absorption band of QD which can reduce the coupling excitation efficiency. The optical properties of QD and MNP must be carefully considered in device optimization and spectrally matched to achieve the best performance.

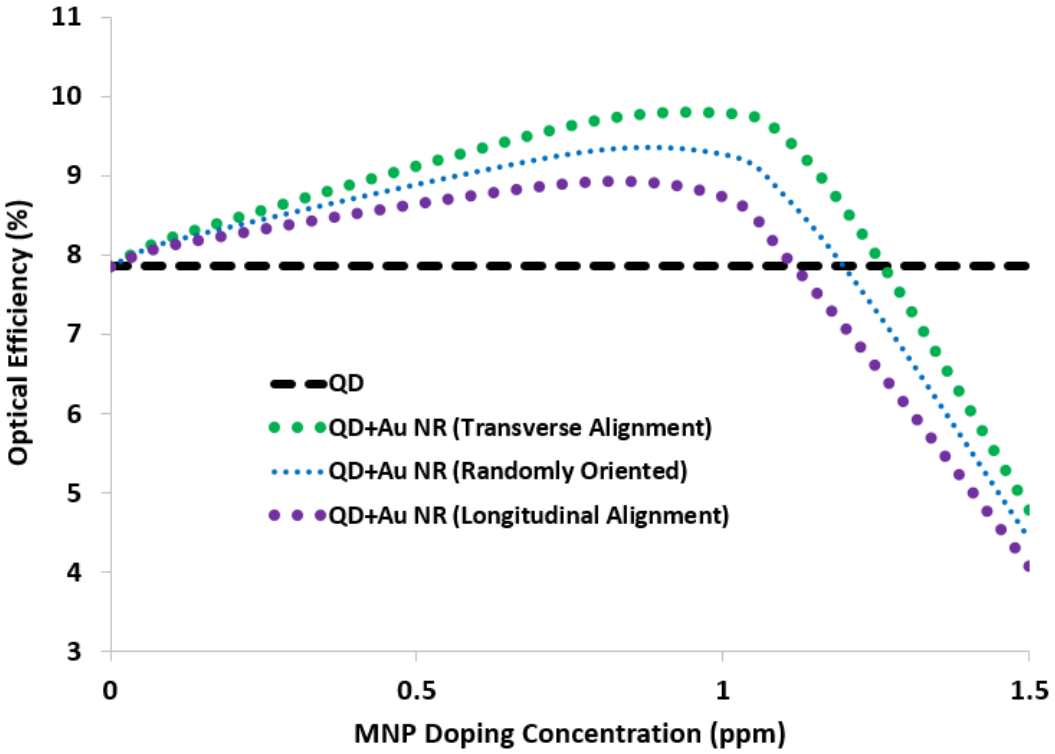

Fig. 7.5: OE of small scale pLSC (45 × 45 × 3 mm) over various Au NR doping concentration in comparison with the performance of LSC devices

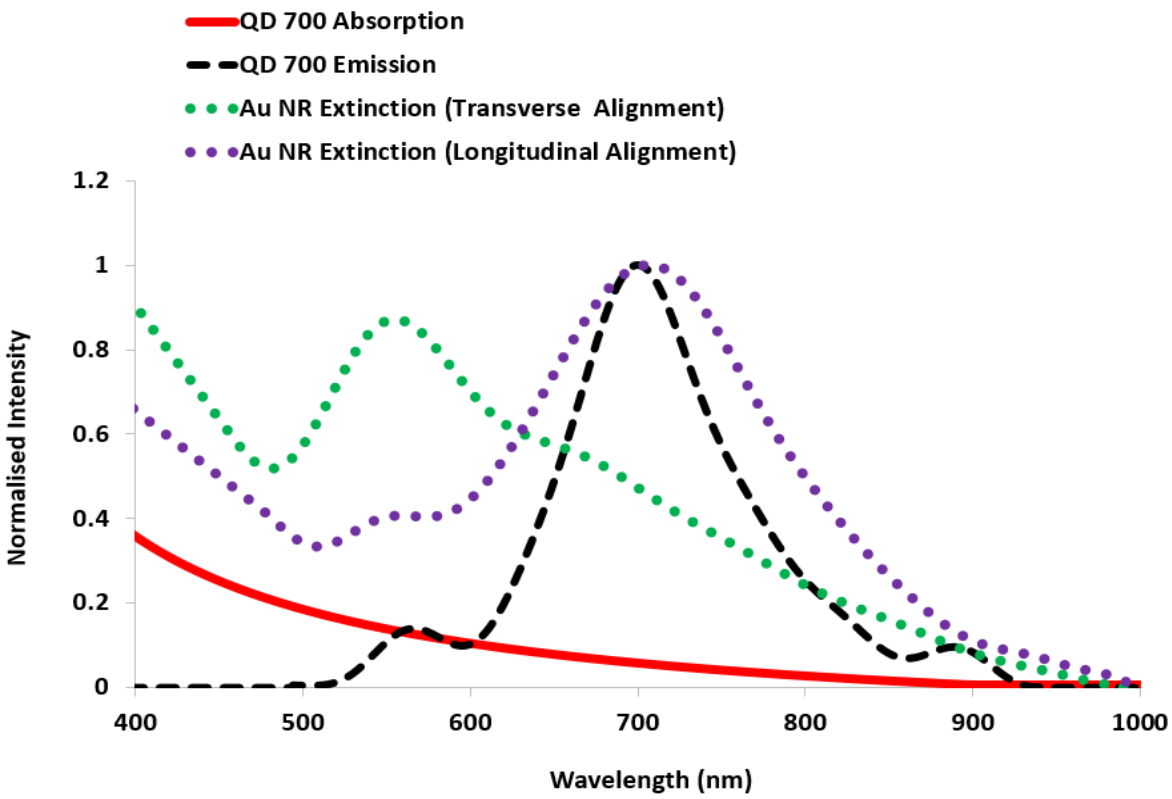

Fig. 7.6: Comparing the optical properties of QD and Au NR (The spectra are normalised to Au NR extinction peak with longitudinal alignment)

Table 7-3: Comparing statistical modelling results of LSC and pLSC

Device Type	**Optimised LSC**	**Optimised pLSC**	
		Longitudinal Alignment	**Transverse Alignment**
QD Concentration (wt %)	**0.09**		
Au NR Concentration (ppm)	**0**	**0.75**	**1**
Reflected (%)	15.67	15.90	15.86
Refracted (%)	84.33	84.10	84.14
Total Thermal Loss (%)	12.10	18.18	17.61
Escape Cone Loss (%)	63.84	56.27	55.83
Reach at Detector (%)	8.39	9.65	10.70
G_g	3.75	3.75	3.75
OE (%)	7.86	8.91	9.80
Integrated Emission Enhancement (%)	-------	+13.36	+24.68%

Fig. 7.7 shows the performance of small pLSCs based on the rate of local diffuse and direct solar radiation. As is shown, pLSC also shows better OE under diffuse solar radiation with the peak of ~11% at 100% diffuse solar radiation.

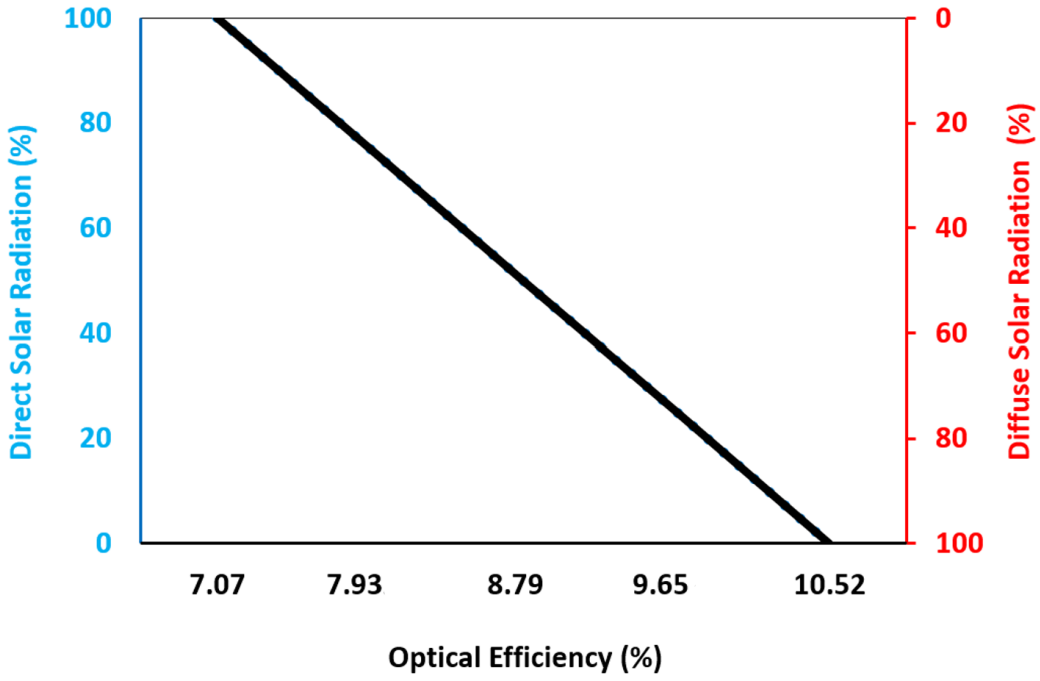

Fig. 7.7: OE of the optimised pLSC based on the rate of local diffuse and direct solar radiation

7.4. Optimising Size of pLSC

Based on the achieved results under global solar radiation in last section, pLSC with Au NR doping concentration of 1 ppm (Transverse Alignment) and QD concentration of 0.09 wt% was the optimised small-scale device which is used here.

Then, the geometric gain of pLSC was increased to achieve the highest solar concentration ratio (C). Fig. 7.8a shows the linear relationship between geometric gain and length and width of the device. As is observed in Fig. 7.8b, OE of pLSC reduced exponentially by increasing geometric gain which was due to waveguiding and thermal losses including scattering, attenuation, quenching, non-unity QY and reabsorption losses. However, C increased from ~42% to ~78% when geometric gain increased from 3.75 (45 × 45 × 3 mm device) to 25 (300 × 300 × 3 mm

device in Fig. 7.8c). Above the geometric gain of 25, C reduced because of significant decrease in OE due to an increase in optical and thermal losses.

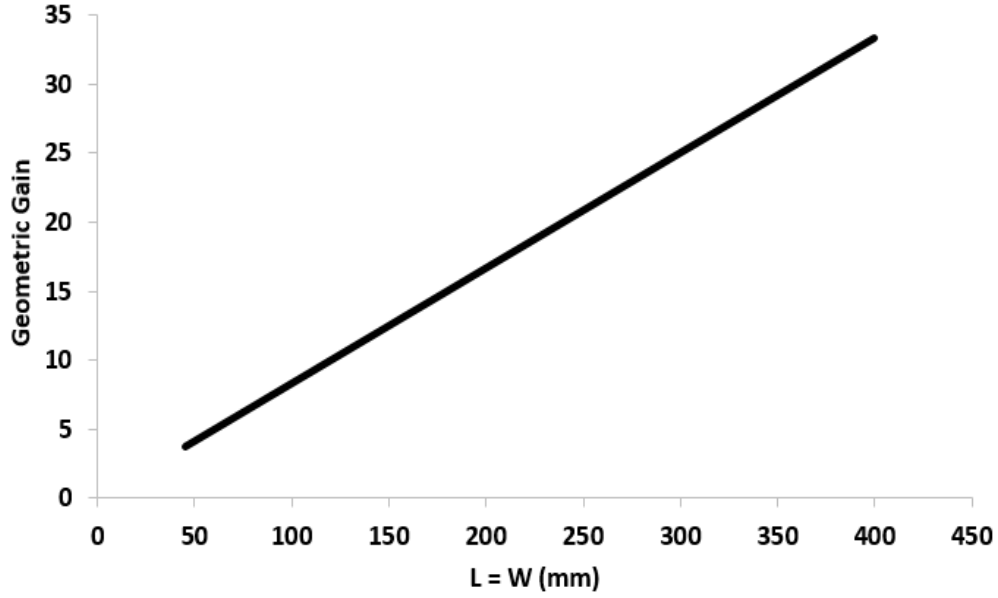

(a)

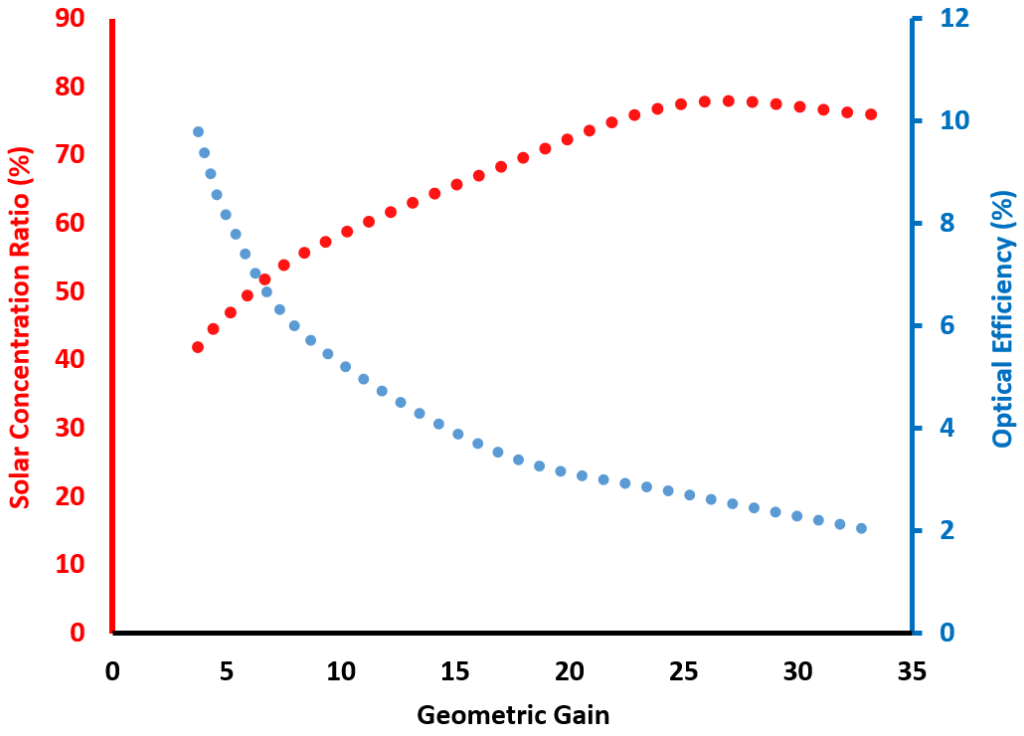

(b)

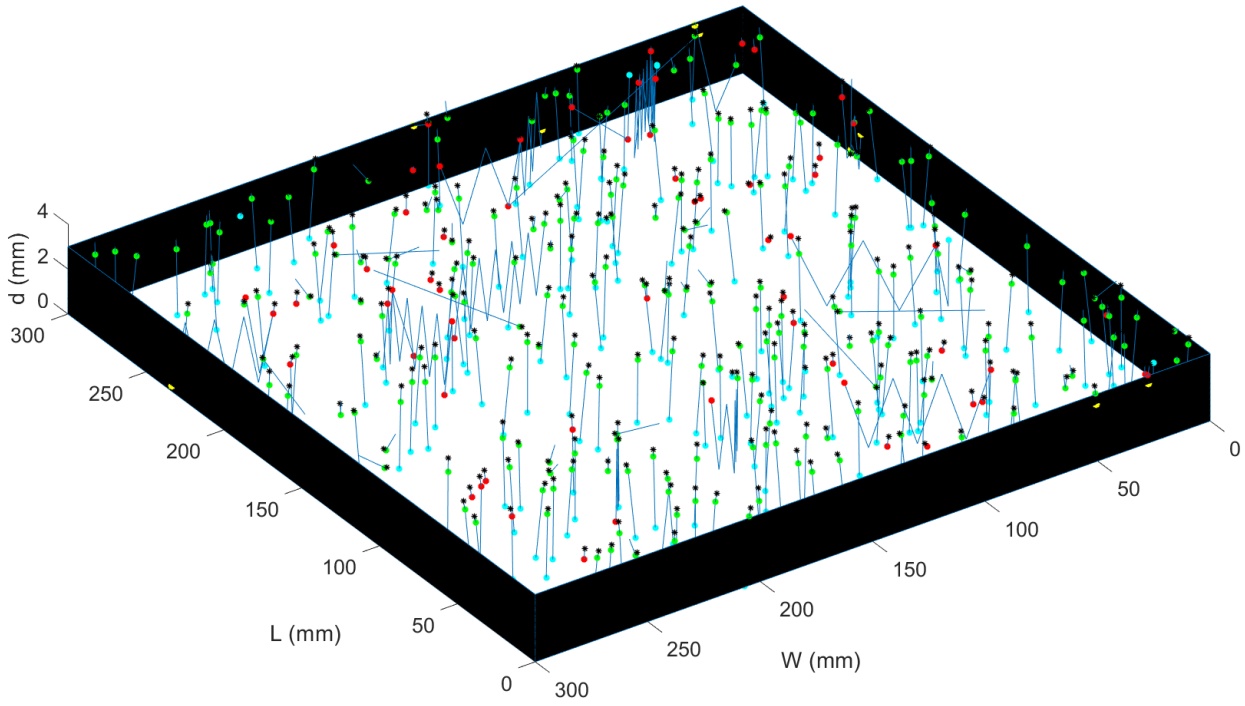

(c)

Fig. 7.8: (a) Geometric gain over size (L=W) variations. (b) OE and solar concentration ratio of pLSC over geometric gain variations. (c) pLSC device with geometric gain of 25 (L=W=300 mm) in PEDAL program under ~300 incident rays

As can be seen in Fig. 7.9, increasing the pLSC size from 45 × 45 × 3 mm to 300 × 300 × 3 mm, the detected radiation spectra at lateral edges is red-shifted. Comparing to the emission spectrum of QD 700, ~8 nm and ~23 nm red-shift were observed in the edge-detected spectra of the small and large devices respectively. This was due to increasing the device pathlength and the number of reabsorption cycles.

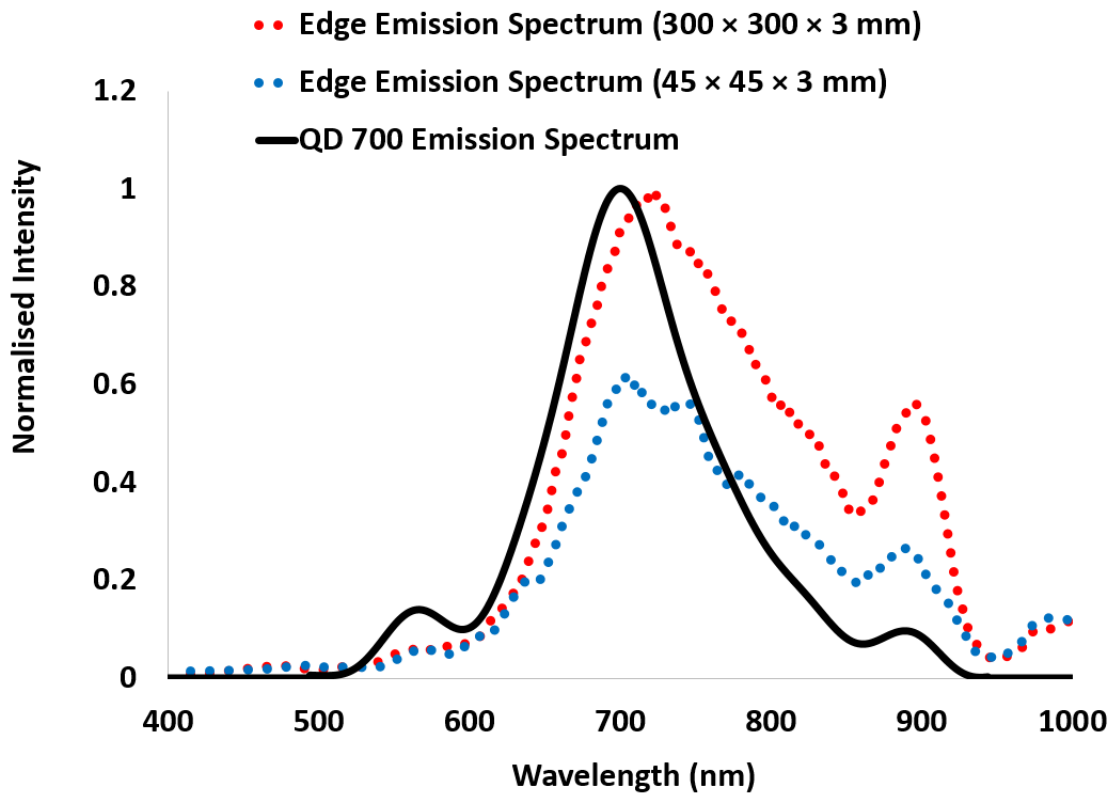

Fig. 7.9: Edge emission spectrum of pLSCs in comparison with QD 700 emission spectrum (normalised to the results of 300 × 300 × 3 device)

Although G_g = 25 is the point for achieving the highest amount of C, the crossing point of OE and C curves in Fig. 7.8 (G_g = 6.5) is the point to obtain the optimised power conversion efficiency (PCE) where the device exhibits the OE and C of ~6.8% and ~51% respectively.

Statistical results for both aforementioned geometric gains can be found in Table 7-4. For G_g = 25, ~16% of the incident solar radiation was reflected from the top surface and the rest (~84%) was refracted into the device. With ~22% thermal and ~59% escape cone losses ~3% of rays reached the detector which resulted in obtaining 2.7% OE and ~78% C. When G_g = 6.5, ~7.3% of rays reached the detector which resulted in obtaining 6.8% OE and ~51% C.

Table 7-4: Statistical modelling results of pLSCs with the highest C and optimised PCE

Test Achievement	**Highest C**	**Optimised PCE**
pLSC Size (mm)	300 × 300 × 3	78 × 78 × 3
G_g	25	6.5
QD Concentration (wt %)	0.09	
Au NR Concentration (ppm)	1	
Reflected (%)	15.84	15.89
Refracted (%)	84.16	84.11
Total Thermal Loss (%)	21.89	18.94
Escape Cone Loss (%)	59.28	57.88
Reach at Detector (%)	2.99	7.29
OE (%)	2.70	6.83
Solar Concentration Ratio (%)	77.54	51.11

The presented pLSC could achieve the geometric gain of ~25 with C of ~80% and OE of ~2.7%. These results are promising in comparison with existing LSC results in literature. For example, recently in (Brennan *et al.*, 2018), maximum $G_g = 7.9$, OE = 1.2% and C = 10% was achieved for a CdSe-ZnS/ZnS QD-based LSCs. At the same G_g, the presented pLSC could achieve around five-times better performance with OE and C of ~6% and ~55% respectively. In (Meinardi *et al.*, 2015), $G_g = 10$, with maximum OE = 3.2% and C = 32% was obtained for a colourless LSC. At the same G_g, the presented pLSC could achieve OE and C of ~5.5% and ~60% respectively.

7.5. PV Selection and Estimating the Performance of Plasmonic Large Scale Plasmonic BIPV (pBIPV) Component Developed by Optimised pLSC

Several optimised pLSCs can be attached to one another to develop a large scale plasmonic BIPV (pBIPV) component with the size of interest. Based on this configuration, a large scale pBIPV component with 1 m^2 area is considered which is developed by the pLSC with G_g = 6.5 (78 × 78 × 3 mm pLSC size). Table 7-5 summarises the specifications of the pBIPV component

where the results were calculated per unit of area (m^2). The number of used pLSCs were ~165/m^2 in pBIPV.

Considering edge-detected spectrum peak of the device (at ~700 nm) and EQE of different solar cells in Fig. 7.10 (Strumenti, 2019), mc-Si was a suitable solar cell and spectrally matched the pLSC optical performance.

Mc-Si can show ~22.3±0.4 % efficiency based on the last update in Solar Cell Efficiency Table (version 52) (Green *et al.*, 2018). Considering efficiency of mc-Si solar cell and modelled OE achieved for the optimised pLSC (6.8%), the PCE was estimated using the method mentioned in (Desmet *et al.*, 2012) to be 1.52% for pBIPV. Giving the PCE values and under the used global solar radiation spectrum (with power of ~740 $W.m^{-2}.nm^{-1}$), the output power density of ~11 W.m^{-2} was obtained.

Table 7-5: The specifications of large scale pBIPV

pBIPV Frame Size (m^2)	1
Size of Used pLSC (mm)	78 × 78 × 3
Number of Used pLSC in pBIPV	165
OE (%)	6.8
Geometric Gain	6.5
Solar Concentration Ratio (%)	51
Selected PV Solar Cell	mc-Si eff = 22.3±0.4 % under the global AM1.5 spectrum (1000 W/m^2) (Green *et al.*, 2018)
Estimated PCE (%)	1.52
Total Incident Power (W/m^2)	740
Output Power Density (W/m^2)	11.22

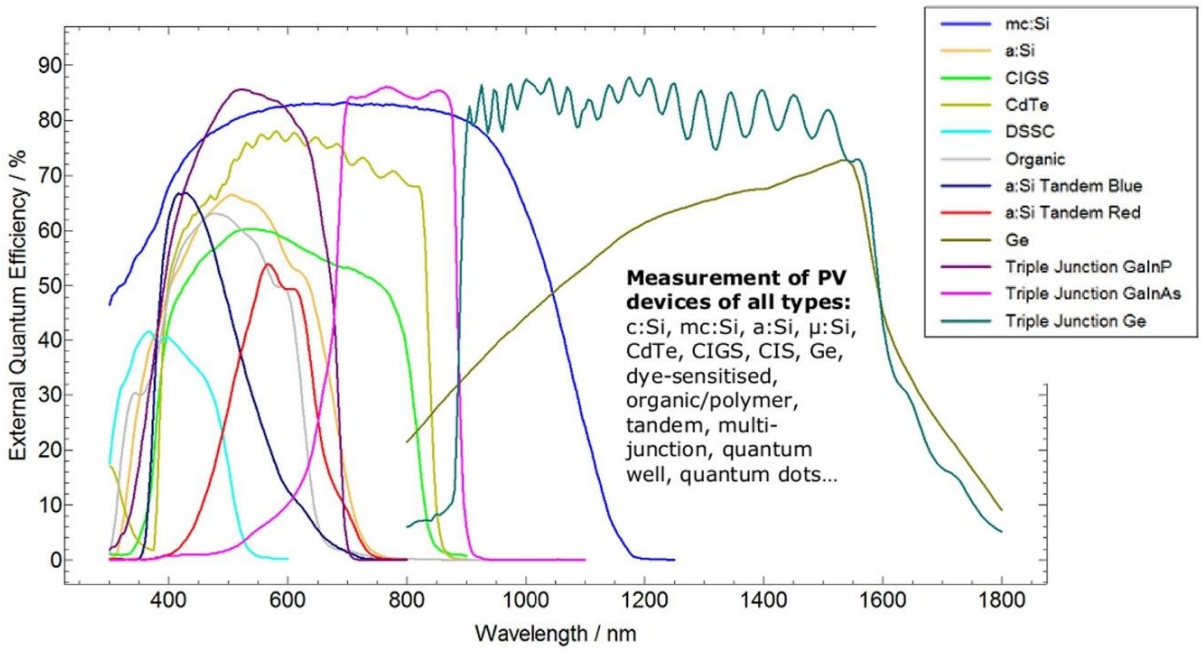

Fig. 7.10: EQE of different solar cells (Strumenti, Last Access: 20/05/2019)

7.6. Proposed Structure for Large Scale pBIPV Component

In this section a structure is proposed for developing large scale pBIPV components to improve its static stability, aesthetics and visual comfort level. The idea of the proposed structure has been inspired from ancient Persian structures (Fig. 7.11a) in which large windows or facades have been built by installing and attaching a number of similar stem components (SC) to achieve the size and shape of interest. The same idea has been also used in other structures later (Fig. 7.11b). The SC could have a simple structure itself while it might be used to create complex large-scale structures.

(a)

(c)

Fig. 7.11: (a) “Palace of Cyrus the Great” (559–530 BC) (rebuilt), Pasargad, Iran (b) “Sainte-Chapelle” (mid-13th Century), Paris

The proposed large scale pBIPV structure is developed by attaching several SCs to one another whose first version has been designed in Autodesk Inventor Professional software (Fig. 7.12a). Each SC includes fours pLS devices. This gives the designer the ability to control the interior visual comfort (including both colour and brightness) using pLS devices with different colours (Fig. 7.12b).

SC can be customised for various types of buildings with different applications. Frame material and colour can be matched to the façade and/or application of the building based on choice.

In case of requiring a glazing pBIPV structure, the frame material can be selected to work as an edge reflector for pLS devices to reduce the required PV cell area. In non-glazing structures, mirror or reflectors (bright or colourful) can be mounted at the back of the structure. The structure can be also covered by selective mirrors to improve the optical performance of the component.

The draft size of each pLS device is 45×45 mm which can be changed and optimised based on the performance of the used pLS devices. Narrow ducts have been designed at back of the structure (Fig. 7.12d) to place wiring

Enlarging the pBIPV component (Fig. 7.12e) does not result in increasing losses and decreasing the performance. The reason is optimisation SC guarantees the optimisation of the large scale pBIPV component which is known as another advantage reducing the design complexity.

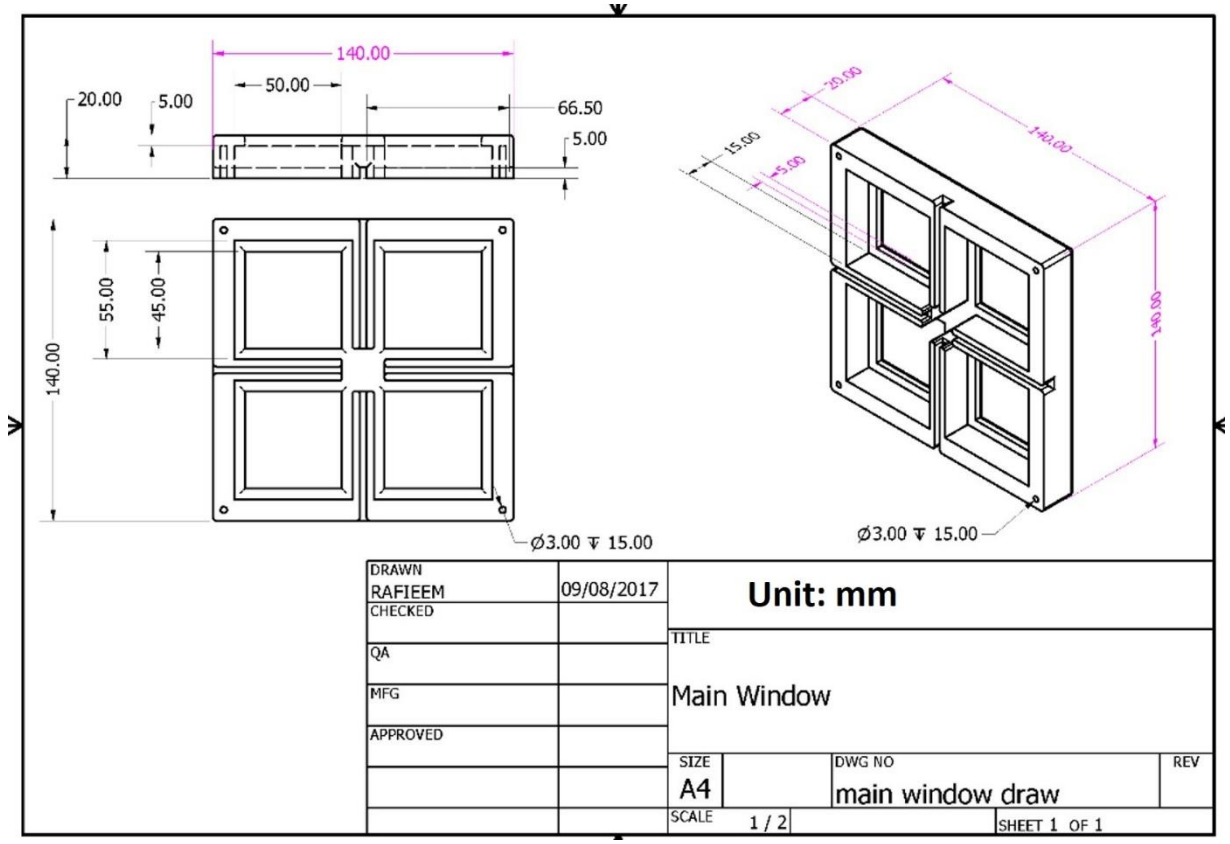
140.00
50.00
20.00
5.00
66.50
5.00
55.00
45.00
140.00
Ø3.00 ↧ 15.00
20.00
15.00
5.00
140.00
140.00
Ø3.00 ↧ 15.00
DRAWN
RAFIEEM
09/08/2017
CHECKED
QA
MFG
APPROVED
Unit: mm
TITLE
Main Window
SIZE
A4
DWG NO
main window draw
REV
SCALE
1 / 2
SHEET 1 OF 1

(a)

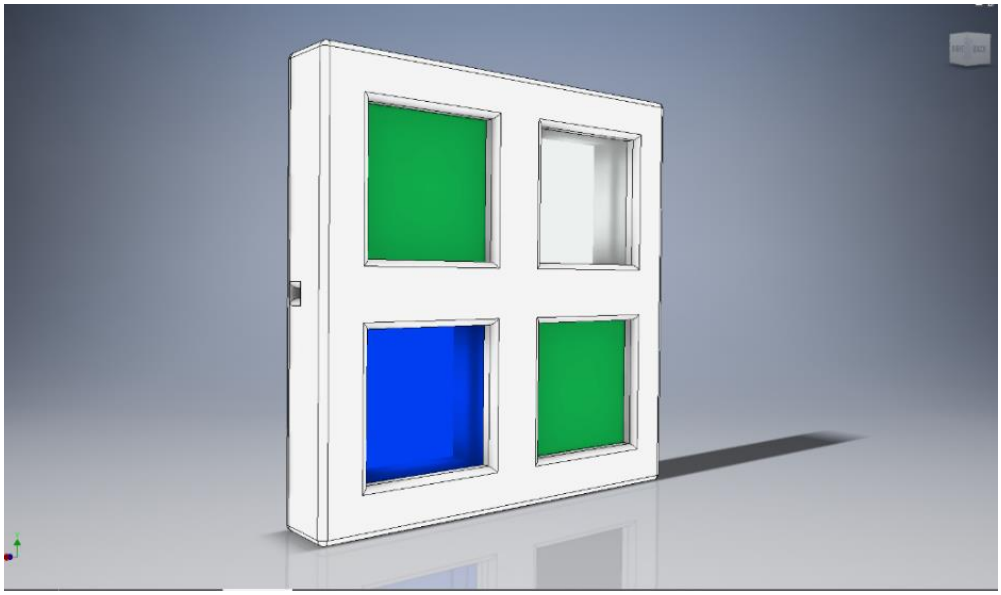

(b)

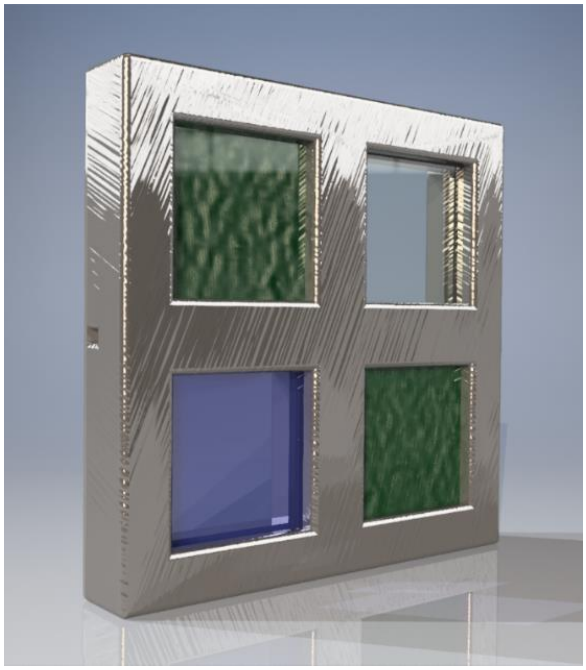

(c)

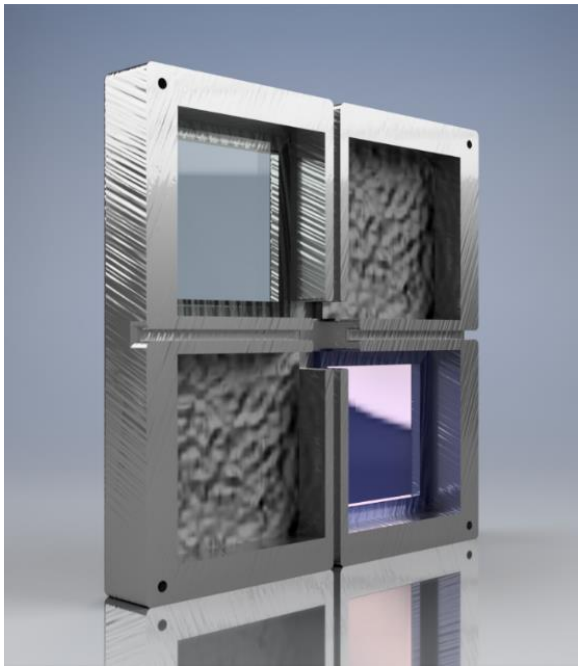

(d)

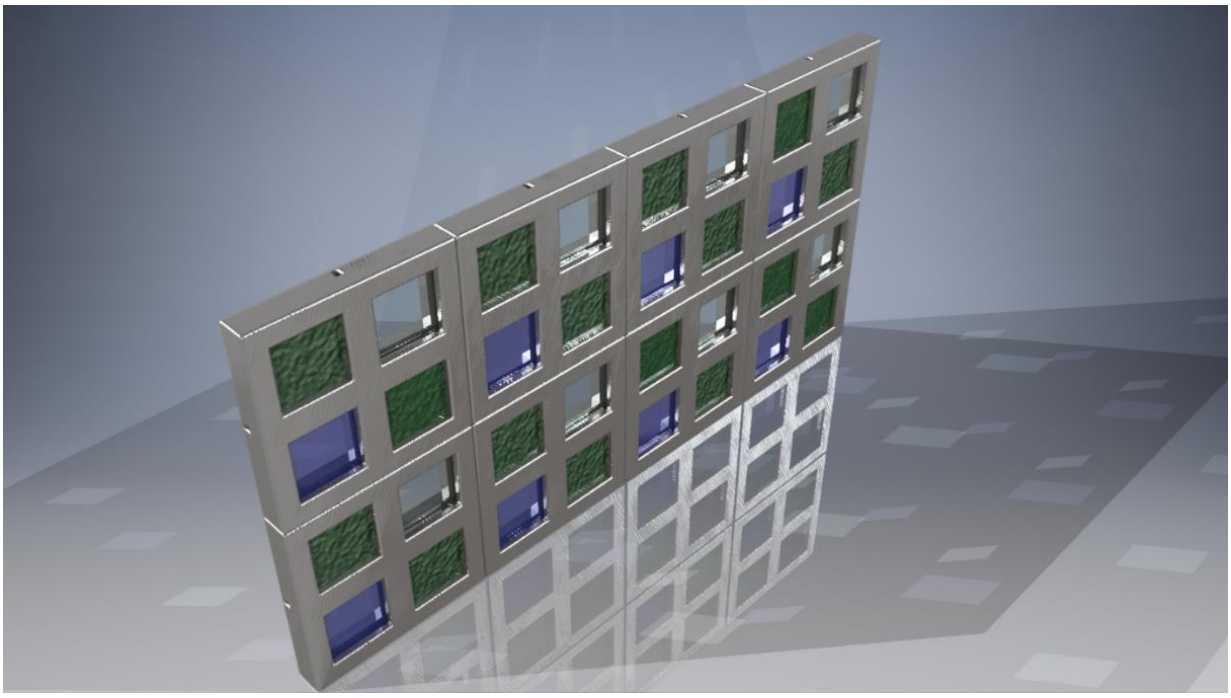

(e)

Fig. 7.12: (a) and (b): The first version of SC designed in Autodesk Inventor Professional software. (c) Front, (d) Back ray tracing view of the proposed SC. (e) Attaching SCs to one another to build up a large scale pBIPV component with size of interest

7.7. Conclusion

In this section, PEDAL was used as a tool to model, optimise and estimate the performance of large scale pBIPV component developing by pLSCs. pLSC was optimised in terms of QD doping concentration, directionality of used Au NP, doping concentrating of Au NP and size (geometric gain) of the device. The impact of incident solar radiation type (direct, diffuse and global) on device performance was also studied where pLSC devices showed the best performance under diffuse solar radiation.

The Chapter also gave valuable information required to be considered in design and optimising pLSCs. The results showed that not only the doping concentration and size of the device characterises the performance of the device; but also, materials (QD and MNP) and their orientation (in case of using NR) must be selected accurately as their optical properties have a great impact on OE. The idea of using SC in fabricating large scale pBIPV components was also proposed. Using the idea improves the static stability, aesthetics and visual comfort level of the large scale pBIPV component. Moreover, by optimising the SC, the large scale pBIPV is also optimised and PCE is independent from size (enlarging) of the pBIPV component.

Chapter 8: Conclusion and Future Works

8.1. Conclusion

Developing façade and building integrated photovoltaic (BIPV) systems can increase the rate of green energy generation and mitigate the environmental impacts of using fossil fuels. While solar radiation has a large wavelength range of ~280 nm to 2500 nm, photovoltaic (PV) modules efficiency is limited by their narrow spectral response and external quantum efficiency (EQE). Their efficiency is also limited by optical losses associated with the absorption and reflection of the module top glass, encapsulation layer and anti-reflective coating layer.

Luminescent solar (LS) devices including luminescent solar concentrator (LSC) and downshifting (LDS) thin film have the potential to be developed as BIPV components and were introduced as low cost technologies to overcome the aforementioned PV challenges and limitations. In LS devices, solar radiation is absorbed by a polymeric waveguide doped with luminescent material, down-converted (in LSC) and redshifted (in LDS) to the wavelength region where PV cell is efficient and then directed to mounted PV solar cell. LS devices inherently suffer from different sources of optical losses such as reflection, non-unity quantum yield (QY), reabsorption, background and escape cone losses which are increased by enlarging the device.

Plasmonic LS (pLS) devices including pLSC and pLDS is an advanced technology in which the plasmonic coupling between luminescent species and metal nano particles (MNPs) can improve the optical performance and efficiency of the device. However, their optimisation process including optimising the doping concentration of luminescent material, MNP and their spectral overlap as well as device size is more complex than LS devices. Developing a model to investigate and analyse the configuration, performance and optical properties of pLS device can be extremely valuable to ease the optimisation process before device fabrication.

The following describes the contribution of this research to fill the aforementioned gaps:

Model Development: This research focused on the development of a novel algorithm and mathematical model to investigate plasmonic coupling between luminescent species and MNPs

which resulted in the development of PEDAL. PEDAL is a novel comprehensive tool used to model the performance and optical properties of both LS devices and pLS devices.

This work critically reviewed different types of LSCs, their nature, specification along with their modelling method based on a Monte Carlo ray tracing (MCRT) algorithm. Information collected from literature review on LS devices and their modelling were used to develop the "Ray Tracer" a 3D MCRT program to model both single and multi-layer LS devices. MCRT was inherently found to be a time-consuming process implemented based on probability calculations of optical phenomena such as absorption, transmission, scattering and attenuation in iterative loops. Computational requirements and accuracy were the main challenges in MCRT algorithm and were solved through this research and enhanced ultimately in PEDAL development.

To model the optical properties of MNPs and their plasmonic effects in pLS devices, a new 3D "Plasmon" program was designed and developed based on finite difference time domain (FDTD) numerical method. Plasmon was validated by modelling a periodic homogenous structure of MNP and comparing the simulation and experimental results. Simulation time, accuracy, memory demand and time steps in FDTD were found dependent on Yee grid resolution; thus, although the model could estimate the experimental results in close agreement, FDTD still required optimization to reduce the memory demand and computational cost. Therefore, a 3D optimized FDTD (OFDTD) was designed and developed which introduced new FDTD approximation terms based on the physical events taking place during the plasmonic oscillations of MNP. The proposed method not only required ~52% less memory than conventional FDTD, but also reduced the calculation requirements by ~9%. The 3D OFDTD method was used to model and obtain the extinction spectrum, surface plasmon resonance (SPR) frequency and the enhancement factor (EF) of the field generated by MNP. The results were compared with traditional FDTD and experimental outputs to validate the model. OFDTD results have been found to be in excellent agreement with experimental results.

An important achievement was combining "Ray Tracer" and "Plasmon" models to develop a novel and uniquely comprehensive program, PEDAL to model pLS devices. In the modelling, the specifications and characteristics of the luminescent material used such as the absorption and emission spectra and MNPs such as the extinction spectrum which can be obtained by Plasmon, were used. Moreover, device dimensions and type of host material were defined in the model. Then, the device was simulated under the incident radiation spectrum of interest.

Two approaches were introduced to enhance the speed and performance of PEDAL. One was based on using an adaptive filter reducing the number of iterations by filtering some parts of the incident radiation spectrum. The filter worked based on detecting the optical procedure with the highest probability and dominant priority to estimate the fate of the ray without running the iterative loop. Although simulation time was reduced significantly using the adaptive filter, the accuracy decreased due to the increase in estimation errors. Therefore, the second approach was proposed based on high performance coding techniques including: (i) avoidance of calculation duplication by detecting similar ray tracing events, (ii) minimizing the conditional statements in storing spatial ray tracing data by labelling the tracing-space and using iterative statements, (iii) prioritizing the optical procedures in the algorithm based on their probability, (iv) enhancing the calculation of the intersection point of incident ray and planes using a direct method, and finally (v) using a look up table. As a result, the final version of PEDAL significantly decreased simulation time while the program results exhibited an average modelling accuracy of ~96%.

A computational method was also introduced and tested to convert the experimental unit of concentration (ppm) to the modelling unit (N/L) used for PEDAL. This conversion was necessary for comparing and validating the MNP experimental and modelling results. The method was validated for different shapes and sizes of particles and modelling results were found to be in very close agreement with experimental outputs. Using the validated method, a conversion graph was obtained for use in PEDAL which could convert doping concentration from ppm to N/L based on the shape and size of MNP.

PEDAL was validated for pLS devices by modelling 9 samples doped with Au nano spheres (Au NS). The emission enhancement peak of the device was found to be closely matched to experimental results. Concentration of MNP was found to be a crucial parameter in pLS device performance. Enhancement occurred only in a very narrow concentration band of MNP. In very low MNP concentrations, small enhancement was observed due to a reduction in plasmonic interaction between MNP and luminescent material. In very high MNP concentrations, the device performance decreased due to an increase in the quenching probability. It was also observed that by changing quantum dot (QD) concentration, MNP doping concentration range (where enhancement is taking place) and enhancement rate were changed. The reason was due to changes in the relative distance between QD and MNP which changed the rate of energy quenching and thermal losses.

Impact of MNP Directionality: The impact of gold nano rod (Au NR) alignment on its optical properties as well as performance of pLSC was also studied through PEDAL. This was investigated in modelling and optimisation of a large scale pLSC doped with QD emitter and Au NR aligned in two directions (longitudinal and transverse alignment). The optical properties of the pLSC was studied in detail. It was found that not only the doping concentration and device size characterise the performance of pLSC; but also, emitter and Au NR must be spectrally matched. The interesting feature of Au NR is its SPR peak can be tuned by changing its alignment directionality. This can be used to match Au NR and QD spectrally to improve the photon density enhancement factor (PDEF) of coupling and ultimately enhance the performance of pLS device.

Large-Scale BIPV: A new structure was also proposed for fabricating large scale BIPV components based on attaching a number of stem components (SC) to develop the BIPV size of interest. While SC has a simple structure, it can be used to create glazing or non-glazing large-scale structures with frame material and colour of interest matched with the building application and requirements. With regards to energy performance, enlarging the SC-based BIPV component does not result in increasing optical losses unlike conventional LSC panels. This is due to the unique and optimised size of SCs attached to one another to develop the large scale BIPV structure with the size of interest. Therefore, optimisation of SC guarantees the optimisation of whole large scale BIPV structure.

Additional Contributions: PEDAL was also used to model and study several other configurations and novel structures of LS devices such as multi-layer thin-film LSC where ~10% OE was obtained. Devices with near-unity quantum yield (QY) and LSC cavity coupling to photonic selective mirrors was also modelled where the increase in light trapping efficiency resulted in achieving ~30 solar concentration ratio. To present PEDAL capabilities, it was also used in modelling of LDS devices where results were found to closely match with experimental results. Different amounts of red-shift was observed in the modelled LDS layers when compared to the solar radiation spectrum. Therefore, the selection of the matrix material is very important

when designing the LDS layer. The matrix material must be a suitable environment for the luminescent species and should exhibit a high transmittance and low scattering over the LDS operating wavelength, 300-500 nm. Also, matrix materials should be highly transparent in the region where the PV cell is efficient so that it does not attenuate the incident rays in this region. It has been observed that, all used matrix materials are transparent after ~300nm; however, their optical response in the region between 300-400nm can significantly change the response and optical properties of LDS layer.

Overall in conclusion, PEDAL has exhibited a promising modelling accuracy and performance providing reliable consistent results. To the date of this thesis submission, PEDAL has been used in modelling, optimisation and analysis of over 50 LS and pLS device configurations. This includes variety of structures whose configurations and performance can be found in both solar energy application group (SEAG) experimental results and data available in the literature. This is an ongoing process and PEDAL is a powerful modelling tool supporting advanced pBIPV manufacturing with the goal of generating more renewable energy in buildings, achieving CO_2 targets and making the world greener.

8.2. Future Work

This thesis mainly focused on modelling, optimisation and analysing of LSC and pLSCs; however, the following steps are suggested for future work in this area:

- **Validation of PEDAL for pLS device doped with Au NR**: The modelling results for pLS devices doped with Au NR can be found in Chapter 7. The alignment of Au NR has been applied through modelling and the pLS device results have been achieved by the same PEDAL algorithm used for Au NS. Although, it was tried to include all plasmonic functions to the model based on the literature so that PEDAL can support modelling pLS devices with both NS and NR, the full alignment of Au NR in pLS has not been implemented experimentally yet. It would be an original idea to compare the modelling and experimental results for this case to evaluate the modelling accuracy and performance and debug the model if required.

- **Validation of pLDS modelling by PEDAL**: PEDAL was used for modelling of LDS devices in Section 6-4 and in future, it can be used to model and validate pLDS experimental results. In LDS device, the device performance has been found very sensitive to optical coupling, thickness of thin film and doping concentration of luminescent material. Although, the modelling algorithm for both pLSC and pLDS are the same, it would be a novel idea to compare the experimental and modelling results of pLDS and study the sensitivity of pLDS performance to input parameters. This will also provide the opportunity and potential to estimate the cost of pLDS implementation in pBIPV manufacturing.

- **Commercialisation of PEDAL**: PEDAL was developed using MATLAB environment and functions. For commercial purposes, it is important to integrate PEDAL as a product and professional computer tool using Microsoft Visual Studio. Applying this step gives the opportunity to exploit and license PEDAL in a professional and industrial level where other groups working in the field of LS and pLS device development can benefit from the services and solutions provided by PEDAL. In addition to the revenue which is earned and increased through the exploitation process, the feedback and comments of the users can be used to extend and improve PEDAL's interface, applications and performance. For example, PEDAL can be extended to model optical components other than only LS and pLS devices such as optical filters, selective mirrors, lens, waveguides.

- **Expansion of PEDAL results for largescale pBIPV development**: In future, the proposed large scale pBIPV component can be developed and analysed. The performance of the component can be compared to the modelling results. As it was discussed, the proposed structure can be developed by combination of both pLSC and pLDS devices. This means the generated power of pBIPV as well as rate of light and heat transferred to the building can be controlled through optimising the area of pLSC and pLDS devices. Therefore, it can be an original idea to study the impact of pLSC and pLDS area not only on the generated green power of pBIPV but also on building comfort parameters such as health and wellbeing, visual comfort, thermal comfort, noise nuisance and ergonomics

- **Realistic economic analysis**: Economic and cost analysis of pLS devices can be undertaken with high accuracy after pBIPV development and considering real generated power as well as all related realistic costs such as manufacturing, labour and balance of system. This can be even investigated more precisely and deeper by considering the cost which is saved through improving the aforementioned building comfort parameters in the following of applying pBIPV component. More accurate economic and payback period analysis as well as highlighting the benefits which are provided by pBIPV components can have a leading and effective role on encouraging the architects, building manufactures and energy managers to investigate on this technology as a green energy solution which not only creates more jobs in the field of renewable energy applications but also can have a positive impact on reducing the pBIPV manufacturing costs through more device fabrications.

Reference

ABDERREZEK, M., FATHI, M., DJAHLI, F. & AYAD, M. 2013. Numerical Simulation of Luminescent Downshifting in Top Cell of Monolithic Tandem Solar Cells. *International Journal of Photoenergy,* 2013.

AHMED, H. 2014. *Materials Characterization And Plasmonic Interaction In Enhanced Luminescent Down-Shifting Layers For Photovoltaic Devices.* PhD, Dublin Institute of Technology.

AHMED, H., DORAN, J. & MCCORMACK, S. 2016. Increased short-circuit current density and external quantum efficiency of silicon and dye sensitised solar cells through plasmonic luminescent down-shifting layers. *Solar Energy,* 126**,** 146-155.

AHMED, H., MCCORMACK, S. & DORAN, J. 2017a. Plasmonic luminescent down shifting layers for the enhancement of CdTe mini-modules performance. *Solar Energy,* 141**,** 242-248.

AHMED, H., RAFIEE, M., CHANDRA, S., SETHI, A. & MCCORMACK, S. Application of concentrating plasmonic luminescent down-shifting layers for photovoltaic devices. Physics, Simulation, and Photonic Engineering of Photovoltaic Devices VI, 2017b. International Society for Optics and Photonics, 100991A.

ALBERS, P. T. M., BASTIAANSEN, C. W. M. & DEBIJE, M. G. 2013. Dual waveguide patterned luminescent solar concentrators. *Solar Energy,* 95**,** 216-223.

ALEXANDRE, M., CHAPA, M., HAQUE, S., MENDES, M. J., ÁGUAS, H., FORTUNATO, E. & MARTINS, R. 2019. Optimum Luminescent Down-Shifting Properties for High Efficiency and Stable Perovskite Solar Cells. *ACS Applied Energy Materials,* 2**,** 2930-2938.

ALONSO-ÁLVAREZ, D., ROSS, D., KLAMPAFTIS, E., MCINTOSH, K. R., JIA, S., STORIZ, P., STOLZ, T. & RICHARDS, B. S. 2015. Luminescent down-shifting experiment and modelling with multiple photovoltaic technologies. *Progress in Photovoltaics: Research and Applications,* 23**,** 479-497.

ALTERMATT, P. P., XIONG, Z., HE, Q., DENG, W., YE, F., YANG, Y., CHEN, Y., FENG, Z., VERLINDEN, P. J. & LIU, A. 2018. High-performance p-type multicrystalline silicon (mc-Si): Its characterization and projected performance in PERC solar cells. *Solar Energy,* 175**,** 68-74.

ALVAREZ, M. M., KHOURY, J. T., SCHAAFF, T. G., SHAFIGULLIN, M. N., VEZMAR, I. & WHETTEN, R. L. 1997. Optical absorption spectra of nanocrystal gold molecules. *Journal of Physical Chemistry B,* 101**,** 3706-3712.

AMENDOLA, V., PILOT, R., FRASCONI, M., MARAGO, O. M. & IATI, M. A. 2017. Surface plasmon resonance in gold nanoparticles: a review. *Journal of Physics: Condensed Matter,* 29**,** 203002.

ANGER, P., BHARADWAJ, P. & NOVOTNY, L. 2006. Enhancement and quenching of single-molecule fluorescence. *Physical review letters,* 96**,** 113002.

ARAVIND, P. & METIU, H. 1980. The enhancement of Raman and fluorescent intensity by small surface roughness. Changes in dipole emission. *Chemical Physics Letters,* 74**,** 301-305.

ASLAN, K. & PÉREZ-LUNA, V. H. 2004. Quenched emission of fluorescence by ligand functionalized gold nanoparticles. *Journal of fluorescence,* 14**,** 401-405.

ASLAN, K., WU, M., LAKOWICZ, J. R. & GEDDES, C. D. 2007. Fluorescent core− shell Ag@ SiO2 nanocomposites for metal-enhanced fluorescence and single nanoparticle sensing platforms. *Journal of the American Chemical Society,* 129**,** 1524-1525.

ASTE, N., ADHIKARI, R. & DEL PERO, C. Photovoltaic technology for renewable electricity production: Towards net zero energy buildings. Clean Electrical Power (ICCEP), 2011 International Conference on, 2011. IEEE, 446-450.

ASTE, N., TAGLIABUE, L. C., DEL PERO, C., TESTA, D. & FUSCO, R. 2015. Performance analysis of a large-area luminescent solar concentrator module. *Renewable Energy,* 76**,** 330-337.

BARDHAN, R., GRADY, N. K., COLE, J. R., JOSHI, A. & HALAS, N. J. 2009. Fluorescence enhancement by Au nanostructures: nanoshells and nanorods. *ACS nano,* 3**,** 744-752.

BARDHAN, R., GRADY, N. K. & HALAS, N. J. 2008. Nanoscale Control of Near-Infrared Fluorescence Enhancement Using Au Nanoshells. *Small,* 4**,** 1716-1722.

BARNES, W. L., DEREUX, A. & EBBESEN, T. W. 2003. Surface plasmon subwavelength optics. *Nature,* 424**,** 824-830.

BARNHAM, K., MARQUES, J. L., HASSARD, J. & O'BRIEN, P. 2000. Quantum-dot concentrator and thermodynamic model for the global redshift. *Applied Physics Letters,* 76**,** 1197-1199.

BATCHELDER, J., ZEWAI, A. & COLE, T. 1979. Luminescent solar concentrators. 1: Theory of operation and techniques for performance evaluation. *Applied Optics,* 18**,** 3090-3110.

BEN SEXTON, S. C., MEHRAN RAFIEE AND SARAH J MCCORMACK 2018. An optimised Quantum Dot Solar Concentrator. *ESEIA Conference on Smart Energy Systems in Cities and Regions.* Dublin Institute of Technology, Dublin, Ireland.

BERENDS, A. C., RABOUW, F. T., SPOOR, F. C., BLADT, E., GROZEMA, F. C., HOUTEPEN, A. J., SIEBBELES, L. D. & DE MELLO DONEGÁ, C. 2016. Radiative and nonradiative recombination in CuInS2 nanocrystals and CuInS2-based core/shell nanocrystals. *The journal of physical chemistry letters,* 7**,** 3503-3509.

BERGREN, M. R., MAKAROV, N. S., RAMASAMY, K., JACKSON, A., GUGLIELMETTI, R. & MCDANIEL, H. 2018. High-Performance CuInS2 Quantum Dot Laminated Glass Luminescent Solar Concentrators for Windows. *ACS Energy Letters,* 3**,** 520-525.

BHARADWAJ, P. & NOVOTNY, L. 2007. Spectral dependence of single molecule fluorescence enhancement. *Optics Express,* 15**,** 14266-14274.

BOMM, J., BÜCHTEMANN, A., CHATTEN, A. J., BOSE, R., FARRELL, D. J., CHAN, N. L. A., XIAO, Y., SLOOFF, L. H., MEYER, T., MEYER, A., VAN SARK, W. G. J. H. M. & KOOLE, R. 2011. Fabrication and full characterization of state-of-the-art quantum

dot luminescent solar concentrators. *Solar Energy Materials and Solar Cells,* 95**,** 2087-2094.

BOMM, J., BÜCHTEMANN, A., FIORE, A., MANNA, L., NELSON, J. H., HILL, D. & VAN SARK, W. G. 2010. Fabrication and spectroscopic studies on highly luminescent CdSe/CdS nanorod polymer composites. *Beilstein journal of nanotechnology,* 1**,** 94.

BOSE, R., FARRELL, D. J., CHATTEN, A. J., PRAVETTONI, M., BÜCHTEMANN, A., QUILITZ, J., FIORE, A., MANNA, L., NELSON, J. & ALVISATOS, A. P. 2008. The effect of size and dopant concentration on the performance of nanorod luminescent solar concentrators.

BOSE, R., FARRELL, D. J., PARDO-SANCHEZ, C., PRAVETTONI, M., MAZZER, M., CHATTEN, A. J. & BARNHAM, K. W. Luminescent solar concentrators: cylindrical design. 24th European Photovoltaic Conference. Hamburg, Germany, 2009.

BRADSHAW, L. R., KNOWLES, K. E., MCDOWALL, S. & GAMELIN, D. R. 2015. Nanocrystals for luminescent solar concentrators. *Nano letters,* 15**,** 1315-1323.

BRENNAN, L. J., PURCELL-MILTON, F., MCKENNA, B., WATSON, T. M., GUN'KO, Y. K. & EVANS, R. C. 2018. Large area quantum dot luminescent solar concentrators for use with dye-sensitised solar cells. *Journal of Materials Chemistry A,* 6**,** 2671-2680.

BRONSTEIN, N. D. 2015. *Material and Optical Design Rules for High Performance Luminescent Solar Concentrators.* PhD Thesis, University of California, Berkeley.

BRONSTEIN, N. D., YAO, Y., XU, L., O'BRIEN, E., POWERS, A. S., FERRY, V. E., ALIVISATOS, A. P. & NUZZO, R. G. 2015. Quantum Dot Luminescent Concentrator Cavity Exhibiting 30-fold Concentration. *ACS Photonics,* 2**,** 1576-1583.

BROVELLI, S., MEINARDI, F. & CARULLI, F. 2018. Colorless luminescent solar concentrator, free of heavy metals, based on at least ternary chalcogenide semiconductor nanocrystals with absorption extending to the near infrared region. Google Patents.

BUFFA, M., CARTURAN, S., DEBIJE, M., QUARANTA, A. & MAGGIONI, G. 2012. Dye-doped polysiloxane rubbers for luminescent solar concentrator systems. *Solar Energy Materials and Solar Cells,* 103**,** 114-118.

CAMBIÉ, D., ZHAO, F., HESSEL, V., DEBIJE, M. G. & NOËL, T. 2017. A Leaf-Inspired Luminescent Solar Concentrator for Energy-Efficient Continuous-Flow Photochemistry. *Angewandte Chemie International Edition,* 56**,** 1050-1054.

CHANDER, N., SARDANA, S. K., PARASHAR, P. K., KHAN, A., CHAWLA, S. & KOMARALA, V. K. 2015a. Improving the short-wavelength spectral response of silicon solar cells by spray deposition of YVO 4: Eu 3+ downshifting phosphor nanoparticles. *IEEE Journal of Photovoltaics,* 5**,** 1373-1379.

CHANDER, S., PUROHIT, A., NEHRA, A., NEHRA, S. & DHAKA, M. 2015b. A Study on Spectral Response and External Quantum Efficiency of Mono-Crystalline Silicon Solar Cell. *International Journal of Renewable Energy Research (IJRER),* 5**,** 41-44.

CHANDRA, S. 2013. *Approach to Plasmonic Luminescent Solar Concentration.* PhD, Dublin Institute of Technology.

CHANDRA, S., DORAN, J., MCCORMACK, S., KENNEDY, M. & CHATTEN, A. 2012. Enhanced quantum dot emission for luminescent solar concentrators using plasmonic interaction. *Solar Energy Materials and Solar Cells,* 98**,** 385-390.

CHANDRA, S., RAFIEE, M., DORAN, J. & MC CORMACK, S. 2018. Absorption coefficient dependent non-linear properties of thin film luminescent solar concentrators. *Solar Energy Materials and Solar Cells,* 182**,** 331-338.

CHAPIN, D. M., FULLER, C. & PEARSON, G. 1954. A new silicon p-n junction photocell for converting solar radiation into electrical power. *Journal of Applied Physics,* 25**,** 676-677.

CHATTEN, A., BARNHAM, K., BUXTON, B., EKINS-DAUKES, N. & MALIK, M. 2004. Quantum dot solar concentrators. *Semiconductors,* 38**,** 909-917.

CHEN, J.-Y., CHIU, Y.-C., SHIH, C.-C., WU, W.-C. & CHEN, W.-C. 2015. Electrospun nanofibers with dual plasmonic-enhanced luminescent solar concentrator effects for high-performance organic photovoltaic cells. *Journal of Materials Chemistry A,* 3**,** 15039-15048.

CHEN, O., ZHAO, J., CHAUHAN, V. P., CUI, J., WONG, C., HARRIS, D. K., WEI, H., HAN, H.-S., FUKUMURA, D. & JAIN, R. K. 2013. Compact high-quality CdSe–CdS core–shell nanocrystals with narrow emission linewidths and suppressed blinking. *Nature materials,* 12**,** 445.

CHEN, W., LI, J., LIU, P., LIU, H., XIA, J., LI, S., WANG, D., WU, D., LU, W. & SUN, X. W. 2017. Heavy metal free nanocrystals with near infrared emission applying in luminescent solar concentrator. *Solar RRL,* 1**,** 1700041.

CHENG, D. & XU, Q.-H. 2007. Separation distance dependent fluorescence enhancement of fluorescein isothiocyanate by silver nanoparticles. *Chemical communications***,** 248-250.

COLLIN, R. 1990. Field Theory of Guided Waves 2nd edn (Piscataway, NJ: IEEE).

COLVIN, V., SCHLAMP, M. & ALIVISATOS, A. P. 1994. Light-emitting-diodes made from cadmium selenide nanocrystals and a semiconducting polymer. *Nature,* 370**,** 354-357.

CONNELL, R., PINNELL, C. & FERRY, V. E. 2018. Designing spectrally-selective mirrors for use in luminescent solar concentrators. *Journal of Optics,* 20**,** 024009.

COROPCEANU, I. & BAWENDI, M. G. 2014. Core/shell quantum dot based luminescent solar concentrators with reduced reabsorption and enhanced efficiency. *Nano letters,* 14**,** 4097-4101.

COROPCEANU, I., ROSSINELLI, A., CARAM, J. R., FREYRIA, F. S. & BAWENDI, M. G. 2016. Slow-injection growth of seeded CdSe/CdS nanorods with unity fluorescence quantum yield and complete shell to core energy transfer. *ACS nano,* 10**,** 3295-3301.

CORREIA, S. F., DE ZEA BERMUDEZ, V., RIBEIRO, S. J., ANDRÉ, P. S., FERREIRA, R. A. & CARLOS, L. D. 2014. Luminescent solar concentrators: challenges for lanthanide-based organic–inorganic hybrid materials. *Journal of Materials Chemistry A,* 2**,** 5580-5596.

CORREIA, S. F., LIMA, P. P., PECORARO, E., RIBEIRO, S. J., ANDRÉ, P. S., FERREIRA, R. A., CARLOS, L. D. J. P. I. P. R. & APPLICATIONS 2016. Scale up the collection

area of luminescent solar concentrators towards metre-length flexible waveguiding photovoltaics. 24**,** 1178-1193.

COUNCIL, E. 2018. *Proposal for a DIRECTIVE OF THE EUROPEAN PARLIAMENT AND OF THE COUNCIL on the reduction of the impact of certain plastic products on the environment* [Online]. Council of the European Union. Available: https://eur-lex.europa.eu/legal-content/en/ALL/?uri=CELEX%3A52018PC0340 [Accessed 23.05.2018].

COURANT, R., FRIEDRICHS, K. & LEWY, H. 1967. On the partial difference equations of mathematical physics. *IBM journal,* 11**,** 215-234.

CURRIE, M. J., MAPEL, J. K., HEIDEL, T. D., GOFFRI, S. & BALDO, M. A. 2008. High-efficiency organic solar concentrators for photovoltaics. *Science,* 321**,** 226-228.

DARVILL, D., CENTENO, A. & XIE, F. 2013. Plasmonic fluorescence enhancement by metal nanostructures: shaping the future of bionanotechnology. *Physical Chemistry Chemical Physics,* 15**,** 15709-15726.

DE BOER, D. K., LIN, C.-W., GIESBERS, M. P., CORNELISSEN, H. J., DEBIJE, M. G., VERBUNT, P. P. & BROER, D. J. 2011. Polarization-independent filters for luminescent solar concentrators. *Applied Physics Letters,* 98**,** 021111.

DE CARDONA, M. S., CARRASCOSA, M., MESEGUER, F., CUSSO, F. & JAQUE, F. 1985. Outdoor evaluation of luminescent solar concentrator prototypes. *Applied optics,* 24**,** 2028-2032.

DE NISI, F., FRANCISCHELLO, R., BATTISTI, A., PANNIELLO, A., FANIZZA, E., STRICCOLI, M., GU, X., LEUNG, N., TANG, B. & PUCCI, A. 2017. Red-emitting AIEgen for luminescent solar concentrators. *Materials Chemistry Frontiers,* 1**,** 1406-1412.

DEBIJE, M., VAN, M.-P., VERBUNT, P., BROER, D. & BASTIAANSEN, C. The effect of an organic selectively-reflecting mirror on the performance of a luminescent solar concentrator. conference; 24th European Photovoltaic Solar Energy Conference (EU PVSEC), 21-25 September 2009, Hamburg, Germany; 2009-09-21; 2009-09-25, 2009. WIP.

DEBIJE, M. G., TZIKAS, C., RAJKUMAR, V. A. & DE JONG, M. M. 2017. The solar noise barrier project: 2. The effect of street art on performance of a large scale luminescent solar concentrator prototype. *Renewable Energy,* 113**,** 1288-1292.

DEBIJE, M. G., VAN, M.-P., VERBUNT, P. P., KASTELIJN, M. J., VAN DER BLOM, R. H., BROER, D. J. & BASTIAANSEN, C. W. 2010. Effect on the output of a luminescent solar concentrator on application of organic wavelength-selective mirrors. *Applied optics,* 49**,** 745-751.

DEBIJE, M. G. & VERBUNT, P. P. 2012. Thirty years of luminescent solar concentrator research: solar energy for the built environment. *Advanced Energy Materials,* 2**,** 12-35.

DEBIJE, M. G., VERBUNT, P. P., NADKARNI, P. J., VELATE, S., BHAUMIK, K., NEDUMBAMANA, S., ROWAN, B. C., RICHARDS, B. S. & HOEKS, T. L. 2011. Promising fluorescent dye for solar energy conversion based on a perylene perinone. *Applied optics,* 50**,** 163-169.

DESMET, L., RAS, A., DE BOER, D. & DEBIJE, M. 2012. Monocrystalline silicon photovoltaic luminescent solar concentrator with 4.2% power conversion efficiency. *Optics letters,* 37**,** 3087-3089.

DORCÉNA, C. J. 2007. *Effects of Metallic Nanoalloys on Dye Fluorescence.* University Libraries, Virginia Polytechnic Institute and State University.

DULKEITH, E., MORTEANI, A., NIEDEREICHHOLZ, T., KLAR, T., FELDMANN, J., LEVI, S., VAN VEGGEL, F., REINHOUDT, D., MÖLLER, M. & GITTINS, D. 2002. Fluorescence quenching of dye molecules near gold nanoparticles: radiative and nonradiative effects. *Physical review letters,* 89**,** 203002.

DULKEITH, E., RINGLER, M., KLAR, T., FELDMANN, J., MUNOZ JAVIER, A. & PARAK, W. 2005. Gold nanoparticles quench fluorescence by phase induced radiative rate suppression. *Nano letters,* 5**,** 585-589.

EARP, A. A., SMITH, G. B., FRANKLIN, J. & SWIFT, P. 2004. Optimisation of a three-colour luminescent solar concentrator daylighting system. *Solar Energy Materials and Solar Cells,* 84**,** 411-426.

EFRIMA, S. & METIU, H. 1979. Classical theory of light scattering by an adsorbed molecule. I. Theory. *The Journal of Chemical Physics,* 70**,** 1602-1613.

EISFELD, A. & BRIGGS, J. S. 2018. Dye Aggregates in Luminescent Solar Concentrators. *physica status solidi (a),* 215**,** 1700634.

EL-BASHIR, S. 2018. Enhanced fluorescence polarization of fluorescent polycarbonate/zirconia nanocomposites for second generation luminescent solar concentrators. *Renewable Energy,* 115**,** 269-275.

EL-BASHIR, S., ALHARBI, O. & ALSALHI, M. 2013a. Thin-film LSCs based on PMMA nanohybrid coatings: device optimization and outdoor performance. *International Journal of Photoenergy,* 2013.

EL-BASHIR, S., BARAKAT, F. & ALSALHI, M. 2013b. Metal-enhanced fluorescence of mixed coumarin dyes by silver and gold nanoparticles: Towards plasmonic thin-film luminescent solar concentrator. *Journal of Luminescence,* 143**,** 43-49.

EL-BASHIR, S., BARAKAT, F. & ALSALHI, M. 2014. Double layered plasmonic thin-film luminescent solar concentrators based on polycarbonate supports. *Renewable Energy,* 63**,** 642-649.

ERICKSON, C. S., BRADSHAW, L. R., MCDOWALL, S., GILBERTSON, J. D., GAMELIN, D. R. & PATRICK, D. L. 2014. Zero-reabsorption doped-nanocrystal luminescent solar concentrators. *ACS nano,* 8**,** 3461-3467.

EU-PARLIAMENT. 2010. *DIRECTIVE 2010/31/EU OF THE EUROPEAN PARLIAMENT AND OF THE COUNCIL of 19 May 2010 on the energy performance of buildings* [Online]. Official Journal of the European Union. Available: https://eur-lex.europa.eu/eli/dir/2010/31/oj [Accessed 20.04.2019].

EU-PARLIAMENT. 2018. *Energy Efficiency In Buildings: energy consumption by sector in the EU* [Online]. Available: https://epthinktank.eu/2016/07/08/energy-efficiency-in-buildings/ [Accessed 20.05.2018].

EU-UNION. 2010. *Directive 2010/31/EU of the European Parliament and of the Council of 19May 2010 on the energy performance of buildings (recast)* [Online]. Available: https://eur-lex.europa.eu/eli/dir/2010/31/oj [Accessed 28.02.2018].

EUROSTAT. 2018. *Renewable energy in the EU* [Online]. European Commission. Available: https://ec.europa.eu/eurostat/documents/2995521/8612324/8-25012018-AP-EN.pdf/9d28caef-1961-4dd1-a901-af18f121fb2d [Accessed 27.08.2018].

FISHER, M., FARRELL, D., ZANELLA, M., LUPI, A., STAVRINOU, P. N. & CHATTEN, A. J. 2015. Utilizing vertically aligned CdSe/CdS nanorods within a luminescent solar concentrator. *Applied Physics Letters,* 106**,** 041110.

FLORES DAORTA, S., PROTO, A., FUSCO, R., CLAUDIO ANDREANI, L. & LISCIDINI, M. 2014. Cascade luminescent solar concentrators. *Applied Physics Letters,* 104**,** 153901.

FREITAS, V. N. T., FU, L., COJOCARIU, A. M., CATTOËN, X., BARTLETT, J. R., LE PARC, R., BANTIGNIES, J.-L., WONG CHI MAN, M., ANDRÉ, P. S. & FERREIRA, R. A. 2015. Eu3+-based bridged silsesquioxanes for transparent luminescent solar concentrators. *ACS applied materials & interfaces,* 7**,** 8770-8778.

FU, Y., ZHANG, J. & LAKOWICZ, J. R. 2010. Plasmon-enhanced fluorescence from single fluorophores end-linked to gold nanorods. *Journal of the American Chemical Society,* 132**,** 5540-5541.

GAJIC, M., LISI, F., KIRKWOOD, N., SMITH, T. A., MULVANEY, P. & ROSENGARTEN, G. 2017. Circular luminescent solar concentrators. *Solar Energy,* 150**,** 30-37.

GALLAGHER, S., NORTON, B. & EAMES, P. 2007. Quantum dot solar concentrators: electrical conversion efficiencies and comparative concentrating factors of fabricated devices. *Solar Energy,* 81**,** 813-821.

GEDDES, C. D. 2017. *Surface plasmon enhanced, coupled and controlled fluorescence*, John Wiley & Sons.

GERSTEN, J. & NITZAN, A. 1980. Electromagnetic theory of enhanced Raman scattering by molecules adsorbed on rough surfaces. *The Journal of Chemical Physics,* 73**,** 3023-3037.

GHENO, A., TRIGAUD, T., BOUCLÉ, J., AUDEBERT, P., RATIER, B. & VEDRAINE, S. 2018. Stability assessments on luminescent down-shifting molecules for UV-protection of perovskite solar cells. *Optical Materials,* 75**,** 781-786.

GHOSH, S. K. & PAL, T. 2007. Interparticle coupling effect on the surface plasmon resonance of gold nanoparticles: from theory to applications. *Chemical reviews,* 107**,** 4797-4862.

GIEBINK, N. C., WIEDERRECHT, G. P. & WASIELEWSKI, M. R. 2018. Resonance-shifting luminescent solar concentrators. Google Patents.

GLASSNER, A. S. 1989. *An introduction to ray tracing*, Elsevier.

GOETZBERGER, A. 1978. Fluorescent solar energy collectors: operating conditions with diffuse light. *Applied physics,* 16**,** 399-404.

GOETZBERGER, A. & GREUBE, W. 1977. Solar energy conversion with fluorescent collectors. *Applied Physics,* 14**,** 123-139.

GOLDSCHMIDT, J. C., PETERS, M., BÖSCH, A., HELMERS, H., DIMROTH, F., GLUNZ, S. W. & WILLEKE, G. 2009. Increasing the efficiency of fluorescent concentrator systems. *Solar Energy Materials and Solar Cells,* 93**,** 176-182.

GRAND, J., ADAM, P.-M., GRIMAULT, A.-S., VIAL, A., DE LA CHAPELLE, M. L., BIJEON, J.-L., KOSTCHEEV, S. & ROYER, P. 2006. Optical extinction spectroscopy of oblate, prolate and ellipsoid shaped gold nanoparticles: experiments and theory. *Plasmonics,* 1**,** 135-140.

GREEN, M. A., HISHIKAWA, Y., DUNLOP, E. D., LEVI, D. H., HOHL-EBINGER, J. & HO-BAILLIE, A. W. 2018. Solar cell efficiency tables (version 52). *Progress in Photovoltaics: Research and Applications,* 26**,** 427-436.

GRIFFINI, G., BELLA, F., NISIC, F., DRAGONETTI, C., ROBERTO, D., LEVI, M., BONGIOVANNI, R. & TURRI, S. 2015. Multifunctional Luminescent Down-Shifting Fluoropolymer Coatings: A Straightforward Strategy to Improve the UV-Light Harvesting Ability and Long-Term Outdoor Stability of Organic Dye-Sensitized Solar Cells. *Advanced Energy Materials,* 5.

GUTIERREZ, G. D., COROPCEANU, I., BAWENDI, M. G. & SWAGER, T. M. 2016a. A Low Reabsorbing Luminescent Solar Concentrator Employing pi-Conjugated Polymers. *Adv Mater,* 28**,** 497-501.

GUTIERREZ, G. D., COROPCEANU, I., BAWENDI, M. G. & SWAGER, T. M. 2016b. A Low Reabsorbing Luminescent Solar Concentrator Employing π-Conjugated Polymers. *Advanced Materials,* 28**,** 497-501.

H. AHMED, S. C., M. RAFIEE, A. SETHI, AND S. J. MCCORMACK 2017. Application of concentrating plasmonic luminescent down-shifting layers for photovoltaic devices. *SPIE Photonics West 2017.*

HA, S.-J., KANG, J.-H., CHOI, D. H., NAM, S. K., REICHMANIS, E. & MOON, J. H. 2018. Upconversion-Assisted Dual-Band Luminescent Solar Concentrator Coupled for High Power Conversion Efficiency Photovoltaic Systems. *ACS Photonics,* 5**,** 3621-3627.

HAISS, W., THANH, N. T., AVEYARD, J. & FERNIG, D. G. 2007. Determination of size and concentration of gold nanoparticles from UV− Vis spectra. *Analytical chemistry,* 79**,** 4215-4221.

HALL, R. & GREENBERG, D. P. 1983. Testbed for realistic image synthesis. *IEEE COMP. GRAPHICS APPLIC.,* 3**,** 10-20.

HERNANDEZ-NOYOLA, H., POTTERVELD, D. H., HOLT, R. J. & DARLING, S. B. 2012. Optimizing luminescent solar concentrator design. *Energy & Environmental Science,* 5**,** 5798-5802.

HILL, S., CONNELL, R., PETERSON, C., HOLLINGER, J., HILLMYER, M. A., KORTSHAGEN, U. R. & FERRY, V. E. 2018. Silicon quantum dot-poly (methyl methacrylate) nanocomposites with reduced light scattering for luminescent solar concentrators. *ACS Photonics*.

HO, W.-J., FENG, S.-K., LIU, J.-J., YANG, Y.-C. & HO, C.-H. 2018. Improving photovoltaic performance of silicon solar cells using a combination of plasmonic and luminescent downshifting effects. *Applied Surface Science,* 439**,** 868-875.

HÖVEL, H., FRITZ, S., HILGER, A., KREIBIG, U. & VOLLMER, M. 1993. Width of cluster plasmon resonances: bulk dielectric functions and chemical interface damping. *Physical Review B,* 48**,** 18178.

HOVEL, H., HODGSON, R. & WOODALL, J. 1979. The effect of fluorescent wavelength shifting on solar cell spectral response. *Solar Energy Materials,* 2**,** 19-29.

HSIEH, Y.-P., LIANG, C.-T., CHEN, Y.-F., LAI, C.-W. & CHOU, P.-T. 2007. Mechanism of giant enhancement of light emission from Au/CdSe nanocomposites. *Nanotechnology,* 18**,** 415707.

HUGHES, M. D., BORCA-TASCIUC, D.-A. & KAMINSKI, D. A. 2017. Highly efficient luminescent solar concentrators employing commercially available luminescent phosphors. *Solar Energy Materials and Solar Cells,* 171**,** 293-301.

INAN, U. S. & MARSHALL, R. A. 2011. *Numerical electromagnetics: the FDTD method*, Cambridge University Press.

INMAN, R., SHCHERBATYUK, G., MEDVEDKO, D., GOPINATHAN, A. & GHOSH, S. 2011. Cylindrical luminescent solar concentrators with near-infrared quantum dots. *Optics express,* 19**,** 24308-24313.

INOUE, S., JIN, T., MACHIDA, K. & ADACHI, G. 1997. Luminescence property and application of rare earth complexes incorporated in ORMOSIL matrices. *Kidorui (Rare Earths),* 30**,** 190-191.

ISHIHARA, H., SARANG, S., CHEN, Y.-C., LIN, O., PHUMMIRAT, P., THUNG, L., HERNANDEZ, J., GHOSH, S. & TUNG, V. 2016. Nature inspiring processing route toward high throughput production of perovskite photovoltaics. *Journal of Materials Chemistry A,* 4**,** 6989-6997.

ITO, N., KAMARUDIN, M. A., HIROTANI, D., ZHANG, Y., SHEN, Q., OGOMI, Y., IIKUBO, S., MINEMOTO, T., YOSHINO, K. & HAYASE, S. 2018. Mixed Sn–Ge Perovskite for Enhanced Perovskite Solar Cell Performance in Air. *The journal of physical chemistry letters,* 9**,** 1682-1688.

JACQUES, S. L. & WANG, L. 1995. Monte Carlo modeling of light transport in tissues. *Optical-thermal response of laser-irradiated tissue.* Springer.

JANG, E., JUN, S., JANG, H., LIM, J., KIM, B. & KIM, Y. 2010. White-Light-Emitting Diodes with Quantum Dot Color Converters for Display Backlights. *Advanced materials,* 22**,** 3076-3080.

JEONG, B. G., PARK, Y.-S., CHANG, J. H., CHO, I., KIM, J. K., KIM, H., CHAR, K., CHO, J., KLIMOV, V. I. & PARK, P. 2016. Colloidal spherical quantum wells with near-unity photoluminescence quantum yield and suppressed blinking. *ACS nano,* 10**,** 9297-9305.

JOHNSON, P. B. & CHRISTY, R.-W. 1972. Optical constants of the noble metals. *Physical review B,* 6**,** 4370.

JOY, D. C. 1995. *Monte Carlo modeling for electron microscopy and microanalysis*, Oxford University Press.

KAJIYA, J. T. The rendering equation. ACM Siggraph Computer Graphics, 1986. ACM, 143-150.

KANELLIS, M., DE JONG, M. M., SLOOFF, L. & DEBIJE, M. G. 2017. The solar noise barrier project: 1. Effect of incident light orientation on the performance of a large-scale luminescent solar concentrator noise barrier. *Renewable energy,* 103**,** 647-652.

KANIYOOR, A., MCKENNA, B., COMBY, S. & EVANS, R. C. 2016. Design and Response of High-Efficiency, Planar, Doped Luminescent Solar Concentrators Using Organic–Inorganic Di-Ureasil Waveguides. *Advanced Optical Materials,* 4**,** 444-456.

KARTHIKEYAN, B. 2010. Fluorescence quenching of Rhodamine-6G in Au nanocomposite polymers. *Journal of Applied Physics,* 108**,** 084311.

KASTELIJN, M. J., BASTIAANSEN, C. W. & DEBIJE, M. G. 2009. Influence of waveguide material on light emission in luminescent solar concentrators. *Optical Materials,* 31**,** 1720-1722.

KAWANO, K., HASHIMOTO, N. & NAKATA, R. Effects on solar cell efficiency of fluorescence of rare-earth ions. Materials Science Forum, 1997. Trans Tech Publ, 311-314.

KENNEDY, M. 2010. *Monte-Carlo Ray-Trace Modelling of Quantum Dot Solar Concentrators.* PhD, Dublin Institute of Technology.

KENNEDY, M., AHMED, H., DORAN, J., NORTON, B., BOSCH-JIMENEZ, P., PIRRIERA, M. D., TORRALBA-CALLEJA, E., TAUSTE, D. G., AUBOUY, L. & DAREN, S. 2015. Large Stokes shift downshifting Eu (III) films as efficiency enhancing UV blocking layers for dye sensitized solar cells. *physica status solidi (a),* 212**,** 203-210.

KENNEDY, M., MCCORMACK, S., DORAN, J. & NORTON, B. 2008. Ray-trace Modelling of Quantum Dot Solar Concentrators.

KENNEDY, M., MCCORMACK, S., DORAN, J. & NORTON, B. 2009. Improving the optical efficiency and concentration of a single-plate quantum dot solar concentrator using near infra-red emitting quantum dots. *Solar Energy,* 83**,** 978-981.

KERROUCHE, A., HARDY, D. A., ROSS, D. & RICHARDS, B. S. 2014. Luminescent solar concentrators: From experimental validation of 3D ray-tracing simulations to coloured stained-glass windows for BIPV. *Solar Energy Materials and Solar Cells,* 122**,** 99-106.

KHAN, A., YADAV, R., SINGH, S., DUTTA, V. & CHAWLA, S. 2010. Eu3+ doped silica xerogel luminescent layer having antireflection and spectrum modifying properties suitable for solar cell applications. *Materials Research Bulletin,* 45**,** 1562-1566.

KITTLER, S., HICKEY, S. G., WOLFF, T. & EYCHMÜLLER, A. 2015. Easy and fast phase transfer of CTAB stabilised gold nanoparticles from water to organic phase. *Zeitschrift für Physikalische Chemie,* 229**,** 235-245.

KLAMPAFTIS, E. & RICHARDS, B. 2011. Improvement in multi-crystalline silicon solar cell efficiency via addition of luminescent material to EVA encapsulation layer. *Progress in Photovoltaics: Research and Applications,* 19**,** 345-351.

KLAMPAFTIS, E., ROSS, D., MCINTOSH, K. R. & RICHARDS, B. S. 2009. Enhancing the performance of solar cells via luminescent down-shifting of the incident spectrum: A review. *Solar Energy Materials and Solar Cells,* 93**,** 1182-1194.

KLIMOV, V. I., BAKER, T. A., LIM, J., VELIZHANIN, K. A. & MCDANIEL, H. 2016. Quality factor of luminescent solar concentrators and practical concentration limits attainable with semiconductor quantum dots. *ACS Photonics,* 3**,** 1138-1148.

KNOWLES, K. E., KILBURN, T. B., ALZATE, D. G., MCDOWALL, S. & GAMELIN, D. R. 2015. Bright CuInS 2/CdS nanocrystal phosphors for high-gain full-spectrum luminescent solar concentrators. *Chemical Communications,* 51**,** 9129-9132.

KOCHUVEEDU, S. T. & KIM, D. H. 2014. Surface plasmon resonance mediated photoluminescence properties of nanostructured multicomponent fluorophore systems. *Nanoscale,* 6**,** 4966-4984.

KRUMER, Z., PERA, S. J., VAN DIJK-MOES, R. J., ZHAO, Y., DE BROUWER, A. F., GROENEVELD, E., VAN SARK, W. G., SCHROPP, R. E. & DE MELLO DONEGÁ, C. 2013. Tackling self-absorption in luminescent solar concentrators with type-II colloidal quantum dots. *Solar Energy Materials and Solar Cells,* 111**,** 57-65.

KRUMER, Z., VAN SARK, W. G., SCHROPP, R. E. & DE MELLO DONEGÁ, C. 2017. Compensation of self-absorption losses in luminescent solar concentrators by increasing luminophore concentration. *Solar Energy Materials and Solar Cells,* 167**,** 133-139.

KÜHN, S., HÅKANSON, U., ROGOBETE, L. & SANDOGHDAR, V. 2006. Enhancement of single-molecule fluorescence using a gold nanoparticle as an optical nanoantenna. *Physical review letters,* 97**,** 017402.

LEDONNE, A., ACCIARRI, M., BINETTI, S., MARCHIONNA, S., NARDUCCI, D. & ROTTA, D. 2008. Enhancement of solar energy conversion efficiency by light harvesting of organolanthanide complexes. *23rd EU PVSEC, Valencia, Spain*.

LEVCHENKO, V. 2018. Luminescence of Europium complex enhanced by surface plasmons of gold nanoparticles for possible application in luminescent solar concentrators. *Journal of Luminescence,* 193**,** 5-9.

LI, C., CHEN, W., WU, D., QUAN, D., ZHOU, Z., HAO, J., QIN, J., LI, Y., HE, Z. & WANG, K. 2015a. Large Stokes Shift and High Efficiency Luminescent Solar Concentrator Incorporated with CuInS2/ZnS Quantum Dots. *Sci Rep,* 5**,** 17777.

LI, C., CHEN, W., WU, D., QUAN, D., ZHOU, Z., HAO, J., QIN, J., LI, Y., HE, Z. & WANG, K. 2015b. Large stokes shift and high efficiency luminescent solar concentrator incorporated with CuInS 2/ZnS quantum dots. *Scientific reports,* 5**,** 17777.

LI, H., WU, K., LIM, J., SONG, H.-J. & KLIMOV, V. I. 2016. Doctor-blade deposition of quantum dots onto standard window glass for low-loss large-area luminescent solar concentrators. *Nature Energy,* 1**,** 16157.

LI, X., QIAN, J., JIANG, L. & HE, S. 2009. Fluorescence quenching of quantum dots by gold nanorods and its application to DNA detection. *Applied Physics Letters,* 94**,** 063111.

LINDEN, S., KUHL, J. & GIESSEN, H. 2001. Controlling the interaction between light and gold nanoparticles: selective suppression of extinction. *Physical review letters,* 86**,** 4688.

LINK, S. & EL-SAYED, M. A. 1999. Spectral properties and relaxation dynamics of surface plasmon electronic oscillations in gold and silver nanodots and nanorods. ACS Publications.

LIU, G., ZHAO, H., DIAO, F., LING, Z. & WANG, Y. 2018. Stable tandem luminescent solar concentrators based on CdSe/CdS quantum dots and carbon dots. *Journal of Materials Chemistry C,* 6**,** 10059-10066.

LIU, J., WANG, K., ZHENG, W., HUANG, W., LI, C. H. & YOU, X. Z. 2013a. Improving spectral response of monocrystalline silicon photovoltaic modules using high efficient luminescent down-shifting Eu3+ complexes. *Progress in Photovoltaics: Research and Applications,* 21**,** 668-675.

LIU, S.-Y., HUANG, L., LI, J.-F., WANG, C., LI, Q., XU, H.-X., GUO, H.-L., MENG, Z.-M., SHI, Z. & LI, Z.-Y. 2013b. Simultaneous excitation and emission enhancement of fluorescence assisted by double plasmon modes of gold nanorods. *The Journal of Physical Chemistry C,* 117**,** 10636-10642.

LUNT, R. R., BULOVIC, V. & BARR, M. C. 2018. Visibly transparent, luminescent solar concentrator. Google Patents.

LYON, L. A., PENA, D. J. & NATAN, M. J. 1999. Surface plasmon resonance of Au colloid-modified Au films: particle size dependence. *The Journal of Physical Chemistry B,* 103**,** 5826-5831.

MAIER, S. A. 2007. *Plasmonics: fundamentals and applications,* Springer Science & Business Media.

MAN, S., ZHANG, H., LIU, Y., MENG, J., PUN, E. & CHUNG, P. S. 2007. Energy transfer in Pr3+/Yb3+ codoped tellurite glasses. *Optical Materials,* 30**,** 334-337.

MARUYAMA, T. & BANDAI, J. 1999. Solar cell module coated with fluorescent coloring agent. *Journal of the Electrochemical Society,* 146**,** 4406-4409.

MARUYAMA, T. & KITAMURA, R. 2001. Transformations of the wavelength of the light incident upon solar cells. *Solar energy materials and solar cells,* 69**,** 207-216.

MARUYAMA, T., SHINYASHIKI, Y. & OSAKO, S. 1998. Energy conversion efficiency of solar cells coated with fluorescent coloring agent. *Solar energy materials and solar cells,* 56**,** 1-6.

MATEEN, F., ALI, M., OH, H. & HONG, S.-K. 2019. Nitrogen-doped carbon quantum dot based luminescent solar concentrator coupled with polymer dispersed liquid crystal device for smart management of solar spectrum. *Solar Energy,* 178**,** 48-55.

MATLAB. 2017. *Mathworks Documentation* [Online]. MathWorks. Available: https://uk.mathworks.com/help/ [Accessed 31.04.2017].

MEINARDI, F., AKKERMAN, Q. A., BRUNI, F., PARK, S., MAURI, M., DANG, Z., MANNA, L. & BROVELLI, S. 2017a. Doped halide perovskite nanocrystals for reabsorption-free luminescent solar concentrators. *ACS Energy Letters,* 2**,** 2368-2377.

MEINARDI, F., BRUNI, F. & BROVELLI, S. 2017b. Luminescent solar concentrators for building-integrated photovoltaics. *Nature Reviews Materials,* 2**,** 17072.

MEINARDI, F., COLOMBO, A., VELIZHANIN, K. A., SIMONUTTI, R., LORENZON, M., BEVERINA, L., VISWANATHA, R., KLIMOV, V. I. & BROVELLI, S. 2014. Large-area luminescent solar concentrators based on/Stokes-shift-engineered/'nanocrystals in a mass-polymerized PMMA matrix. *Nature Photonics,* 8**,** 392-399.

MEINARDI, F., EHRENBERG, S., DHAMO, L., CARULLI, F., MAURI, M., BRUNI, F., SIMONUTTI, R., KORTSHAGEN, U. & BROVELLI, S. 2017c. Highly efficient luminescent solar concentrators based on earth-abundant indirect-bandgap silicon quantum dots. *Nature Photonics,* 11**,** 177.

MEINARDI, F., MCDANIEL, H., CARULLI, F., COLOMBO, A., VELIZHANIN, K. A., MAKAROV, N. S., SIMONUTTI, R., KLIMOV, V. I. & BROVELLI, S. 2015. Highly efficient large-area colourless luminescent solar concentrators using heavy-metal-free colloidal quantum dots. *Nature nanotechnology*.

MERKX, E., TEN KATE, O. & VAN DER KOLK, E. 2017. Rapid optimization of large-scale luminescent solar concentrators: evaluation for adoption in the built environment. *Optics express,* 25**,** A547-A563.

METIU, H. & DAS, P. 1984. The electromagnetic theory of surface enhanced spectroscopy. *Annual Review of Physical Chemistry,* 35**,** 507-536.

MING, T., ZHAO, L., YANG, Z., CHEN, H., SUN, L., WANG, J. & YAN, C. 2009. Strong polarization dependence of plasmon-enhanced fluorescence on single gold nanorods. *Nano letters,* 9**,** 3896-3903.

MIRERSHADI, S. & AHMADI-KANDJANI, S. 2015. Efficient thin luminescent solar concentrator based on organometal halide perovskite. *Dyes and Pigments,* 120**,** 15-21.

MIRKIN, C. & RATNER, M. 1997. Controlled synthesis and quantum-size effect in gold-coated nanoparticles. *Annu Rev Phys Chem,* 101**,** 1593.

MOSKOVITS, M. 1985. Surface-enhanced spectroscopy. *Reviews of modern physics,* 57**,** 783.

MOUDAM, O., ROWAN, B. C., ALAMIRY, M., RICHARDSON, P., RICHARDS, B. S., JONES, A. C. & ROBERTSON, N. 2009. Europium complexes with high total photoluminescence quantum yields in solution and in PMMA. *Chemical Communications***,** 6649-6651.

MSDN. 2017. *Developer Network* [Online]. Microsoft. Available: https://msdn.microsoft.com/en-us/default.aspx [Accessed 31.04.2017].

MYROSHNYCHENKO, V., RODRÍGUEZ-FERNÁNDEZ, J., PASTORIZA-SANTOS, I., FUNSTON, A. M., NOVO, C., MULVANEY, P., LIZ-MARZÁN, L. M. & DE ABAJO, F. J. G. 2008. Modelling the optical response of gold nanoparticles. *Chemical Society Reviews,* 37**,** 1792-1805.

NAKAMURA, T. & HAYASHI, S. 2005. Enhancement of dye fluorescence by gold nanoparticles: analysis of particle size dependence. *Japanese Journal of Applied Physics,* 44**,** 6833.

NEEDELL, D. R., ILIC, O., BUKOWSKY, C. R., NETT, Z., XU, L., HE, J., BAUSER, H., LEE, B. G., GEISZ, J. F. & NUZZO, R. G. 2018. Design Criteria for Micro-Optical Tandem Luminescent Solar Concentrators. *IEEE Journal of Photovoltaics***,** 1-9.

NIKOLAIDOU, K., SARANG, S., HOFFMAN, C., MENDEWALA, B., ISHIHARA, H., LU, J. Q., ILAN, B., TUNG, V. & GHOSH, S. 2016. Hybrid Perovskite Thin Films as Highly Efficient Luminescent Solar Concentrators. *Advanced Optical Materials,* 4**,** 2126-2132.

NOLASCO, M. M., VAZ, P. M., FREITAS, V. T., LIMA, P. P., ANDRÉ, P. S., FERREIRA, R. A., VAZ, P. D., RIBEIRO-CLARO, P. & CARLOS, L. D. 2013. Engineering highly efficient Eu (III)-based tri-ureasil hybrids toward luminescent solar concentrators. *Journal of Materials Chemistry A,* 1**,** 7339-7350.

NREL. 2019. *Reference Solar Spectral Irradiance: Air Mass 1.5* [Online]. Available: https://rredc.nrel.gov/solar//spectra/am1.5/ [Accessed 31.05.2019].

ORENDORFF, C. J., SAU, T. K. & MURPHY, C. J. 2006. Shape-Dependent Plasmon-Resonant Gold Nanoparticles. *Small,* 2**,** 636-639.

OSINKINA, L. 2014. *Interactions of molecules in the vicinity of gold nanoparticles.* lmu.

PAGLIARO, M., CIRIMINNA, R. & PALMISANO, G. 2010. BIPV: merging the photovoltaic with the construction industry. *Progress in Photovoltaics: Research and Applications,* 18**,** 61-72.

PRAVETTONI, M., FARRELL, D. J., CHATTEN, A. J., BOSE, R., KENNY, R. P. & BARNHAM, K. W. External quantum efficiency measurements of luminescent solar concentrators: a study of the impact of backside reflector size and shape. 24th European Photovoltaic Solar Energy Conference. Hamburg, Germany, 2009a. 332-335.

PRAVETTONI, M., PRAVETTONI, F., VIRTUANI, A., KENNY, R. P., CHATTEN, A. J. & BARNHAM, K. W. Outdoor characterization of luminescent solar concentrators and their possible architectural integration on a historically relevant site in Milan (Italy). Photovoltaic Specialists Conference (PVSC), 2009 34th IEEE, 2009b. IEEE, 000187-000192.

PROISE, F. 2014. *Study and realisation of micro/nano photovoltaic cells and their concentration systems.* Paris 6.

PROTESESCU, L., YAKUNIN, S., BODNARCHUK, M. I., KRIEG, F., CAPUTO, R., HENDON, C. H., YANG, R. X., WALSH, A. & KOVALENKO, M. V. 2015. Nanocrystals of cesium lead halide perovskites (CsPbX3, X= Cl, Br, and I): novel optoelectronic materials showing bright emission with wide color gamut. *Nano letters,* 15**,** 3692-3696.

PV-LIGHTHOUSE. 2017. Available: https://www.pvlighthouse.com.au/ [Accessed 31.01.2017].

RADZIEMSKA, E. 2006. Effect of temperature on dark current characteristics of silicon solar cells and diodes. *International Journal of Energy Research*, 30**,** 127-134.

RAETHER, H. 1988. *Springer tracts in modern physics*, Springer-Verlag.

RAFIEE, M., AHMED, H., CHANDRA, S. & MCCORMACK, S. 2017a. Improving the Mathematical Model for Luminescent Down-Shifting Layers by Investigating their Loss Mechanisms. *33rd European PV Solar Energy Conference and Exhibitions (EU PVSEC 2017),*. Amsterdam, Netherlands.

RAFIEE, M., AHMED, H., CHANDRA, S., SETHI, A. & MCCORMACK, S. J. Monte Carlo Ray Tracing Modelling of Multi-Crystalline Silicon Photovoltaic Device Enhanced by Luminescent Material. 2018 IEEE 7th World Conference on Photovoltaic Energy Conversion (WCPEC)(A Joint Conference of 45th IEEE PVSC, 28th PVSEC & 34th EU PVSEC), 2018a. IEEE, 3139-3141.

RAFIEE, M., CHANDRA, S., AHMED, H., BARNHAM, K. & MCCORMACK, S. J. 2018b. Optical Coupling Sensitivity Study of Luminescent PV Devices Using Monte Carlo Ray Tracing Model. *World Renewable Energy Congress – 18.* University of Kingston, London, UK.

RAFIEE, M., CHANDRA, S., AHMED, H., BARNHAM, K. & MCCORMACK, S. J. 2020. Optical Coupling Sensitivity Study of Luminescent PV Devices Using Monte Carlo Ray-Tracing Model. *Renewable Energy and Sustainable Buildings.* Springer.

RAFIEE, M., CHANDRA, S., AHMED, H. & MCCORMACK, S. 2017b. Analysis of Luminescent Solar Concentrator Performance Using a Ray Tracing Algorithm: Modelling, Optimization and Validation. *13th Photovoltaic Science, Applications and Technology Conference C99 (PVSAT-13).* Bangor, UK.

RAFIEE, M., CHANDRA, S., AHMED, H. & MCCORMACK, S. 2017c. Quantum Dot Luminescent Solar Concentrator: Optimization of Concentration and Thickness. *33rd European PV Solar Energy Conference and Exhibitions (EU PVSEC 2017),.* Amsterdam, Netherlands.

RAFIEE, M., CHANDRA, S., AHMED, H. & MCCORMACK, S. J. 2019. An overview of various configurations of Luminescent Solar Concentrators for photovoltaic applications. *Optical Materials,* 91**,** 212-227.

RAKIĆ, A. D., DJURIŠIĆ, A. B., ELAZAR, J. M. & MAJEWSKI, M. L. 1998. Optical properties of metallic films for vertical-cavity optoelectronic devices. *Applied optics,* 37**,** 5271-5283.

RAMPI, M. A., SCHUELLER, O. J. & WHITESIDES, G. M. 1998. Alkanethiol self-assembled monolayers as the dielectric of capacitors with nanoscale thickness. *Applied Physics Letters,* 72**,** 1781-1783.

REINDERS, A., KISHORE, R., SLOOFF, L. & EGGINK, W. 2018. Luminescent solar concentrator photovoltaic designs. *Japanese Journal of Applied Physics,* 57**,** 08RD10.

REINECK, P., GÓMEZ, D., NG, S. H., KARG, M., BELL, T., MULVANEY, P. & BACH, U. 2013. Distance and wavelength dependent quenching of molecular fluorescence by Au@ SiO2 core–shell nanoparticles. *ACS nano,* 7**,** 6636-6648.

REISFELD, R., LEVCHENKO, V. & SARAIDAROV, T. 2011. Interaction of luminescent dyes with noble metal nanoparticles in organic–inorganic glasses for future luminescent materials. *Polymers for Advanced Technologies,* 22**,** 60-64.

RENNY, A., YANG, C., ANTHONY, R. & LUNT, R. R. 2018. Luminescent Solar Concentrator Paintings: Connecting Art and Energy. *Journal of Chemical Education*.

RICHARDS, B. & MCINTOSH, K. 2007. Overcoming the poor short wavelength spectral response of CdS/CdTe photovoltaic modules via luminescence down-shifting: ray-tracing simulations. *Progress in Photovoltaics: Research and Applications,* 15**,** 27-34.

RITCHIE, R. 1957. Plasma losses by fast electrons in thin films. *Physical Review,* 106**,** 874.

RONDÃO, R., FRIAS, A. R., CORREIA, S. F., FU, L., DE ZEA BERMUDEZ, V. N., ANDRÉ, P. S., FERREIRA, R. A. & CARLOS, L. D. 2017. High-performance near-infrared luminescent solar concentrators. *ACS applied materials & interfaces,* 9**,** 12540-12546.

ROSS, D., ALONSO-ALVAREZ, D., KLAMPAFTIS, E., FRITSCHE, J., BAUER, M., DEBIJE, M. G., FIFIELD, R. M. & RICHARDS, B. S. 2014. The Impact of Luminescent Down Shifting on the Performance of CdTe Photovoltaics: Impact of the Module Vintage. *IEEE Journal of Photovoltaics,* 4**,** 457-464.

ROSS, D., KLAMPAFTIS, E., FRITSCHE, J., BAUER, M. & RICHARDS, B. S. 2012. Increased short-circuit current density of production line CdTe mini-module through luminescent down-shifting. *Solar Energy Materials and Solar Cells,* 103**,** 11-16.

ROTH, S. D. 1982. Ray casting for modeling solids. *Computer graphics and image processing,* 18**,** 109-144.

ROTHEMUND, R. 2014. Optical modelling of the external quantum efficiency of solar cells with luminescent down-shifting layers. *Solar Energy Materials and Solar Cells,* 120**,** 616-621.

ROWAN, B. 2007. The development of a quantum dot solar concentrator. *Doctoral***,** 12.

ROWAN, B. C., WILSON, L. R. & RICHARDS, B. S. 2008. Advanced Material Concepts for Luminescent Solar Concentrators. *IEEE Journal of Selected Topics in Quantum Electronics,* 14**,** 1312-1322.

ŞAHIN, D. & ILAN, B. 2013. Radiative transport theory for light propagation in luminescent media. *JOSA A,* 30**,** 813-820.

ŞAHIN, D., ILAN, B. & KELLEY, D. F. 2011. Monte-Carlo simulations of light propagation in luminescent solar concentrators based on semiconductor nanoparticles. *Journal of Applied Physics,* 110**,** 033108.

SALEM, A., MANSOUR, A., EL-SAYED, N. & BASSYOUNI, A. 2000. Outdoor testing and solar simulation for oxazine 750 laser dye luminescent solar concentrator. *Renewable energy,* 20**,** 95-107.

SANGUINETI, A., MONGUZZI, A., VACCARO, G., MEINARDI, F., RONCHI, E., MORET, M., COSENTINO, U., MORO, G., SIMONUTTI, R. & MAURI, M. 2012. NIR emitting ytterbium chelates for colourless luminescent solar concentrators. *Physical Chemistry Chemical Physics,* 14**,** 6452-6455.

SARAIDAROV, T., LEVCHENKO, V., GRABOWSKA, A., BOROWICZ, P. & REISFELD, R. 2010. Non-self-absorbing materials for Luminescent Solar Concentrators (LSC). *Chemical Physics Letters,* 492**,** 60-62.

SCAFFARDI, L., PELLEGRI, N., DE SANCTIS, O. & TOCHO, J. 2004. Sizing gold nanoparticles by optical extinction spectroscopy. *Nanotechnology,* 16**,** 158.

SCHNEIDER, J. B. 2010. *Understanding the finite-difference time-domain method.* Washington State University.

SCHRECENGOST, J. R., BOWSER, S. D., WEIBLE, S. W., SOLOMON, J. M., MINNER, L. J., GRESH, J. T. & WITTMERSHAUS, B. P. 2018. Increasing the area of a white scattering background can increase the power output of a luminescent solar concentrator. *Solar Energy,* 170**,** 132-137.

SETHI, A. 2017. Metal Nanoparticle Synthesis for Use in Plasmonic Luminescent Devices. Trinity College Dublin.

SETHI, A. 2019. *Metal Nanoparticle Synthesis for Use in Plasmonic Luminescent Devices.* PhD, Trinity College Dublin.

SETHI AND RAFIEE, M. A. A., CHANDRA, S., AHMED, H. & MCCORMACK, S. 2019. Unified Methodology for Fabrication and Quantification of Gold Nanorods, Gold Core Silver Shell Nanocuboids, and Their Polymer Nanocomposites. *Langmuir,* 35**,** 13011-13019.

SEXTON, B. 2018. *Luminescent Solar Devices for Building Integrated Components.* Master, Trinity College Dublin.

SHARMA, M., GUNGOR, K., YELTIK, A., OLUTAS, M., GUZELTURK, B., KELESTEMUR, Y., ERDEM, T., DELIKANLI, S., MCBRIDE, J. R. & DEMIR, H. V. 2017. Near-Unity Emitting Copper-Doped Colloidal Semiconductor Quantum Wells for Luminescent Solar Concentrators. *Advanced Materials,* 29**,** 1700821.

SHCHERBATYUK, G., INMAN, R., WANG, C., WINSTON, R. & GHOSH, S. 2010. Viability of using near infrared PbS quantum dots as active materials in luminescent solar concentrators. *Applied Physics Letters,* 96**,** 191901.

SHOLIN, V., OLSON, J. & CARTER, S. 2007. Semiconducting polymers and quantum dots in luminescent solar concentrators for solar energy harvesting. *Journal of applied physics,* 101**,** 123114.

SLOOFF, L., KINDERMAN, R., BURGERS, A., BAKKER, N., VAN ROOSMALEN, J., BÜCHTEMANN, A., DANZ, R. & SCHLEUSENER, M. 2007. Efficiency enhancement of solar cells by application of a polymer coating containing a luminescent dye. *Journal of solar energy engineering,* 129**,** 272-276.

SLOOFF, L., KINDERMAN, R., BURGERS, A., BÜCHTEMANN, A., DANZ, R., MEYER, T., CHATTEN, A., FARELL, D., BARNHAM, K. & VAN ROOSMALEN, J. The luminescent concentrator illuminated. Photonics Europe, 2006. International Society for Optics and Photonics, 61970K-61970K-8.

SLOOFF, L. H., BENDE, E. E., BURGERS, A. R., BUDEL, T., PRAVETTONI, M., KENNY, R. P., DUNLOP, E. D. & BÜCHTEMANN, A. 2008. A luminescent solar concentrator with 7.1% power conversion efficiency. *physica status solidi (RRL)-Rapid Research Letters,* 2**,** 257-259.

SOL, J. A., TIMMERMANS, G. H., VAN BREUGEL, A. J., SCHENNING, A. P. & DEBIJE, M. G. 2018. Multistate Luminescent Solar Concentrator "Smart" Windows. *Advanced Energy Materials,* 8**,** 1702922.

SOLANKI, C. S. 2015. *Solar photovoltaics: fundamentals, technologies and applications*, PHI Learning Pvt. Ltd.

SOLLER, T., RINGLER, M., WUNDERLICH, M., KLAR, T., FELDMANN, J., JOSEL, H.-P., MARKERT, Y., NICHTL, A. & KÜRZINGER, K. 2007. Radiative and nonradiative rates of phosphors attached to gold nanoparticles. *Nano Letters,* 7**,** 1941-1946.

SONG, H.-J., JEONG, B. G., LIM, J., LEE, D. C., BAE, W. K. & KLIMOV, V. I. 2017. Performance Limits of Luminescent Solar Concentrators Tested with Seed/Quantum-Well Quantum Dots in a Selective-Reflector-Based Optical Cavity. *Nano letters,* 18**,** 395-404.

SÖNNICHSEN, C., FRANZL, T., WILK, T., VON PLESSEN, G., FELDMANN, J., WILSON, O. & MULVANEY, P. 2002. Drastic reduction of plasmon damping in gold nanorods. *Physical review letters,* 88**,** 077402.

STRANIK, O., NOONEY, R., MCDONAGH, C. & MACCRAITH, B. D. 2007. Optimization of nanoparticle size for plasmonic enhancement of fluorescence. *Plasmonics,* 2**,** 15-22.

STRUMENTI, M. 2019. *SOLAR CELL CHARACTERISATION* [Online]. Available: http://2mstrumenti.com/pve300/ [Accessed 20/05/2019].

SUMNER, R., EISELT, S., KILBURN, T. B., ERICKSON, C., CARLSON, B., GAMELIN, D. R., MCDOWALL, S. & PATRICK, D. L. 2017. Analysis of optical losses in high-efficiency CuInS2-based nanocrystal luminescent solar concentrators: balancing absorption versus scattering. *The Journal of Physical Chemistry C,* 121**,** 3252-3260.

ŠVRČEK, V., SLAOUI, A. & MULLER, J.-C. 2004. Silicon nanocrystals as light converter for solar cells. *Thin Solid Films,* 451**,** 384-388.

TAFLOVE, A. 1980. Application of the finite-difference time-domain method to sinusoidal steady-state electromagnetic-penetration problems. *IEEE Transactions on Electromagnetic Compatibility***,** 191-202.

TAflOVE, A. & HAGNESS, S. C. 1995. Computational electrodynamics: the finite-difference time-domain method. *Norwood, 2nd Edition, MA: Artech House, l995*.

TAFLOVE, A. & HAGNESS, S. C. 2005. *Computational electrodynamics: the finite-difference time-domain method,* Artech house.

TAM, F., GOODRICH, G. P., JOHNSON, B. R. & HALAS, N. J. 2007. Plasmonic enhancement of molecular fluorescence. *Nano letters,* 7**,** 496-501.

TOVMACHENKO, O. G., GRAF, C., VAN DEN HEUVEL, D. J., VAN BLAADEREN, A. & GERRITSEN, H. C. 2006. Fluorescence enhancement by metal-core/silica-shell nanoparticles. *Advanced materials,* 18**,** 91-95.

TSOI, S., BROER, D. J., BASTIAANSEN, C. W. & DEBIJE, M. G. 2010. Patterned dye structures limit reabsorption in luminescent solar concentrators. *Optics express,* 18**,** A536-A543.

TUMMELTSHAMMER, C., BROWN, M. S., TAYLOR, A., KENYON, A. J. & PAPAKONSTANTINOU, I. 2013. Efficiency and loss mechanisms of plasmonic luminescent solar concentrators. *Optics express,* 21**,** A735-A749.

TUMMELTSHAMMER, C., PORTNOI, M., MITCHELL, S. A., LEE, A.-T., KENYON, A. J., TABOR, A. B. & PAPAKONSTANTINOU, I. 2017. On the ability of förster resonance energy transfer to enhance luminescent solar concentrator efficiency. *Nano Energy,* 32**,** 263-270.

TUMMELTSHAMMER, C., TAYLOR, A., KENYON, A. & PAPAKONSTANTINOU, I. 2016. Losses in luminescent solar concentrators unveiled. *Solar Energy Materials and Solar Cells,* 144**,** 40-47.

VAN DER ZANDE, B. M., KOPER, G. J. & LEKKERKERKER, H. N. 1999. Alignment of rod-shaped gold particles by electric fields. *The Journal of Physical Chemistry B,* 103**,** 5754-5760.

VAN SARK, W., MORAITIS, P., AALBERTS, C., DRENT, M., GRASSO, T., L'ORTIJE, Y., VISSCHERS, M., WESTRA, M., PLAS, R. & PLANJE, W. 2017. The "Electric Mondrian" as a luminescent solar concentrator demonstrator case study. *Solar RRL,* 1**,** 1600015.

VAN SARK, W. G. 2013. Luminescent solar concentrators–A low cost photovoltaics alternative. *Renewable Energy,* 49**,** 207-210.

VAN SARK, W. G., BARNHAM, K. W., SLOOFF, L. H., CHATTEN, A. J., BÜCHTEMANN, A., MEYER, A., MCCORMACK, S. J., KOOLE, R., FARRELL, D. J. & BOSE, R. 2008. Luminescent Solar Concentrators-A review of recent results. *Optics Express,* 16**,** 21773-21792.

VAN SARK, W. G. J. H. M. 2005. Enhancement of solar cell performance by employing planar spectral converters. *Applied Physics Letters,* 87**,** 151117.

VAN SARK, W. G. J. H. M., MEIJERINK, A., SCHROPP, R. E. I., VAN ROOSMALEN, J. A. M. & LYSEN, E. H. 2005. Enhancing solar cell efficiency by using spectral converters. *Solar Energy Materials and Solar Cells,* 87**,** 395-409.

VASILIEV, M., ALAMEH, K., BADSHAH, M. & KIM, S.-M. Semi-transparent energy-harvesting solar concentrator windows employing infrared transmission-enhanced glass and large-area microstructured diffractive elements. Photonics, 2018. Multidisciplinary Digital Publishing Institute, 25.

VIAL, A., GRIMAULT, A.-S., MACÍAS, D., BARCHIESI, D. & DE LA CHAPELLE, M. L. 2005. Improved analytical fit of gold dispersion: Application to the modeling of extinction spectra with a finite-difference time-domain method. *Physical Review B,* 71**,** 085416.

VISHWANATHAN, B., REINDERS, A. H. M. E., DE BOER, D. K. G., DESMET, L., RAS, A. J. M., ZAHN, F. H. & DEBIJE, M. G. 2015. A comparison of performance of flat and bent photovoltaic luminescent solar concentrators. *Solar Energy,* 112**,** 120-127.

VOSSEN, F. M., AARTS, M. P. & DEBIJE, M. G. 2016. Visual performance of red luminescent solar concentrating windows in an office environment. *Energy and Buildings,* 113**,** 123-132.

WALDRON, D. L., PRESKE, A., ZAWODNY, J. M., KRAUSS, T. D. & GUPTA, M. C. 2017. PbSe quantum dot based luminescent solar concentrators. *Nanotechnology,* 28**,** 095205.

WANG, B., LI, B., SHEN, T., LI, M. & TIAN, J. 2018a. ZnSe quantum dots downshifting layer for perovskite solar cells. *Journal of energy chemistry,* 27**,** 736-741.

WANG, C., HIRST, L. S. & WINSTON, R. Optical design and efficiency improvement for organic luminescent solar concentrators. SPIE Optical Engineering+ Applications, 2011a. International Society for Optics and Photonics, 81240O-81240O-10.

WANG, C., WINSTON, R., ZHANG, W., PELKA, D. G. & CARTER, S. A. 2011b. Size-and structure-dependent efficiency enhancement for luminescent solar concentrators. *Journal of Photonics for Energy,* 1**,** 015502.

WANG, D.-S., CHEW, H. & KERKER, M. 1980. Enhanced Raman scattering at the surface (SERS) of a spherical particle. *Applied optics,* 19**,** 2256-2257.

WANG, T., ZHANG, J., MA, W., LUO, Y., WANG, L., HU, Z., WU, W., WANG, X., ZOU, G. & ZHANG, Q. 2011c. Luminescent solar concentrator employing rare earth complex with zero self-absorption loss. *Solar Energy,* 85**,** 2571-2579.

WANG, X., WANG, T., TIAN, X., WANG, L., WU, W., LUO, Y. & ZHANG, Q. 2011d. Europium complex doped luminescent solar concentrators with extended absorption range from UV to visible region. *Solar Energy,* 85**,** 2179-2184.

WANG, Z., ZHAO, X., GUO, Z., MIAO, P. & GONG, X. 2018b. Carbon dots based nanocomposite thin film for highly efficient luminescent solar concentrators. *Organic Electronics,* 62**,** 284-289.

WEBER, W. & LAMBE, J. 1976a. Luminescent greenhouse collector for solar radiation. *Applied Optics,* 15**,** 2299.

WEBER, W. & LAMBE, J. 1976b. Luminescent greenhouse collector for solar radiation. *Applied optics,* 15**,** 2299-2300.

WEN, C., FU, C., TANG, J., LIU, D., HU, S. & XING, Z. 2012. The influence of environment temperatures on single crystalline and polycrystalline silicon solar cell performance. *Science China Physics, Mechanics and Astronomy,* 55**,** 235-241.

WENHAM, S. R. 2012. *Applied photovoltaics*, Routledge.

WHITTED, T. An improved illumination model for shaded display. ACM Siggraph 2005 Courses, 2005. ACM, 4.

WILSON, L. & RICHARDS, B. 2009. Measurement method for photoluminescent quantum yields of fluorescent organic dyes in polymethyl methacrylate for luminescent solar concentrators. *Applied optics,* 48**,** 212-220.

WILSON, L. R., KLAMPAFTIS, E. & RICHARDS, B. S. 2017. Enhancement of power output from a large-area luminescent solar concentrator with 4.8× concentration via solar cell current matching. *IEEE Journal of Photovoltaics,* 7**,** 802-809.

WU, K., LI, H. & KLIMOV, V. I. 2018. Tandem luminescent solar concentrators based on engineered quantum dots. *Nature Photonics,* 12**,** 105.

XU, L., YAO, Y., BRONSTEIN, N. D., LI, L., ALIVISATOS, A. P. & NUZZO, R. G. 2016. Enhanced photon collection in luminescent solar concentrators with distributed Bragg reflectors. *ACS Photonics,* 3**,** 278-285.

XU, X., RAY, R., GU, Y., PLOEHN, H. J., GEARHEART, L., RAKER, K. & SCRIVENS, W. A. 2004. Electrophoretic analysis and purification of fluorescent single-walled carbon nanotube fragments. *Journal of the American Chemical Society,* 126**,** 12736-12737.

YAMADA, K., WADA, Y. & KAWANO, K. 2000. Improvement of efficiency of solar cells by application of the rare earth ions doped fluorescent glass. *Kidorui (Rare Earths),* 36**,** 252-253.

YAMADA, N., NGUYEN ANH, L. & KAMBAYASHI, T. 2010. Escaping losses of diffuse light emitted by luminescent dyes doped in micro/nanostructured solar cell systems. *Solar Energy Materials and Solar Cells,* 94**,** 413-419.

YANG, C. & LUNT, R. R. 2017. Limits of visibly transparent luminescent solar concentrators. *Advanced Optical Materials,* 5**,** 1600851.

YANG, W., MA, Z., TANG, X., FENG, C., ZHAO, W. & SHI, P. 2008. Internal quantum efficiency for solar cells. *Solar Energy,* 82**,** 106-110.

YEE, K. 1966. Numerical solution of initial boundary value problems involving Maxwell's equations in isotropic media. *IEEE Transactions on antennas and propagation,* 14**,** 302-307.

YOON, J., LI, L., SEMICHAEVSKY, A. V., RYU, J. H., JOHNSON, H. T., NUZZO, R. G. & ROGERS, J. A. 2011. Flexible concentrator photovoltaics based on microscale silicon solar cells embedded in luminescent waveguides. *Nature communications,* 2**,** 343.

ZHANG, J., WANG, M., ZHANG, Y., HE, H., XIE, W., YANG, M., DING, J., BAO, J., SUN, S. & GAO, C. 2015. Optimization of large-size glass laminated luminescent solar concentrators. *Solar Energy,* 117**,** 260-267.

ZHAO, H., BENETTI, D., JIN, L., ZHOU, Y., ROSEI, F. & VOMIERO, A. 2016. Absorption Enhancement in "Giant" Core/Alloyed-Shell Quantum Dots for Luminescent Solar Concentrator. *Small,* 12**,** 5354-5365.

ZHAO, H., BENETTI, D., TONG, X., ZHANG, H., ZHOU, Y., LIU, G., MA, D., SUN, S., WANG, Z. M. & WANG, Y. 2018. Efficient and stable tandem luminescent solar concentrators based on carbon dots and perovskite quantum dots. *Nano Energy,* 50**,** 756-765.

ZHAO, H., ZHOU, Y., BENETTI, D., MA, D. & ROSEI, F. 2017. Perovskite quantum dots integrated in large-area luminescent solar concentrators. *Nano energy,* 37**,** 214-223.

ZHAO, Y. & LUNT, R. R. 2013. Transparent Luminescent Solar Concentrators for Large-Area Solar Windows Enabled by Massive Stokes-Shift Nanocluster Phosphors. *Advanced Energy Materials,* 3**,** 1143-1148.

ZHAO, Y., MEEK, G. A., LEVINE, B. G. & LUNT, R. R. 2014. Near-Infrared Harvesting Transparent Luminescent Solar Concentrators. *Advanced Optical Materials,* 2**,** 606-611.

ZHOU, Y., BENETTI, D., FAN, Z., ZHAO, H., MA, D., GOVOROV, A. O., VOMIERO, A. & ROSEI, F. 2016. Near infrared, highly efficient luminescent solar concentrators. *Advanced Energy Materials,* 6**,** 1501913.

ZHOU, Y., BENETTI, D., TONG, X., JIN, L., WANG, Z. M., MA, D., ZHAO, H. & ROSEI, F. 2018a. Colloidal carbon dots based highly stable luminescent solar concentrators. *Nano Energy,* 44**,** 378-387.

ZHOU, Y., ZHAO, H., MA, D. & ROSEI, F. 2018b. Harnessing the properties of colloidal quantum dots in luminescent solar concentrators. *Chemical Society Reviews*.

ZHU, M., LI, Y., TIAN, S., XIE, Y., ZHAO, X. & GONG, X. 2019. Deep-red emitting zinc and aluminium co-doped copper indium sulfide quantum dots for luminescent solar concentrators. *Journal of colloid and interface science,* 534**,** 509-517.

Appendices

Appendix 1: Ray Tracer GUI Panels and Their Contents

- **Input Configuration Panel**

The inputs of the system, different parameters and specifications of the layer are defined in this panel. Imported spectra (solar radiation, attenuation and scattering spectra of the host material and absorption and emission spectra of the luminescent material) in this version are from 300 to 1200 nm. The "Input Configuration" panel includes the following inputs:

Host Material Type: Host material of the device can be selected. Based on the selection, the attenuation coefficient and scattering coefficient profiles of the host material are loaded to the algorithm.

Radiation Spectrum: Spectrum and the type (direct, diffuse, global) of the incident solar radiation can be imported to the system as an excel file.

Absorption Coefficient: Wavelength dependent absorption coefficient spectrum of the luminescent materials can be imported to the system as an excel file in 1/cm.

Emission Spectrum: Wavelength dependent emission spectrum of the luminescent materials can be imported to the system as an excel file.

n1: the refraction index of the outer area (such as air).

n2: the refraction index of the host material.

Length (mm): Length of the layer in mm.

Width (mm): Width of the layer in mm.

Thickness (mm): Thickness of the layer in mm.

PV Efficiency: Efficiency in PV panels can be selected as a constant number between 0 - 1.

Mirror Reflectivity: Reflectivity of the mirror in the structure can be selected as a constant number between 0 - 1.

QY: QY of the selected luminescent material can be selected as a constant number between 0 - 1.

Exposing Time(s): Exposing time (t_{ex}) of the incident solar radiation to the device can be selected in seconds.

Sampling Steps (nm): Wavelength steps of the irradiated input light

Draw Rays: User can determine whether or not to visually view the ray traces in the device while simulating.

PV Plane: User can select the planes attached to PV.

Mirror Plane: User can select the planes attached to mirror.

- **Summary/Results Panel:**

User can find a summary of the results obtained for each simulation such as the parameters of the configured device, input energy and, number of rays and final output data and save the screen as a summary sheet. In addition, all final results mentioned in the Section 3-1-1 can be exported as an excel file.

- **Graphs Panel**

This panel generates and shows three graphs (1) the final structure of configured device; (2) profile of the input energy, and (3) output energy spectrum.

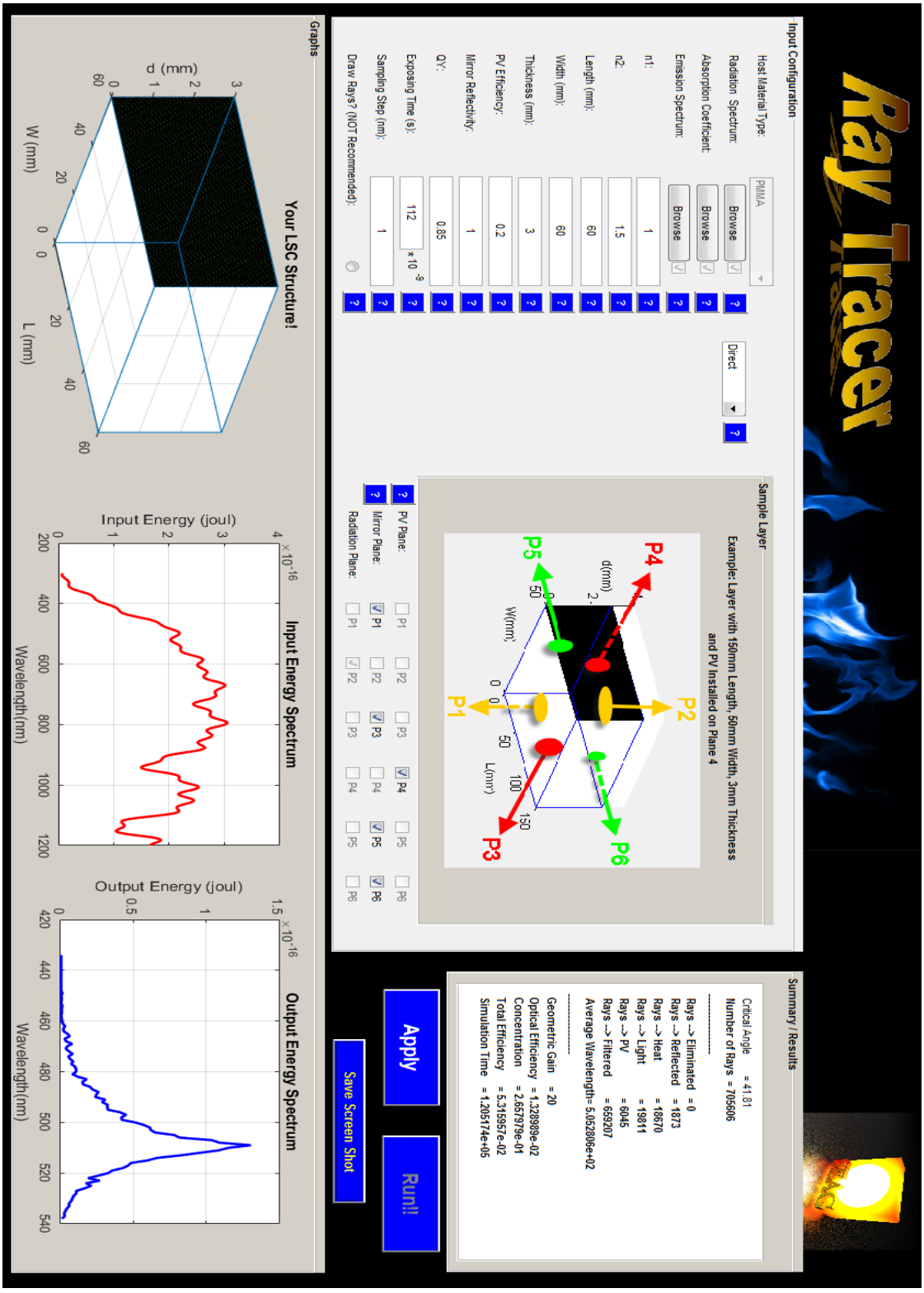

Fig. A.1: The designed GUI for the developed Ray Tracer program

Appendix 2: PEDAL GUI Panels and Their Contents

- **Panel:**

The details about the input solar radiation and used PV cell are defined in this part of the GUI which includes:

Number of Layers: The number of layers coupled to each other in the luminescent solar devices can be selected each of which can be separately configured in "Input Configuration" section.

Wavelength Range (nm): The wavelength range of interest of the modelling can be selected.

Radiation in Watts?: The user can define the type of radiation (direct, global, diffuse) and unit of the input irradiance. (Note that the unit of the input irradiance is given in $W.m^{-2}.nm^{-1}$ in some experiments and more often is given as arbitrary unit (a.u.) intensity of the solar radiation (number of photons)).

Radiation Spectrum: The radiation spectrum is imported to the software as excel file.

PV?: The user is able to select whether the modelled device includes a PV cell on the detector plane or not. Then, they can import the external quantum efficiency (EQE) spectrum of the used PV solar cell to the program.

Perimeter Refraction Index: Refraction index of the device perimeter is selected.

Mirror Reflectivity: Reflectivity of the mirror in the structure can be selected as a constant number between 0 - 1.

Exposing Time(s): Exposing time (t_{ex}) of the incident solar radiation to the device can be selected in seconds.

Sampling Steps (nm): Wavelength steps of the irradiated input solar radiation.

Draw Rays: User can determine whether or not to visually view the ray traces in the device while simulating.

Project Title (Optional): The user can select an optional name for the model.

- **Input Configuration:**

In this section, each layer of the device can be separately configured by importing the input parameters. After configuring the selected layer, user may save the layer by clicking on "Save Layer" button and then configure the next layer(s). The parameters in this section include:

Layer: The working layer is selected for customisation.

MNP Coupled?: User can determine whether MNP is coupled to luminescent material in the selected layer (pLS device modelling) or not (LS device modelling)

MNP PDEF: The PDEF of the used MNP is imported to the program as an excel file.

MNP Extinction: Wavelength and concentration (N/L) dependent extinction spectrum of the MNP can be imported to the system as an excel file.

Extinction Peak: The resonance peak value of the extinction spectrum with particular concentration (N/L)

Distributed Coupling Distance?: User can determine the coupling distance between the MNP and luminescent molecule in nm. Alternatively, they can select "distributed coupling distance radio button" by which the distance between the MNP and luminescent molecule is randomly selected based on the concentration (N/L) of materials.

MNP CF: The concentration factor of MNP is imported which is a factor used to apply different concentrations (N/L) of the material to the algorithm.

QY: Quantum Yield (QY) of the selected luminescent material can be selected as a constant number between 0 - 1.

Absorbance: Wavelength and concentration (wt %) dependent absorbance spectrum of the luminescent material can be imported to the system as an excel file.

Emission: Wavelength dependent emission spectrum of the luminescent materials can be imported to the system as an excel file.

Luminescent CF: The concentration factor of luminescent material.

Host Material Type: The host material of the layer is selected which characterises the attenuation and scattering losses.

Refraction Index: The refraction index of the host material.

Length (mm): Length of the layer in mm.

Width (mm): Width of the layer in mm.

Thickness (mm): Thickness of the layer in mm.

Detector Plane: User can select the detector planes which may couple to PV cell. (Based on the provided Sample Layer)

Mirror Plane: User can select the planes coupled to mirror. (Based on the provided Sample Layer)

Radiation Plane: User can select the plane irradiated by the input radiation spectrum. (Based on the provided Sample Layer)

- **Summary/Results:**

After configuring the device, user will be able to run the simulation by clicking on "Apply" and then "Run!!" buttons. If there is any errors or mismatches in the configured parameters, the software warns the user to correct them. After finishing the simulation, a summary of the results (such as number of rays, the rate of different losses, rate of the rays received by the detector plane, input and output energy, optical efficiency, solar concentration ratio, current density of the PV and simulation time) will be shown in the "Summary/Results" section. The screen can be also saved as a summary sheet by clicking on "Save Screen Shot" button. Final results can be exported as an excel file.

- **Graphs:**

This panel generates and shows three graphs including: (1) the final structure of the configured device; (2) profile of the input, and (3) output spectra

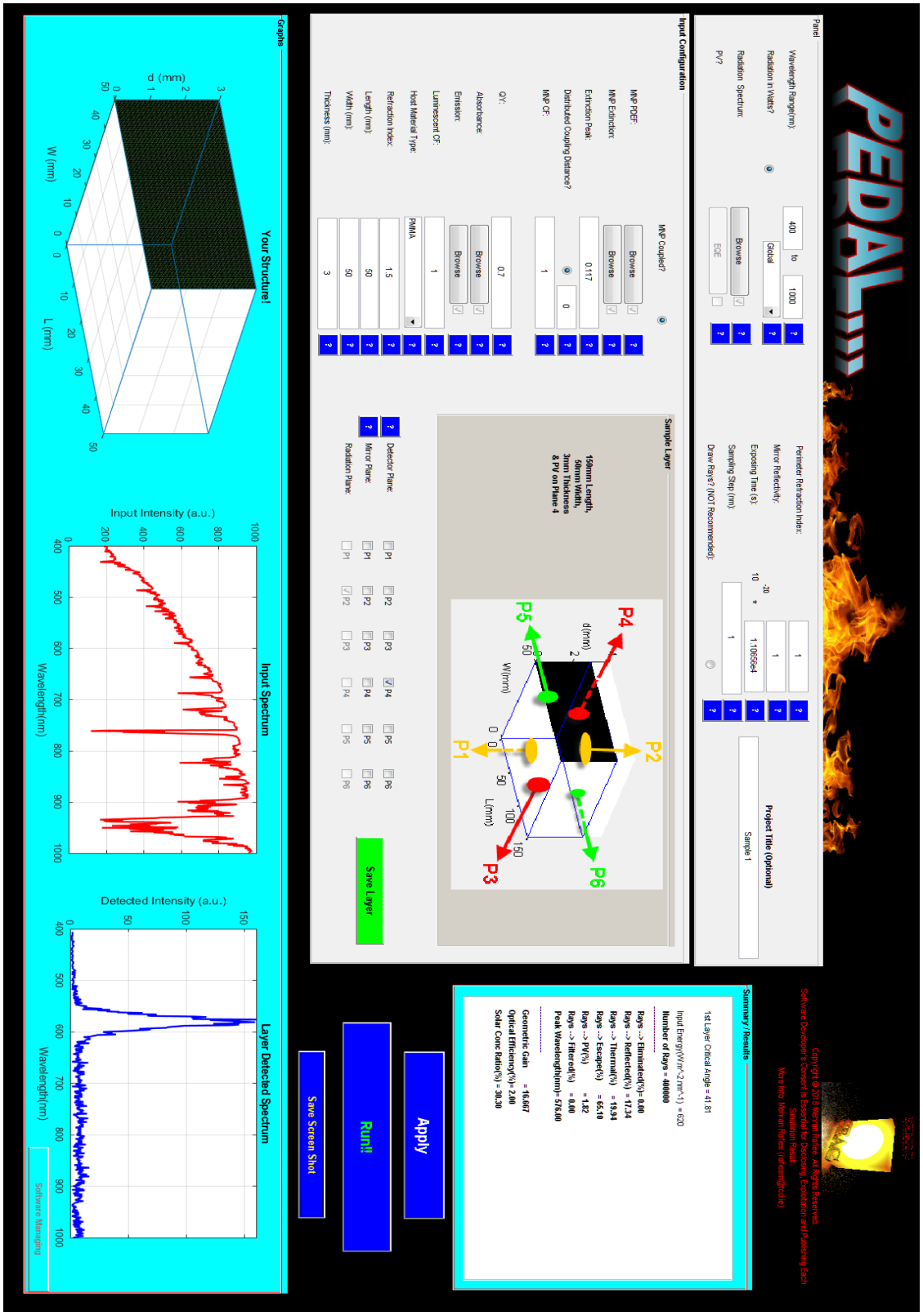

Fig. A.2: The designed GUI for the developed PEDAL program

Appendix 3: List of Publications

Patents (Under Process):

1. *Pedal Software: 3D Simulation Tool for Modelling of Plasmonically Enhanced Luminescent PV Devices,* (B.No. MR03-805-01 25/Jan/2019)

Publications (Published/Under Publication Process):

1. *An Overview of Various Configurations of Luminescent Solar Concentrators for Photovoltaic Applications,* Mehran Rafiee, Subhash Chandra, Hind Ahmed, and Sarah J McCormack, Optical Materials, 2019. 91, 212-227.
2. *A Unified Methodology for Fabrication And Quantication of Gold Nanorods, Gold Core Silver Shell Nanocuboids and Their Polymer Nanocomposites,* Arunima Sethi and Mehran Rafiee, , Subhash Chandra, Hind Ahmed and Sarah J McCormack, Langmuir ACS Publication, 2019, 35, 40, 13011-13019.
3. *Optical Coupling Sensitivity Study of Luminescent PV Devices Using Monte Carlo Ray Tracing Model*, Mehran Rafiee, Subhash Chandra, Hind Ahmed, Keith Barnham and Sarah J McCormack, In Renewable Energy and Sustainable Buildings (pp. 869-877). Springer, Cham.
4. *Absorption Coefficient Depended Non-linear Properties of Thin Film Luminescent Solar Concentrator,* Subhash Chandra, Mehran Rafiee, John Doran and Sarah McCormack, ELSEVIER-Solar Energy Materials and Solar Cells, 2018, 182, 331-338.
5. *Doping Concentration Tuning and Plasmonic Optical Properties Modelling of Metal Nano Particles Utilizing FDTD Method,* Mehran Rafiee, Subhash Chandra, Hind Ahmed, Aaron Glenn, Conor McLoughlin and Sarah J McCormack, Trans Tech Publications, 2019. (Under Publication Process)
6. *Towards Reducing Computational Costs of Finite Difference Time Domain Algorithm in Plasmonic Optical Properties Modelling of Metal Nanoparticles,* Mehran Rafiee, Subhash Chandra, Hind Ahmed, Conor McLoughlin, Aaron Glenn and Sarah J McCormack, Trans Tech Publications, 2019. (Under Publication Process)
7. *Latest Advances in Novel Plasmonic Lumienscent Solar Devices,* Sarah J McCormack, Mehran Rafiee, Arunima Sethi, Subhash Chandra and Hind Ahmed, Trans Tech Publications, 2019. (Under Publication Process)

Publications (Under Review):

8. *Small and Large Scale Plasmonically-Enhanced Luminescent Solar Concentrator for Photovoltaic Applications: Modelling, Validation and Optimisation*, Mehran Rafiee, Subhash Chandra, Hind Ahmed, Keith Barnham and Sarah J McCormack, Applied Energy. (Under Review)

Conferences:

1. *Optical Coupling Sensitivity Study of Luminescent PV Devices Using Monte Carlo Ray Tracing Model,* Mehran Rafiee, Subhash Chandra, Hind Ahmed, Keith Barnham and Sarah J McCormack, World Renewable Energy Congress – 18 & Exhibition (WREC), 30 July - 3 August 2018, Kingston University, London – UK.
2. *Monte Carlo Ray Tracing Modelling of Multi-Crystalline Silicon Photovoltaic Cell Enhanced by Luminescent Material,* Mehran Rafiee, Hind Ahmed, Subhash Chandra, Arunima Sethi and Sarah J McCormack, 7th World Conference on Photovoltaic Energy Conversion (WCPEC-7), 10-15 June 2018, Waikoloa, Hawaii, USA.
3. *Improving the Mathematical Model for Luminescent Down-Shifting Layers by Investigating their Loss Mechanisms,* Mehran Rafiee, Hind Ahmed, Subhash Chandra and Sarah J McCormack, 33rd European PV Solar Energy Conference and Exhibitions (EU PVSEC 2017), 24-29 September 2017, Amsterdam, Netherlands.
4. *Quantum Dot Luminescent Solar Concentrator: Optimization of Concentration and Thickness,* Mehran Rafiee, Subhash Chandra, Hind Ahmed, and Sarah J McCormack, 33rd European PV Solar Energy Conference and Exhibitions (EU PVSEC 2017), 24-29 September 2017, Amsterdam, Netherlands.
5. *Analysis of Luminescent Solar Concentrator Performance Using a Ray Tracing Algorithm: Modelling, Optimization and Validation,* Mehran Rafiee, Subhash Chandra, Hind Ahmed, and Sarah J McCormack 13th Photovoltaic Science, Applications and Technology Conference C99 (PVSAT-13), 5-7 April 2017, Bangor, UK.
6. *Application of concentrating plasmonic luminescent down-shifting layers for photovoltaic devices*, H. Ahmed, S. Chandra, Mehran Rafiee, A. Sethi, and S. J. McCormack. SPIE OPTO, 2017.
7. *An optimised Quantum Dot Solar Concentrator,* Ben Sexton, Subhash Chandra, Mehran Rafiee and Sarah J McCormack, ESEIA Conference on Smart Energy Systems in Cities and Regions, 10 - 12 April 2018, Dublin Institute of Technology, Dublin, Ireland.
8. *Novel Plasmonic Luminescent Solar Devices for Building Integrated Photovoltaic Systems,* Sarah J McCormack, Subhash Chandra, Mehran Rafiee, Arunima Sethi, Sarah Gilligan and Hind Ahmed, World Renewable Energy Congress – 18 & Exhibition (WREC), 30 July - 3 August 2018, Kingston University, London – UK.